INSTITUTE OF NATURAL AND APPLIED SCIENCES
UNIVERSITY OF ÇUKUROVA

Ph.D. THESIS

Eda ÇETİNÖRGÜ

INVESTIGATION OF STRUCTURAL, OPTICAL AND ELECTRICAL CHARACTERISTICS OF ZnO-SnO_2 THIN FILMS DEPOSITED BY FILTERED VACUUM ARC DEPOSITION SYSTEM

DEPARTMENT OF PHYSICS

ADANA / 2007

THE INSTITUTE OF NATURAL AND APPLIED SCIENCE
ÇUKUROVA UNIVERSITY

INVESTIGATION OF STRUCTURAL, OPTICAL AND ELECTRICAL CHARACTERISTICS OF ZnO-$Sn0_2$ THIN FILMS DEPOSITED BY FILTERED VACUUM ARC DEPOSITION SYSTEM

By Eda ÇETÎNÖRGÜ
A THESIS of DOCTOR of PHILOSOPHY
PHYSICS DEPARTMENT

We certify that the thesis titled above was reviewed and approved for the award of degree of the Doctor of Philosophy by the board of jury on 12/04/2007.

Signature:	Signature:... ,.....	Signature:__ .....
Prof. Dr. Yüksel UFUKTEPE	Prof. Samuel GOLDSMITH	Prof. Dr. Birgül YAZICI
Supervisor	Jury	Jury
Signature:	Signature:	
Prof. Dr. Metin OZDEMÎR	Prof. Dr. Emirullah MEHMETOV	
Jury	Jury	

This Ph.D Thesis is performed in Physics Department of the Institute of Natural and Applied Science of ÇUKUROVA University

Registration Number:

Prof. Dr. Aziz ERTUNÇ Director
The Institute of Natural and Applied Science Signature and Seal

This study was financially supported by the Research Found of Çukurova University. **Project Number .FBE.2004.D.4**

ABSTRACT

Ph.D. THESIS

INVESTIGATION OF STRUCTURAL, OPTICAL AND ELECTRICAL CHARACTERISTICS OF ZnO-SnO_2 THIN FILMS DEPOSITED BY FILTERED VACUUM ARC DEPOSITION SYSTEM

Eda ÇETİNÖRGÜ

DEPARTMENT OF PHYSICS
INSTITUTE OF NATURAL AND APPLIED SCIENCES
UNIVERSITY of ÇUKUROVA

Supervisor: Prof. Dr. Yüksel UFUKTEPE

Year: 2007, Pages: 299
Jury : Prof. Dr. Yüksel UFUKTEPE
Prof. Samuel GOLDSMITH
Prof. Dr. Metin ÖZDEMİR
Prof. Dr. Birgül YAZICI
Prof. Dr. Emirullah MEHMETOV

The objectives of the present research were the deposition of zinc stannate thin films using FVAD system, and the investigation of the effect of deposition conditions and the post-deposition annealing on the properties of deposited films. The chemical concentration, crystal structure, surface morphology, electrical resistivity and optical properties were determined. In addition, the characteristics of the zinc stannate thin films were compared with those of ZnO and SnO_2 thin films deposited using the same FVAD system. Chemical and thermal stability of the deposited films were also determined.

The ZnO-SnO_2 thin films were deposited using zinc cathodes that contained Sn with different atomic percentages by filtered vacuum arc deposition (FVAD) system on UV fused silica (UVFS) and glass substrates. The films were deposited using a range of background oxygen pressure, arc current, and substrate temperature. The oxygen background pressure was in the range 0.53 to 1.06 Pa. The substrate temperature was room temperature, 200 or 400 °C. The arc current of the vacuum arc was in the range 150 to 300 A and the deposition time was 60 s to 240 s. In addition, post-deposition annealing was applied and tested whether it improves the properties of deposited films in air or argon atmospheres.

Key Words: Filtered Vacuum Arc, ZnO-SnO_2, Optical Characterization, Resistivity, Chemical and Thermal Stability.

ÖZ

DOKTORA TEZİ

FİLTRELİ VAKUM ARK DEPOLAMA SİSTEMİYLE ÜRETİLEN ZnO-SnO_2 İNCE FİLMLERİN YAPISAL, OPTİKSEL VE ELEKTRİKSEL ÖZELLİKLERİNİN İNCELENMESİ

Eda ÇETİNÖRGÜ

ÇUKUROVA ÜNİVERSİTESİ
FEN BİLİMLERİ ENSTİTÜSÜ
FİZİK ANABİLİM DALI

Danışman: Prof. Dr. Yüksel UFUKTEPE
Yıl: 2007, Sayfa: 299
Jüri : Prof. Dr. Yüksel UFUKTEPE
Prof. Samuel GOLDSMITH
Prof. Dr. Metin ÖZDEMİR
Prof. Dr. Birgül YAZICI
Prof. Dr. Emirullah MEHMETOV

Araştırma konusunun amaçları ZnO-SnO_2 ince filmleri FVAD sistemini kullanarak depolamak, ve depolama koşullarının etkileri ve depolama sonrası tavlama işleminin depolanan filmlerin özelliklerine etkisinin araştırılmasıydı. Kimyasal komposisyon, kristal yapı, yüzey morfolojisi, elektriksel özdirenç ve optik özellikler belirlendi. Ek olarak, depolanan ZnO-SnO_2 ince filmlerin karakteristikleri aynı FVAD sistemini kullanarak üretilen ZnO, ve SnO_2 ince filmler ile karşılaştırıdı. Depolanan filmlerin kimyasal ve ısısal kararlıklarıda aynı zamanda test edildi.

ZnO-SnO_2 ince filmler farklı Sn atomik konsantrasyonları içeren çinko katotlar kullanılarak UV fuse silica (UVFS) ve cam alttabanlar üzerine FVAD sistemiyle üretildi. Filmler farklı oksijen basınç, ark akım, ve alttaban sıcaklıkları kullanılarak depolandı. Oksijen basıncı 0.53 Pa -1.06 Pa aralığında alındı. Alttaban sıcaklığı oda sıcaklığı, 200 veya 400^{o}C olarak ayarlandı. Vakum ark akımı 150-300 A ve depolama zamanı 60-240 s aralığındaydı. Ek olarak, depolanan filmlerin özelliklerinin hava veya argon atmosferinde iyileştiği depolama sonrası uygulanan tavlama ve testle belirlendi.

Anahtar Kelimeler: Filtreli Vakum Ark, ZnO-SnO_2, Optik Karakterizasyon, Özdireç, Kimyasal ve Termal Dayanıklılık.

ACKNOWLEDGMENTS

Productive research and educational achievement require the collaboration and support of many people. A Ph.D. project is no exception, and in fact its building blocks are laid over the years with the contribution of numerous people. As I complete this thesis, bringing to a close another chapter in my life, I wish to take this opportunity to write a few lines to express my gratitude and appreciation to the many people who have assisted and supported me in this long journey. This is perhaps the easiest and at the same time hardest chapter which I have to write. It will be simple to name all the people that helped to get this done, but it will be tough to thank them enough. I will nonetheless try, and if your name is not listed, rest assured that my gratitude is not less than for those listed below.

I would like to thank all my colleagues in the Department of Physics at the University of Çukurova, especially those who had direct supervision of my work, namely: Prof. R. Esen for direction and guidance at the beginning of my studies; and my supervisor, Prof. Y. Ufuktepe for his support during the last two years; my committee members, Prof. M. Özdemir, and Prof. Emirullah Mehmetov, and Prof. B. Yazıcı through title changes, indeed entire project changes, leaves of absence and more so they too deserve my thanks. In addition, I am grateful to all my friends from the physics department of the university of Çukurova, for being a surrogate family during the many years and assisting me in many different ways to run smoothly. From the staff, Güzide Ünlü and Dr. Cebrail Gümüş, Yiğit Yıldız, Filiz Karaömerlioğlu and my closest friend Gülçim is especially thanked for her care and attention and deserve special mention.

All of the work was performed in the Electrical Discharge and Plasma Laboratory at Tel-Aviv University in Israel where I met wonderful people. Each of them left something in my heart and increased my scientific knowledge through countless discussions. I would like to express my gratitude to all colleagues who contributed in many ways to my work described in this thesis; I am sincerely grateful to my supervisor, Professor Reuven (Raymond) Boxman, for giving me the

opportunity to work with him and his help and advice during the two years in his lab. His guidence, inspiration, encouragement and help in every aspect of this work and critical reading of this thesis and enormous suggestions on this work would have been beneficial. I am especially indebted to you Ray, for accepting me and helping to open another chapter in my life. In addition, to Dr. Valdimir Zhitomirsky, Dr. Evegeny Gidalevich, Dr. Nahum Parkansky, Dr. Boris Alterkop, Dr. Yitzhak Beilis, Mr. Michael Govberg, Mr. Yohanan Sivan, Mr. Zedu (Dudu) Abunie, Mr. Dima Grach, Mr. Dima Gindin, Miss Orly Goldstein, Mrs Lisa Vinokorov, Mr. Arie Shnaiderman, Mr. Harry Marks, and special thanks to Mr. Alexey Shashurin for technical help during my experiments and your friendship. Thanks for all good happy moments of scientific or personal discussions in the laboratory.

I must also thank Dr. Larissa Burstein for XPS, Dr. Zahava Barkay for AFM and EDS/SEM, Dr. Yuri Rosenberg for XRD, Dr. Lev Nagli for spectrophotometry and Mr. Mark Oksman for spectroscopic ellipsometry measurements. Their incurable enthusiasm for the work and experience with the process allowed them to both encourage me and commiserate with me appropriately. Their timely comments were invaluable.

My overwhelming thanks goes to my advisor and committee chair, Prof. Samuel (Shmuel) Goldsmith, who has in every way been available as a resource be it emotionally, socially, scholarly, or administratively. I can not overstate the importance of his involvement in my graduate career and life. In a strange sense, I am sorry to see the thesis finished since our discussinons about physics, literature, music were such an encouraging and rejuvenating part of my life. His family, particularly his wife Racheal, put up with my frequent visits and often frantic phone calls; a courtesy for which I am very grateful. Dear Shmuel, with your enthusiasm, inspiration, and great efforts to explain things clearly and simply, you helped to make many things fun for me. Throughout my thesis-writing period, you provided encouragement, sound advice, good teaching, good company, and lots of good ideas. I would have been lost without you. If I could call somebody as my best friend you are the one that is always there being for me. Although, I know that it is not enough to say “thank you”, I want to thank you for all the things you gave and showed me.

My final words go to my family and my parents and my brother;

I would like to thanks my aunt Ferah her husband Mustafa, my uncle Öner, my dearest grandmother and all my cousins specially to Gökçe (my princes) believing and encouraging me during all these years.

I am forever indebted to my mother (Pınar), my father (Ali) and brother (Ahmet) for their understanding, endless patience and for always being with me, drying my tears, making me laugh and strongly supporting me when I needed it, and offering a hand during this long journey. They bore me, raised me, supported me, taught me, and loved me no matter the long absense. They always encouraged me to do what I wanted to do, and to fight for it. Overall they taught me that love recognises no barriers or no time.

Last but not least important to my father because I wish you could have seen me finishing this thesis... although I know you have...

I love all of you...

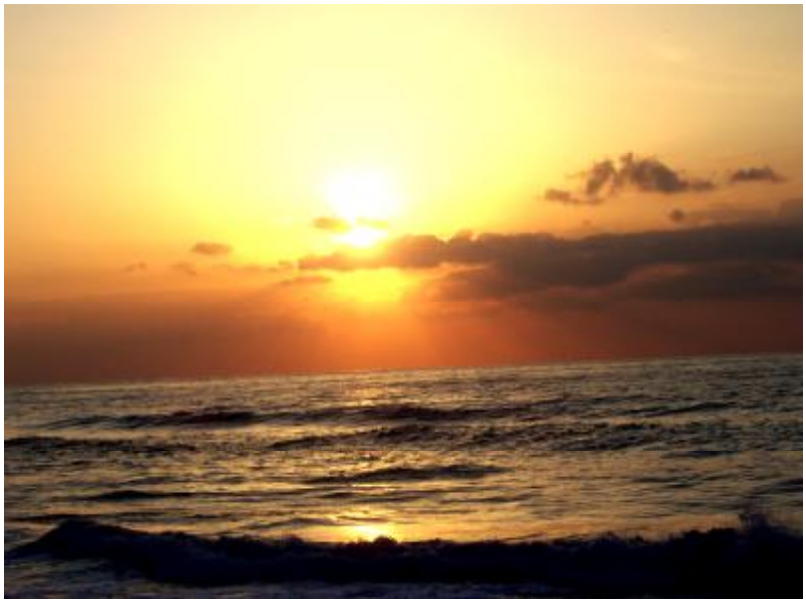

Tel-Aviv Beach (2007)

CONTENTS **PAGE**

TABLE CAPTIONS **PAGE**

FIGURE CAPTIONS **PAGE**

SYMBOLS AND ABBREVIATIONS

f_b	:Potential Barrier
f_w	:Work Function
$\vec{p}$	:Induced Dipole Moment
$\vec{P}$	:Macroscopic Polarization
c	:Light velocity, lattice spacing
d_{cal}	:Calculated Thickness
d_{mea}	:Measured Thickness
I_{arc}	:Arc Current
I	:Current
I_i	:Incident Light Intensity
I_t	:Transmitted Light Intensity
I_r	:Reflected Light Intensity
D	:Grain Size
n_c	:Number of Crystallites
n_e	:Electron Density
n_i	:Ion Density
n_p	:Common Charged Particle Density
n_g	:Gas (Neutral) Density
p	:Pressure
l	:Electrode Distance and Sample Length
d	:Film Thickness
b	:Sample Width
$t_{1,2,3}$	:Probe Distances
r_c	:Charge Density
$\vec{H}$	:Magnetic Field
m	:Magnetic Permability
m_o, m_g	:Mobility and Grain Boundary Mobility
e	:Dielectric Function
$\vec{J}$	:Current Flux
$\hat{q}$, $\hat{k}_i$	:Wave Vector
$m_{e,h}$	:Electron (e), Hole (h) Effective Mass
e	:Electric Charge
C_{ij}	:Elastic Stiffnes Constant
$\hat{D}$	:Complex Displacement
f_{ij}	:Oscillator Strength

N_e :Formal Anion Valency
N_c :Nearest Neighbor Cations Coordinate Number
$N_{1,2}$:Number of Carrier in Grains and Grain Boundaries
Z_a :Effective Number of Valance Electrons Per Anion
r :Electrical Resistivity
$R_{s,r}$:Sheet Resistance, Resistance
R :Surface Reflection
E_g, E^t :Optical ($_g$) and Vertical (^{t}) Energy Band Gap
$\vec{E}$:Electric Field
E :Energy
E_b :Binding Energy
E_o :Oscillator Energy
E_d :Dispersion Energy
$E_{s,n}$:Conductivity ($_\sigma$) and Carrier ($_n$) Activation Energy
E_k :Kinetic Energy
$\tilde{N}$:Complex Refractive Index
n :Refractive Index
k :Extinction Coefficient
n, w :Frequency
w_o :Resonance Frequency
l :Wavelength
y :Psi
D :Delta
G :Damping Coefficient
Å :Angstrom
W_{vol} :Volume of the Crystal
s_{st} :Stress
s :Conductivity
a :Absorption Coefficient
$\hat{a}$:Complex atomic Polarizability
$N_d(E)$:Density of States
T :Transmission
T_{exp} :Measured Transmission
T_c :Calculated Transmission
T_{sub} :Substrate Transmission
T_p :Plasma Temperature
T_i :Ion Temperature
T_e :Electron Temperature
T_s :Substrate Temperature
T_{sub} :Substrate Transmission

$\mathbf{T_m}$	**:**Melting Temperature
V	**:**Voltage
$\mathbf{V_B}$	**:**Breakdown Voltage
x_i	**:**Fractional Ionization of Plasma
c^2	**:**Chi Square
c_e	**:**Macroscopic Electric Susceptibility
Y	**:**Sputter Yield
AES	**:**Auger Electron Spectroscopy
AFM	**:**Atomic Force Microscopy
AZO	**:**Al doped Zinc Oxide
BEMA	**:** Bruggeman Effective Medium Approximation
CEMS	**:**Conversion Electron Mössbauer Spectroscopy
CRT	**:**Cathod Ray Tube
CSP	**:**Chemical Spray Pyrolysis
CVD	**:**Chemical Vapor Deposition
DC	**:**Diode
DLE	**:**Deep Level Emission
DOS	**:**Density of States
EDS	**:**Energy Dispersive Spectroscopy
EMA	**:**Effective Medium Approach
EPMA	**:**Electron Probe Microanalyses
ESCA	**:**Electron Spectroscopy for Chemical Analyses
FTIR	**:**Fourier Transform Infrared
FVAD	**:**Filtered Vacuum Arc Deposition
FWHM	**:**Full Width Half Maximum
HRSEM	**:**High Resolution Scanning Electron Microscopy
IAD	**:**Ion Assisted Deposition
IBS	**:**Ion Beam Sputtering
IR	**:**Infrared
ITO	**:**Indium Tin Oxide
KK	**:**Kramer Kroning
MBE	**:**Molecular Beam Epitaxy
MCS	**:**Multi Cathode Spots
MP	**:**Macroparticle
MSE	**:**Mean Square Error
NBE	**:**Near Band Edge
NIR	**:**Near Infrared
PC	**:**Polycarbonate
PECVD	**:**Plasma Enhanced Chemical Vapor Deposition
PL	**:**Photoluminescence

PLD :Pulsed Laser Deposition
PMMA :Polymethylmethacrylate
PVD :Physical Vapor Deposition
RBS :Rutherford Backscattering
RF :Radio Frequency
RIE :Reactive Ion Etching
RMS :Root Mean Square
RT :Room Temperature
RTA :Rapid Thermal Annealing
SCS :Single Cathode Spot
SE :Spectroscopic Ellipsometry
SEM :Scanning Electron Microscopy
SPM :Scanning Probe Microscopy
SS :Sum of Squares
STM :Scanning Tunelling Microscopy
SZM :Structure Zone Model
TCO :Transparent Conducting Oxide
TEM :Transmission Electron Microscopy
TL :Tauc-Lorentz
TO :Tin Oxide
UPS :Ultraviolet Photoelectron Spectroscopy
UV :Ultraviolet
UVFS :Ultraviolet Fused Silica
VAD :Vacuum Arc Deposition
VAPE :Vacuum Arc Plasma Evaporation
VASE :Variable Angle Spectroscopic Ellipsometry
VIS :Visible
XPS :X-ray Photoelectron Spectroscopy
XRD :X-ray Diffraction
ZTO :Zinc Stannate

1. INTRODUCTION

1.1. Preface

This work is part of the requirements for a PhD degree in physics at Çukurova University. The research was conducted in the Electrical Discharge and Plasma Laboratory at Tel-Aviv University. The research subject is the investigation of the characteristics of ZnO, SnO_2, ZnO:Sn and zinc stannate thin films, the latter is being one of the promising transparent and conducting oxide materials (TCOs).

TCO thin films are semiconducting materials with a large energy band gap and also have relatively high electrical conductivity, high optical transmittance in the visible region, and high reflectance in the IR region. This unique combination of physical properties: transparency and electrical conductivity, makes them suitable for a variety applications in optoelectronic devices. Consequently, various techniques for the growth of these films have been recently intensively investigated. The growth technique plays a significant role in determining the properties of these films, because the same material deposited by two different techniques usually may have different micro and macro properties. The simultaneous occurrence of high optical transparency (>80%) in the visible spectrum and low electrical resistivity (10^{-3} Ωcm or less) is not possible in an intrinsic stoichiometric oxides, because of the large optical band gap (>2 eV). Partial transparency and fairly good conductivity may be obtained in very thin (≤ 10 nm) films of metals. On the other hand, the only way to have transparent conductors is to populate the conduction band with electrons in spite of the wide band gap by controlled creation of non-stoichiometry or the introduction of appropriate dopands. These conditions are very conveniently obtained in oxides of cadmium (Cd), tin (Sn), indium (In), zinc (Zn) and their alloys in thin film form, prepared by a number of different deposition techniques. The first report of a transparent conducting oxide (TCO) was published in 1907, when Badeker reported that thin films of Cd metal deposited in glow discharge chamber could be oxidized to become transparent while remaining electrically conducting. Since then, the commercial value of these thin films has been recognized, and the

transparent and electrically conducting oxide films (TCO), e.g., In_2O_3:Sn (ITO), SnO_2 (TO), ZnO and ZnO:Al (AZO), have been extensively studied owing to their variety of applications in optoelectronic devices and as gas sensors. The optoelectronic applications include the following: transparent electrodes for flat panel displays, solar cells, light emitting diodes, and transparent heating elements for aircraft and automobile windows, heat reflecting mirrors for glass windows, and antireflection coatings (Chopra ***et al.***, 1982, and Minami, 2005). However, the application of ZnO and SnO_2 thin films is sometimes limited because these materials could become unstable in certain chemically aggressive and/or elevated temperature environments. Thus, while ZnO films are more stable in activated hydrogen environments than SnO_2 and ITO, they are neither stable in oxidizing environments at high temperatures, nor are they chemically stable in acidic and basic solutions. In contrast, SnO_2 films show high stability in acidic and basic solutions and oxidizing environments at high temperatures, but they are easily reduced by hydrogen-activated plasma at high temperatures. These instability problems of ZnO and SnO_2 films are especially apparent when they are prepared on substrates at low temperatures and without doping.

Until recently, the electro-optical properties of the TCOs have not severely limited their performance in flat-panel displays or other optoelectronic devices. However, it has become apparent in recent years that this situation will not persist indefinitely, and that there will inevitably be a need for TCOs of superior properties with the continued development of these devices. As the areas of major applications of TCOs increase, demand will grow for materials having lower sheet resistance while retaining good optical properties. New materials must be developed with lower resistivity than previously achieved and with optical properties superior to those of the present generation of TCOs.

One family of new transparent conducting oxide materials is based on the combinations of ZnO and SnO_2 materials. One of these attractive Zn-Sn-O materials is zinc stannate with two phases, $ZnSnO_3$ and Zn_2SnO_4. They are attractive because they are composed of non-toxic and inexpensive elements. This ternary TCO material is promising for future research, as proposed by Minami (2005), since they

have high transmission both in visible and also the near IR spectral regions and their electrical, optical, chemical and physical properties can be changed by altering the chemical composition. The research on advanced TCO materials also focuses on applying other deposition methods. The various deposition methods intended to obtain a wide spectrum of TCO thin films include: spray pyrolysis, sol-gel, pulsed laser deposition (PLD), vacuum arc evaporation, magnetron sputtering, and filtered vacuum arc deposition (FVAD). Using FVAD systems, thin SnO_2, ZnO, AZO, Sb doped SnO_2 and Sb doped ZnO films were deposited at relatively higher deposition rates. The as-deposited TO films were *n*-type semiconductors with electrical resistivity in the range $(5\text{-}8)\times10^{-4}$ Ωcm, and film transmittance in the visible range was up to 85%. The resistivity of the Sb doped TO films did not change with the doping; however, annealing these samples in air up to 350°C decreased the resistivity by ~20%. Furthermore, the average resistivity of the undoped ZnO films was $\sim10^{-2}$-10^{-3} Ωcm, and crystalline ZnO and ZnO:Sb thin films (100-900 nm) were deposited at rates up to 14 nm/s (David *et al*., 2004, 2005). The physical characteristics of these films (electrical conductivity, light transmittance, internal stress, structure and chemical composition) were shown to significantly depend on the deposition parameters – background pressure of oxygen, vacuum arc current and deposition duration.

However, the application of FVAD method to deposit zinc stannate (ZTO) or a film consisting of a combination of ZnO and SnO_2 has not yet been investigated. Thus, the proposed research will investigate the physical characteristics of FVA deposited ZnO, SnO_2, ZnO:Sn and zinc stannate transparent conducting oxide thin films.

1.2. Objectives and Their Significance

The objectives of the present research are:

1. Deposition of zinc stannate thin films using a FVAD system.

2. Defining the deposition condition for films with the highest optical transmission, lowest electrical resistivity, and good stability in acidic and basic environments.
3. Comparing the characteristics of the zinc stannate thin films to those of ZnO and SnO_2 thin films deposited using the same FVAD technique and apparatus.

The program to achieve the research objectives consists of the following steps:

- Deposit ZnO, SnO_2, ZnO:Sn and zinc stannate thin films using a dc FVAD system, applying various deposition parameters.
- Characterize the deposited films.
- Correlate deposition parameters with physical properties.
- Optimize the optical transmission and the conductivity of FVA deposited ZnO, SnO_2, ZnO:Sn and zinc stannate thin films.
- Study the effect of annealing on the characteristics of ZnO, SnO_2, ZnO:Sn and zinc stannate thin films.
- Study the effect of an aggressive environment on film characteristics (Acidic/Basic environments, and temperature dependence of resistivity).

It is expected that by studying the various deposition parameters of ZnO, SnO_2, ZnO:Sn and zinc stannate thin films, some improved thin films might be discovered. The research for an improved TCO involves the study of the structural, electrical and optical properties as a function of the deposition parameters of the films. Highly transparent, conducting and stable ZnO, SnO_2, ZnO:Sn and zinc stannate thin films will be determined. These films have the potential to overcome current TCO problems such as instability at high temperatures and with time.

1.3. Principal Results

In this research, ZnO, SnO_2, ZnO:Sn and zinc stannate thin films have been grown by filtered vacuum arc deposition (FVAD), using the following atomic percentage of Sn: 0at.%, 10at.%, 30at.%, 50at.% and 100at.%. The oxygen background pressure was generally 0.53 to 1.06 Pa, and was varied in steps of 0.13 Pa. The substrate temperatures were room temperature (RT), 200, 400 and 500°C. The vacuum arc currents were 150, 200, 250 and 300 A, and the deposition time was varied between 30 s to 240 s depending on material and deposition conditions used. The effect of post-deposition annealing in air and Ar atmospheres was studied, the chemical stability of films was tested in acidic, basic solutions, and the effect of high temperature on the resistance was studied. The deposited films were characterized using the following diagnostics:

- Thickness: surface profilometry (Alfa-Step),
- Composition: X-ray photoelectron spectroscopy (XPS)
- Film structure: X-ray diffraction spectroscopy (XRD)
- Surface morphology: atomic force microscopy (AFM) and scanning electron microscopy (HRSEM)
- Resistivity: two or four probes method
- Optical parameters: normal incidence transmission and variable angle spectroscopic ellipsometry (VASE)

The thickness of the films was measured using Alfa-Step profilometry and was also derived from the optical analysis. The thickness depended on the deposition oxygen pressure, arc current and the deposition time. The highest deposition rate was 11 nm/s.

A significant correlation between the cathode and film compositions was observed. Thin films of ZnO and SnO_2 were non-stoichiometric, having a deficiency

or excess of O, respectively. The deposition of ZnO and SnO_2 thin films on heated substrates and annealing of the films produced stoichiometric films. Furthermore, the average percentage of the Sn in the film was close to that in the cathode for Zn:Sn alloy cathodes, but varied slightly with the deposition pressure. The films deposited using 50at.% Sn cathodes were close to the stoichiometric zinc stannate (Zn:Sn:O) thin films with atomic concentration ratio 2:1:4. In addition, it was found that the film surface contained a high percentage of carbon and a small percentage of Cu which can be attributed to the absorption of CO_2 from the atmosphere and Cu from the Cu cathode cup, respectively.

The polycrystalline ZnO thin films had a *c*-axis orientation (strong (002) diffraction line) under all deposition conditions used. The XRD data indicated that the crystalline quality of the film was improved by substrate heating (400^{o}C) and also by annealing in argon (Ar) atmosphere at 400 and 600^{o}C. The grain size was in the range 12-59 nm, and increased with substrate and annealing temperatures. Similar results were also observed from AFM and HRSEM analyses. The deposited films were mostly compressively stressed. However, post-deposition annealing produced tensile stress.

The room temperature (RT) deposited SnO_2 films were amorphous, independent of the deposition pressure and the arc current used. However, polycrystalline SnO_2 films were produced on 400^{o}C heated substrates, and the annealing improved the crystallinity of RT deposited films. The calculated average grain size using AFM was ~20 nm for films deposited on 400^{o}C substrates, and the annealing increased grain size up to 34 nm. The surface grain size of films deposited on heated substrates and also annealed films also showed similar results with XRD analyses.

All zinc stannate thin films deposited on RT and 400^{o}C substrates were amorphous, and annealing in Ar at 500^{o}C for 50 min, and in O_2 at 500^{o}C for 60 min did not change their structure. AFM analyses indicated an improvement in surface structure with increased substrate temperature in which the deposited films had smoother (less rugged) surface.

The average optical transmission of the films was in the range 80-90%, and was affected by substrate heating and post-deposition annealing. The optical transmission edge of all films shifted to shorter wavelengths with increasing substrate or annealing temperature, indicating improved UV transmission. The average optical transmission of ZnO thin films increased with annealing temperature in the visible spectral region. In contrast, SnO_2 and zinc stannate film transmission was strongly affected in the UV region but not in the VIS. The measured transmission and ellipsometer spectra were analyzed by utilizing the single dielectric oscillator or Tauc-Lorentz (TL) oscillator model with Gaussian broadening. The parametric semiconductor model was used for ZnO and SnO_2 films since they had a graded film structure whereas for the homogeneous zinc stannate films the TL model was used. The complex refractive index, with real and imaginary parts, $n(\lambda)$ and $k(\lambda)$, were derived from the relation $\varepsilon(\lambda) = (n(\lambda)–ik(\lambda))^2$. An interface layer, representing an upper surface layer, was assumed between the bulk of the film and air interface. Application of this model decreased significantly the mean square error (MSE) of the fit from 33 to 12 or less depending on the film and deposition conditions, where MSE value indicates the quality of fitting, wherein the ideal case MSE=1. For all films, the derived refractive indices and the extinction coefficients decreased with increasing wavelength and were in the range 2.3 to 1.85 and 0.5 to ~0, respectively. The zinc stannate films had higher n and k than ZnO and SnO_2 films. Substrate heating and the post-deposition annealing lowered the optical constants. Generally, no correlation was observed between the deposition pressure and the optical constants of the films.

The optical energy band gap, E_g, of the films was determined, assuming a direct optical transition between the valance and conduction bands. The E_g values for as-deposited ZnO and SnO_2 films were ~3.2 eV and 3.9 eV, respectively. Annealing in Ar increased E_g for SnO_2 films up to 4.35 eV, but no significant change was observed for ZnO films. In addition, the optical energy band gap of ZnO:Sn and zinc stannate thin films increased with Sn concentration (Sn: 10at.%, 30at.% and 50at.%) from 3.4 eV to 3.7 eV for as-deposited films.

The electrical resistivity depended on the oxygen background pressure during growth, the substrate temperature, the Sn concentration in the films, and the annealing temperature. The resistivity of ZnO and the SnO_2 films decreased with increasing deposition pressure and were ~ 10^{-2} and 10^{-3} Ωcm, respectively. However, all RT deposited ZnO:Sn and zinc stannate thin films were highly resistive while increased substrate temperature with high deposition pressure (~0.80 Pa) produced conducting films with resistivity 10^{-2} Ωcm.

The chemical stability of deposited thin films was tested in HCl (18%) and NaOH (15%) solutions for 27 h. The ZnO thin films deposited on RT and 400^{o}C substrates were dissolved after ~10 min of immersion in both solutions. The RT deposited zinc stannate thin films were also dissolved after approximately in 2 h immersion in the solutions. However, zinc stannate thin films deposited on 400^{o}C substrates were more stable than the RT deposited ones, as they did not dissolve after 27 h in NaOH, but they did dissolve in HCl after 2 h. SnO_2 thin films deposited on RT substrates were immersed in HCl solution dissolved after 2 h, however, those immersed in NaOH did not dissolved after 27 h, whereas, the immersion in HCl, and NaOH of 400^{o}C deposited SnO_2 thin films did not affect their optical properties. Similarly, the electrical properties of SnO_2 thin films deposited on RT and 400^{o}C was not affected by the immersion in both solutions whereas, the effect of immersion in acidic and basic solution on the electrical properties of zinc stannate thin films could be studied for films deposited on 400^{o}C substrates. In this case the immersion in NaOH solution did not affect the electrical properties of films, which remained ~10^{-2} Ωcm.

Thermal stability of the film resistance was determined using a two point probe technique in the range 28^{o}C (RT) to 200^{o}C. The resistance of zinc stannate thin films was less affected by heating than ZnO and SnO_2 films.

1.4. Publications

Most of the results in this thesis have been published in the following papers:

1. E. Çetinörgü, S. Goldsmith, and R.L. Boxman, "Air annealing effects on the optical properties of ZnO-SnO_2 thin films deposited by a filtered vacuum arc deposition system", Semicond. Sci. Technol., 21, 364-9 (2006).

2. E. Çetinörgü, S. Goldsmith, and R.L. Boxman "Optical Properties of ZnO-SnO_2 Thin Films Deposited by Filtered Vacuum Arc", J. Phys. D: Appl. Phys., 39(9) 1878 (2006).

3. E. Çetinörgü, S. Goldsmith, V.N. Zhitomirsky, R.L. Boxman, C.L. Bungay, "Optical Characterization of ZnO Thin Films Deposited by Filtered Vacuum Arc System", Semicond. Sci. Technol., 21, 1303-1310 (2006).

4. E. Çetinörgü, S. Goldsmith, and R.L. Boxman, "Effect of Deposition Conditions on the Characteristics of ZnO-SnO_2 Thin Films Deposited by Filtered Vacuum Arc", Thin Solid Films, 515(3) 880 (2006).

5. E. Çetinörgü, S. Goldsmith, Z. Barkay, R.L. Boxman, "The Dependence of Filtered Vacuum Arc Deposited ZnO-SnO_2 Thin Films Characteristics on Substrate Temperature", J. Phys. D: Appl. Phys., :39, 5245 (2996)

6. E. Çetinörgü, S. Goldsmith, "The effect of substrate temperature on filtered vacuum arc deposited zinc oxide and tin oxide thin films" (Accepted/ J. Crystal Growth)

7. E. Çetinörgü, S. Goldsmith, R.L. Boxman, "The effect of annealing on filtered vacuum arc deposited ZnO thin films" (Accepted/ Surface and Coatings Technology)

8. E. Çetinörgü, S. Goldsmith, Yu. Rosenberg, R.L. Boxman, "Influence of annealing on the physical properties of filtered vacuum arc deposited tin oxide thin films" (Submitted to J. Non-Crystalline Solids)

9. E. Çetinörgü, S. Goldsmith, R.L. Boxman, "Post-deposition annealing on the optical properties of filtered vacuum arc deposited ZnO-SnO_2 (Accepted for publication in J. Phys. :Condens. Matter)

1.5. Outline of Thesis

The 1st chapter of thesis (Introduction) presents the back ground of the research, the objectives and their significance, and principal results with published papers.

The 2nd chapter (Literature Survey) presents a general overview of various deposition techniques, electrical discharges, vacuum arcs physics, and the optical and electrical properties of solids and semiconductors. In this section, some basic concepts and theory of FVAD technique, thin film formation and optical principles with some specific background of published work on ZnO, SnO_2 and zinc stannate films and characteristics are surveyed.

In the 3rd chapter (Experimental Apparatus and Procedures), the deposition apparatus and procedure, and the film analyses methods used in this study are presented and discussed.

In the 4th chapter (Experimental Results) the results of experiments are presented, and specifically the physical properties of FVAD ZnO, SnO_2, ZnO-SnO_2 and zinc stannate thin films are reported as functions of the deposition and post-deposition annealing conditions,.

In the 5th chapter (Discussion) the experimental results are discussed and compared to previously published data, and the conclusions from this work are summarized in chapter 6 (Conclusions).

In the final part of this thesis the references are listed and in the Appendix the optical analysis programs are shown.

2. LITERARTURE SURVEY

2.1. Introduction

In the following sections TCOs and their applications, thin film deposition techniques, the theoretical background of some physical properties of semiconductors, and some relevant published works on ZnO, SnO_2, zinc stannate and Zn-Sn-O thin films are presented. One of the major issues relevant for the deposition of TCO thin films is the effects of deposition conditions on the film properties and applicability. There is a strong correlation between the method, the deposition conditions and the obtained film properties. There have been several published works on the characteristics of ZnO and SnO_2 thin films deposited by filtered vacuum arc deposition (Goldsmith, 2006). In contrast, there has been no prior report of FVA deposited zinc stannate films. Hence, in this literature survey, while FVA deposited ZnO and SnO_2 thin films are reviewed, the review of ZnO:Sn, zinc stannate thin films only covers such films deposited by others methods. In addition, the effect of annealing on the characteristics of films obtained using FVAD and other deposition systems will also be reviewed.

2.2. Transparent Conducting Oxides (TCOs) and their Applications

Studies of transparent and highly conducting semiconducting oxide films have attracted the attention of many research workers due to their wide range applications both in industry and in research. Thin films of some metallic oxides, such as cadmium oxide and indium oxide, have been known for a long time to be optically transparent and electrically conducting. Thin films of cadmium oxide (CdO), produced by thermal oxidation of sputtered cadmium films, and were first reported by Badeker (1907). Thin films (~100-200 Å) of metals such as Ag, Mg, Cu, Fe, etc. have also been found to have similar properties, but these films, in general, are not very stable - they are affected by the environment, and their optical and electrical properties change with time. On the other hand, some metal oxide coatings

are widely applied because their stability and hardness are superior to those of thin metallic films.

The wide ranging applications of these coatings have prompted much research on their deposition and characterization. Various TCO films are applied in optoelectronics, including touch panels, and electroluminescent, plasma, and field emission displays. In addition, these coating are also used as heat reflective coatings, energy efficient windows, gas sensors, as transparent electrodes in photovoltaics cells, and as fire retarding materials. As transparent conductors, these films are also be used as vehicle and aircraft windscreen defrosters.

Heterojunction solar cells with an integral conducting transparent layer offer the possibility of fabrication of low-cost solar cells with performance characteristics suitable for large scale terrestrial applications. The conducting transparent film permits the transmission of solar radiation directly to the active region with little or no attenuation. In addition, the conducting transparent films can serve simultaneously as a low resistance conductor to the junction and as an antireflection coating for the active region. Solar cells utilizing these types of coatings are now widely fabricated, e.g. SnO_2/Si, In_2O_3/Si. Furthermore, these films can be used as gas sensors, by utilizing the large changes in their conductance produced by the charge exchange with absorbed gas molecules. The electron concentrations in the conduction band in a semiconductor sensor can vary approximately linearly with the pressure of the gaseous environment, over a range of up to eight decades, while variations in carrier mobility are generally small. This large and reversible variation in conductance with active gas pressure has made semiconducting materials attractive for the gas sensing devices (Hartnagel ***et al.***, 1995).

There is a large number of TCOs -- the most commonly known ones are the binary compounds, SnO_2, ZnO, In_2O_3, Ga_2O_3, and CdO. Doping is generally applied to improve their electrical conductivity, and the most common doped TCOs are In_2O_3:Sn, In_2O_3:F, SnO_2:F, SnO_2:Sb, ZnO:Al. In_2O_3:Sn (ITO) is the most commonly used TCO because of its excellent electrical and optical properties. However, there are several problems with ITO, in particular the high cost and scarcity of In, and in addition the tendency of ITO to fracture on flexible substrates. In the 1990s, an effort

was begun to develop other TCO films suitable to replace ITO. This effort involved the study of a variety of ternary and more complex TCO materials, such as Zn_2SnO_4, Cd_2SnO_4, $In_4Sn_3O_{12}$, and $GaInO_3$, based on combinations of binary compounds like ZnO, CdO, In_2O_3, and SnO_2, producing not only ternary compounds, but also some multi-component oxides composed of combinations of these ternary compounds. However, there are few reports on these materials. The use of ternary and multi-component oxides makes possible designing TCO films suitable for specialized applications because their electrical, optical chemical and physical properties can be controlled by altering their chemical composition. Although they have low resistivity, thin films containing Cd, such as In-doped CdO, Cd_2SnO_4, and $CdSnO_3$, are of lower practical use because of the toxicity and cost of these materials (Minami, 2000).

Consequently, there are efforts to improve and also develop new TCO compounds by doping zinc oxide (ZnO), tin oxide (SnO_2) and zinc stannate (ZTO), and by utilizing a variety of deposition techniques, e.g., spray pyrolysis, chemical vapor deposition (CVD), sputtering, pulsed laser deposition (PLD) and filtered vacuum arc deposition (FVAD), as TCO characteristics depend also on its deposition method.

2.3. Thin Film Deposition Techniques

As mentioned above, thin film properties are strongly dependent on the method of deposition, the substrate materials, the substrate temperature, the rate of deposition, and the background pressure. Specific applications in modern technology demand such film properties as high optical reflection/transmission, hardness, adhesion, non-porosity, high mobility of charge carriers, chemical inertness toward corrosive environments, and stability with respect to temperature. Somewhat less required properties are stoichiometric composition and high orientation in single crystal films. The need for new and improved optical and electronic devices stimulated, in addition, the study of thin solid films of single elements, as well as binary and ternary systems, with controlled composition and specific properties, and

has consequently accelerated efforts to develop different thin film deposition techniques. The thin film deposition techniques can be classified according to the scheme shown in (Figure 2.1):

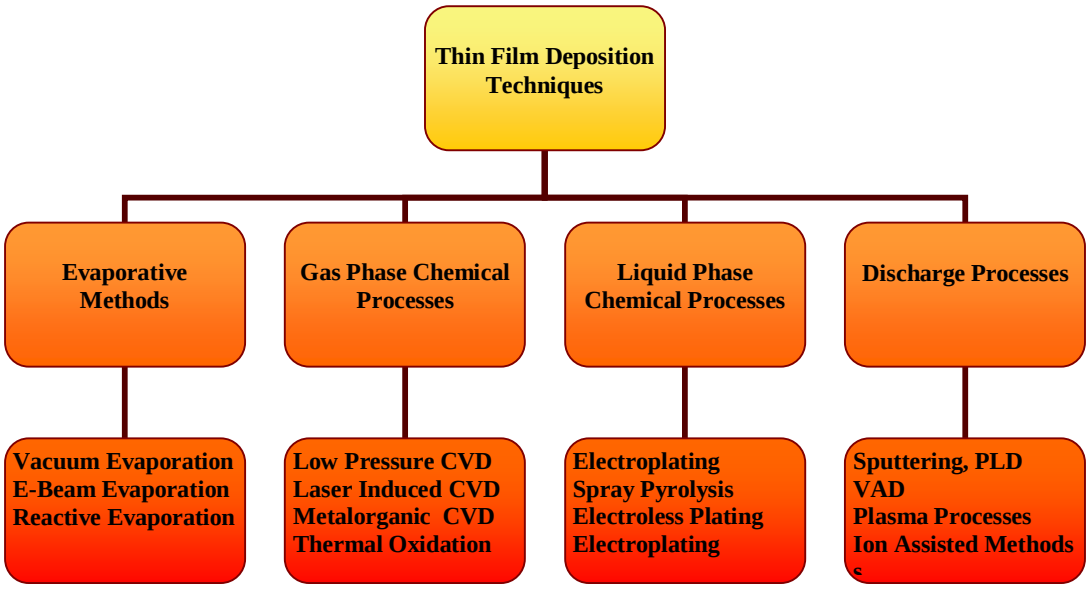

Figure 2.1. A schematic diagram of thin film deposition techniques

The common techniques that have been used to grow TCO films include Chemical Vapor Deposition (CVD), Spray Pyrolysis, Reactive Evaporation, Sputtering, Plasma Assisted Reactive Evaporation, Ion Beam Sputtering, Ion Plating and Filtered Vacuum Arc Deposition (FVAD). Each of these techniques has its own advantages and disadvantages. For example, spray techniques are very cheap, deposition parameters easily controllable but the produced films are unstable. On the other hand, among the thin films deposition techniques, the plasma processes produce good quality (e.g. good adhered thin films with a well defined microstructure, and high transmission and conductivity) TCO thin films.

The purpose of this section is to describe briefly the commonly used deposition techniques for TCOs with their advantages and disadvantages.

2.3.1. Vacuum Evaporation

Vacuum evaporation (including sublimation) is a physical vapour deposition (PVD) process where material is thermally vaporized from a source and reaches the substrate without collision with gas molecules in the space between the source and substrate. The trajectory of the vaporized material is "line-of-sight." Typically, vacuum evaporation is conducted in a gas pressure range of 10^{-5} to 10^{-9} Torr, depending on the level of contamination that can be tolerated in the deposited film (Seshan *et al.*, 2002). The basic system and evaporator source configurations are shown in Figure 2.2.

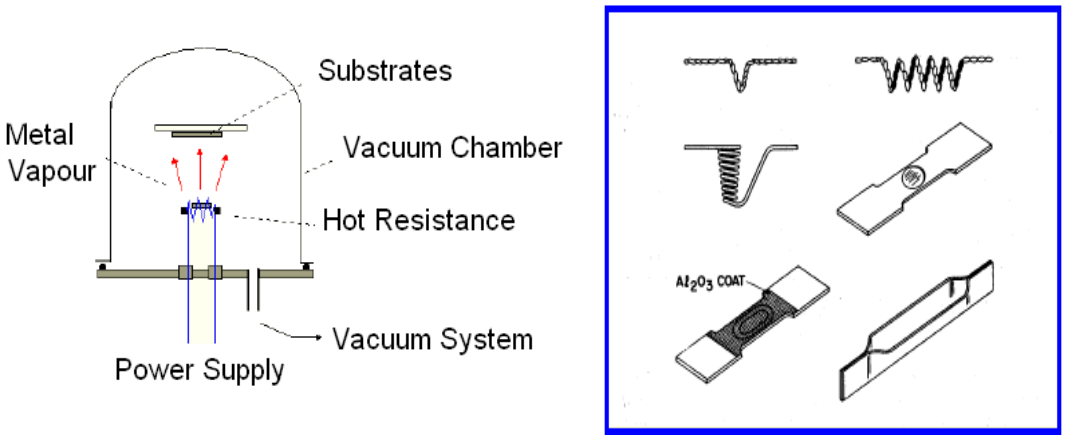

Figure 2.2. Conventional vacuum evaporation system and evaporator source configurations (Hartnagel *et al.*, 1995).

Deposition of thin films by evaporation is very simple and convenient, and is the most widely used technique. One merely has to produce a vacuum environment, and give a sufficient amount of heat to the evaporant to attain the desired vapor pressure, and allow the evaporated material to condense on a substrate kept at a suitable temperature (Harthanel *et al.*, 1995). The important process parameters are the substrate material, source and substrate temperatures, source-substrate distance, and background gas composition and pressure. . Evaporants with an extraordinary range of chemical reactivity and vapor pressures have been deposited. This variety

leads to a large diversity of source designs including resistance-heated filaments, electron beams, crucibles heated by conduction, radiation, or rf-induction, arcs, exploding wires, and lasers.

2.3.2. Spray Pyrolysis

Spray pyrolysis is basically a chemical deposition technique in which fine droplets of a solution containing the desired species are sprayed on a preheated substrate. The spray technique differs from other chemical solution deposition techniques in that the film is formed on a substrate kept outside the solution, which is sprayed onto the heated substrate to produce the final film, either by pyrolytic or hydrolytic chemical reaction of the liquid droplets. A typical reaction family is shown below:

$$MCl_x + yH_2O \rightarrow MO_y + xHCl \qquad \text{Eq. (2.1)}$$

in which *M* is the metallic element in the oxide film, e.g. Sn, In, Zn. Spray pyrolysis of TCO films such as SnO_2, ZnO, and In_2O_3, and recently zinc stannate films ($ZnSnO_3$) have been investigate extensively with the objective of meeting the demands in large area coatings. Although the thickness distribution of the deposited films is not very uniform, spray pyrolysis is of great practical interest, because in certain cases both small pieces and also large glass panels can be coated continuously in air and at reasonable temperatures (~400^{o}C).

A schematic diagram of a modern spray deposition technique is shown in Figure 2.3. Spray pyrolysis can easily adopted for mass production of large area coatings for industrial applications. Deposition rates and film thickness can be easily controlled, and the films can be conveniently doped by dissolving the required concentration of the dopant in the spray solution. There are relatively few process parameters which must be controlled -- flow of carrier gas Q, concentration of the solution, solution flow q, droplet radius, distance between nozzle and substrate,

temperature of gaseous environment, substrate temperature and speed through the furnace v.

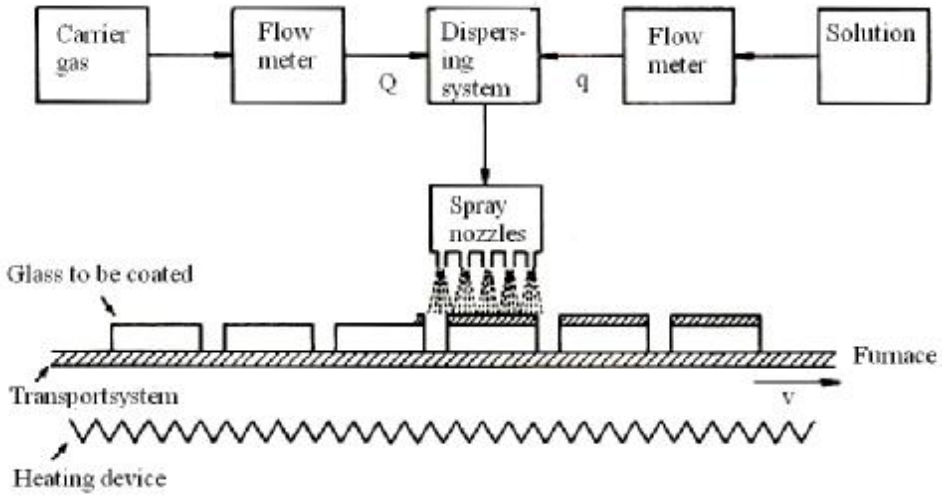

Figure 2.3. A schematic diagram for the conventional spray pyrolysis technique (Gläser *et al*., 2000).

Although this technique has the advantage of low equipment cost compared with vacuum deposition techniques, the overall cost of the materials is high when coating large areas. This is because only a small fraction of the material supplied to the spray is deposited on the substrate, and a large fraction of the droplets being carried out of the coating region. Also, many droplets, especially the small ones, vaporize before reaching the substrate and do not contribute to the formation of the required film. Attempts have been made to modify simple spray systems in order to produce homogeneous and reproducible films by ultrasonic spray pyrolysis (Pulker, 1984, and Hartnagel *et al*., 1995).

2.3.3. Chemical Vapor Deposition (CVD)

Chemical Vapour Deposition (CVD) is a material synthesis method in which the constituents in the vapour phase react to form a solid film on a substrate. Gas precursors can be used directly, and liquid precursors can be used with a bubbler, in

which a carrier gas is passed through the liquid. The chemical reaction is an essential part of this technique and should be well understood. Various types of chemical reactions are utilized in CVD (Figure 2.4) for the formation of solids. In one type of reaction, a vapor precursor that contains the material to be deposited is decomposed by reduction, e.g. using hydrogen at an elevated temperature. Decomposition is accomplished by thermal activation. Alternatively, plasma activation may be used to reduce or decompose the pre-cursor at a lower temperature than with thermal activation.

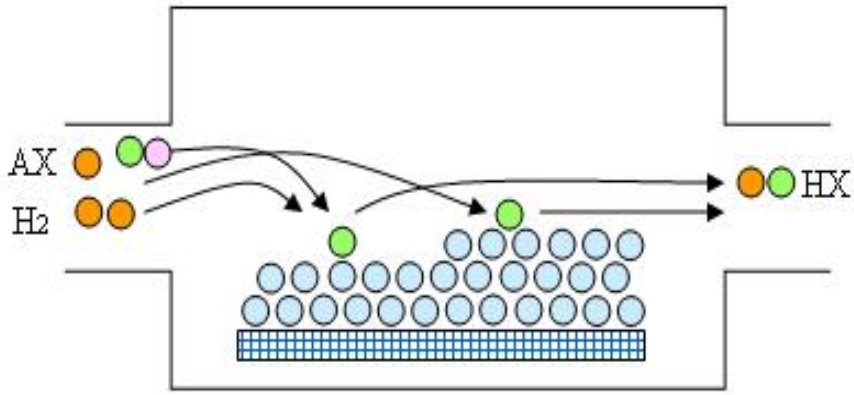

Figure 2.4. A schematic drawing of the CVD technique (Hartnagel *et al*., 1995).

CVD processes have numerous other names, such as metalorganic CVD when a plasma is used to induce or enhance decomposition and reaction; low-pressure CVD when the pressure is less than ambient; and low-pressure plasma enhanced CVD PECVD when the pressure is low enough that ions can be accelerated to appreciable energies from the plasma.

2.3.4. Pulsed Laser Deposition (PLD)

Pulsed laser deposition (PLD) is an evaporation technique in which a laser pulse is used to ablate target material, producing a local plasma jet. The plasma also contains energetic molecular clusters and macroparticles. The emission of these

macroparticles is a serious drawback. A solution to this problem is to use crossed laser induced evaporation plumes to discriminate macroparticles ejected from the target. The energy of the evaporated material depends on the laser pulse energy. The energy spectrum of the plasma particles consists of a major relatively low-energy component (1-100 eV) and a minor high-energy component (up to a few keV) (Gorbunov *et al.*, 1996). As this energetic impact of the evaporated material is kept responsible for a layer growth with smooth surfaces, a choice of the proper laser pulse energy is required. Each laser pulse evaporates a well-defined amount of material. Multilayer films can be very accurately controlled by varying the number of laser pulses.

2.3.5. Plasma Deposition Techniques

2.3.5.1. Plasma Fundamentals and Plasma Sources

Plasma is an ionized gas, which is basically a collection of charged particles free to move randomly or collectively under the influence of an electrical field, and is macroscopically electrically neutral as illustrated in Figure 2.5.

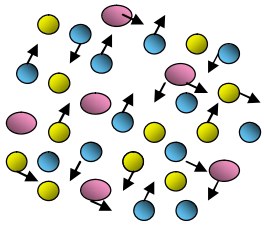

Figure 2.5. A schematic view of plasma (neutrals:blue, electrons:yellow and ions:pink) (Anders, 2000).

Plasma is often called the fourth state of matter. As we know, a solid substance in thermal equilibrium generally passes into a liquid state as the temperature is increased at a fixed pressure, and the liquid passes into a gas as the temperature is further increased. At a sufficiently high temperature, the molecules in the gas decompose to form a gas of atoms that move freely in random directions,

except for infrequent collisions between atoms. If the temperature is further increased, then the atoms decompose into freely moving charged particles (electrons and positive ions), and the substance enters the plasma state. This state is characterized by a common charged particle density $n_e \approx n_i \approx n_p$ particles/m^3 and, in equilibrium, a temperature $T_e = T_i = T$, where "e" and "i" indicate electron and ion. The temperatures required to form plasmas from pure substances in thermal equilibrium range from roughly 4000 K for easy-to-ionize elements to 20 000 K for hard–to-ionize elements. The fractional ionization of plasma is defined by:

$$x_{iz} = \frac{n_i}{n_g + n_i} \qquad \text{E.q. (2.2)}$$

where n_g is the retained neutral gas density. x_{iz} is unity for fully ionized plasmas, and $x_{iz} << 1$ for weakly ionized plasmas. Much of the matter in the universe is in the plasma state -- stars, as well as most interstellar matter, are plasmas. Although stars are plasmas in thermal equilibrium, the radiation and the charged particles are almost never in thermal equilibrium in low-pressure discharges, either between themselves or with their surroundings. Because these discharges are electrically driven and weakly ionized, the applied power preferentially heats the mobile electrons, while the heavy ions efficiently exchange energy by collisions with the background gas. Hence, for these plasmas T_e is higher than T_i. In Figure 2.6, different kinds of plasmas on a log n_p versus log T_e diagram are identified. There is an enormous range of densities and temperatures for both laboratory and space plasmas. Two important types of processing discharges, (1) low-pressure glow discharges and (2) high-pressure arc discharges, are indicated in Figure 2.6, where the glow is characterized by $T_e \approx 1$ to 10 eV, $T_i << T_e$, and $n_p \approx 10^8$ to 10^{13} cm^{-3}, and the arc by $T_e \approx 0.5$ to 2 eV and $n_p \approx 10^{14}$ to 10^{19} cm^{-3}, and the light and heavy particles are more nearly in thermal equilibrium, with $T_i \leq T_e$ (Anders, 2000).

The most commonly used method of generating and sustaining a low-temperature plasma for technological applications is by applying an electric field to a neutral gas. Any volume of a neutral gas always contains a few electrons and ions

that are formed, for example, as the result of the interaction of cosmic rays or radioactive radiation with the gas. These electrons are accelerated by the electric field and new charged particles may be created when the electrons collide with atoms and molecules in the gas or when ions collide with the surfaces of the electrodes. This leads to an avalanche of charged particles that is eventually balanced by charge carrier losses, so that a steady-state plasma develops (Condrads and Schmidt, 2000).

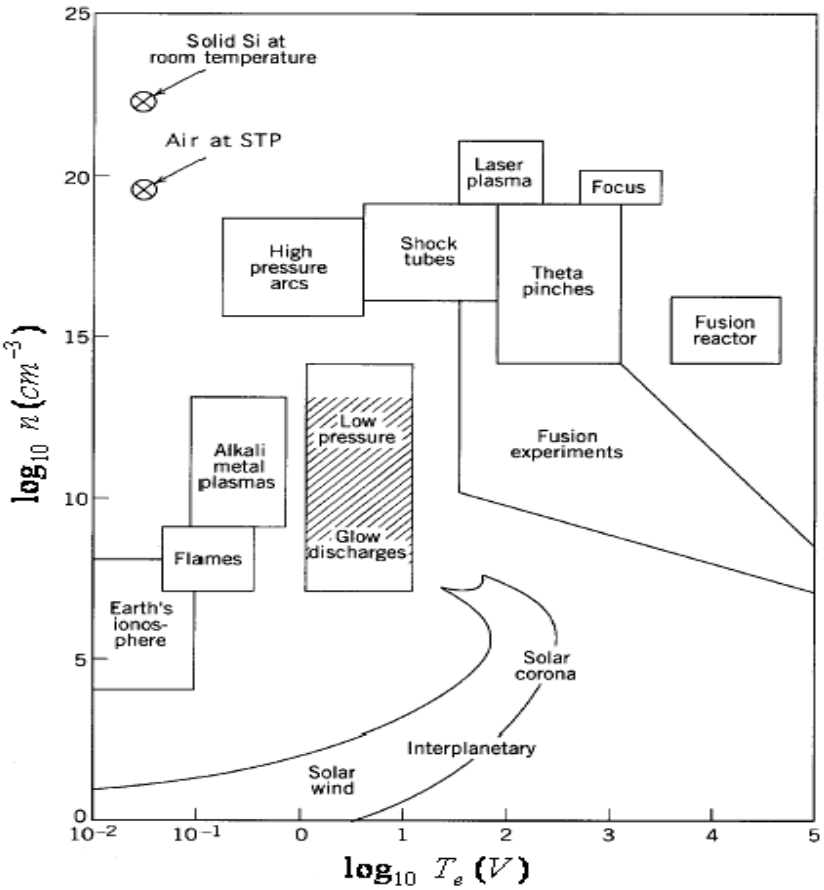

Figure 2.6. Classification of plasmas according to electron temperature and density (Anders, 2000).

Figure 2.7 characterizes vapours and plasmas produced by various sources such as glow discharges, cathodic arcs, and neutral vapour, according to the degree of ionization, and atom/ion energies. It may be seen that the plasma produced by the cathodic vacuum arc has high ion energy and degree of ionization.

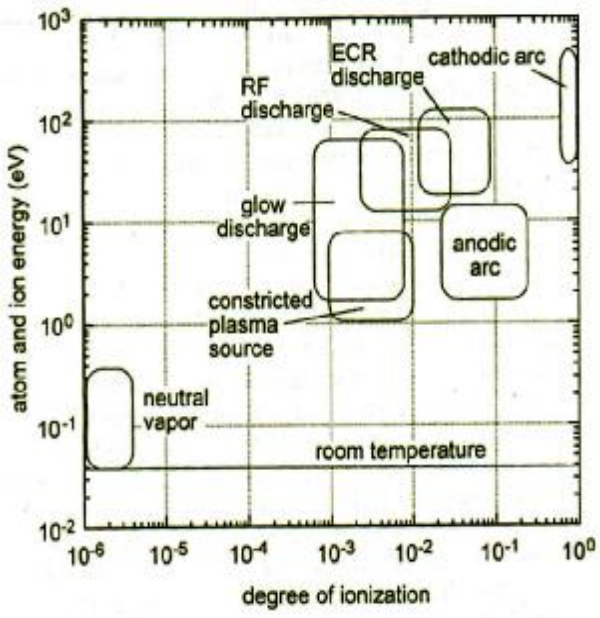

Figure 2.7. Vapour and plasma produced by various sources (Anders, 2000).

2.3. 5.2. Basic Theory of Electrical Discharges and Plasmas

In this section the basic theory of electrical discharges and plasma physics needed to understand plasma deposition are presented. An electrical discharge is the passage of electrical current through a medium or device which is normally insulating. An example is lightning, where the medium is air, which under normal conditions is a very poor conductor. If we hold two electrodes a few millimeters apart, and connect each to one pole of an ordinary battery, no perceptible electrical current flows through the insulating air. However, if the applied voltage is sufficiently high, electrical breakdown occurs in the gas and ions and electrons are formed. The negatively charged electrons and positively charged ions move freely under the applied voltage, and their movement constitutes an electric current. Lightning, an example of electrical breakdown in air and a subsequent electrical discharge, is illustrated in Figure 2.8.

Figure 2.8. The electrical breakdown of the air(http://hurriyetim.com.tr,2007)

A relatively simple experiment introduces us to several fundamental types of discharge. Two metal electrodes connected to a dc power supply are inserted into a glass tube (Figure 2.9). The tube can be evacuated and filled with various gases at different pressures. The voltage between the electrodes and the current in the circuit are measured.

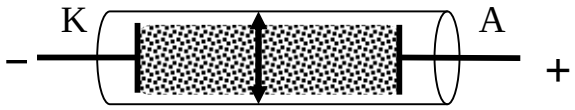

Figure 2.9. Typical gas discharge tube (Raizer, 1991)

If a low voltage is applied to the electrodes (several tens of volts) no visible effects are produced, although supersensitive instruments would record an extremely low current, on the order of 10^{-15} A, from collection of charges generated in the gas by cosmic rays and natural radioactivity. If the gas is intentionally irradiated by a radioactive or X-ray source, a current up to 10^{-6} A can be produced, but no light will be observed by an unaided eye. The electric current exists only while the irradiation is maintained, and thus discharge is not self-sustaining. As the voltage is raised, the current first increases as more of the charges produced by ionization are collected by the electrodes before recombining. However, once the field is sufficient to collect all of the charges, the current ceases to grow and saturates, being limited by the rate of ionization from the irradiation. However, if the voltage is raised sufficiently further,

the current sharply increases at a critical value of V and light emission is observed – this is the breakdown voltage.

Discharges in a dc electric field can be classified as (a) non-self sustaining and (b) self sustaining types. The latter include (1) glow discharges, (2) arc discharges, (3) Townsend's dark discharge, (5) corona discharges and (5) spark discharges. The breakdown voltage, and main characteristics of the discharges (e.g. voltage current characteristic, structure of the discharge) depend on the geometry of the electrodes and the vessel, the gas, and the electrode material.

The voltage-current characteristic is highly nonlinear, as seen in Figure 2.10. Three general regions can be identified on the diagram above, the dark discharge region, the glow discharge, and the arc discharge. Each of these general regions encompasses many interesting phenomena.

Dark Discharge

The regime between A and E on the voltage-current characteristic is termed a dark discharge because, except for corona discharges and the breakdown itself, the discharge is invisible to the eye.

A – B In the ***background ionization*** region, the electric field applied along the axis of the discharge tube sweeps out the ions and electrons created by ionization from background radiation. Background radiation from cosmic rays, radioactive minerals, or other sources, produces a constant and measurable degree of ionization. The ions and electrons migrate to the electrodes in the applied electric field producing a weak electric current. Increasing voltage sweeps out an increasing fraction of these ions and electrons.

B – C If the voltage between the electrodes is sufficiently increased, all of the electrons and ions will be collected at the electrodes, and the current will saturate. In the ***saturation region***, the current remain constant while the voltage is increased. This current depends linearly on the radiation source strength, a regime useful in some radiation counters.

C – E If the voltage across the low pressure discharge tube is increased beyond point C, the current will rise exponentially. The electric field is now high enough so the electrons initially present in the gas can acquire enough energy before reaching the anode to ionize neutral atoms, leading to an avalanche of electron and ion production. The region of exponentially increasing current is called the ***Townsend discharge***.

D – E ***Corona discharges*** occur in Townsend dark discharges in regions of high electric field near sharp points, edges, or wires in gases prior to electrical breakdown. If the coronal cuurents are high enough, sufficient light may be emmitted for the corona discharge to be visible to the eye. For low currents, the entire corona is dark, and is sometimes called a dark discharge. Related phenomena include the ***silent electrical discharge***, an inaudible form of filamentary discharge, and the ***brush discharge***, a luminous discharge in a non-uniform electric field where many corona discharges are active at the same time and form streamers through the gas.

E Electrical breakdown occurs in Townsend regime with the aid of secondary electrons emitted from the cathode due to ion or photon impact. At the breakdown, or sparking, potential V_B, the current might increase by a factor of 10^4 to 10^8, and is usually limited only by the internal resistance of the power supply connected between the plates. If the internal resistance of the power supply is very high, the discharge tube cannot draw enough current to break down the gas, and the tube will remain in the corona regime with small corona points or brush discharges being evident on the electrodes. If the internal resistance of the power supply is relatively low, then the gas will break down at V_B, and move into the glow discharge regime. The breakdown voltage for a particular gas and electrode material depends on the product of the pressure and the distance between the electrodes, ***pl***, as expressed in Paschen's law (1889).

Glow Discharge

The glow discharge regime owes its name to the fact that the plasma is luminous. The gas glows because the energetic electrons collisionally excite atoms to

higher energetic states, and the excited atoms emit photons as they decay to lower energy states. The applications of glow discharge include dc parallel plate plasma reactors, “magnetron” discharges used for depositing thin films.

F – G After a discontinuous transition from E to F, the gas enters the ***normal glow*** region, in which the voltage is almost independent of the current over several orders of magnitude in the discharge current. The electrode current density is independent of the total current in this regime. This means that the plasma is in contact with only a small part of the cathode surface at low currents. As the current is increased from F to G, the fraction of the cathode occupied by the plasma increases, until plasma covers the entire cathode surface at point G.

G – H In the ***abnormal glow*** regime above point G, the voltage increases significantly with the increasing total current in order to force the cathode current density above its natural value and provide the desired current. Starting at point G and moving to the left, a form of hysteresis is observed in the voltage-current characteristic. The entire surface of the electrode is now covered by the discharge and the only way in which the current can be increased is by increasing the cathode fall, so that secondary electrons gain more energy and cause more ionisation. The discharge maintains itself at considerably lower currents and current densities than at point F and only then makes a transition back to Townsend regime.

Arc Discharges

H – K At point H, the electrodes become sufficiently hot that the cathode emits electrons thermionically. If the DC power supply has a sufficiently low internal resistance, the discharge will undergo a glow-to-arc transition, H-I. In the ***arc regime***, from I through K, the discharge voltage decreases as the current increases, until large currents are achieved at point J, and after that the voltage increases slowly as the current increases. The basic properties of arc discharges are presented in detail in section “2.3.5.5”.

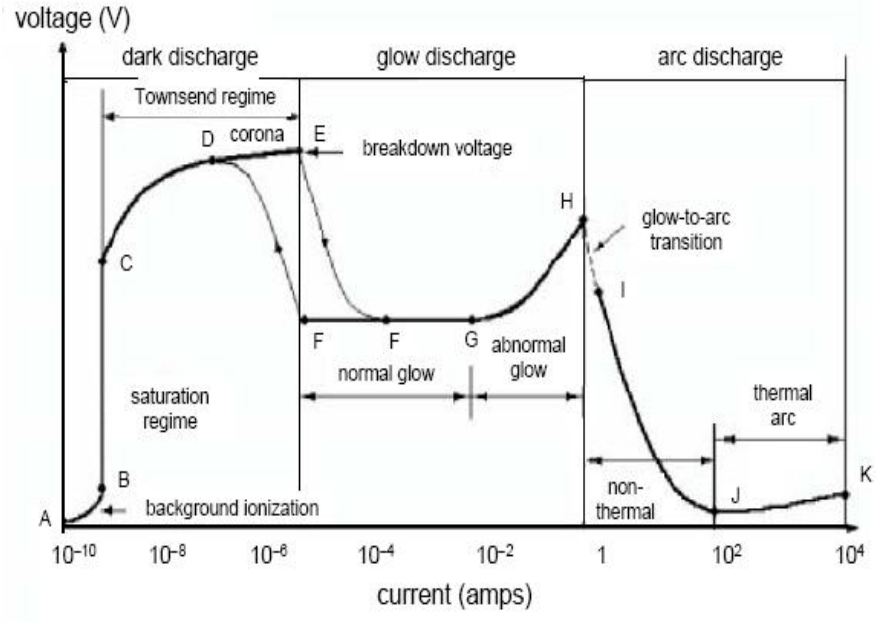

Figure 2.10. Voltage-Current characteristics of DC discharges(http://science-education.pppl.gov)

2.3.5.3. Sputter Deposition

Sputter deposition is a widely used technique, based on the glow discharge, for the deposition of films,. Sputtering is used for film deposition on semiconductor wafers, on magnetic media and head surfaces, for coating tools and cutting surfaces for wear resistance, the surfaces of automobile parts, for coating the insides of plastic bags, and wide range of other applications. Sputtering is a surface erosion process by energetic particles, a sort of atomic sandblasting. Sputter deposition the accumulation of these atoms which were blasted off the surface onto a nearby sample (Seshan *et al*., 2002).

Sputtering occurs whenever any particle strikes a surface with enough energy to dislodge an atom from the surface. The sputter yield is the ratio of the number of emitted particles per incident particle:

$$Y=(\text{No. of emitted particles} / \text{No. of incident particles}) \qquad \text{Eq. (2.3)}$$

Sputtering can be caused by many incident species, including atoms, ions, electrons, photons, and neutrons as well as molecules and molecular ions. However, in almost all practical applications, sputtering utilizes ion bombardment, usually either with inert gas ions such as Ar^+ and Kr^+, or small molecular ions such as N_2^+, O_2^+. The sputtering yield for bombardment of a surface with an ion or an atom of the same energy will be virtually identical; physical sputtering relies on the transfer of physical momentum and kinetic energy from the incident particle to the surface atoms, and this is independent of the particle's charge. The sputtering process is shown generically in Figure 2.11. The incident particle impacts the surface or near surface atoms of the solid with sufficient energy to break bonds and dislodge atoms. One or more atoms may be removed from the solid, and known as the sputtered atoms.

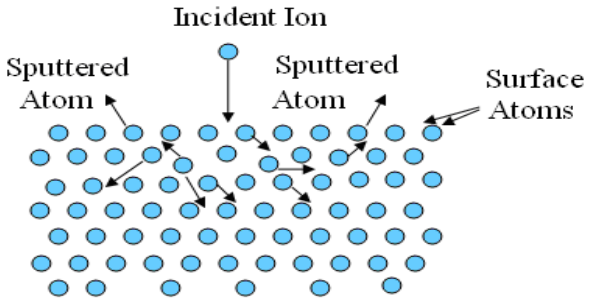

Figure 2.11. Principle of sputtering process (Seshan *et al.*, 2002).

The incident particle energies in the hundreds of eV range needed for sputtering are much easier to arrange for ions than for neutral atoms -- the ions can be readily accelerated by an electric field within a vacuum chamber. There are two classes of systems used to generate the ions: plasmas and ion beams. The only difference here is that in the plasma source, the surface to be bombarded is immersed in the plasma, and in the ion beam case, the plasma is physically separated from the target and contained within an ion source, from which the ion beam is extracted and directed to the substrate surface. Plasma sputtering involves the creation of gas plasma (usually a glow discharge in an inert gas such as argon) by applying voltage

between a cathode and anode. In the simplest diode sputtering arrangement, the cathode is used as a target holder and the anode is used as substrate holder. Sputtering is normally performed at a pressure of 10^{-2}-10^{-3} Torr and there are three modes of exciting the plasma: dc, rf, and magnetron.

2.3.5.3.(1). Diode, Radio Frequency and Magnetron Sputtering

The simplest sputtering plasma device, the diode, comprises an anode and a cathode inside a vacuum system (Figure 2.12). Under the right conditions, with adequate voltage across the electrodes and the appropriate gas pressure, the gas will breakdown and the glow discharge plasma will form. The plasma potential is slightly more positive than the anode potential.

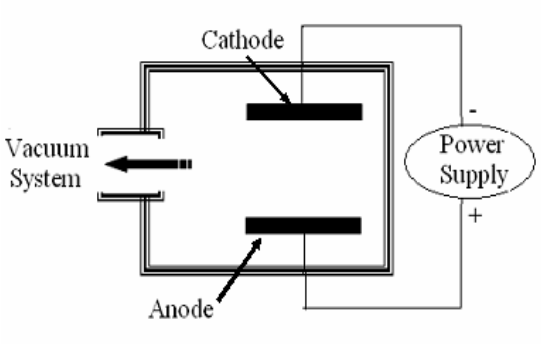

Figure 2.12. A simple diode sputtering device (Seshan *et al.*, 2002).

Simple diode plasmas were historically first used to both erode surfaces and for sputter deposition. However, they have been limited in their applicability, by low rates and the requirement that the electrodes must be conductors. If one of the electrodes is insulating, it charges rapidly, and additional current is suppressed. This effect can occur if a reactive gas, such as oxygen or nitrogen, is introduced into the plasma, which may result in the formation of an insulating oxide or nitride film on the electrode surfaces. Therefore, DC diode sputtering is not an appropriate technology for deposition most compounds and dielectrics. By operating the plasma diode with an rf potential, rather than dc, these problems can be overcome.

The rf and dc diodes share the same basic configuration, but differ in the power supply frequency. The most common rf sputtering frequency is 13.56 MHz, although experiments have run in the range 60 Hz to 80 MHz or more. This eliminates charge buildup on an insulating surface by providing equal numbers of ions, and then electrons, during alternate half-cycles of the excitation voltage, and thus eliminating the accumulation of net charge. This allows insulators to be sputtered and metals to be sputtered in reactive gases. There is an additional degree of ionization with rf-powered plasma due to additional energy transmitted to the plasma electrons at the oscillating sheath. The net result is a higher plasma density, compared to dc-powered plasmas, and the ability to operate at lower system pressures (0.5-120 mPa).

Magnetron sputtering was developed to achieve higher deposition rates on large areas, with low substrate heating. Magnetron sputtering systems also operate in a diode configuration, with either in dc or rf excitation, but differ from the previously described dc and rf sputtering by the imposition of a magnetic field in the vicinity of the cathode. Magnetron sputtering sources are the current workhorse of the sputter deposition field, used in perhaps 95% of all sputtering applications. In order to enhance the probability of collisions of electrons with Ar atoms at a given pressure in the chamber, the path of the electrons has to be made longer. This is achieved by the addition of the magnetic field. While the field does not significantly influence the motion of the heavy ions, the Lorenz-force causes the electrons to move in a circular path. The combined effect of the magnetic field and the perpendicular electric field will force the electrons to follow a cycloid path rather then being immediately extracted from the plasma to the anode by the electric field. The increased path length increases the probability that an electron will ionize a gas atom before reaching the anode. This allows the discharge to be sustained at a lower pressure, which in turn increases the energy of the ions striking the target surface and thus the sputtering rate, and reduces the number of collisions between the sputtered atoms and gas molecules, thus increasing the deposition rate and energy of the depositing atoms.

2.3.5.3.(2). Reactive Sputtering

Reactive sputtering is widely used for producing coatings of compounds. Metal atoms are sputtered from a metallic target, and sufficient reactive gas is added to the chamber to form the desired compound at the substrate. In Figure 2.13, a schematic diagram of the "reactive sputter deposition" technique is presented.

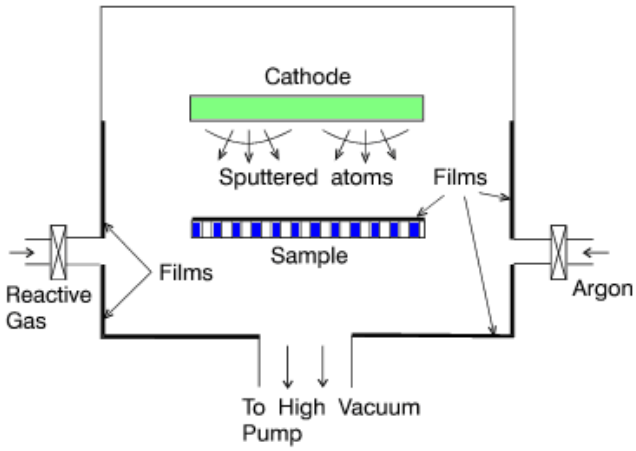

Figure 2.13. Schematic drawing of a reactive deposition chamber (Hartnagel *et al.*, 1995).

In addition, when compounds composed of multiple elements are to be deposited upon substrates, the composition of the deposited film often differs from the composition of the target. This originates from the fact that the compounds decompose during the sputtering, though the situation varies according to the chemical bond strength between the components. The concentration of the more volatile component, such as oxygen and nitrogen, is reduced in the deposited film. Simultaneously, the target composition also changes. To compensate for this, reactive gas of the volatile component should be added into the plasma.

2.3.5.4. Ion Beam & Ion Assisted Deposition

Structural, electrical and optical properties of thin films depend mainly on the energies of the deposition species. In conventional evaporation processes, atoms of

the source material have energies less than 1 eV and in sputtering techniques is ~10 eV, however, this deposition energy is still insufficient to produce coatings that can tolerate the extreme conditions encountered in many wear-resistant applications. The properties and the structure of the deposited films can be improved by increasing the substrate temperature during deposition or by applying a bias to the substrate. However, the substrate may limit the temperature that can be used. For such applications, where deposition of highly adherent coatings is required at low temperatures, ion assisted deposition techniques are promising alternatives of the sputtering or evaporation processes. The deposition energies in these processes are of the order of a few hundred electron volts. Two general arrangements are most popular for application of the ion source to thin film coating. First, ions from the source can be directed at a target which is sputtered, and the sputtered material deposited as a thin film. This is termed ion beam sputter deposition (IBS). Second, ions from the source can be directed to the substrate which is being coated with material generated by some independent technique. This is termed ion assisted deposition (IAD). Schematic drawings of IBS and IAD systems are presented in Figures 2.14(a) and (b), respectively.

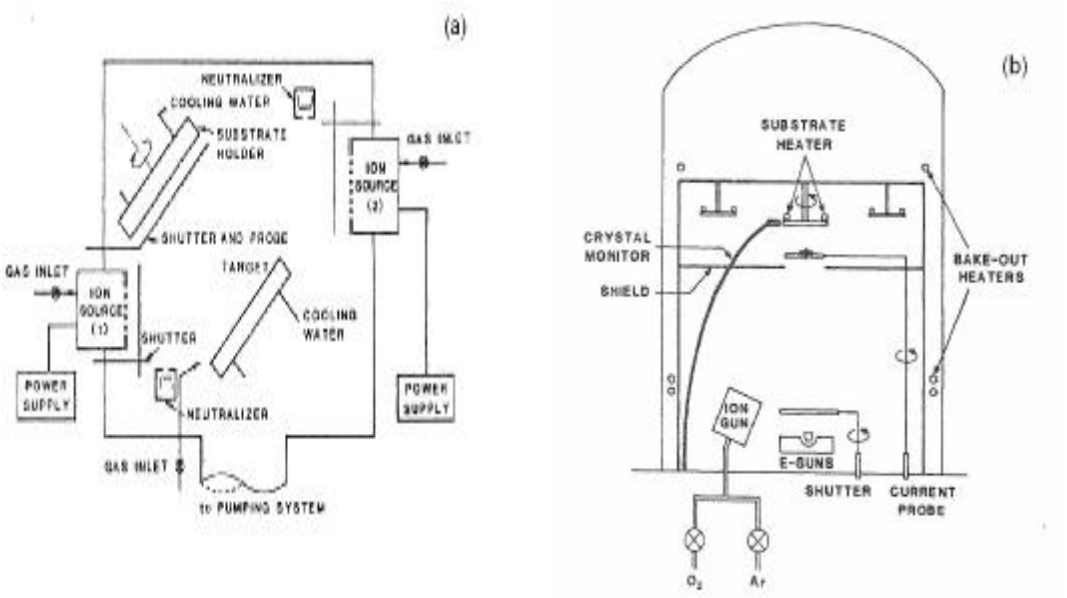

Figure 2.14. Schematic drawings of a) IBS, and b) IAD systems (Seshan *et al.*, 2002).

2.3.5.5. The Arc Discharges

The arc discharge is a high-current (~1-10^5 A), low-voltage discharge (~10-100 V), in contrast with the low-current (10^{-4}-10^{-1} A), high-voltage glow discharge (>200 V). This characteristics distinguishes the arc discharge from the glow discharge, in which the cathode fall is hundreds of volts. The small cathode fall in the arc results from electron emission mechanisms at the cathode that differ from those in the glow discharge. These mechanisms are capable of supplying a greater electron current from the cathode, nearly equal to the total discharge current. Arc cathodes emit electrons as a result of several effects: thermionic, field emission, and the combined thermionic- field emission. The cathode is the location of spots (cathode spots) where the current density is also greater (10^2-10^4 A/cm^2 in some modes and 10^4-10^7 A/cm^2 in other modes) than in glow discharges (~155 A/cm^2 for copper cathode in air at 1 atm pressure) (Raizer, 1991).

The arc discharges are characterized by a negative-resistance V-I characteristic. Arc cathodes receive large amounts of energy from the arc current and the cathode reach high temperature, either over the entire cathode area or just locally, usually for short time intervals. The cathodes are eroded by vaporization. Electrons for the discharge are supplied by a ***cathode spot*** that is a much more efficient electron emitter than the glow discharge cathode phenomena. The current density in the cathode spot is high and constant.

The clasification of dc discharges may be based on the characteristics of cathode processes, plasma state in the positive column, or the medium (gas or vapour of cathode material) in which the current sustained. The arc discharges can be classified as: a) Arcs with a hot thermionic cathode, b) arcs with external cathode heating, c) high pressure and very high pressure arcs d) low pressure and vacuum arcs, and e) cold cathode arcs.

Thermal effects play an important role in arcs. The arc cathode may be heated as a whole to a temperature about 3000 K, or even higher; in such cathodes thermoionic emmission plays an important role. The arc is anchored at a fixed spot on the cathode surface. The current density from this large area is ~10^2-10^4 A/cm^2.

Only refractory materials withstand this high temperature. There must be sufficient ions to keep the cathode hot. These arcs are often used in plasmatrons, welding machines, and arc furnances. Alternatively, the cathode is externally heated, at least until the arc is established, to help starting the arc. In some cases, as in gas rectifier diodes, the cathode is continuously heated. These cathodes are coated by an oxide with a low work function to stimulate copious electron emission. External heating of the cathode does not significantly affect the nature of the discharge. This type of arc is employed in some low pressure devices. High pressure and very high pressure arcs operate in the range 0.1-10 atm and >10 atm, respectively. Very high pressure arcs have an important application in high pressure lamps. The low pressure arcs operate at 10^{-3}-10^{0} Torr, the plasma in their positive column is strongly non-equilibrium, and is similar to the glow discharge plasma with respect to temperatures and degree of ionization. Vacuum arcs are initiated between electrodes placed in vacuum but but intense erosion and vaporization of the metal electrodes immediately fills the "interelectrode" region with metal vapor plasma.

2.3.5.5.(1). Vacuum Arc Deposition

In recent years, there has been much progress in use of ion and plasma beams in both research and technology. Plasma systems are used in many industrial applications for material surface modification and the production of coatings and thin films. Primary applications include depositing films for electronic and optical functions as well as protective coatings against oxidation, corrosion, and wear. The vacuum arc is frequently used in industry to deposit hard and decorative coatings. It is a high current electrical discharge between conducting electrodes located prior to arc ignition in a vacuum ambient, and the current is conducted in the interelectrode region by plasma comprised of highly ionized metal vapor which was evolved from the surface of electrodes by the action of the arc itself (Boxman ***et al.***, 1986, Boxman and Goldsmith, 1989). Figure 2.15 presents a schematic view of a reactive vacuum arc deposition system.

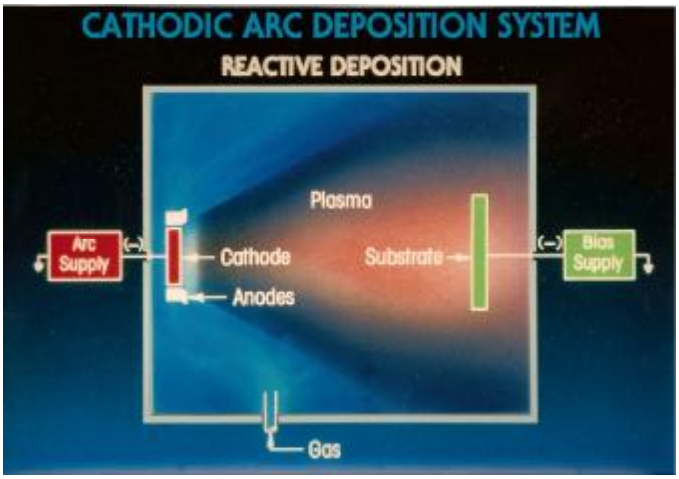

Figure 2.15. Reactive vacuum arc deposition system (Lindfors *et al*., 1986).

2.3.5.5.(2). Cathode Spots and Particle Generation at Cathode Spots

Vacuum arcs can be classified by their principle source of metallic plasma e.g. cathodic and anodic vacuum arcs. Plasma generation in the cathodic vacuum arc is highly localized at minute, non-stationary spots called ***cathode spots.*** Spot formation is necessity to provide sufficient power density for plasma formation by electrode evaporation, high electron flux emission, and subsequent ionization of the metallic vapor (Daalder, 1981). The plasma conducts the current between cathode and anode. Liquid micron size droplets, also known as macroparticles, are generated by the plasma-liquid interaction at cathode spots. Plasma pressing on the molten cathode material in and near the cathode spots ejects some of the molten material sideways (Figure 2.16). The production of macroparticles is inherently connected to the existence of non-stationary cathode spots. The cathode spot plasma is characterized by very high density and temperature and therefore pressure, which can exceed atmospheric pressure. Driven by the very high pressure gradient near the spot, in conjunction with electron-ion coupling, ions are accelerated to supersonic velocities on the order of 10^4 m/s.

In low current vacuum arcs (<100 A), the principal plasma source is, in most cases, one or a few cathode spots, which produces high velocity plasma jets directed away from the cathode. At sufficiently low current, only a single cathode spot (SCS)

operates. The current limits for the SCS arc are the minimum current needed for sustaining the arc (~1 A), and the maximum current that can be carried by a single cathode spot, which depends on the cathode material (Daalder, 1975). In general, the number of cathode spots and their distribution depends on the system parameters and electrode materials (i.e. electrode shape, electrode surface, impurities). As the current is increased, the number of cathode spots will increase proportionally (Daalder, 1981). Ideally, if a sufficient number of spots are present and randomly distributed over the cathode surface, the plasma jets merge and form a relatively uniform plasma region that fills most of the interelectrode space. This kind of vacuum arc will be called the multi cathode spot (MCS) vacuum arc.

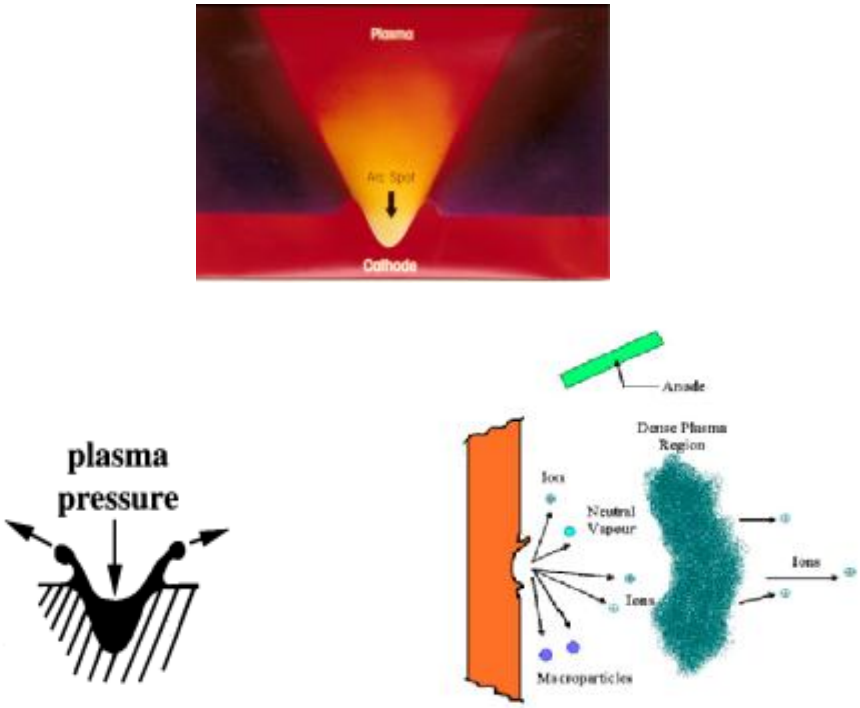

Figure 2.16. The production of plasma and macro-particles (Anders, 2000, Tay, 2006).

2.3.5.5.(3). Interelectrode Plasma

The interelectrode region of the vacuum arc discharge extends from the cathode spot plasma to the anode sheath. At low and medium arc current, it contains

a plasma beam created at the cathode spots, metallic vapor emitted from the arc electrodes, and a stream of macroparticles also emitted by the cathode. The interelectrode plasma moves away from the cathode, and all or part of it condenses on the anode. The interelectrode plasma conducts the arc current from the anode to the cathode.

The interelectrode plasma has received relatively little attention in previous studies of the vacuum arc, in comparison to investigations of electrode phenomena. It is usually assumed that the interelectrode plasma is a passive current conductor with relatively low resistance, where 15% to 30% of the input energy is consumed depending on the discharge geometry. However, detrimental effects of anode spots on the operation of high current vacuum arc interrupters drew attention to the interelectrode plasma. When an anode spot exists, it becomes a very intense source of metallic plasma, vapor and macroparticles. Several models have been proposed to explain anode spot formation, and most of them depend on the interaction between the interelectrode plasma and the anode. The characteristics of interelectrode plasma in cathodic arcs (i.e. without anode spots) is presented below and the cathodic arc is discussed in terms of the number of cathode spots, where, single cathode spot (SCS) and multi cathode spot (MCS) arcs represents relatively low and high current, depending on material, respectively. A schematic representation of the MCS interelectrode plasma concept is presented in Figure 2.17.

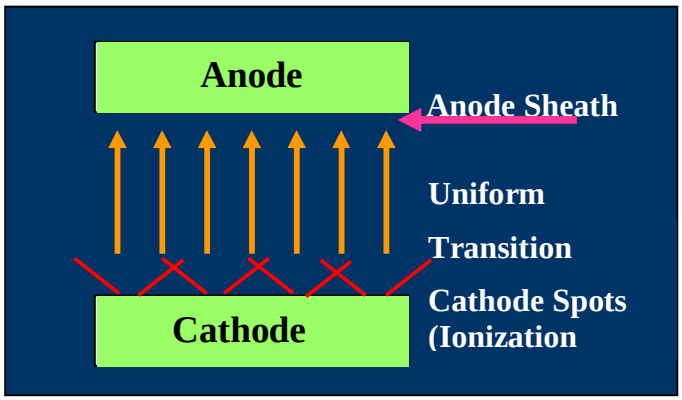

Figure 2.17. General structure of the MCS interelectrode plasma (Boxman *et al.*, 1995).

The ideal description of the MCS interelectrode plasma should be taken with some reservations. In many cases, the distribution of the cathode spots on the cathode surface is not uniform and, as result, the plasma of the interelectrode region is not uniform. External fields can force the cathode spots to reside at certain locations on the cathode spot, leading to marked deviations from a uniform distribution of the interelectrode plasma. However, as we show below, the general characteristics of the plasma can be studied within a good approximation, assuming it to be uniform.

The MCS vacuum arc interelectrode plasma can be characterized by the following parameters: i) electron temperature, ii) electron density, iii) mass flow velocity, iv) average degree of ionization, v) electric current density. In addition to these, the spatial plasma distribution and the ionization equilibrium are also very important characteristics of the plasma. The experimental observation which is the key to modeling the MCS arc is that the number of cathode spots present on the cathode surface is proportionate to the arc current. Thus the average current per cathode spot is a constant whose value depends on the cathode material. The average current per cathode spot for various materials has been collected in Table 2.1.

Table 2.1. Average cathode spot currents (Boxman *et al*., 1995)

Cathode Material	Spot Current (A)
Mercury	0.4-0.7
Cadmium	8-15
Zinc	9-20
Indium	15-18
Aluminum	30-50
Copper	75-100
Titanium	70
Carbon	200

2.3.5.5.(4). Plasma and Macroparticle Transport

Vacuum arc deposition (VAD) technology prevails over other technologes in high-tech hard coatings due to its high deposition rate and the high ionicity of depositing particles. One of the important advantages of the vacuum arc process is the formation of a copious quantity of energetic ions of the cathode material. This is in contrast to other physical vapor deposition techniques such as magnetron sputtering and electron beam evaporation where the depositing species forming the coating are primarily neutral atoms. The ions generated by the vacuum arc are multiply-charged and with a near optimal kinetic energy (few tens of eV) for forming dense and adherent coatings on complex shaped substrates. However, plasma production in a vacuum arc discharge is always accompanied by a flux of macroparticles (Ryabchikov and Stepanov, 1998).

These liquid droplets or solid debris, known collectively as macroparticles (MPs) are also produced at the cathode spot (Boxman, 2001). In Figure 2.18 a cathodic arc generated macroparticle of erbium is shown.

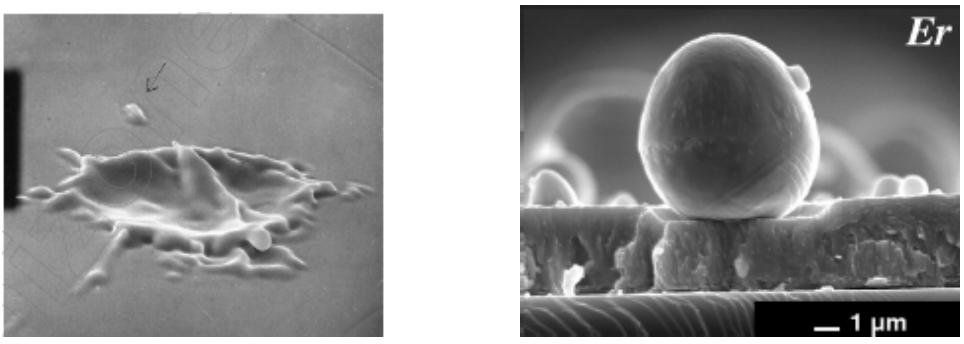

(a) Cathode (b) Substrate

Figure 2.18. Cathode spot crater formation (a) and Cathodic arc erbium macroparticle deposited (b) during growth of an erbia film (Anders, 2000).

Most of the MPs emitted by the cathode have velocities in the range 10-800 m/s, directed initially almost parallel to the cathode surface. The largest part of the macroparticle mass flow is carried by droplets having a diameter of a few microns.

As the macroparticles traverse the plasma, they will interact with the plasma. The slower, smaller macroparticles can be significantly deflected towards the anode from their initially radial trajectory by the pressure of the cathode-emitted ions impinging on them. Furthermore, the ion flux heats the macroparticles, and the smaller and slower macroparticles can arrive at a steady state temperature in the range of 2000-2600 K, at which temperature the heat flux from ion bombardment is balanced by evaporative cooling of the macroparticles. Macroparticle evaporation is thought to be the primary source of neutrals observed in the plasma region of the MCS arc. However, the neutrals emitted from the macroparticles will typically be ionized before they get very far. The ions thus created will initially have thermal velocities characteristics of the surface temperature of macroparticles (~800 m/s), slow in comparison with the cathode-emitted ions. The production rate of macroparticle originated ions depends on the product of the current density, and density of the macroparticles, while the density of the macroparticles depends on the cathode material and geometry, arc discharge current, and cathode thermal regime.

Macroparticles in the plasma flow forms defects in the deposited coatings. This degrades the quality of coatings, especially in the case of thin coatings in which thickness is comparable to the MP dimensions (Ryabchikov and Stepanov, 1998). These particles must be removed if the plasma source is to be used for the production of high quality optoelectronic films or indeed any application where smooth; defect free coatings are required (Bilek and Anders, 1999). Thus creation of simple and effective systems for removing MPs from the plasma flow is important and in the next section it is discussed in detail.

2.3.5.5.(5). Principles of MP Filtering and MP Filters

Because of the severe drawback for many applications from the MPs, the use of vacuum arc deposition is limited despite its many attractive properties (Boxman ***et al.***, 1995). Many approaches have been proposed and tested for the elimination of MPs from cathodic vacuum arc plasmas. The most successful separate the ionized plasma particles from MPs by their vast difference in charge-to mass ratio.

Macroparticle filtering has been reviewed a number of times (Boxman and Goldsmith, 1992, Alterkop *et al*., 1996, 1998, Bilek and Anders, 1999, Martin and Bendavid, 2001, Boxman and Zhitomirsky, 2006).

Most successful are curved magnetic filters, originally introduced by Aksenov and coworkers in the late 1970s (Anders, 2000) in which ions are guided to a substrate that is not in a line of sight with the cathode spot. In an axial magnetic field, electrons follow the magnetic field lines because they are magnetized, that is, their gyration radius is much smaller than the filter radius, and their collision frequency is smaller than the gyration frequency. In contrast, ions are usually not magnetized because their gyration radii are much larger than the electron's and larger than the filter radius. The non-magnetized plasma ions follow the magnetically guided electrons electro-statically so as to keep the plasma quasi neutral and thus the plasma is transported along the magnetic field lines by combined magnetic field and electric field mechanisms, which affect the electrons and ions respectively. Macroparticles may be slightly charged but the mass-to-charge ratio is vastly greater than the corresponding ratio for electrons and ions, because of this they move along almost straight trajectories, and in the case of curved filters impact the filter wall, and are thus essentially removed from the plasma. Often baffles are incorporated into magnetic ducts to lower the probability that a MP might bounce of the wall and thus still arrive at the substrate surface.

Macroparticle filters can be categorized by their architecture, mode of operation, and geometry. According to their architecture they can be categorized as "closed" and "open". However, in all the main goal of the filter design is to increase plasma transport efficiency through the filter and reduce the macroparticle flux to the substrate. Figures 2.18(a-f) present some filter configurations; more detailed information on filtering of macroparticles and filter types were can be obtained from Anders (1999), Miernik *et al*. (1999) and Boxman and Zhitomirsky (2006).

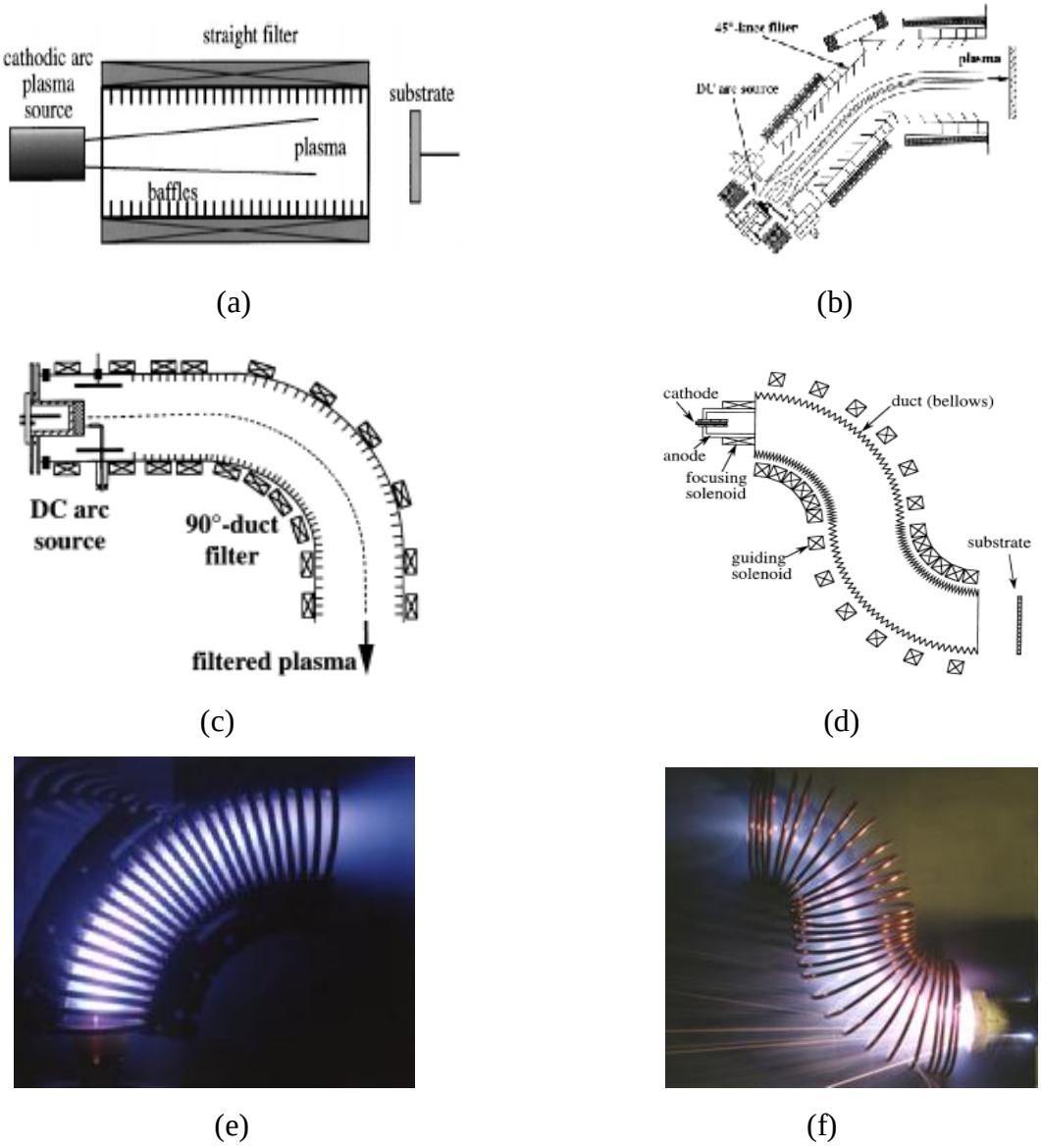

Figure 2.19. Different MP filter configurations, (a) straight filter, (b) knee filters, (c) 90^o closed architecture torus filter, (d) S-shape closed architecture filter, (e) 90^o open architecture tourus filter, (f) S-shape open architecture filter.

In Figure 2.19(a) the straight filter is presented. Here the applied axial magnetic field collimates the plasma and thus direct it towards the substrate and thus enhances the plasma density and deposition rate. Only a small fraction of macroparticles reach the substrate; the others are caught or reflected by the baffles. However, not all of the macroparticles are eliminated due to line of sight between the cathode and the substrate. The straight filters generally have higher plasma

transmission than curved filters and the macroparticle reduction achieved may be adequate for some coating applications. The plasma density in straight filters decays exponentially with attenuation lengths, which is typically between 10 and 25 cm (Anders, 1999).

An alternative filter is a combination of straight and curved sections used in the knee filter (Figure 2.19(b)). Because plasma losses increase with the filter bend angle, it is reasonable to design a non-line of sight filter that has a relatively small bend angle. In the knee filter, the MP reflection can be reduced by baffles inserted in the two straight duct sections. Among various filter designs described in literature the most common filter design is the magnetic filter with a 90^o bend (quarter torus) as shown in Figure 2.19(c). The filter consists of a curved part which is surrounded by magnetic coils generating a curved axial field. To reduce the particle transport by multiple reflections, baffles can be inserted in to the duct. Aksenov and co-workers found that biasing the duct positively (~ +(10-20) V) improves the plasma transport and filter efficiency. This feature was also recognized by Anders and co-workers and Bilek and co-workers. This type of filter has been widely used during the last decade. While Aksenov and co-workers developed a relatively large system (duct length about 1 m) for d.c. plasma operation, this equipment can easily be scaled. Small systems suitable for pulsed arc operation (duct length about 10 cm) show the same principal features. The S-shaped filter was also developed to further reduce the macroparticle flux through the substrate (Figure 2.19(f)). Plasma loses in such systems become severe and they are primarily useful for ultra thin film applications. In Figures 2.19(e,f), the open architecture or freestanding 90^o and S-duct filters are presented, respectively. They were designed for use in pulsed FVAD systems while closed filters are preferred for use in dc FVAD systems. The open 90^o and S-duct filters do not have a duct. The magnetic field is produced by a few turns of a field coil. Macroparticles leave the plasma through openings between the field windings or stick to the coils. The idea behind the open filter is to reduce the surface from which MPs might bounce.

2.4. Film Formation –Fundamentals

Thin film coatings are finding ever increasing applications in high technology. Due to the non-equilibrium nature of PVD methods, the resulting micro-structure and properties of films strongly dependent on deposition systems and deposition conditions used, and in a number of cases the micro-structure and properties are directly responsible for the film's successful application.

In this section, ion surface interaction with the substrate, the basic film nucleation growth processes and structure zone models are presented to explicate the effects of the deposition conditions on the deposited films.

2.4.1. Ion Surface Interaction

The energy transferred from an ion to the growing film surface significantly affects the film properties. The effects produced by the impact of energetic ions (>20 eV) with a solid are shown in Figure 2.20. The incoming ion loses energy by inelastic collisions, which produce electronic excitation, and by elastic collisions which displace atoms from their lattice positions. The recoiling atoms in turn initiate secondary collisions until the energy is dissipated within a small volume of the growing film. When the energy transferred by these collisional cascades to the surface atoms exceeds the surface binding energy, surface atoms may be removed (sputtered). Depending upon conditions, the sputtered surface atoms may include host substrate atoms, desirable deposited atoms, and undesirable contaminant atoms. The vacancies produced in the cascade increase the diffusion rate and the interaction between vacancies and atoms leads to diffusion.

The bombardment of ions with energy of 40-1000 eV during film growth has been shown to enhance adatom mobility, increase sticking coefficients, remove weakly absorbed surface atoms, and alter the nucleation mechanism. Furthermore, the displacement of surface atoms and the formation of vacancies at or close to the surface of the growing film by bombarding ions show push surface atoms into

interstitial sites deeper in the material so that surface atoms are depleted and the film is densified at greater depths (Bendavid, 1998).

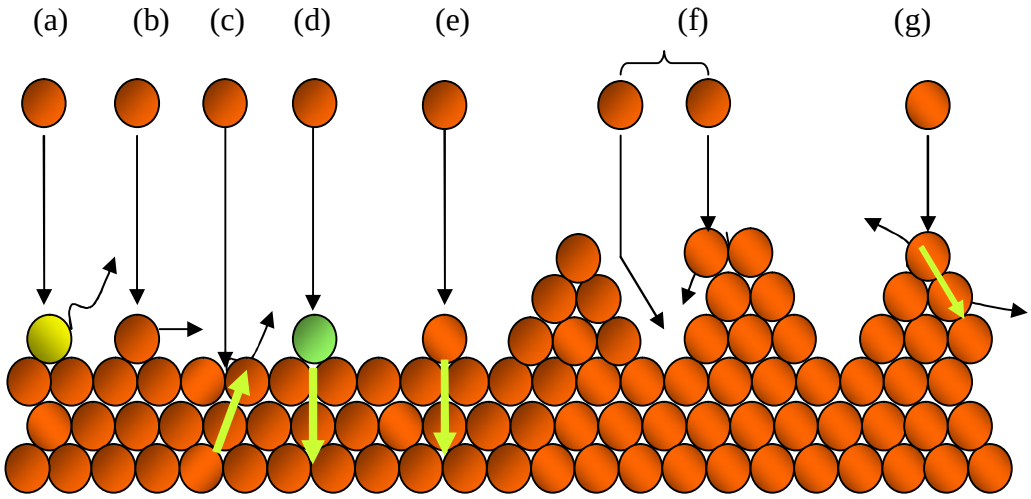

Figure 2.20. Effects of bombarding ions on the surface (a) adsorbate removal (b) lateral displacement, (c) surface vacancy created by sputtering, (d) impurity implantation, (e) implantation of film atom by knock-on, (f) void filling due to ion enhanced surface mobility and forward sputtering, (g) break up of 3D nucleus (Bendavid, 1998).

2.4.2. Film Nucleation and Growth

Thin film formation involves the formation of growth nuclei and film growth around these nuclei. Also, as mentioned before, the growth is dependent on the energy of the depositing particles, and their interaction with the atoms in the solid. Furthermore, the nucleation and the initial film growth processes depend upon the surface energy. In Figure 2.21, several processes involving nuclei (or atom clusters) on a substrate are illustrated. Nucleation and film growth involve individual atoms or molecules striking the substrate surface, condensing onto the surface by equilibrating energetically with the surface atoms, diffusion on the surface, and clustering to form nuclei which grow together and evolve into the final coating. The balance between growth and dissolution processes is governed by the total free energy of the cluster, relative to an assembly of individual atoms.

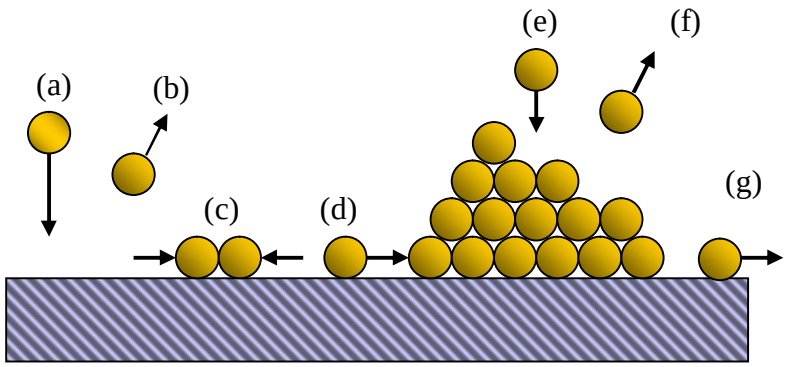

Figure 2.21. Schematic diagram of atomic processes in the nucleation of deposited film atoms on a substrate, (a) atom deposition on substrate, (b) re-evaporation from substrate, (c) cluster nucleation, (d) diffusion to cluster, (e) atom deposition on a cluster, (f) re-evaporation from a cluster, and (g) dissociation of a cluster (Bendavid, 1998).

The nucleation and growth of a PVD thin film has been observed to occur by three distinctly different processes as shown in Figure 2.22. The first of these processes is called the “layer by layer”, or Frank-van der Merwe, mode. In this mode, the layers of film grow one on top another. This mode is necessary for growing heteroepitaxial films. In addition, this process is applicable to the case where coating atoms bind more strongly to the substrate than each other, adatom surface mobility is high, and good atomic matching exists across the film/substrate interface. The second process is the island, or Volmer-Weber, mode, in which separated three dimensional islands grow on the substrate. With time and continued adatom flux, the clusters proceed to grow into larger islands, and coalesce into a continuous film. The last growth mode is called the “mixed layer + island)” or Stranski-Krastanov, mode. In this mode, first some continuous monolayers are formed, and then islands grow. After initial nucleation, the islands grow until they touch one another and form a continuous network. Whenever there is growth from islands, there may remain spaces, i.e. grain boundaries, between the islands. These boundaries significantly influence the electrical and optical properties of the films.

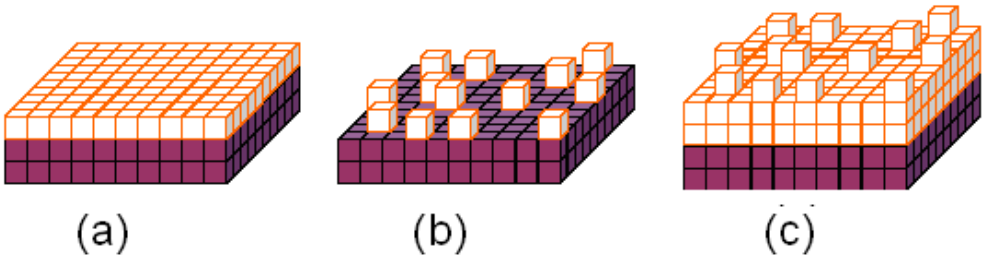

Figure 2.22. Schematic diagrams of growth modes; (a) Frank-van der Merwe (b) Volmer-Weber, (c) Stranski-Krastanov.

The main difference in nucleation and the growth process between thermal evaporation, sputtering and ion based deposition techniques is the particle energy, *e.g.* the ion based techniques have one or two orders of magnitude higher particle energies. Thus, the effect on the nucleation and growth can be seen by improved film adhesion, enhanced adatom surface mobility that may be reduce the growth temperature of epitaxial films.

2.4.3. Film Growth and Microstructure

Thin film properties are usually different than the bulk properties and these differences caused by various impurities, defects, and density variation with thickness, and the surface interfaces. In addition, the microstructure of the films depends on the material, residual gas pressure, deposition and/or annealing temperature, and particle energies. The coating condensation process can be pictured mainly in three steps. First, incident atoms/ions transfer kinetic energy to the lattice and become loosely bonded “adatoms”; the energy transfer is efficient, even for energetic sputtered atoms. These adatoms then diffuse over the surface, exchanging energy with the lattice and other adsorbed species, until they either are desorbed or, more commonly, trapped at low energy lattice sites. Finally the incorporated atoms readjust their positions within the lattice by bulk diffusion process. The growth process is affected by the following four process: *shadowing* – a simple geometric interaction between arriving particles and the roughness of the growing surface, *surface diffusion* – mobility of particles at surfaces and interfaces such as grain boundaries. Surface diffusion is dominant at medium substrate temperatures. *Bulk*

diffusion – mobility of particles in the volume of grains, this process is dominant relatively high substrate temperatures comparable to surface diffusion. *Desorption or re-crystallization* – phase change in the film as function of substrate temperature, thickness, and post deposition annealing. These processes can be qualified in terms of the characteristic roughness of the coating surface, the activation energies for the surface and bulk diffusion, and the sublimation energy.

The microstructures of coatings produced by PVD processes are usually described by maps called as a zone models which are the function of deposition conditions (Monterio, 2001). Movchan and Demchishin in 1969 (as presented by Thornton, 1977) proposed a zone model for classification of the grain boundary morphology of PVD deposited thick metal and oxide films. They concluded that the coatings could be represented as a function of T_s / T_m in terms of three distinct zones shown in Figure 2.23(a) each with its own characteristic structure and physical properties, where T_s and T_m are the substrate temperature and melting temperature of the film material, respectively. Later, Thornton (1974, 1975) modified this model by including Ar pressure on the second axis to investigate the influence of gas pressure in sputtering system. A transition zone (*T*) between zones 1 and 2 consisting of dense array of poorly defined fibrous grains was defined in the model. In Figure 2.23(b) and 2.23(c), the structure zone model proposed by Thornton and the superposition of this zone model are illustrated schematically.

Zone I, where T_s / T_m <0.26-0.3, is classified as low temperature regime and consists of tapered crystals with domed tops which are separated by voided boundaries that are not influenced by heat treatment at high T_s / T_m. The internal structure of the crystal is poorly defined, with high dislocation density. The crystal diameter increases with T_s / T_m and that dependence indicates very low activation energy and implies very low surface diffusion. Zone I is associated with coating flux shadowing that is not overcome by adatom surface diffusion (Figure 2.23(a)).

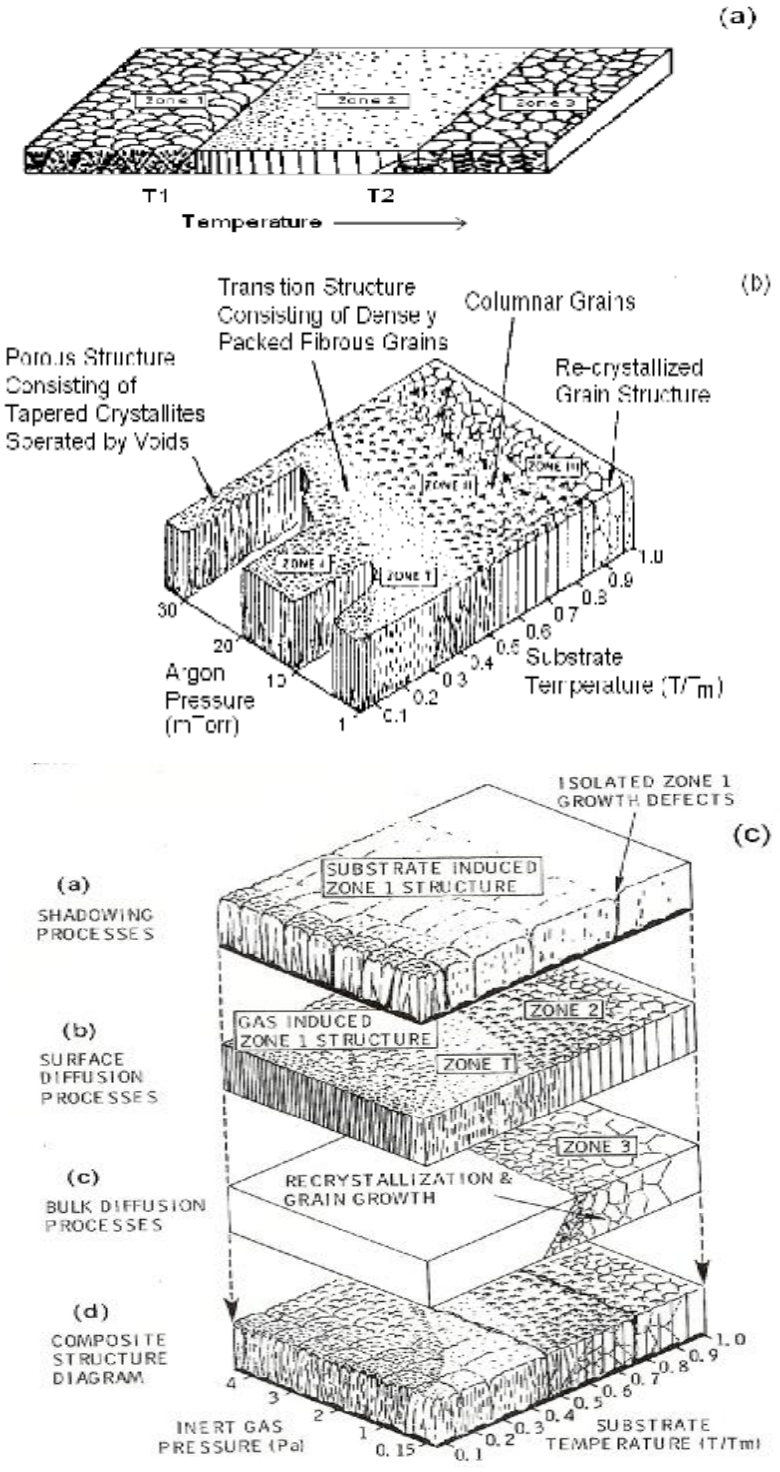

Figure 2.23. Structure zone models for coating growth (a) Model proposed by Movchan & Demchishin, (b) Model proposed by Thornton, (c) Schematic representation showing the superposition of physical processes that establishes structural zones (Thornton,1977).

Zone T, consists of a dense array of poorly defined fibrous grains resulting from gas scattering of the sputtered vapor, thereby randomizing the directions of the incidence of the coating flux to the substrate. As can be seen from Figure 2.23 (b), this zone is located between Zone I and II. Zone *T* structure is defined as the form taken by Zone structure in the limit of zero T_s / T_m on an infinitely smooth substrate. However the range of the zone may be different in various deposits because of the kinetic energy of particles produced in different deposition systems.

Zone II, where 0.26-0.3< T_s / T_m < 0.45, consists of columnar grains which may approach a near-equiaxed shape, and separated by distinct, dense, grain boundaries; the surface has a smooth, mat appearance and is more free of defects than Zone I. However, dislocations are primarily in boundary regions. Grain size increase with T_s / T_m ratio and may extend through the coating thickness at high T_s / T_m. Surface diffusion occurs with activation energies ~0.1-0.3 eV.

Zone III, where T_s / T_m >0.45, can be characterized by bulk diffusion processes such as re-crystallization and grain growth, and classified by equiaxed or columnar grains with a bright surface. The grain diameters increase with T_s / T_m and yield an activation energy corresponding to that of bulk self-diffusion. Zone III is recognized by dense grain and twin boundaries, and by grain shapes that do not coincide with the substrate and coating surface topographies.

In addition to structure zone models (SZM) proposed by Movchan and Demchishin and later by Thornton, a different zone model was conceived to describe microstructures of films produced by processes that include energetic particles by Messier *et al*. (1984). The inclusion of ion energy in this model led to an increase of the stability domain of the zone *T* with increasing particle energy. Figure 2.24 shows the revised structure zone model of thick films as function of both bombardment- and thermal –induced mobility.

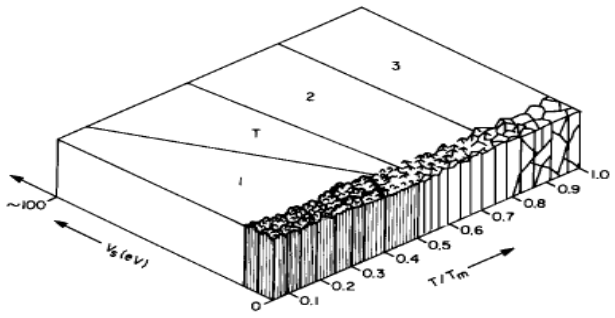

Figure 2.24. Modified structure zone model showing the effects of both bombardment and thermally induced mobility (Messier *et al*., 1984).

In Figure 2.24 the effect of thermal and bombardment effects on the low mobility zone I structures are presented. As can be seen from the figure at no bombardment, the zone *T* is small, and with increasing bombardment energy the width of the zone *T* is increases. However, there is no significant change at high thermal energy region is observed.

In the revised zone model, the thickness effect is also taken into account by Messier *et al*. (1984). In this model all physical structure column /void sizes are considered and assigned as sub zones 1A, 1B, 1C, 1D, 1E which correspond to the five distinct levels presented in Figure 2.25(a). As can be seen from the figure the larger sizes of columns are grown with increasing thickness. The zone 1A is the smallest size level (1-3 nm) while the zone 1E represents the 300 nm column sizes. At the beginning of the growth fine grains are present and with increasing thickness the conical columns grown and fractal structure can be observed. An example of growth zone model proposed by Messier *et al*. (1984) presented in Figure 2.25(b). In their evolutionary model for the low bombardment conditions nano-, micro-, macro-void structures were recognized and with increasing thickness these voids and column sizes also increased.

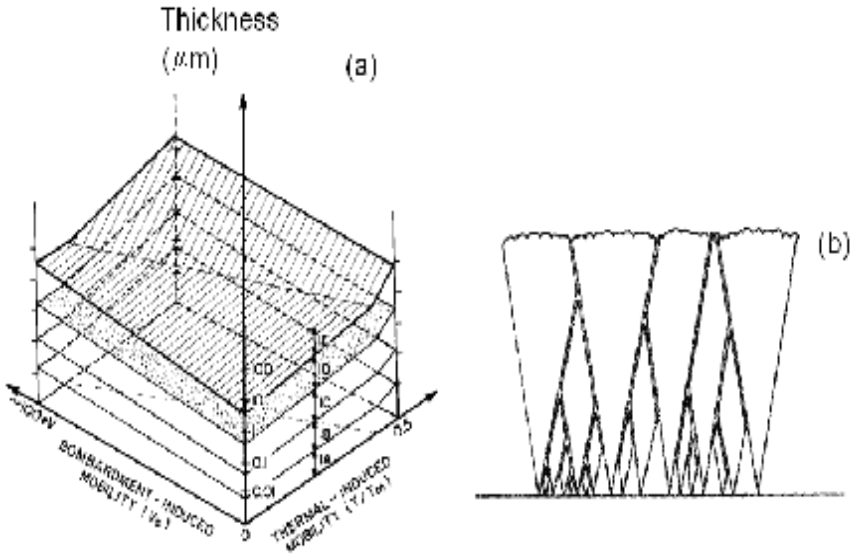

Figure 2.25. Modified structure zone model, (a) showing the effect of thickness, (b) cross section of columnar growth model. Messier *et al*., 1984, 1986).

Zone models which predict coating microstructure as a function of primary deposition variables such as the substrate temperature and inert gas pressure are useful for sorting experimental data. Furthermore, it should be noted the annealing process has also effect on structure of the films. The deposition process is controlled primarily by surface diffusion while the annealing is controlled by bulk and grain boundary diffusion. Thus depositing at a low temperature and annealing at a higher temperature does not produce the same microstructure, and generally not the same phases, as depositing at a high temperature. High deposition temperature generally yield a high temperature phase, followed by carefully controlled anneal, is often an effective method for obtaining a particular phase with a particular particle size and distribution.

2.5. Post-Deposition Process –Annealing

Annealing, in metallurgy and materials science, is a heat treatment wherein the microstructure of a material is, altered, causing changes in its properties such as strength and hardness. It is a process that produces equilibrium conditions by heating

and maintaining at a suitable temperature, and then cooling very slowly. The primary purpose of annealing is to reduce the hardness of material and facilitate the progress of subsequent manufacturing operations. It is generally used after casting, forging or rolling to soften metals and alloys and minimize the residual stress, improve cold working properties, increase ductibility by carefully controlling the microstructure. There are several phases in the annealing process, with the first being the recovery phase, which results in softening of the metal through removal of crystal defects and the internal stresses which they cause. The second phase is re-crystallization, where new grains nucleate and grow to replace those deformed by internal stresses. If annealing is allowed to continue once re-crystallization has been completed, grain growth will occur, in which the microstructure starts to coarsen and may cause the metal to have less than satisfactory mechanical properties. Although, the known common application of the annealing is in metal tool manufacturing, in semiconductor industry it has been used, e.g. silicon wafers are annealed, so that dopand atoms, usually boron, phosphorus or arsenic, can be incorporated into substitutional positions in the crystal lattice, resulting in a drastic changes in the electrical properties of the semiconducting material. The annealing is also applied to certain group of metal oxides such as ZnO, SnO_2. In addition, the structure and optical properties of semiconductors can be changed by annealing drastically to obtain better crystallinity with higher transmission, Shalev (2004).

2.6. Optical Properties of Solids

This section presents an introduction to the fundamental optical properties of solids. The aim is to develop an understanding of the relation between measurable optical properties and the dielectric function, and the microscopic and electronic structure of the solids. In the first part of this section, Maxwell's equations are presented. In the second part, absorption and dispersion relations and later, some optical methods of determination of the optical constants are presented.

2.6.1. Maxwell's Equations & the Dielectric Function

Transmission of visible and infrared radiation through conducting media and the behavior of such radiation at the interfaces between different media are aspects of the general behavior of electromagnetic waves which are governed by Maxwell's field equations. The optical property, usually available directly from experiment, is the frequency-dependent reflectance or transmittance; the property most directly related to the electronic structure of a solid is the dielectric function. To interpret experimental measurements in terms of the fundamental electronic properties of solid requires an understanding of Maxwell's equations, the nature of the interaction between electromagnetic fields and matter, and an understanding of the dielectric function from a fundamental microscopic viewpoint.

The properties of the medium can now be included in Maxwell's equations. Then we get the following set of equations:

$$\vec{\nabla}.(e\,\vec{E}) = 4\pi r_c \qquad \text{Eq. (2.4)}$$

$$\vec{\nabla}\times\vec{E} = -\frac{m}{c}\frac{\partial \vec{H}}{\partial t} \qquad \text{Eq. (2.5)}$$

$$\vec{\nabla}.(m\,\vec{H}) = 0 \qquad \text{Eq. (2.6)}$$

$$\vec{\nabla}\times\vec{H} = \frac{1}{c}\frac{\partial}{\partial t}(e\,\vec{E}) + \frac{4\pi s}{c}\vec{E} + \frac{4\pi}{c}\vec{J} \qquad \text{Eq. (2.7)}$$

where, r is the charge density, $\vec{E}$ is the electric field, $\vec{H}$ is the magnetic field, m is the magnetic permeability, e is the dielectric function of the material, s is the electrical conductivity, c is the light velocity, and $\vec{J}$ is the current flux. These equations are given in Gaussian units and it should be noted that the e and s are function of frequency, w. When we consider the interaction of light with a macroscopically electrically neutral medium, the equations can be simplified; (a)

$r_c = 0$, and, (b) for isotropic media, there is no spatial variation in *e*. Thus, as $m \cong 1$ in non-ferromagnetic media, we obtain:

$$\vec{\nabla}.\vec{E} = 0 \qquad \text{Eq. (2.8)}$$

$$\vec{\nabla}\times\vec{E} = -\frac{1}{c}\frac{\partial H}{\partial t} \qquad \text{Eq. (2.9)}$$

$$\vec{\nabla}.\vec{H} = 0 \qquad \text{Eq. (2.10)}$$

$$\vec{\nabla}\times\vec{H} = \frac{e}{c}\frac{\partial \vec{E}}{\partial t} + \frac{4ps}{c}\vec{E} \qquad \text{Eq. (2.11)}$$

$$\vec{\nabla}\times(\vec{\nabla}\times\vec{E}) = \vec{\nabla}(\vec{\nabla}.\vec{E}) - \vec{\nabla}^2\vec{E} \qquad \text{Eq. (2.12)}$$

Using the vector identity (Eq. (2.12)) and the equations (2.9) and (2.11) we get the equation;

$$\vec{\nabla}(\vec{\nabla}.\vec{E}) - \vec{\nabla}^2\vec{E} = -\frac{\varepsilon}{c^2}\frac{\partial^2\vec{E}}{\partial t^2} - \frac{4\pi\sigma}{c^2}\frac{\partial \vec{E}}{\partial t} \qquad \text{Eq. (2.13)}$$

The wave equation for a plane wave propagating in an energy absorbing medium can be obtained by using Eq. (2.8);

$$\vec{\nabla}^2\vec{E} = \frac{\varepsilon}{c^2}\frac{\partial^2\vec{E}}{\partial t^2} + \frac{4\pi\sigma}{c^2}\frac{\partial \vec{E}}{\partial t} \qquad \text{Eq. (2.14)}$$

The solutions are necessarily restricted to transverse plane waves because $\vec{\nabla}.\vec{E} = 0$ in the absence of a net charge density. The conductivity term in Eq. (2.14) should be called the optical conductivity. This is because the energy absorption with which we are concerned is that arising from electronic transitions accompanying

photon absorption. At sufficiently long wavelengths transverse optical conductivity approaches the ordinary dc conductivity for isotropic materials (Wooten, 1972).

If we consider, propagation of a single plane wave within an isotropic medium, and anticipating that the wave vector must be complex to describe energy dissipation of the wave, we write:

$$\vec{E} = \vec{E}_0 \exp i(\hat{q}.\vec{r} - wt) \qquad \text{Eq. (2.15)}$$

where $\vec{E}_0$ is perpendicular to the wave vector $\hat{q}$. If we solve Eq. (2.14) for Eq. (2.15) we find:

$$\hat{q}^2 = \frac{\omega^2}{c^2}(\varepsilon + i\frac{4\pi\sigma}{\omega}) \qquad \text{Eq. (2.16)}$$

We now define a complex refractive index $\hat{n}$ such that;

$$\hat{q} = (\frac{w}{c})\hat{n} = (\frac{w}{c})(n + ik) \qquad \text{Eq. (2.17)}$$

where n and k are the refractive index and extinction coefficient, respectively. If we rewrite Eq. (2.15),

$$\vec{E} = \vec{E}_0\left[\exp-(\frac{w}{c}\vec{k}.\vec{r})\right]\exp i(\frac{w}{c}\vec{n}.\vec{r} - wt) \qquad \text{Eq. (2.18)}$$

The first exponent in the equation correspond to the absorption in the medium, and the second corresponds to the refractive index real part, the former one which describes the fractional decrease in intensity with distance and can be rewritten as;

$$a = \frac{2w\,k}{c} = \frac{4p\,k}{l} \qquad \text{Eq. (2.19)}$$

and, the second one describes a wave traveling with phase velocity c/*n*, hence the earlier identification of n as the refractive index. Eqs. (2.16) and (2.17) can be used to obtain expression for *e* and s in terms of *n* and *k* and can be described as:

$$\varepsilon = (n^2 - k^2) \qquad \text{Eq. (2.20)}$$

$$\frac{4\pi\sigma}{\omega} = 2nk \qquad \text{Eq. (2.21)}$$

The complex dielectric function, $\hat{e}$, can be described as:

$$\hat{e} = e_1 + ie_2 \qquad \text{Eq. (2.22)}$$

where e_1 and e_2 are real and imaginary parts of the dielectric function, respectively.

2.6.2. Dispersion and Absorption Theory of Solids

The classical theory of dispersion and absorption is mainly due to the response of bound and free electrons to the electromagnetic field. If only the former contribute, the material is a non-conducting dielectric whereas the latter one is predominant in metals. For semi-conductors both bound and free electron contribution becomes important (Moss, 1961). The former gives rise to the intense absorption to the short wavelength side of the main absorption edge, whilst at longer wavelengths free carrier absorption becomes important, and the classical theory of dispersion and absorption, which is mainly due Lorentz and Drude, is applicable. The Lorentz model is applicable to insulators; its quantum mechanical analog includes all direct interband transitions, where the final state of electrons lies in a different band

for all transitions but no change in $\vec{k}$ - vector (momentum) in the reduced zone scheme. The drude model is applicable, at the relevant frequencies, to the free electrons in metals and to the free electrons in conducting oxides; its quantum mechanical analog includes intraband transitions, where intraband transitions denote all transitions not involving the reciprocal lattice vector (Wooten, 1972). Both the Lorentz and the Drude models are classical and *ad hoc*, but are still useful as starting points and for developing a feeling for optical properties.

The modern theory and modeling of dispersion relations use basic quantum physics approach. Two basic concepts are introduced: “photons” and “absorption rate between levels that involve photon absorption and electron transition rates”. Generally, the optical phenomena in semiconductors are related to the existing valence and conduction bands. The conduction bands should not necessarily be populated. The energy gap between these levels, E_g, is usually larger than 2 eV if the material is transparent in the VIS. In addition, modern theory also introduces the use of Kramer–Kroning (KK) relations that specify the rule “the effect cannot come before the cause”. This ensures that polarization does not occur before the arrival of the photons or electromagnetic wave. With the modeling of the dispersion relation in semiconductors, it is usually assumed that levels close to those existing in crystalline materials are also found in amorphous solids. Hence, the quantum models apply both to crystalline and amorphous semiconductors.

2.6.2.1. Dispersion Relations

2.6.2.1.(1). The Lorentz Oscillator

In pure dielectrics the wavelength or frequency dependence of the optical constants may be explained simply on the basis of the classical treatment of Lorentz which considers the solid as an assembly of oscillators which are set in forced vibration by the radiation. In the Lorentz model, the atom with electrons that are bound to the nucleus resemble a small mass bound to a large mass by a spring. The

equation of motion of an electron bound to the nucleus, with damping force, is described by the expression;

$$m\frac{d^2x}{dt^2}+m\Gamma\frac{dx}{dt}+mw_o^2x=-e\vec{E}_{loc} \qquad \text{Eq. (2.23)}$$

where m is the electronic mass, e is the magnitude of electronic charge, Γ is the damping coefficient, ω_o is the resonance frequency, and $\vec{E}_{loc}$ is the local electric field acting on the electron as a driving force. In this model the nucleus mass is assumed to be infinite, where we can take the mass of the lattice infinitive, and the force arising from the interaction between the electron and the magnetic field of the light wave is neglected since the velocity of electron is small compared with c. The solution of this equation shows that x varies sinusoidally at the electric field frequency with amplitude given by;

$$\vec{x}=\frac{-e\,\vec{E}_{loc}/m}{w_o^2-w^2-iw\,\Gamma} \qquad \text{Eq. (2.24)}$$

and, the induced dipole moment is;

$$\vec{p}=-e\mathbf{r}=\frac{e^2\,\vec{E}_{loc}}{m}\frac{1}{(\omega_o^2-\omega^2)-i\Gamma\omega} \qquad \text{Eq. (2.25)}$$

If the displacement r is sufficiently small, a linear relationship exists between $\vec{p}$ and $\vec{E}$ that can be written as;

$$\vec{p}=\hat{a}(w)\vec{E}_{loc} \qquad \text{Eq. (2.26)}$$

where $\hat{a}(w)$ is the frequency-dependent atomic polarizability. From Eqs. (2.25) and (2.26), the polarizability for a one-electron atom is seen to be;

$$\vec{a}(w) = \frac{e^2}{m} \frac{1}{(w_o^2 - w^2) - i\Gamma w} \qquad \text{Eq. (2.27)}$$

The polarizability is complex because of the inclusion of a damping term. As a result, the polarization differs in phase from the local field at all frequencies. If there are *N* atoms per unit volume, the macroscopic polarization can be given by the relation;

$$\vec{P} = N\langle \vec{p} \rangle = N \hat{a} \langle \vec{E}_{loc} \rangle = c_e \vec{E} \qquad \text{Eq. (2.28)}$$

To relate the microscopic atomic polarizability to the macroscopic electric susceptibility, it is necessary to know the relationship between the microscopic field $\vec{E}_{loc}$ and the macroscopic field $\vec{E}$. Except for some limiting ideal cases, this is a problem of considerable complexity. In general, $\langle \vec{E}_{loc} \rangle \neq \vec{E}$ since $\langle \vec{E}_{loc} \rangle$ is usually an average over atomic sites, not over regions between sites. For free electron in metals though, we can argue that since the conduction electrons are not bound, the field felt by the conduction electrons is on the average just the macroscopic field $\vec{E}$. Then, of course, we should let $w_o = 0$ in Eq. (2.23) because the conduction electrons are not bound. The result is just the Drude model for metals. However, what we shall do is something in between. We will keep the restoring force term, but still assume for simplicity that $\vec{E}_{loc} = \vec{E}$. Such a model contains all the essential features to describe the optical properties; but it must be remembered that in the detail analyses of specific real solids, it is necessary to consider carefully what the correct field to use is. Proceeding with our assumptions, then, we have;

$$\vec{P} = N\hat{a}\vec{E} = c_e\vec{E} \qquad \text{Eq. (2.29)}$$

We are now ready to get an expression for the dielectric function in terms of the atomic polarizability. But we now have an energy loss mechanism explicitly included with the result that the atomic polarizability is now complex. This means also that the fields $\vec{E}, \vec{P}$, and $\vec{D}$ are not in phase. If we define complex displacement $\hat{D}$ such that

$$\hat{D} = \hat{e}\vec{E} = \vec{E} + 4p\vec{P} = \hat{E}^{ext} \qquad \text{Eq. (2.30)}$$

This is equivalent to defining $\hat{D}$ as;

$$\hat{D} = \vec{D} + i(4p/w)\vec{J} \qquad \text{Eq. (2.31)}$$

The physical quantities $\vec{E}, \vec{D}$ and $\vec{J}$ are generally written in complex notation;

$$\vec{D} = D_o \exp i(\vec{q}.\vec{r} - w\,t) \qquad \text{Eq. (2.32)}$$

Since this notation explicitly shows the phase, and in addition simplify the mathematical manipulations. Values for these physical quantities are obtained by taking the real part of the complex expressions used for these quantities. Although $\hat{D}$ can also be written in complex notation, the values for the physical quantities that $\hat{D}$ represents are not obtained by taking the real part of $\hat{D}$. The quantity $\hat{D}$ is truly a complex quantity and represents the real part of $\vec{D}$ and $\vec{J}$. The true values for $\hat{D}$

must be obtained from the right-hand side of Eq. (2.31) by taking the real parts of $\vec{D}$ and $\vec{J}$.

Having recognized that there is a truly complex $\hat{D}$, we shall from here on generally follow convention and write simply $\vec{D}$. We shall explicitly designate complex quantities only for properties of the medium, e.g., the complex dielectric function $\hat{e}$ and the complex polarizability $\hat{a}$.

$$\hat{e} = 1 + 4pN\hat{a} \qquad \text{Eq. (2.33)}$$

Using Eq. (2.27), this becomes

$$\hat{e} = 1 + \frac{4pNe^2}{m}\frac{1}{(w_o^2 - w^2) - i\Gamma w} \qquad \text{Eq. (2.34)}$$

From Eq. (2.34) and the definitions is Eqs. (2.20) – (2.22), we get, for non-magnetic materials,

$$e_1 = n^2 - k^2 = 1 + \frac{4pNe^2}{m}\frac{(w_o^2 - w^2)}{(w_o^2 - w^2)^2 + \Gamma^2 w^2} \qquad \text{Eq. (2.35)}$$

$$e_2 = 2nk = \frac{4pNe^2}{m}\frac{\Gamma w}{(w_o^2 - w^2)^2 + \Gamma^2 w^2} \qquad \text{Eq. (2.36)}$$

If we consider classical atoms with more than one electron per atom, we can extend the previous results. Let N_j be the density of electrons bound resonance frequency w_j. then,

$$\hat{e} = 1 + \frac{4p\,e^2}{m}\sum_j \frac{N_j}{(w_o^2 - w^2) - i\Gamma_j w} \qquad \text{Eq. (2.37)}$$

$$\sum_j N_j = N \qquad \text{Eq. (2.38)}$$

The corresponding quantum mechanical equation which can be written

$$\hat{e} = 1 + \frac{4p\,e^2}{m} \sum_j \frac{N\,f_j}{(w_j^2 - w^2) - i\Gamma_j w} \qquad \text{Eq. (2.39)}$$

where f_i is the oscillator strength. There is a formal similarity between Eqs. (2.37) and (2.39), but the meanings of some corresponding terms are quite different. In Eq. (2.37), w_j is the resonance frequency of a bound electron, whereas in Eq. (2.39), it is the transition frequency of an electron between two atomic states separated in energy by hw_j. The oscillator strength f_j is a measure of the relative probability of a quantum mechanical transition to pass from state *i* to state *j*. For free atoms, it satisfies the sum rule;

$$\sum_j f_j = 1 \qquad \text{Eq. (2.40)}$$

Now, return to Eqs. (2.35) and (2.36) and consider the frequency dependence of e_1 and e_2 for a solid made of a collection of single-electron classical atoms. The frequency dependence is illustrated graphically in Fig. 2.26. Figure 2.26 shows that except for a narrow region near w_o where e_1 decreases with increasing frequency. This is called anomalous dispersion. We can find the width of the region of anomalous dispersion as follows. Equating the derivative of Eq. (2.35) to zero;

$$(w_o^2 - w_m^2)^2 = \pm w_o^2 \Gamma^2 \qquad \text{Eq. (2.41)}$$

Where w_m is the frequency at which e_1 is a maximum or a minimum. If the region anomalous dispersion is reasonably narrow, $w_m \approx w_o$,

$$(w_o - w_m) = \pm\Gamma/2 \qquad \text{Eq. (2.42)}$$

and the full width of the region of anomalous dispersion is Γ. In the absence of an energy loss mechanism, there is a singularity at w_o. If $\Gamma \approx 0$, e_2 versus w is a bell-shaped curve which is symmetric about w_o. Small values of Γ compared with w_o cause little distortion. From Eq. (2.36), the maximum value of e_2 is;

$$e_2(\max) = \frac{4pNe^2}{\Gamma w_o} \qquad \text{Eq. (2.43)}$$

Figure 2.26 shows the contribution of the electronic polarizability to the dielectric constant. There are also other contributions. For example, in ionic crystals, in the infrared region, there is an absorption spectrum and polarization associated with the direct stimulation of vibrational modes of the ions by means of electromagnetic radiation. The Lorentz model also describes that situation. Figure 2.27 shows the general form of the polarizability to be expected in a material consisting of three discrete modes of oscillation. Although all the modes of oscillation contribute to the polarizability and to the dielectric constant, the contributions of ionic motions are small compared with electrons.

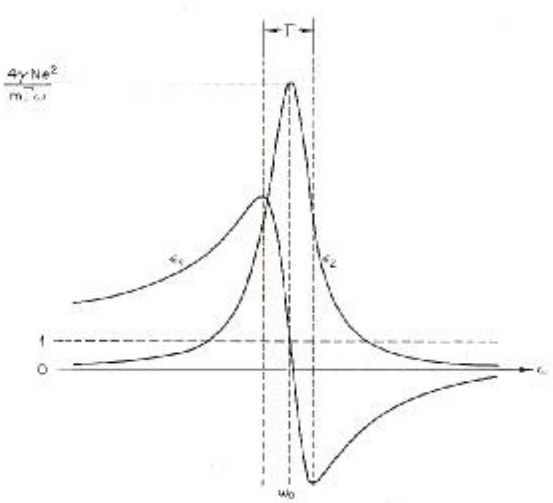

Figure 2.26. Frequency dependence of e_1 and e_2 (Wooten, 1972).

When only the electronic contributions to the dielectric constant is considered, the low frequency dielectric constant of a material will mean the dielectric constant at the low frequency end of the visible region, a frequency that is still high compared with the lattice vibrations or molecular oscillations in the crystal. Using we use Eqs. (2.20)-(2.22) we find that for non magnetic materials;

$$n = \left\{ \frac{1}{2} \left[(e_1^2 + e_2^2)^{1/2} + e_1 \right] \right\}^{1/2} \qquad \text{Eq. (2.44)}$$

$$k = \left\{ \frac{1}{2} \left[(e_1^2 + e_2^2)^{1/2} - e_1 \right] \right\}^{1/2} \qquad \text{Eq. (2.45)}$$

and the front surface reflection coefficient R is given by the relation:

$$R = \frac{(n-1)^2 + k^2}{(n+1)^2 + k^2} \qquad \text{Eq. (2.46)}$$

Using Eqs. (2.35), (2.36), and Eqs. (2.44), (2.45) with the reflectivity of solids (Eq. (2.46)), the frequency dependent behavior of a solid can be explained by in terms of whether it is primarily reflecting, absorbing or transparent. The characteristics of transparent, reflecting and absorbing regions are presented in Figures 2.28 and 2.29.

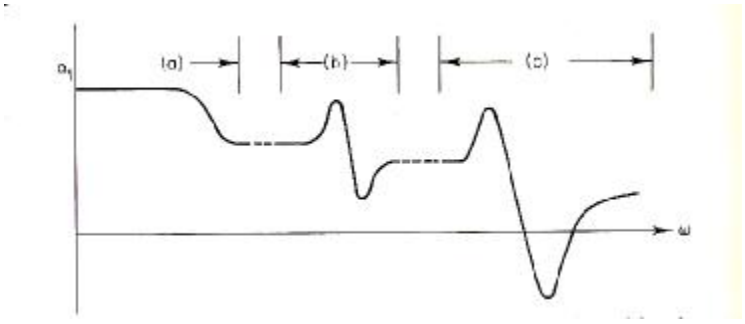

Figure 2.27. Frequency dependence of contributions to the polarizability arising from orientation of (a) permanent dipoles (microwave), (b) ionic lattice vibrations (infrared), and (c) displacement of electrons (visible and ultraviolet) (Wooten, 1972).

In region I, $w << w_o$, $e_2 = 2nk = 0$, and $e_1 = n^2 - k^2 > 1$. We may thus conclude that $k = 0$, $n > 1$, and $e_1 = n^2$. Thus, region I is characterized by high transparency, no absorption, and small reflectivity for insulators. In this region, the reflectivity arises from the induced polarization current corresponding to the valence electrons oscillating out of phase with the incident radiation. There is no absorption for this process, but the interference of the incident beam with the waves reradiated by the valence electrons does lead to appreciable reflectivity. That the Lorentz model is qualitatively correct for semiconductors and insulators is also indicated by the dependence of e_1 on band gap. Thus, if we identify hw_o as corresponding approximately to the band gap, then e_1 should decrease with increasing band gap.

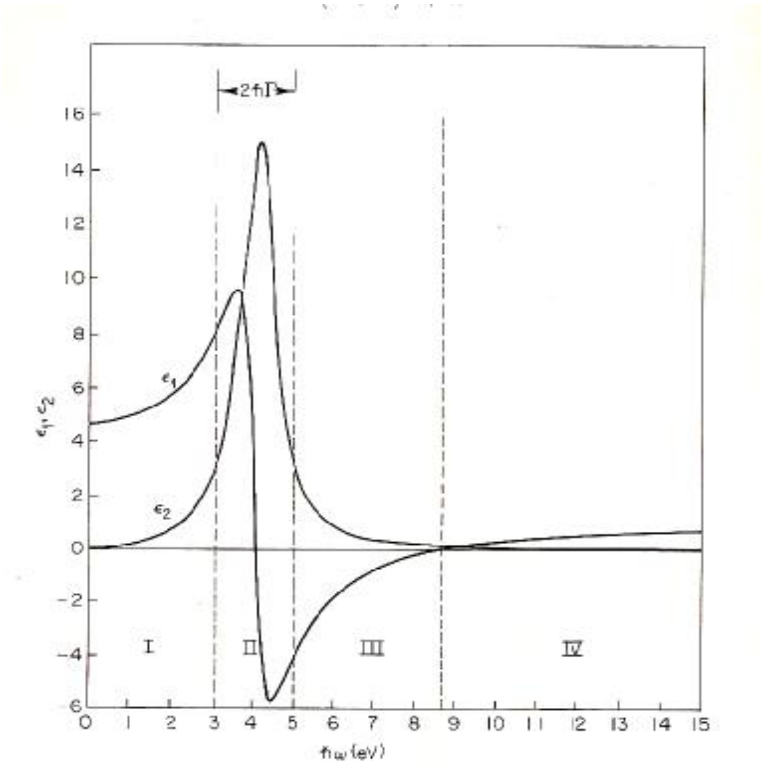

Figure 2.28. Spectral dependence of e_1 and e_2 that the values were calculated using $hw_o = 4eV$, *and* $4pNe^2/m = 60$ (Wooten, 1972).

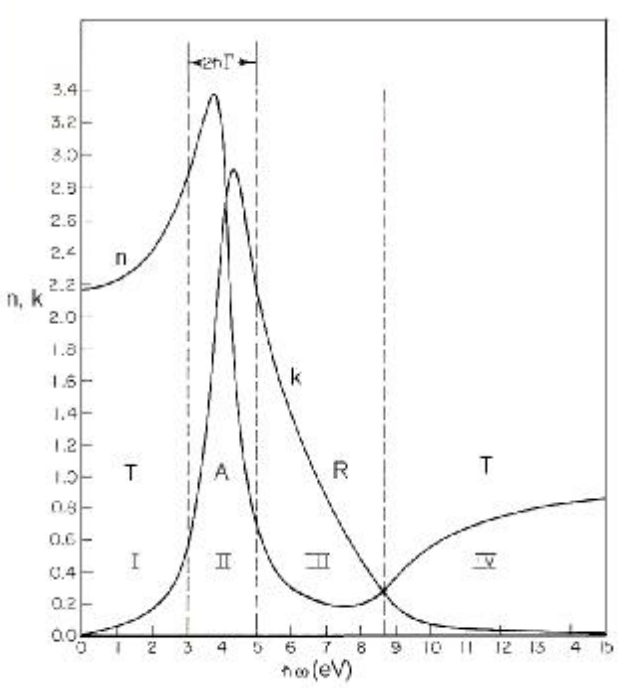

Figure 2.29. Spectral dependence of *n* and *k* calculated from the values of Figure 2.27 (Wooten, 1972).

Region II of Figures 2.28-2.29 is characterized by strong absorption. There may also be appreciable reflectivity in this region. That simply means that although the values of *n* and *k* may be high, leading to appreciable reflectivity, the light that is not reflected is strongly absorbed in the material.

In region III, $w >> w_o$, and the electrons of the insulator respond as if they were free electrons. This is because the photon energy much greater than the binding energy of the electron. The insulator thus has a metallic reflectance. For good insulators, this region lies well into the vacuum ultraviolet and can not be observed virtually. However, for semiconductors like Si and Ge, the band gap lies in the infrared and the region of metallic reflectance is in the visible.

The region IV is defined by $e_1 = 0$. This happens at a frequency w_p called plasma frequency. From equation 2.35, assuming $w >> w_o >> \Gamma$, we find:

$$w_p = \frac{4p\,N e^2}{m} \qquad \text{Eq. (2.47)}$$

2.6.2.1.(2). Semi-Empirical Equations

The optical constants of a material vary with wavelength (dispersion), and hence, dispersion models for the optical parameters of thin film semiconductors are useful for material characterization. Dispersion models help reduce the number of parameters used to describe a material. The optical analysis of the optical parameters depends on a group of semi-empirical equations well established in literature (Born and Wolf, 1970). Common dispersion models include the Cauchy and Sellmeier relationships for transparent materials and oscillator models (Lorentz, Drude, Gaussian, Tauc-Lorentz …) for absorbing materials. These formulas follow directly from the classical Lorentz oscillator model. Below, each of these dispersion relations is described in further detail.

A. Cauchy / Sellmeier

These equations are strictly empirical and were first proposed by Cauchy (1789-1827), and later by Sellmeir (1871). They express the dependence of n on wavelength in the case when the absorption is negligible ($k = 0$). They are well suited to transparent materials like SiO_2 or BK glass in the VIS and NIR.

The index of refraction, $n(\lambda)$, for transparent materials can be described with the Cauchy dispersion model, given as:

$$n(l) = A_n + \frac{B_n}{l^2} + \frac{C_n}{l^4} \qquad \text{Eq. (2.48)}$$

where A_n, B_n, and C_n, are parameters and l is the wavelengths.

The Sellmeier equation is usually expressed in following form:

$$n^2(l) = A_n + \frac{B_n l^2}{l^2 - C_n^2} \qquad \text{Eq. (2.49)}$$

where A_n, B_n, and C_n are also parameters. In many cases, A_n is initially set to 1.

In the case where $l >> C_n$, the Sellmeier formula can be expressed in series. The truncated series gives actually the well known Cauchy equation. Furthermore, it should be note that these equations are classical and a quantum form of these equations with better physical foundation was presented by Wemple and DiDomenico (1971).

B. Wemple and DiDomenico

The fundamental electronic excitation spectrum of a sample generally described in terms of frequency dependent complex dielectric function as described before by Eq. (2.22). The real and imaginary parts of the complex dielectric constant are not independent quantities; they are connected through the Kramers-Kronig (KK) relations. Both e_1 and e_2 contains all the desired response information about the optical parameters, since the real and imaginary parts of complex dielectric function can be expressed by KK relations (Greenaway and Harbeke, 1968):

$$e_1 = 1 + \frac{2}{p} P \int_0^\infty \frac{w' e_2(w')}{w'^2 - w^2} dw'$$

$$e_2 = -\frac{2w}{p} P \int_0^\infty \frac{e_1(w') - 1}{w'^2 - w^2} dw' \qquad \text{Eq. (2.50)}$$

where P denotes the principle part of the integral. In materials with a band gap ideally only photons with energy above the gap are absorbed. Hence, the lower limit of ω', in the integration over e_2 in the upper formula in Eq. (2.50) is not 0, but w_1, where $\mathbf{h}\omega_\tau$ is the band gap energy. In the TCO oxides $\mathbf{h}\omega_\tau$ >2 eV, and the integration starts at frequencies above the VIS. The expression for $e_1(\omega)$ when ω is in the VIS, is related to optical absorption above the gap by the expression:

$$e_1(w) - 1 = n^2(w) - 1 = \frac{2}{p} P \int_{w_t}^{\infty} \frac{w' e_2(w')}{w'^2 - w^2} dw' \qquad \text{Eq. (2.51)}$$

in the equation w_t is the threshold frequency, $w < w_t$, and e_1 is the square of the refractive index because k was assumed to be zero. The frequency is assumed to lies above all lattice vibrational modes that only electronic excitations are being considered, in addition, the integration should done over all relevant frequencies and over the full Brillouin zone.

Wemple and DiDomenico derived the real part of the dielectric constant using time dependent perturbation theory;

$$e_1(w) = 1 + \frac{e^2}{p^2 m} \sum_{i,j} \int_{BZ} \frac{f_{ij}^a(\vec{k})}{w_{ij}^2(\vec{k}) - w^2} d^3k \qquad \text{Eq. (2.52)}$$

where e and m are the charge and the mass. The sum extends over all bands i and j that $i \neq j$ and the interband oscillator strength for polarization direction a is given by f_{ij}^a. To calculate the frequency dependence of the dielectric constant they present the Eq. (2.52) for a single group of valance and conduction bands:

$$e_1(w) = 1 + \frac{4p e^2}{\Omega_{vol} m} \sum_{\vec{k}} \frac{f_{cv}^a(\vec{k})}{w_{cv}^2(\vec{k}) - w^2} \qquad \text{Eq. (2.53)}$$

where Ω_{vol} is the volume of the crystal, and c and v denote conduction and valance bands, respectively. Furthermore, making an approximation that the valence electron contributes to the interband transitions in the Brillouin zone by one oscillator, they wrote the Eq. (2.53) as:

$$e_1(w) = 1 + w_p^2 \sum_n \frac{f_n}{w_n^2 - w^2} \qquad \text{Eq. (2.54)}$$

where f_n is the electric dipole oscillator strength associated with transitions at frequency w_n. Isolating the first oscillator and combining the other high–order contributions with the first resonant oscillator and retaining terms to order w^2 then yields the single oscillator approximation:

$$e_1(w) - 1 \approx \frac{F}{E_o^2 - E^2} \qquad \text{Eq. (2.55)}$$

where F and E_o are related to f and w_n and they are connected to each other by $E_d = F/E_o$.

$$n^2 - 1 = \frac{E_o E_d}{E_o^2 - E^2} \qquad \text{Eq. (2.56)}$$

where n is the refractive index for specified direction of light polarization, E, E_o and E_d are the photon energy, energy of the effective dispersion oscillator (near the main peak of the e_2 spectrum), and the dispersion energy, respectively. Experimental verification of this equation was obtained by showing that the plotting of $1/(n^2-1)$ versus E^2 for a large sample of covalent oxides is linear (Wemple and DiDomenico, 1971).

The Wemple and DiDomenico (1971, 1973) model is essentially the quantum formulation of the classical Sellmeir model, or the classical oscillator model. As was mentioned above it assumes $k = 0$ for $E < E_g$. The magnitude of E_d indicates the strength of the transition whereas the value of E_o indicates the optical oscillator energy. Furthermore, E_d has a general empirical expression applicable to over 100 widely different ionic and covalent crystalline solids:

$$E_d = b\, N_c Z_a N_e \qquad \text{Eq. (2.57)}$$

where N_c, Z_a and N_e are the nearest neighbor cation coordination number, the formal anion valency and the effective number of valence electrons per anion, respectively, and b (0.37±0.04 eV for covalent, and 0.24±0.03 eV for ionic materials) is a constant whose value depends on the chemical bonding character of material, related to the charge distribution and chemical bonding and in this manner, shows the dependence of the optical properties on structure of the material. Thus, the variation of these parameters between samples could indicate the differences between samples not only in their optical constants but also show differences in structure and material arrangement.

C. Tauc–Lorentz Model

A quantum treatment of the dispersion where $E > E_g$ was given by Tauc *et al*. (1966) for the imaginary part of the dielectric function above the band edge, which is given by the relation:

$$e_2(E) = \frac{A_T (E - E_g)^2}{E^2} \qquad \text{Eq. (2.58)}$$

where A_T is a constant, and E_g is the optical band gap energy. This equation describes interband transitions provided $e_2(E) = 0$ for $E < E_g$, however, the case $e_2(E) > 0$ in the range $E < E_g$ was not included in the model.

Recently, Jellison and Modine (1996a) developed the Tauc-Lorentz (TL) model to express the optical parameters n and k of various materials also in the range $E < E_g$ for $k(E) > 0$. The TL model is obtained by multiplying Eq. (2.58) by the Lorentz expression of e_2 (Eq. (2.36)) and describes e_2 by 4 parameters: E_g, A, E_o and C (Jellsion, and Modine, 1996a)). The expression for e_1 as function of photon energy is for $E < E_g$ and $E > E_g$ is obtained by the usual KK integral. This model works

particularly well for amorphous materials and will ensure that $k = 0$ below the band gap.

$$e_2 = 2nk = \frac{A_L E_o C E}{(E^2 - E_o^2)^2 + C^2 E^2} \qquad \text{Eq. (2.59)}$$

where E_o is the peak transition energy and C is the broadening term one can obtain:

$$e_{2TL}(E) = \left[\frac{A E_o C (E - E_g)^2}{(E^2 - E_o^2)^2 + C^2 E^2} \frac{1}{E} \right], \quad E > E_g$$
$$= 0 \qquad E \le E_g \qquad \text{Eq. (2.60)}$$

The details of the integration were reported by Jellison and Modine (1996a, 1996b).

D. Gaussian Model

The Gaussian oscillator features a Gaussian line shape for the e_2 spectra, with a KK consistent line shape for the e_1 spectra:

$$e_{n2} = A_n e^{-\left(\frac{E - E_n}{B r_n}\right)} + A_n e^{-\left(\frac{E + E_n}{B r_n}\right)} \qquad \text{Eq. (2.61)}$$

$$e_{n1} = \frac{2}{p} P \int_{R_g}^{\infty} \frac{w' e_{n2}(E)}{w'^2 - E^2} dw'$$

2.6.2.1.(3). Absorption Theory

As indicated previously, both bound and free electrons produce significant absorption in semiconductors. There are altogether four types of electrons to be

considered: 1) inner shell electrons, 2) valence band electrons, 3) free carriers – including holes as well as electrons, and 4) electrons bound to localized impurity centers or defects of some type.

The first group does not contribute to either absorption or dispersion in the spectral regions with which we are concerned, and will not be considered furthermore. Absorption by the second type of electrons is of the greatest importance in the study of the fundamental optical properties of semiconductors. It involves transitions of valence electrons across the forbidden band gap, E_g, to the conduction band by optical excitation. In an ideal semiconductor at zero temperature the valance band would be completely full, so that an electron could not be excited to a higher energy state within the band itself. The only possible absorption is that of quanta sufficiently energetic for the electrons to be excited across the forbidden zone into the empty conduction band. In practice the resulting absorption spectrum is a continuum of intense absorption at short wavelengths, bounded by a more or less steep absorption edge beyond which the material is relatively transparent. However, a number of different phenomena may be associated with the incidence of light on a semiconductor. In Figure 2.30, a schematic of the optical absorption spectrum vs. energy of the photons is presented. Different types of optical absorption phenomena may be observed as function of frequency: 1) transitions of high lying bands, 2) excitons, 3) fundamental absorption (valance to conduction band transitions and Urbach tail), 4) Impurity absorption, 5) free carrier absorption and 6) Reststrahlen absorption.

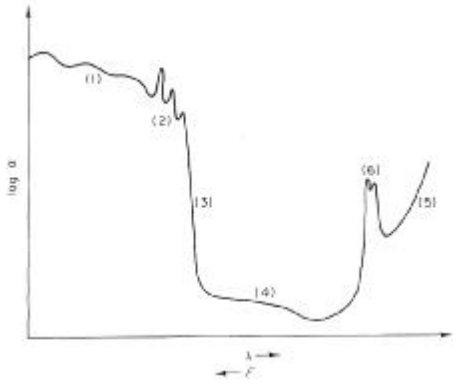

Figure 2.30. Different types of optical absorption

2.6.2.1.(4). Direct Fundamental Absorption

The direct absorption transition between two energy levels (valance and conduction bands) is presented in Figure 2.31(a), as function of the electron momentum vector $\vec{k}$, and where the upper edge of the valence band and the lower edge of the conductance band are marked by bold lines. The intensity of the absorption due to direct transitions is determined primarily by the numbers of occupied states in the valance band and unoccupied states in the conduction band, which are energetically within $h\nu$ of each other, and on the transition probability. In Figure 2.31(a) the conduction band minimum and the valance band maximum occur at $\vec{k} = 0$, hence, the absorption edge occurs at $h\nu = E_g$; where E_g is the minimum width of the forbidden energy zone of the semiconductor. The quantum mechanical selection rule states that if $\vec{k}_i$ and $\vec{k}_f$, are the wave vectors of the electron in its initial and final state, and $\vec{q}$ is the wave vector of the radiation, then $\vec{k}_f - \vec{k}_i = \vec{q}$. As for wavelengths of the order of 1 *m*m, or larger, $\vec{q}$ is very small compared with $\vec{k}$, the selection rule becomes $\vec{k}_f = \vec{k}_i$, so that the electrons with a given wave number in a particular band can only make transitions to states in a higher band having the same wave number –i.e. in Figure 2.31(a) only "vertical" transitions are allowed. "Non-vertical" transitions are nominally forbidden. In particular it does not mean that the latter do not occur at all, but that absorption due to such transitions is of much lower intensity.

In the case of Figure 2.31(a) the absorption would be intense for all $h\nu > E_g$ and cease more or less abruptly at $h\nu = E_g$. However, if the minimum in the conduction band occurs in a different region of $\vec{k}$ space than the maximum of the valance band (Figure 2.31(b)) then the intense absorption will cease at the wavelength, corresponding to the minimum vertical energy band gap (E^t) –i.e. $h\nu = E'$. Under normal conditions there will always be some factors present which

are sufficient to cause relaxation of the selection rules and so permit non-vertical transitions to occur to some degree, and the momentum being conserved probably by interactions with phonons, so that absorption will in general continue with reduced intensity for frequencies down to $h\nu = E_g$, where E_g is again the minimum energy gap.

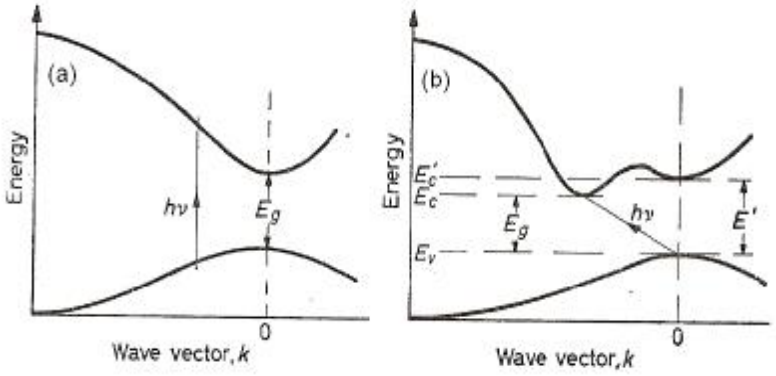

Figure 2.31. Possible energy bands in semiconductors and (a) direct, (b)indirect transitions (Moss, 1961).

If we assume that the energy zones are spherical symmetrical with curvatures corresponding to the effective masses m_e and m_h we have;

$$E - E_g = h^2k^2 / 2m_e + h^2k^2 / 2m_h \qquad \text{Eq. (2.62)}$$

In 1956, the absorption was defined by Fan;

$$a = \frac{p\, e^2}{nm} f_{if} N(E) \qquad \text{Eq. (2.63)}$$

where, f_{if} is the oscillator strength for the transition and given by the relation;

$$f_{if} = \frac{2}{3mhn} |M|^2 \qquad \text{Eq. (2.64)}$$

and, M is the matrix element governing the transition probability, N_d (E) is the density of states function where E is the energy. Using the density of states in $\vec{k}$ space is simply;

$$\frac{dN_d}{d\vec{k}} = 2(4p\vec{k}^2) \qquad \text{Eq. (2.65)}$$

we can write $N_d(E)$ in the momentum space, between E+dE;

$$\frac{dN_d(E)}{dE} = 8ph^{-3}\left[\frac{2m_e^3 m_h^3 (E - E_{g)}}{(m_e + m_h)^3}\right]^{1/2}$$
$$= 8ph^{-3}\left\{2m_r^3 (E - E_g)\right\}^{1/2} \qquad \text{Eq. (2.66)}$$

If we assume that near the absorption edge the transition probability is approximately constant (independent of frequency) then the frequency dependence of the absorption coefficient is determined only by the $(E - E_g)^{1/2}$ term. The magnitude of the absorption coefficient is given by Smith (1969) as;

$$a = \frac{e^2 (2m_r)^{3/2}}{ncm_e h^2 e_o}(hn - E_g)^{1/2} \qquad \text{Eq. (2.67)}$$

which for typical semiconductor with n= 4, and m_e = m_h = m gives an absorption coefficient of a = 4000cm^{-1} at 0.05 eV above the energy band gap.

The problem of indirect transitions has been treated by Bardeen *et al*. (1954) on the basis that the quantum mechanical selection rule for conservation of momentum is satisfied by either the absorption or emission of a phonon simultaneously with the photon absorption. The detail of the calculations and the theory can found within the paper of Bardeen *et al*. (1954), Moss, (1961).

2.7. Electrical Transport and Conductivity

2.7.1. Transport Phenomena in Semiconductor Films

Transport phenomenon is the term applied to the motion of charge carriers under the action of internal or external fields. In the absence of an electric field, the electron gas in a semiconductor is in an equilibrium state, which is established as a result of the interaction of electrons with lattice defects. Such defects include lattice imperfections, thermal vibrations of the lattice (phonons) and impurity atoms.

If an electric field $\vec{E}$ applied to a material, an electric current will flow, that density $\vec{J}$ is given by the relation:

$$\vec{J} = s\ \vec{E} \qquad \text{Eq. (2.68)}$$

where, s is called the electrical conductivity of material. The reciprocal of electrical conductivity is known as electrical resistivity r. For a rectangular shaped sample (Figure 2.32) the resistance R_r is given by;

$$R_r = r\left(\frac{l}{bd}\right) \qquad \text{Eq. (2.69)}$$

where l is the length, b is the width and d is the thickness of the sample. If $l = b$, equation becomes:

$$R = \frac{r}{d} = R_s \qquad \text{Eq. (2.70)}$$

The quantity R_s is known as the sheet resistance and it is the resistance of one square of the film and is independent of the size of the square. The sheet resistance is expressed in ohms/square.

The most commonly used method for measuring the sheet resistance R_s is a four–point probe technique. A typical schematic setup is shown in Figure 2.32(b). When the probes are placed on a material of semi infinite volume, the resistivity is given by:

$$r = \frac{V}{I}\frac{2p}{1/t_1 + 1/t_2 - 1/(t_1+t_2) - 1/(t_1+t_3)} \qquad \text{Eq. (2.71)}$$

where, V and I are the applied voltage and the curent, and t_1, t_2, t_3 are the distances between probes. When $t_1 = t_2 = t_3 = t$ the Eq. (2.71) can be written:

$$r = \frac{V}{I} 2p\, t \qquad \text{Eq. (2.72)}$$

If the material is in the form of an infinitely thin film resting on an insulating support, Eq. (2.72) leads to:

$$r = \frac{V}{I}\frac{p\, d}{\ln 2} \qquad \text{or} \qquad \frac{r}{d} = R_s = 4.53\frac{V}{I} \qquad \text{Eq. (2.73)}$$

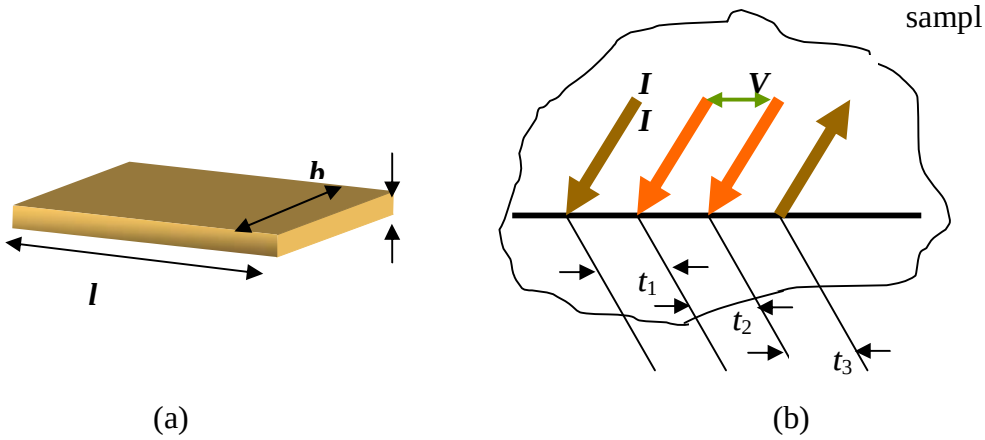

(a) (b)

Figure 2.32. (a) Rectangular shaped sample, **(b)** Four point probe measurement technique.

2.7.2. Electrical Conduction in Polycrystalline Films

Over the past few decades, a great deal of interest has been devoted to the study of the electrical transport properties of granular semiconducting materials, i.e., semiconducting material comprising crystalline or amorphous grains (Weis *et al.*, 2002). The commonly adopted viewpoint is that these properties are largely determined by potential barriers built up at grain boundaries due to charge carrier trapping into interface states (Taylor *et al.*, 1952). Carrier transport across these barriers is mostly described in terms of the traditional thermoionic-emission model, or the thermoionic- field-emission model, in which corrections allowing for quantum tunneling through the barriers are included.

Grain boundaries generally contain fairly high densities of interface states, which trap free carriers from the bulk of the grain and scatter free carriers by virtue of the inherent disorders and the presence of trapped charges. The interface states results in a space charge region in the grain boundaries. Due to this space charge region, band bending occurs, resulting in potential barriers that obstruct charge transport. The most commonly used model to explain the transport phenomenon in polycrystalline films due to Petritz (Hartnagel *et al.*, 1995). According to his model, the current density is given by the relation

$$\vec{J} = \left[e m_0 N \exp\left(\frac{-e f_b}{kT}\right) \right] \vec{E} \qquad \text{Eq. (2.74)}$$

where $m_o = (C_b / n_c kT)$, f_b is the height of the potential barrier, n_c is the number of crystallites per unit length along the film, $\vec{E}$ is the electric field, and C_b is a factor that is barrier dependent.

The grain boundary potential barrier f_b is related to N_1 and N_2, the number of carriers in the grain and the grain boundary, respectively, by the relation;

$$f_b = kT \ln\left(\frac{N_1}{N_2}\right) \qquad \text{Eq. (2.75)}$$

The quantity in the bracket in Eq. (2.74) is nothing other than the conductivity of charge carriers dominated by grain boundaries (s_g).

$$s_g = eNm_0 \exp(\frac{-ef_b}{kT}) \qquad \text{Eq. (2.76)}$$

Thus the grain boundary limited mobility can be written as:

$$m_g = m_0 \exp(\frac{-ef_b}{kT}) \qquad \text{Eq. (2.77)}$$

Seto (1975) modified the pre-exponential term in Eq. (2.77) on the assumption that (i) current flows between grains by thermionic emission and (ii) conduction in the crystallites is much bigger than that through the grain boundary. The resulting relation of mobility:

$$m_g = el'(2p\, m^* kT)^{-1/2} \exp(\frac{-ef_b}{kT}) \qquad \text{Eq. (2.78)}$$

where l' is the grain size. Orton *et al* (Hartnagel *et al.*, 1995) showed that the pre-exponential term can be written in a more generalized way as:

$$m_0 = el'\{8/(pb^2 kTm^*)\}^{1/2} \qquad \text{Eq. (2.79)}$$

where *b* is numerical constant. In general, the grain boundary mobility can be written as:

$$m_g = m_0' T^{-1/2} \exp(\frac{-ef_b}{kT}) \qquad \text{Eq. (2.80)}$$

where $m_0 = m_0' T^{-1/2}$. Later works have shown that the conductivity term in Eq. (2.76) should be written more generally as;

$$s_g = s_0 \exp(\frac{-E_s}{kT}) \quad \text{Eq. (2.81)}$$

where E_σ is the conductivity activation energy. Similarly,

$$N = N_0 \exp(\frac{-E_n}{kT}) \quad \text{Eq. (2.82)}$$

where E_n is the carrier activation energy. Further,

$$E_s = E_n + ef_b \quad \text{Eq. (2.83)}$$

2.8. Thin Film Diagnostics and Optical Models

In this section the diagnostics methods and models used in the optical characterization are reviewed. The composition, structure and morphology were analyzed using electron dispersive spectroscopy (EDS), X-ray photoelectron spectroscopy (XPS), X-ray diffraction (XRD), atomic force microscopy (AFM) and scanning electron microscopy (SEM/HRSEM). The optical and electrical properties were investigated using normal incidence transmission, and spectroscopic ellipsometry. The resistivity was determined using four point resistance measurements, and the thickness of the films was determined by profilometry and from optical analyses where the thickness was one of the fitted parameters. Furthermore, the thermal stability measurements were done using the two point probe technique. Below, each of the diagnostic method is reviewed.

2.8.1. Composition, Structure and Morphology Analyses

2.8.1.1. Energy Dispersive X-Ray Spectroscopy (EDS)

Energy dispersive X-ray spectroscopy (EDS or EDX) is a compositional microanalysis technique used in conjunction with scanning electron microscopy (SEM) in which features as small as 1 μm can be analyzed. EDS detects the characteristic X-rays emitted from the sample during bombardment by an electron beam, to characterize the elemental composition of the analyzed volume. When the sample is bombarded by the SEM's electron beam, X-ray photons, which are produced by transitions between deep atomic levels, are ejected from the atoms comprising the sample's surface. The X-ray energy is characteristic of the element from which it was emitted.

When an X-ray strikes the EDS detector, it creates a charge pulse that is proportional to the energy of the X-ray. The charge pulse is converted to a voltage pulse (which remains proportional to the X-ray energy) by a charge-sensitive preamplifier. The signal is then sent to a multi-channel analyzer where the pulses are sorted by voltage. The spectrum of X-ray energy versus counts is evaluated to determine relative abundance of emitted X-rays versus their energy, and hence the elemental composition of the sampled volume.

Qualitative Analysis –The sample X-ray transitions energy derived from the EDS spectrum can be compared with known characteristic X-ray energy values to determine the presence of an element in the sample. Elements with atomic numbers ranging from that of beryllium to uranium can be detected. The minimum detection limits vary from approximately 0.1 to a few atomic percent, depending on the element and the sample matrix.

Quantitative Analysis – Quantitative results can be obtained from the relative X-ray counts at the characteristic energy levels for the sample constituents. Semi-quantitative results are readily available without standards by using mathematical corrections based on the analysis parameters and the sample composition. The accuracy of non-standard analysis depends on the sample composition. Greater

accuracy is obtained using known standards with structure and composition similar to that of the unknown sample.

Elemental Mapping – Characteristic X-ray intensity can be measured relative to lateral position on the sample. Variations in X-ray intensity at any characteristic energy value indicate the relative concentration for the applicable element across the surface. One or more maps are recorded simultaneously using image brightness intensity as a function of the local relative concentration of the element(s) present. About 1 μm lateral resolution is possible.

Line Profile Analysis – The SEM electron beam can be scanned along a pre-selected line across the sample while X-rays are detected for discrete positions along the line. Analysis of the X-ray energy spectrum at each position provides plots of the relative elemental concentration for each element versus position along the line.

2.8.1.2. Photoelectron Spectroscopy

Photoelectron spectroscopy utilizes photo-ionization and energy-dispersive analysis of the emitted photoelectrons to study the composition and electronic state of the surface region of a sample. The technique is differentiated according to the source of exciting radiation into: ***X-ray Photoelectron Spectroscopy (XPS)*** which uses X-ray with energy in the range 200-9000 eV to excite core-levels, and ***Ultraviolet Photoelectron Spectroscopy (UPS)*** which uses vacuum UV (10-45 eV) radiation to excite valence levels.

2.8.1.2.(1). X-Ray Photoelectron Spectroscopy (XPS)

X-ray photoelectron spectroscopy (XPS) is a surface analytical technique, which is based upon the photoelectric effect, where inner shells electrons (core electrons) are ejected by X-ray photons. Each atom on the surface has core electrons with the characteristic binding energies that are conceptually, though not strictly, equal to the ionization energy of that electron. When X-rays hit the sample surface, the energy of the X-ray photon could be completely adsorbed by the core electron. If

the photon energy, *hn*, is appropriate, the core electron will then escape from the atom, and has some probability to also escape from the surface with a kinetic energy of E_k. The emitted electron is referred to as a photoelectron.

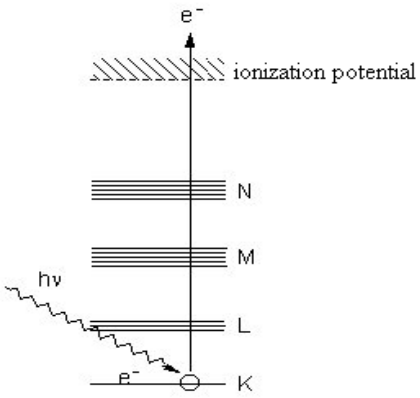

Figure 2.33. Schematic diagram of excitation of core electrons.

The binding energy of the core electron is give by the Einstein relationship:

$$E_b = hn - E_k - f_w \qquad \text{Eq. (2.84)}$$

where *hn* is the X-ray photon energy; E_k is the kinetic energy of the photoelectron, which is measured by an energy analyzer; and f_w is the work function induced by the analyzer, ~4-5 eV. f_w is compensated electronically, giving the binding energy as:

$$E_b = hn - E_k \qquad \text{Eq. (2.85)}$$

For insulating samples, once the photoelectrons are emitted out of the sample surface, a positive charge zone will establish quickly on the sample surface. As a result, the sample surface acquires a positive potential *K* (varying typically from several volts to tens of volts) and the kinetic energies of the detected core electrons are likewise reduced:

$$E_b = hn - (E_k - K) \qquad \text{Eq. (2.86)}$$

Surface charging shifts the XPS peaks to higher energies. If this occurs, the binding energy has to be calibrated with an internal reference peak. The C 1s peak from the adventitious carbon-based contaminants, with a binding energy of 284.8eV, is commonly used as the reference. An alternative strategy to handle surface charging is to neutralize the surface charge during data acquisition with a low-energy electron flood. The electron flood source can be tuned to provide the right current to push the XPS peaks back to its uncharged position.

The core electrons of each element have a unique binding energy, which serves as an identifying "fingerprint". Thus almost all elements except for hydrogen and helium can be identified by measuring the binding energy of their core electrons. Furthermore, the binding energy of core electrons is sensitive to the chemical environment of the atom. The same atom bonded to the different atomic neighbors will have slightly different binding energies for its core electrons. The variation of binding energy shifts the corresponding XPS peak, by 0.1-10eV. This effect is termed the "chemical shift", and is applied to determine the chemical status of surface atoms. Therefore, XPS is also known as electron spectroscopy for chemical analysis (ESCA).

Since the photoelectron current associated with a given element is dependent upon the atomic concentration of that element in the sample surface, XPS is used to not only identify the elements but also quantify the chemical composition. After the peak intensity (corrected to the background) is obtained, the atomic concentration of an element, P_i, can be expressed as:

$$P_i = \frac{I_i / S_i}{\sum_i I_i / S_i} \qquad \text{Eq. (2.87)}$$

where I_i is the peak intensity for element i, and S_i is the sensitivity factor for that peak i.

As stated above, XPS and EDS could used for analyze surface composition. Inner bulk composition can be obtained by sputtering upper layers of the material, using an appropriate high energy ion gun. Ar ions are the most common ones used in sputtering layers of the material. Often, the removal of the surface layers expose material that is not contaminated by atoms adsorbed from the environment.

2.8.1.3. X-Ray Diffraction (XRD)

X-ray diffraction (XRD) is a powerful technique used to uniquely identify the crystalline phases present in materials and to measure their structural properties (strain state, grain size, epitaxy, phase composition, preferred orientation, and defect structure). XRD is also used to determine the thickness of thin single or multi layer films, and the atomic arrangements (phase of atoms) in amorphous materials (including polymers) and interfaces. X-ray diffraction method is commonly used because it is non-destructive. XRD of thin-films is important in many technological applications, because of its abilities to accurately determine strain and to uniquely identify the presence and composition of phases. In semiconductor and optical materials applications, XRD is used to measure the strain state, orientation, and defects in epitaxial thin films, which affect their electronic and optical properties.

The crystalline size D can be evaluated from the full-width-half-maximum (FWHM) value of the reflections of the films, using the Scherer equation:

$$D = \frac{0.9\, l}{w.Cos(q)} \qquad \text{Eq. (2.88)}$$

where w is the broadening of the diffraction line measured at half its maximum intensity in radians and λ is wavelength of the X-rays (often the Cu K_α line at 0.15406 nm). The lattice parameters of the films can be calculated according to Bragg's law:

$$n\,l = 2\,d\,Sin(q) \qquad \text{Eq. (2.89)}$$

where n is taken as unity, λ is the wavelength of the radiation and d is interplanar spacing between the crystalline planes that reflect in the direction θ. The parameter d_{hkl} depends on the crystalline structure and can be calculated using:

$$d_{hkl} = \frac{c}{\sqrt{h^2 + k^2 + l^2}} \quad \text{for ZnO crystal for (002) plane} \qquad \text{Eq. (2.90)}$$

$$d_{hkl} = \frac{1}{\sqrt{\frac{h^2 + k^2}{a^2} + \frac{l^2}{b^2}}} \quad \text{for } SnO_2 \text{ crystal} \qquad \text{Eq. (2.91)}$$

where h, k, and l are the Miller indices (hkl), and a, b and c are the lattice parameters.

The stress, s_{st}, parallel to the film surface for ZnO films, can be calculated using (Wang *et al*., 2003):

$$s_{st} = \frac{2C_{13}^2 - C_{33}(C_{11} + C_{12})}{2C_{13}} \frac{(c - c_0)}{c_0} \qquad \text{Eq. (2.92)}$$

where the coefficients C_{ij} are the elastic stiffness constants of single crystal ZnO (C_{11}=208.8 GPa, C_{12}=119.7 GPa, C_{13}=104.2 GPa, and C_{33}=213.8 GPa) and c and c_0 (0.5206 nm) are the measured and stress free c-axis lattice constants, respectively. Also diffraction peak shifts compare to the standard reflection peak values can be used to observe the elastic stress in the films.

2.8.1.4. Scanning Electron Microscopy (SEM)

Scanning electron microscopy (SEM) is a method for high-resolution imaging of surfaces. SEM has much higher magnification (>100,000) and greater depth of

field (up to 100 times) than that of light microscopy. The electrons are generated by electron gun above the sample chamber. In Figure 2.34, a schematic of SEM is shown.

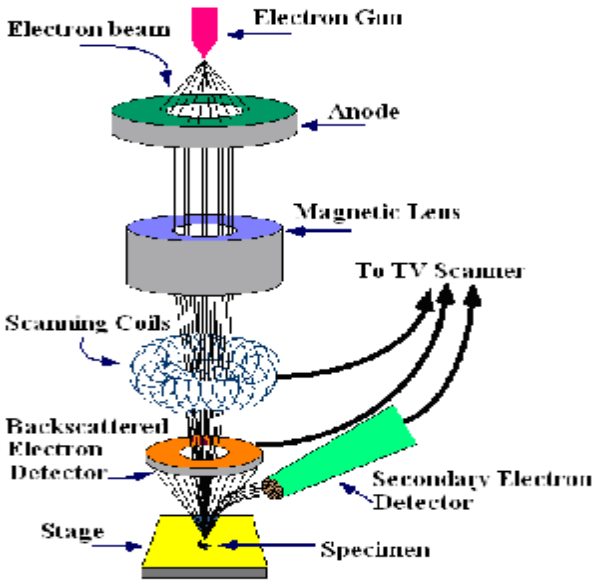

Figure 2.34. Schematic of Scanning Electron Microscopy (SEM) (O'connor *et al*., 1992).

Scanning coils near the end of the column direct the focused beam onto the sample surface. The electron beam is scanned in a raster pattern over the surface for imaging. The beam can also be focused at a single point or scanned along a line for X-ray analysis. The beam can be focused to a final probe diameter as small as about 10 Å. The incident electrons cause electrons to be emitted from the sample due to elastic and inelastic scattering on and near the sample surface. High-energy electrons which are scattered by elastic collisions, typically with a sample atom nucleus, are referred to as backscattered electrons. The energy of backscattered electrons will be comparable to that of the incident electrons. Emitted lower-energy electrons resulting from inelastic scattering are called secondary electrons. Secondary electrons can be formed by collisions with the nucleus where substantial energy loss occurs or by the ejection of loosely bound electrons from the sample atoms. The energy of secondary electrons is typically 50 eV or less.

To create an SEM image, the incident electron beam is scanned in a raster pattern across the sample's surface. The emitted electrons are detected at each position in the scanned area by an electron detector. The intensity of the emitted electron signal is displayed as brightness on a cathode ray tube (CRT). By synchronizing the CRT scan to that of the scan of the incident electron beam, the CRT display displays the morphology of the sample surface area scanned by the beam. Magnification of the CRT image is the ratio of the image display size to the sample area scanned by the electron beam.

The SEM column and sample chamber are at a moderate vacuum to allow electrons to travel freely from the electron beam source to the sample and from the sample to the detectors. High-resolution imaging is done with the chamber at higher vacuum, typically from 10^{-5} to 10^{-7} Torr. Imaging of nonconductive, volatile, and vacuum-sensitive samples can be performed at higher pressures.

2.8.1.5. Atomic Force Microscopy (AFM)

Atomic Force Microscopy (AFM) is a form of scanning probe microscopy (SPM) where a small probe is scanned across the sample to obtain information about the sample surface. The atomic force microscope can be operated either in air or in vacuum and via two primary modes (contact or non-contact). The basic operating principles of the AFM remain the same: the AFM uses a probe that has a micro-fabricated tip mounted on a flexible cantilever. The AFM probe tip is very sharp, often less than 100 Å diameter. The tip is slowly scanned across the surface of a sample, just a few angstroms away from the surface (non-contact mode) or in contact with it (contact mode). The force between the atoms on the surface of the material and those on the tip deflect the tip. The magnitude of the deflection depends on the separation between the surface atoms and the tip atoms and on the atomic forces between them (Van der Waals forces or Pauli exclusion forces, etc.). The information gathered from the probe’s interaction with the surface can be as simple as physical topography or as diverse as measurements of the material’s physical, magnetic, or chemical properties. These data are collected as the probe is scanned in a raster

pattern across the sample to form a map of the measured property relative to the X-Y position. Thus, the AFM microscopic image shows the variation in the measured property, e.g., height or magnetic domains, over the area imaged.

In Figure 2.35, a schematic diagram of an AFM system is shown. The deflection can be recorded in various ways, the most common of which uses a laser focused on the top of the cantilever and reflected onto photodetectors. The photodetector signals are used to map the tip deflection with resolutions down to the atomic and nano scales. The lateral and vertical movements of the tip or sample are controlled by piezoelectric transducers and a feedback loop that produce voltage differences proportional to the movement.

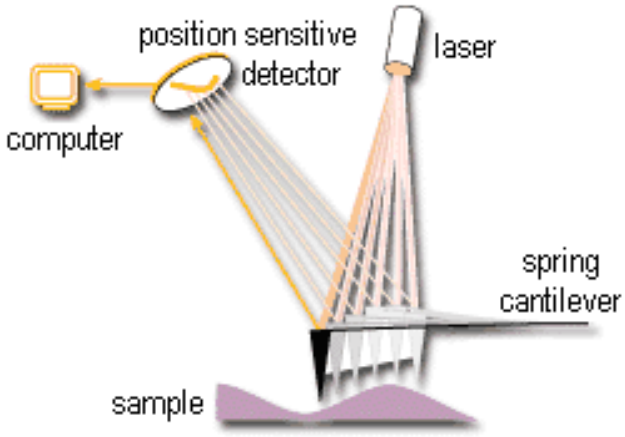

Figure 2.35. Schematic diagram of an AFM (http://www.che.utoledo.edu, 2006).

2.8.2. Optical Measurements

2.8.2.1. Transmission and Reflection

Collimated light incident on a transparent substrate with a thin film may be transmitted or reflected, as shown in Figure 2.36. The incident light impinges on the sample at some arbitrary angle q_i with respect to the direction normal to the sample

surface. At the boundary, part of the light will be reflected at angle q_r while the other part will be transmitted through the sample at angle q_t .

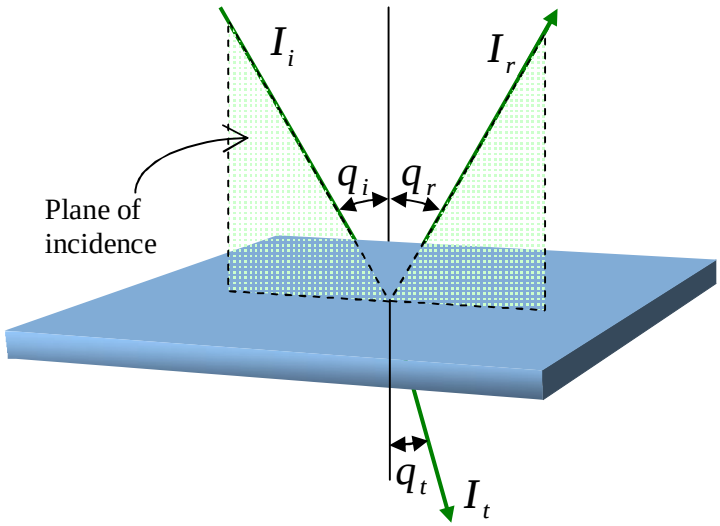

Figure 2.36. Schematic diagram of the incident, reflected, and transmitted beams.

Snell's law requires that all three beams and the normal to the surface be in the plane of incidence (shaded green in Figure 2.36). The transmission and reflection measurements acquire the intensity ratios, T and R respectively, over a given range of wavelengths. T and R are defined as the ratio of the light intensity being transmitted I_t or reflected I_t over the incident light intensity I_i on the sample, as shown in Eqs. (2.93) and (2.94):

$$T = \frac{I_t}{I_i} \qquad \text{Eq. (2.93)}$$

$$R = \frac{I_r}{I_i} \qquad \text{Eq. (2.94)}$$

In Figure 2.37, the schematic diagram of the measurement of transmission is seen.

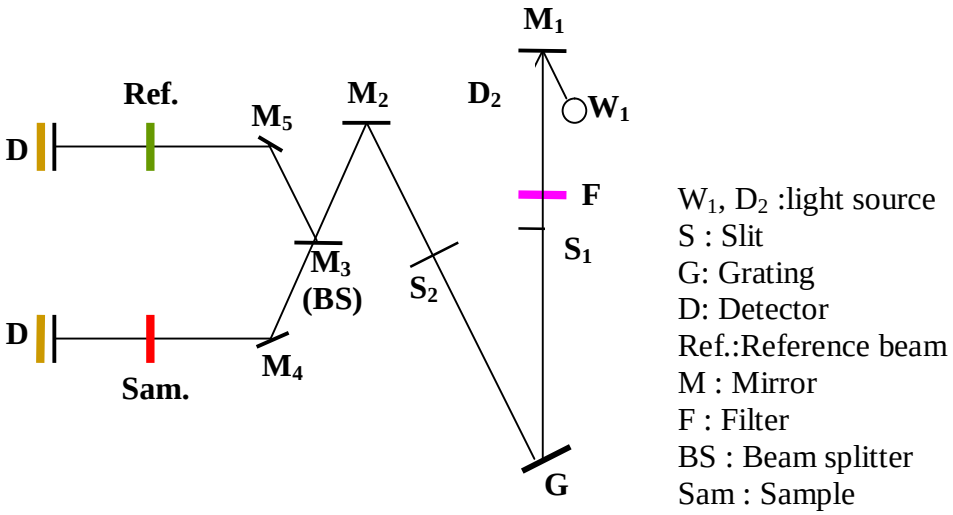

Figure 2.37. Schematic diagram of double beam spectrophotometer

The light from the light source is converged and enters to the monochromator and is dispersed by the grating in the monochromator and converges onto the exit slit. The light that has passed through the exit slit is monochromatic. This light is split into two beams, one going to the sample to be measured and the other to the reference sample. The light that passed through the sample or reference sample is incident upon the silicon photodiode alternatively.

2.8.2.2. Spectroscopic Ellipsometry

Ellipsometry measures the change in polarization state of light reflected from the surface of a sample. The mathematical theory for ellipsometric analysis is based on the Fresnel reflection or transmission equations for polarized light encountering boundaries in planar multilayered materials. These come from solutions to Maxwell's equations. The ellipsometric measurement is normally expressed in terms of Psi(Ψ) and Delta(Δ):

$$\tan(\Psi)e^{i\Delta} = \frac{R_p}{R_s} \qquad \text{Eq. (2.95)}$$

where R_p and R_s are the complex Fresnel reflection coefficients of the sample for p- (in the plane of incidence) and s- (perpendicular to the plane of incidence) polarized light, illustrated in Figure 2.38. Spectroscopic Ellipsometry (SE) measures the complex ratio R as a function of wavelength. Variable Angle Spectroscopic Ellipsometry (VASE) performs the above measurement as a function of both wavelength and angle of incidence.

Since ellipsometry measures the ratio of two values it is highly accurate and reproducible, and no reference material is necessary. Because it measures a phase quantity 'Δ' (as well as an amplitude ratio), it is very sensitive even to the presence of very thin films. Use of Spectroscopic Ellipsometry (SE) results in increased sensitivity to multiple film parameters, and as well, eliminates the 'period' problem, associated with interference oscillations in thick films. Another feature of SE is that it measures data at the wavelength of interest, which is of particular importance for industrial problems such as development of lithography at new wavelengths. Adding multiple angles to spectroscopic capability provides new information because of the different optical path lengths traversed, and it optimizes sensitivity to the unknown parameters.

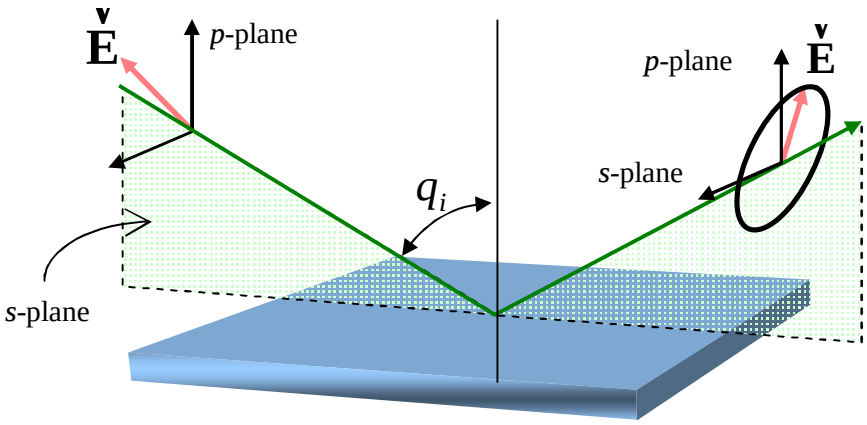

Figure 2.38. Schematic geometry of an ellipsometry experiment (www.uta .edu/optics/research/ellipsometry/ellipsometry.htm, 2006).

Many desired material parameters can be extracted by variable angle spectroscopic ellipsometry (VASE) analysis, including layer thickness, surface and/or interfacial roughness and optical constants. In Figure 2.39, the photo of spectroscopic ellipsometry developed by J.A Woollam is presented.

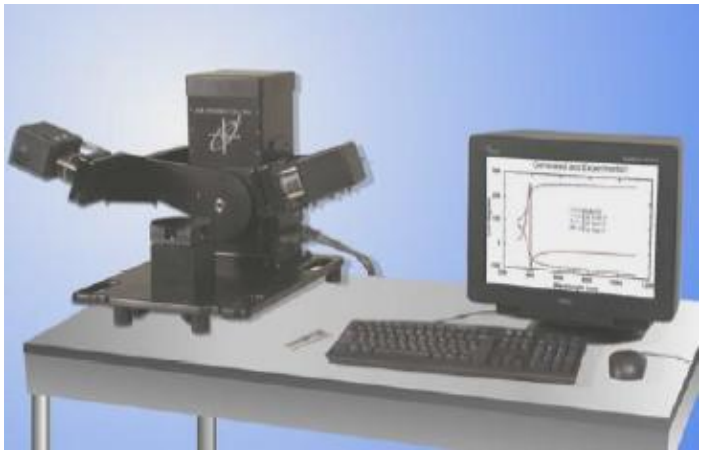

Figure 2.39. Over all view of spectroscopic ellipsometry.

The ellipsometric ψ and Δ data measured on bulk sample, i.e., negligible transmission through the sample, can be directly inverted into the "pseudo-optical" constants of the material, assuming that surface oxide and/or roughness effects are negligible this transform is given by Eq. (2.96), in which 'ϕ' is the angle of incidence, and 'r_r' is the complex ellipsometric ratio defined in Eq. (2.96);

$$\hat{e} = e_1 + ie_2 = (n+ik)^2 = \sin(f)^2.\left[1+\tan(f)^2.(\frac{1-r_r}{1+r_r})^2\right] \qquad \text{Eq. (2.96)}$$

Spectroscopic ellipsometry, like all other optical metrology techniques, requires (Woollam, *et al.*, 1999)**:**

- Acquiring data (Ψ and Δ). Data is typically acquired versus wavelength and angle of incidence.

- Building an optical model that describes the sample structure using as much information about the sample as possible. It is important to account for all layers in the sample structure. Generating theoretical data from the optical model that corresponds to the experimental data, i.e., reconstructing $\Psi(\lambda)$ and $\Delta(\lambda)$ by varying the parameters of the model dielectric functions.
- Comparing the generated data to experimental data. The parameters in the optical model, such as thin film thickness and/or optical constants or both, are varied to try and reconstruct the measured Ψ and Δ data by producing a "best fit" to the experimental data. Regression algorithms are used to vary unknown parameters and minimize the difference between the generated and experimental data.
- Physical parameters of the sample such as film thickness, optical constants, composition, surface roughness, etc. are obtained once a good "fit" to the experimental data is achieved.

The SE data for this report were taken from 191 to 989 nm and at multiple angles of incidence (45°-75° by 5°). Variable angles improve confidence, as light travels different paths through the film. All data analysis was performed with WVASE version 3.51 software package. The characterization of the optical constants and thickness of semiconductor thin films is a major part of this research, and ellipsometry is one of the methods of determining these quantities.

2.8.3. Optical Data Analyses

The knowledge of accurate values of the wavelength dependent complex refractive index of thin solid films is very important, both from a fundamental and a technological viewpoint. Numerous methods have been devised for the determination of the complex refractive index and the other optical parameters of films using

normal incidence transmission and spectroscopic ellipsometry measurements. In this section some of the optical analyses methods and procedures are described.

2.8.3.1. Analysis of Normal Incidence Transmission Data

The optical characterization of a thin film by transmission and reflection measurements is a well-known issue. Rigorous expressions for the transmittance *T* and the reflectance *R* of a thin uniform film with smooth interfaces and of constant thickness deposited onto a transparent substrate were presented by Heavens (1965). Once the experimental values of *R* and *T* are known, the mathematical problem consists in reconstructing their values by calculating the real and imaginary parts of the film complex refractive index, *n* and *k*, respectively, as function of wavelength. A difficulty arises as the expressions cannot be inverted to permit the direct calculation of *n* and *k* from the experimental values of *R* and *T*. As a consequence, many numerical and graphic methods were developed to facilitate the resolution of the equations.

One of the methods of the derivation of the functions $n(\lambda)$, $k(\lambda)$, and film thickness of dielectric and semiconducting thin films deposited onto transparent or semitransparent substrates, using the transmission spectra measured at normal incidence, was proposed by Cisneros (1998). The mathematical procedures used in that study makes use of some properties of the transmittance that permit the separate calculation of the optical parameters in two regions: the low- and the high-absorption regions, respectively. The formulas for the reflection and transmission used in the calculation of the optical parameters of a thin film deposited onto a thick substrate should include the reflections from the second interface of the substrate; otherwise the results will be affected by systematic and significant errors. The derivation of the expressions for the transmittance and reflectance is made in two steps. The first one gives the well-known transmittance and reflectance of the film with smooth and parallel faces bounded by two semi-infinite media. In the second step the multiple incoherent reflections from the substrate–air interface are included to yield the final expressions.

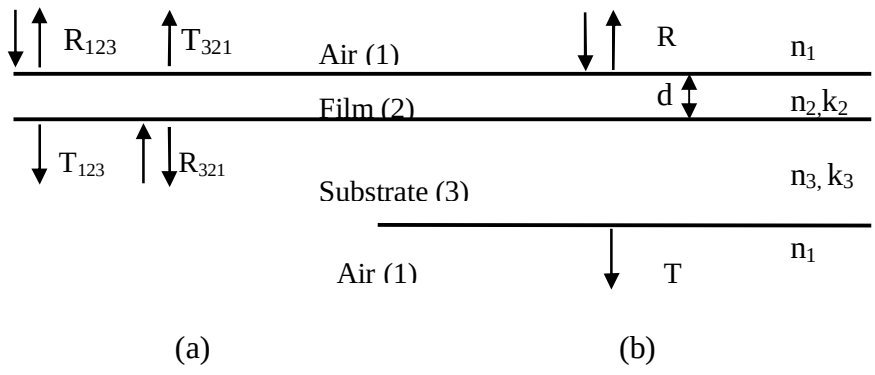

Figure 2.40. Optical parameters and directions of the transmittance and reflectance adopted for the film-substrate assembly: (a) semi infinite (b) finite substrate (Cisneros, 1998).

To permit the characterization of both transparent and absorbing films, a complex refractive index of the film is used throughout this study. The analysis of the optical spectrum of the sample, which usually includes the interference fringe region and the absorption edge, yields the refractive index and the absorption coefficient of the film. The thickness of the thin film is also obtained, frequently with a better precision than for the result obtained from an independent measurement.

For the first step of the calculation (semi-infinite substrate) the film complex refractive index $\tilde{N}_2 = n_2 + ik_2$ and thickness *d*, bounded by two semi-infinite transparent media of real refractive indices $\tilde{N}_1 = n_1$ and $\tilde{N}_3 = n_3$ is considered; see Figure 2.40(a). Usually the incident medium is air with n_1=1. The amplitudes of the reflected and the transmitted electric fields with respect to the incident field at each interface *ij* are given by the corresponding Fresnel coefficients:

$$r_{ij} = \frac{\tilde{N}_i - \tilde{N}_j}{\tilde{N}_i + \tilde{N}_j}, \qquad t_{ij} = \frac{2\tilde{N}_i}{\tilde{N}_i + \tilde{N}_j} \qquad \text{Eq. (2.97)}$$

The complex refractive indices $\tilde{N}_j = n_j + ik_j$ with j =1,2,3 correspond to the incident medium, film, and substrate, respectively, according to Figure 2.40. The

amplitudes of the electric field of the waves transmitted and reflected by the film are given by the following coefficients, where both incidence directions, (123) and (321), are considered:

$$t_{123} = \frac{t_{12}t_{23}\exp(i\gamma/2)}{1+r_{12}r_{23}\exp(i\gamma)} \quad \text{Eq. (2.98)}$$

$$t_{321} = \frac{t_{32}t_{21}\exp(i\gamma/2)}{1+r_{32}r_{21}\exp(i\gamma)} \quad \text{Eq. (2.99)}$$

$$r_{123} = \frac{r_{12}r_{23}\exp(i\gamma/2)}{1+r_{12}r_{23}\exp(i\gamma)} \quad \text{Eq. (2.100)}$$

$$r_{321} = \frac{r_{32}r_{21}\exp(i\gamma/2)}{1+r_{32}r_{21}\exp(i\gamma)} \quad \text{Eq. (2.101)}$$

where the phase difference of the wave between the two interfaces $\psi/2$ of the film is defined by:

$$\gamma = 4\pi N_2 d/\lambda \quad \text{Eq. (2.102)}$$

and λ is the vacuum wavelength of the light. The complex angle Ψ is separated into its real and imaginary parts:

$$\mathrm{Re}(\gamma) = 4\pi n_2 d/\lambda = \delta \quad \text{Eq. (2.103)}$$

$$\mathrm{Im}(\gamma) = 4\pi k_2 d/\lambda = \alpha d \quad \text{Eq. (2.104)}$$

$\alpha = 4\pi k_2/\lambda$ is usually called the absorption coefficient of the film; δ is referred to as the phase angle. The values of the refractance and the transmittance of the film, according to electromagnetic theory are defined by:

$$R_{123} = r_{123} r_{123}^{*} \quad \text{Eq. (2.105)}$$

$$R_{321} = r_{321} r_{321}^{*} \quad \text{Eq. (2.106)}$$

$$T_{123} = (n_3 / n_1) t_{123} t_{123}^{*} \quad \text{Eq. (2.107)}$$

The transmittances in both directions are equal when the substrate is transparent. The effect of the finite substrate (see Figure 2.40(b)), is introduced by means of the following expressions, which are valid for transparent and weakly absorbing substrates:

$$R = \frac{R_{123} + (T_{123}^2 - R_{123} R_{321}) p U^2}{1 - p R_{321} U^2} \quad \text{Eq. (2.108)}$$

$$R' = \frac{(1-2p) R_{321} U^2 + p}{1 - p R_{321} U^2} \quad \text{Eq. (2.109)}$$

$$T = \frac{(1-p) T_{123} U}{1 - p R_{321} U^2} \quad \text{Eq. (2.110)}$$

R and R' are the reflectances in the (123) and (321) directions, respectively, and T is the value of the transmittance of the assembly (film+substrate), according to Figure 2.40(b). Any weak absorption in the substrate is taken into account by the factor U, which can be determined separately as indicated below.

$$U^{-1} = \frac{(1-p)^2}{2T_{sub}} + \left[\frac{(1-p)^4}{4T_{sub}^2} + p^2 \right]^{1/2} \quad \text{Eq. (2.111)}$$

where, T_{sub} substrate transmission. To calculate U it is necessary to know n_1 and n_3 and to measure the transmittance T_{sub} of the naked substrate. If the transmittance of the substrate and the refractive index of the incident medium are known, the refractive index of the substrate is determined by:

$$n_3 = n_1\left[\frac{1}{T_{sub}} + \left(\frac{1}{T_{sub}^2} - 1\right)^{1/2}\right] \qquad \text{Eq. (2.112)}$$

The factor, p, is the reflectivity of the 1–3 interface. Usually, in the substrates used for transmission experiments, the absorption is zero or small; in these cases the term k_3^2 can be dropped.

$$p = \left[(n_1 - n_3)^2 + k_3^2\right] / \left[(n_1 + n_3)^2 + k_3^2\right] \qquad \text{Eq. (2.112)}$$

Substituting R_{321} and T_{123} from Eqs. (2.106) and (2.107), respectively, into Eq. (2.110) and after a straightforward but tedious calculation, one gets for the transmittance:

$$T = \frac{A\exp(ad)}{B\exp(2ad) + C\exp(ad) + D} \qquad \text{Eq. (2.113)}$$

where A, B, C, and D are algebraic functions of the optical constants and thickness of the film and adjacent media. In the low absorption region of the spectrum the factor C in Eq. (2.113) is responsible for the modulation of the transmittance. They adopted the following simplifying definitions to write Eq. (2.113):

$$A = 16\,n_3(1-p)(n_2^2 + k_2^2)U$$
$$B = st - Us\,u\;p$$
$$C = \left[2(4n_3k_2^2 - ZY)\cos j + 4k_2(n_3Y + Z)\sin j\right] - pU^2\left[4k_2(Z - n_3Y)\sin j - 2(ZY + 4n_3k_2^2)\cos j\right] \qquad \text{Eqs. (2.114)}$$
$$D = uu - U^2tu\;p$$

$$\begin{aligned} u &= (n_1 - n_2)^2 + k_2^2 \\ u &= (n_2 - n_3)^2 + k_2^2 \\ s &= (n_1 + n_2)^2 + k_2^2 \\ t &= (n_2 + n_3)^2 + k_2^2 \\ Y &= n_2^2 - n_1^2 + k_2^2 \\ Z &= n_2^2 - n_3^2 + k_2^2 \end{aligned} \qquad \text{Eq. (2.115)}$$

The optical constants (*n*, *k*) of films can be derived by expressing the dielectric function according to the dispersion models that were described in section "2.6.2.1" and obtained parameters can used in transmission equation (Eq.(2.113)). Moreover, the quality of the fit can be determined by minimizing the object function defined by the sum of squares (SS):

$$SS = \frac{1}{N-M}\sum_{i=1}^{N}\left[T_c(l_i) - T_{\exp}(l_i)\right]^{1/2} \qquad \text{Eq. (2.116)}$$

where *N* is the number of the data points. As the number of data points, *N*, was much larger than 100, the correction corresponding to the number of fitted parameters (*M*) was not significant in Eq. (2.116) (Lurie and Moore, 1994).

2.8.3.2. Analysis of Spectroscopic Ellipsometry (VASE) Data

The ellipsometric data of samples that comprise several optically different layers can be analyzed by a model which reconstructs the measured sample using

layers for each material. Thickness and optical constants (*n* and *k*) describe each layer over the measured wavelength range, with estimates for any unknown properties. An example model is shown below (Figure (2.41)) with a UVFS substrate (layer 0) and two coatings above (layer 1 and 2).

2 SnO2	200 nm
1 ZnO	100 nm
0 UVFS	1 mm

Figure 2.41. Layer model: an example.

The unknown properties of the sample are defined by the model "fit" parameters. These parameters are actually those of the layers dielectric functions and film thickness. The software automatically adjusts these parameters to improve the agreement between the measured and model-generated (reconstructed) data. This agreement is quantified via the Mean Squared Error (MSE).

The MSE describes the difference between experimental data and model predicted data:

$$MSE = \frac{1}{2N-M}\sum_{i=1}^{N}\left[\left(\frac{y_i^{\mathrm{mod}} - y_i^{\mathrm{exp}}}{s_{y,i}^{\mathrm{exp}}}\right)^2 + \left(\frac{\Delta_i^{\mathrm{mod}} - \Delta_i^{\mathrm{exp}}}{s_{\Delta,i}^{\mathrm{exp}}}\right)^2\right] = \frac{1}{2N-M}\,c^2 \qquad \text{Eq. (2.117)}$$

where the subscript "*i*" identifies each unique wavelength and angle of incidence, s_{dev} is the standard deviation, *N* is the total number of (Y, Δ) pairs, *M* is the number of "fit parameters", and "exp" and "mod" signify experimental and calculated values. Another common estimator, chi-square (c^2), is also defined. The MSE compares the merit of different models to help find a physical sample description that best matches (MSE =1) the experimental measurement. Furthermore, to improve the fitting quality the surface roughness can be described using the Bruggeman effective medium

approximation (BEMA). The effective medium approximation (EMA) used to combine two or three materials and form an “effective” mixed layer. Physical interpretation of EMA theory involves small particles of one material suspended within a host material. Under this approximation, the optical constants can be mixed to satisfy electromagnetic equations. In practice, the EMA is commonly used to describe surface or interfacial roughness, porous layers, and polycrystalline materials. The approximation is valid when features are less than $1/10^{th}$ the wavelength of probe light. Larger roughness may scatter and depolarize light. Therefore, thick layers are not modeled correctly with an EMA. In Figure 2.42, surface roughness and the effective medium approach are presented. In practice, roughness is represented by a single, planar layer, with thickness varying to provide the best approximation of the surface properties.

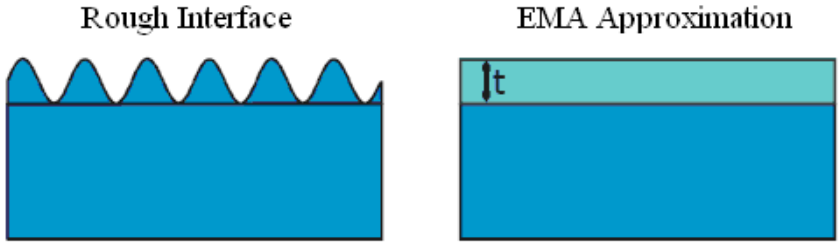

Figure 2.42. Schematic of film surface roughness and EMA approximation

If the complex index of refraction varies through the film (with depth), such variation could affect the ellipsometric measurement. Although it is difficult to describe the exact depth profile, the ellipsometer can estimate the “trend”. Figure 2.43 represents index variation in the films as function of thickness. Ellipsometry theory works with planar layers, so the index variation must be approximated as a series of “slabs” with varying index. The index at the surface can be larger or smaller than the index at the bottom of the film.

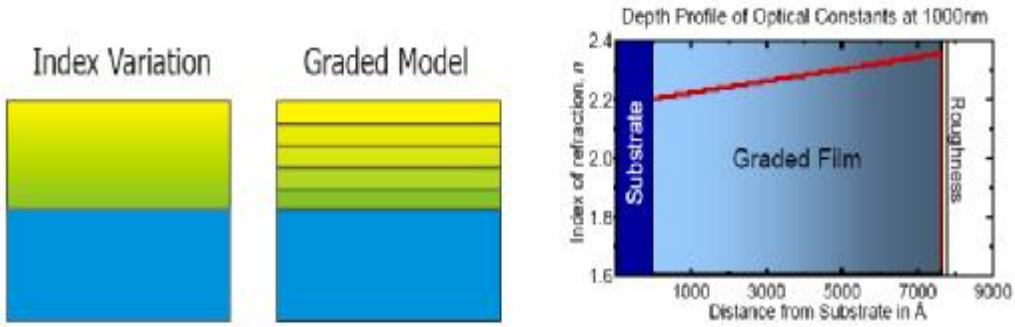

Figure 2.43. Depth profile of the optical constants using a graded model.

In addition to the optical constants, the film thickness *d* could also be determined by the fitting process using spectroscopic ellipsometry (SE) data. In Figure 2.44, from the illumination of film surface during SE measurement is presented. When film thickness varies within the measured spot, the ellipsometer measures an average thickness. The variation also "rounds" any sharp features in the experimental data. The effects caused by thickness non-uniformity are calculated using a series of slightly different thickness values to correctly interpret the data. Non-uniformity can also introduce depolarization, so this can help quantify the thickness non-uniformity if the measurement includes depolarization.

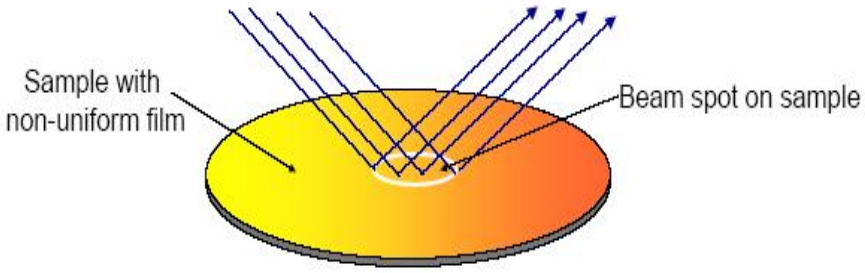

Figure 2.44. Thickness measurement from film surface by SE

2.9. ZnO

In this section a review of the scientific literature on ZnO thin films is presented. There has been lately great interest in ZnO semiconductor materials, as

seen from the surge of the relevant number of publications. The experimental values of the optical energy band gap between the valance and conduction bands, E_g, for undoped ZnO are in the range 3.2 – 3.4 eV, depending on the deposition method and also depending on the internal film stress, on the substrate material, on the deposition temperature and on annealing. The radiation transmission in the UV, VIS, and IR regions significantly depends on E_g and the type of the electronic transition. The band gap of ZnO can be tuned via divalent substitutions on the cation site to produce heterostructures. For example, Cd substitution leads to a reduction in the band gap to ~3.0 eV and Mg substitution on the Zn site in epitaxial films can increase the band gap to approximately 4.0 eV, while still maintaining a wurtzite structure.

ZnO is a II-VI compound semiconductor whose bonding resides at the borderline between covalent and ionic. The crystal structure of deposited ZnO thin films is generally hexagonal (wurtzite), and the film is usually polycrystalline. The lattice constants of wurtzite ZnO at room temperature is $a = 3.250$ Å and $c = 5.206$ Å. The structure of wurtzite ZnO is presented in Figure 2.45. The Zn atoms are tetrahedrally coordinated to four O atoms, where the Zn *d* electrons hybridize with O *p* electrons. Carrier electron population in nominally undoped ZnO has been attributed to Zn interstitials and/or oxygen vacancies. The electron hall mobility at room temperature in ZnO single crystals is on the order of 50 $cm^2V^{-1}s^{-1}$. While the electron mobility is slightly lower than that for GaN, ZnO has a higher theoretical saturation velocity. Intrinsic ZnO is a very good insulator, with resistivity $r = 10^{12}$ Ωcm. However, deposited non-stoichiometric thin films are n-type semiconductors with a resistivity that could be $\geq 2x10^{-4}$ Ωcm (Minami, 2005). The resistivity of polycrystalline ZnO film can be affected by carrier depletion in the grain boundaries, and also by carrier density in films.

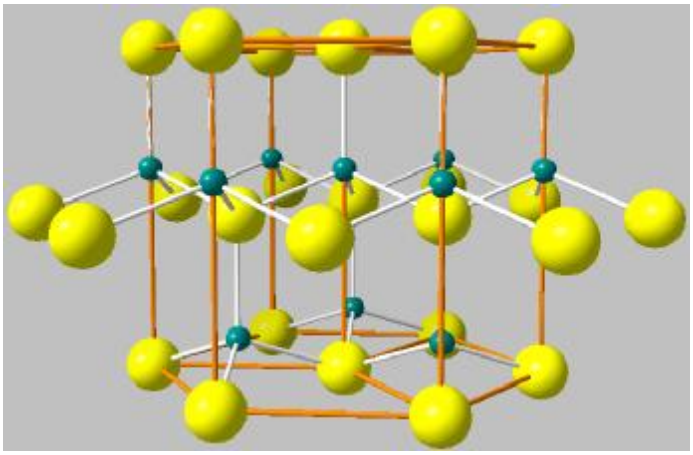

Figure 2.45. The structure of wurtzite ZnO crystal.

Table 2.2. Properties of wurtzite ZnO crystal (Özgür *et al.*, 2005; Batzil and Diebold, 2006)

Property	ZnO
Mineral name	Zincite
Crystal structure	Hexagonal, wurtzite
Lattice constants [nm]	a=0.325, c= 0.521
Density [g cm^{-3}]	5.67
Melting point [^{o}C]	1975
Melting point of metal [^{o}C]	420
Static dielectric constant	8.66
Band Gap [eV]	3.4
Refractive index	2.008, 2.029
Exciton binding energy [meV]	60
Electron effective mass	0.24
Electron Hall mobility at 300 K [cm^2/Vs]	200
Hole effective mass	0.59
Hole mobility at 300 K [cm^2/Vs]	5-50

The intrinsic defect levels that transform ZnO to *n*-type material lay approximately 0.01-50 meV below the conduction band. In addition, UV and visible emission has been observed due to radiative transitions from these states and from excitonic levels. A blue-green emission, centered at around 500 nm in wavelength, has been explained by transitions involving self activated centers formed by a doubly ionized zinc vacancy and an ionized interstitial Zn^{+}, oxygen vacancies, donor-acceptor pair recombination involving an impurity acceptor, and/or interstitial O. The optical properties of ZnO, studied using photoluminescence, photoconductivity and absorption, revealed the intrinsic bound exciton state and the defect states in the gap. A strong room temperature near-band edge UV photoluminescence peak at ~3.2 eV is attributed to an exciton state, as exciton binding energy is on the order of 60 meV. Some of properties of ZnO are presented in Table 2.2.

2.9.1. FVAD ZnO Thin Films

In the text below the detailed review of the literature reporting the characteristics of FVAD ZnO thin film is presented.

2.9.1.1. Structure and Morphology

The microstructure and morphology of ZnO thin films had been extensively studied under various growth conditions by several groups using X-ray diffraction (XRD), scanning electron microscopy (SEM), and atomic force microscopy (AFM). Deposited films were generally polycrystalline with a hexagonal wurtzite structure independent of deposition conditions. Surface morphology (roughness and grain size) were found to be in the range 0.9 to 17 nm and 20 nm to 100 nm, depending on the deposition conditions.

Xu *et al* (2001a, 2001b, 2001c) FVA deposited ZnO thin films with various substrate temperatures and substrate bias. The films deposited at room temperature (RT) were amorphous, however, the films grown at higher substrate temperatures with substrate bias had a hexagonal structure with (100), (002), (101), (110) and

(103) directions. Although, the films deposited on 190^{o}C substrates had an additional (002) peak, the films deposited at higher substrate temperatures (>190^{o}C) without substrate bias had only (103) diffraction lines, and the diffraction intensity of the (103) peak increased with increasing substrate temperature from 230^{o}C to 440^{o}C. The crystallinity of the films deposited at 230^{o}C improved when a bias voltage of –50 V was applied during deposition. However, when the bias voltage increased to –200 V, the films changed their crystal orientation from (002) *c*-axis orientation to (100), (101) and (110) and the diffraction lines were broadened indicating poor film quality. Very uniform nano-crystalline structures, ~200 nm in size, were observed on 230^{o}C substrates without substrate bias, and the large crystals of 0.5 –1 *m*m in size were measured with increasing substrate bias to –50 V at 230^{o}C substrate temperature, however, the samples deposited at higher bias voltages (~ –200 V) had an amorphous phase with irregular features. The root mean square (RMS) roughness was 1.17, 2.63, 4.51 and 4.56 nm for substrate temperatures of 120^{o}C, 230^{o}C, 320^{o}C and 440^{o}C, respectively. The increase in surface roughness was attributed to the increase in grain size. The bias voltage also influenced the roughness, with 7.6 nm, 17.2 nm and 8.6 nm RMS values reported with floating 0, –50 V and –200 V bias at 230^{o}C.

Wang *et al*. (2003) studied ZnO thin film structure as function of deposition pressure in the range 2×10^{-4} to 1×10^{-3} Torr. The XRD full width at half-maximum (FWHM) was affected by many factors, including grain size, inhomogeneous stress distribution and crystal quality. They derived the non-uniform stress distribution from the broadening and position of the (002) diffraction line. The stress in films was compressive and it decreased from –3.2 GPa to nearly zero as function of increased deposition pressure from 2×10^{-4} to 10×10^{-4} Torr. They attributed the variation of film stress with pressure to energy of the particles impacting the film surface during deposition (and not to the thermal stress due to various linear thermal expansion coefficients of the substrate). The (002) diffraction line intensity increased with deposition pressure. The sample surfaces were analyzed by optical microscopy and SEM. The films showed a very smooth, uniform grain size and void free surface. No macroparticles were observed on the deposited samples. The AFM analyses revealed

that the films were composed of well faceted grains and the grain size decreased with increasing deposition pressure. The observed RMS roughness also decreased from 3.9 nm to 0.9 nm with deposition pressure.

Lee *et al*. (2004) also investigated polycrystalline ZnO thin films. He measured the (002) diffraction line intensity and width as functions of the substrate temperature, substrate bias, and deposition pressure. The intensity increased and the FWHM decreased with substrate temperature, indicating an increase in grain size. A transition from compressive stress to tensile stress was observed when the temperature varied from 100^{o}C to 420^{o}C. Thermal stress was caused by the difference in thermal expansion coefficients of the film and the substrate. The observed internal stress as a function of substrate bias first increased with increased bias voltage from 0.2 to 3.1 GPa and then decreased and converged to a value of approximately 1.5 GPa at –200 V bias voltage. The surface roughness and the grain size were analyzed as functions of the substrate temperature (180– 420^{o}C). The RMS increased with temperature until it reached the maximum of 9.75 nm at 360^{o}C, and then decreased. However, in all cases the grain size increased with the deposition temperature.

Tse *et al*. (2004) studied the microstructure and morphology of ZnO films using XRD, transmission electron microscopy (TEM) and SEM. High quality *c*-axis oriented thin films were deposited on heated substrates. They observed an amorphous layer between the substrates and the ZnO films, using TEM. The FWHM of the (002) peak decreased from 0.5 to 0.24^{o} when the deposition temperature increased to 420^{o}C, indicating that the average grain size increased with substrate temperature. The film deposited at room temperature (RT) consisted of small grains. The average grain size increased from 27 nm to 126 nm when the deposition temperature increased from RT to 420^{o}C.

David *et al*. (2004, 2005) also studied the effect of the deposition pressure and the arc current on ZnO thin films. The films were polycrystalline and the crystal plane orientation varied with the oxygen pressure and arc current, and tended to be aligned normal to the substrate surface. The grain sizes were 10–35 nm. The compressive stress in samples deposited with arc current in the range 100–150 A,

decreased with the pressure from –2.5 to –1.5 GPa, however, increased in samples deposited with arc current ranging from 200 to 300 A.

2.9.1.2. Composition

The chemical composition of the films was determined using XPS on their surface and in their bulk by David *et al*. (2005) and Xu *et al*. (2001a). The surfaces of their films contained significant concentrations of carbon atoms (C) (20at.%), while the bulk was almost free of C contamination. The reported atomic concentration ratio of O to Zn (R_{OZn}) on the film surface was >1, and they attributed this effect of oxygen adsorption on film surface after or during deposition. In addition, David *et al*. (2005) reported R_{OZn} in the bulk as 0.7-0.8 for RT deposited films, whereas more stoichiometric films at 230^{o}C (R_{OZn}~1.1) for film bulk was reported by Xu *et al*. (2001a). Furthermore, Xu *et al*. (2001a) observed excess of oxygen in film bulk for films deposited on 430^{o}C heated substrates under floating conditions. For a substrate bias voltage of ~ –200 V at 230^{o}C substrate temperature, the R_{OZn} value decreased to 0.61. This behavior was attributed to the faster penetration of Zn ions into the films, the breaking of Zn-O bonds and the release oxygen. In 2001, Xu *et al*. (2001b) also reported on the effect of substrate temperature on the composition. R_{OZn} for samples deposited at 230^{o}C and 430^{o}C was 1.16 and 1.29, respectively. Also these results compared with Raman spectra in which again excess of oxygen observed.

2.9.1.3. Optical Analyses

The optical properties and the parameters of FVAD ZnO thin films were obtained by optical transmission, photoluminescence (PL) and Raman spectral measurements in reported works. It was observed that FVAD film transmittance improved with increasing of the oxygen pressure. Wang *et al*. (2003) studied the effect of deposition pressure on the film transmission. The films had a transmission as high as 90% when deposited with pressure above 3.5×10^{-4} Torr. The optical band

gap was 3.32 eV at 3.5×10^{-4} Torr, and decreased to 3.27 eV as the oxygen pressure was increased to 8×10^{-4} Torr. David *et al*. (2004) also reported a similar trend with film transmittance around 80–90% depending on film thickness and wavelength.

The effects of substrate temperature and substrate bias were reported by Xu *et al*. (2001a). The films deposited at RT were brownish. A very sharp absorption edge was observed in the films deposited at 230^{o}C. The films deposited at 430^{o}C had larger band tails, indicating that the interstitial oxygen energy levels were near the band edge. Negative correlation was observed between transmission and bias voltage by Xu *et al*. (2001a), with the transmission reduced to 60% at a bias voltage of –200 V. They attributed this to oxygen deficiency in films. The average transmittance of the films deposited at high substrate temperature and low bias voltage was over 80% in the visible spectrum.

David *et al*. (2004, 2005) studied the correlation between the optical parameters and deposition conditions. The absorption coefficient, (a), increased with the arc current. The lowest a was measured for films deposited with 100 A arc current and was ~6×10^{3} cm^{-1}, resulting in ~90% transmission in a 210 nm thick film. The extinction coefficient k decreased as function of the deposition pressure, and also as function of wavelength. The largest values of k were derived for 400 nm wavelength: k = 0.55, 0.37 and 0.20 for films deposited at 0.26, 0.33 and 0.4 Pa pressure, respectively. At higher deposition pressures, when the films were highly transparent, the values of k were of the order of 10^{-2}–10^{-3}, and $k = 10^{-8}$ was found at 400 nm for 0.73 Pa. The refraction index, n, had a more complex dependence on the pressure. The values of the refraction index of films at 560 nm wavelength were 1.601, 2.360 and 2.167, when deposited with 0.26, 0.33 and 0.40 Pa oxygen pressures, respectively.

Wang *et al*. (2003) studied PL of FVAD ZnO thin films at RT as a function of the deposition pressure (3.5×10^{-4} – 8×10^{-4} Torr). In general, PL emission for ZnO thin films could be divided into two categories: near band edge (NBE) excitonic UV emission and defect related deep level emission (DLE) in the visible range. The observed PL spectra were composed of these two emissions, where the UV emission is near the band edge and a broad DLE band was at ~610 nm. The intensity of this

band increased with higher deposition pressure. The effect of substrate temperature on the PL spectra was reported by Xu *et al.* (2001a, 2001b, 2001c); the PL peaks shifted to higher energy with higher substrate temperatures; reached the maximum at 230^{o}C and then shifted to lower energy with further temperature increase. A strong PL emission peak at 378 nm was observed from the films deposited at 230^{o}C due to NBE and the shift of PL peaks to the lower energy values was ascribed to the large band tail of the film, which was induced by defects in the non-stoichiometric film.

2.9.1.4. Electrical Analyses

The use of transparent ZnO thin films in optoelectronic devises depends on their electrical resistivity. The resistivity of FVAD ZnO films varies over a wide range, and is noticeably affected by the deposition conditions, (Goldsmith, 2006). Xu *et al.* (2001c) studied the effect of substrate temperature on electrical properties such as resistivity, hall mobility, and the carrier concentration of ZnO thin films. The determined carrier concentration in films deposited at 120^{o}C was ~3.51×10^{22} cm^{-3} and decreased to 3.31×10^{18} cm^{-3} with increased substrate temperature (~430^{o}C). Further temperature increase increased the carrier concentration in films. The film resistivity increased drastically, from 2.38×10^{-4} to 1.31 Ωcm, when the substrate temperature was increased from 120^{o}C to 320^{o}C, but it decreased with a further increase of the substrate temperature. The hall mobility decreased from 0.748 to 0.145 cm^{2}/Vs when the substrate temperature was increased from 120^{o}C to 190^{o}C, and then increased up to 8.83 cm^{2}/Vs when the temperature was further increased to 440^{o}C. Wang *et al.* (2003) reported on the electrical characteristics of ZnO films as a function of deposition pressure. The resistivity first decreased with increased deposition pressure and reached a minimum resistivity of 4.1×10^{-3} Ωcm and then increased. The carrier concentration decreased with pressure; however, the hall mobility first increased from 2 to 15 cm^{2}/Vs with increasing pressure from 2×10^{-4} Torr to 8×10^{-4} Torr, and then decreased up to 10 cm^{2}/Vs at 10×10^{-4} Torr. The deposited films conductivities were stable in air during storage periods of several months.

David *et al*. (2004, 2005) also studied the effects of deposition pressure and additionally the arc current on electrical film characteristics. The electrical resistivity of the films was in the range $(1–5)\times10^{-2}$ Ωcm, depending weakly on deposition parameters, and no apparent correlation could be established between the resistivity and the pressure or arc current. The carrier concentration and the mobility were 4.8×1019 cm^{-3} and 11.6 cm^2/Vs, respectively.

2.10. SnO_2

Tin oxide (SnO_2) belongs to the important family of oxide materials that combine low electrical resistance with high optical transparency in the visible range of electromagnetic spectrum. Stannic oxide SnO_2 is the prototype of transparent conductor, being a wide band gap (3.6 eV) material with up to 97% optical transparency in the visible range (for films of thickness 0.1–1 *m*m), yet having a resistivity of 10^{-4}-10^6 Ωcm, considerably lower than most semiconductors (10^{-3}–10^9 Ωcm). For these reasons, SnO_2 and its alloy with In_2O_3 is widely used technologically as a transparent electrical contact in flat-panel displays and in solar cells. Another property of SnO_2 and other TCOs is that although they are transparent in visible they are highly reflective of infrared radiation. This property is responsible for today's dominant use of SnO_2 as an energy conserving material. SnO_2 coated architectural windows, for instance, allow transmitting light but keeping the heat out or in the building depending on the climate region. Many of the binary TCOs already possess a high conductivity due to intrinsic defects, i.e. oxygen deficiencies. Non-stoichiometry, in particular oxygen deficiency, makes it a conductor. Kılıç and Zunger (2002) showed that the formation energy of oxygen vacancies and tin interstitials in SnO_2 is very low and thus these defects form readily, explaining the often observed high conductivity of pure, but non-stoichiometric, SnO_2. In all applications of these materials the charge carrier concentration and thus the conductivity is further increased by extrinsic dopants. In the case of SnO_2 these are commonly Sb as a cation dopant and F as an anion dopant. Commonly observed phases of polycrystalline tin oxide include rutile structure SnO_2 and litharge structure

SnO in crystalline forms corresponding to tin oxidation states +4 and +2, respectively. In Figure 2.46, the rutile tetragonal lattice structure of SnO_2 is presented and in Table 2.3, the physical properties of SnO_2 are summarized.

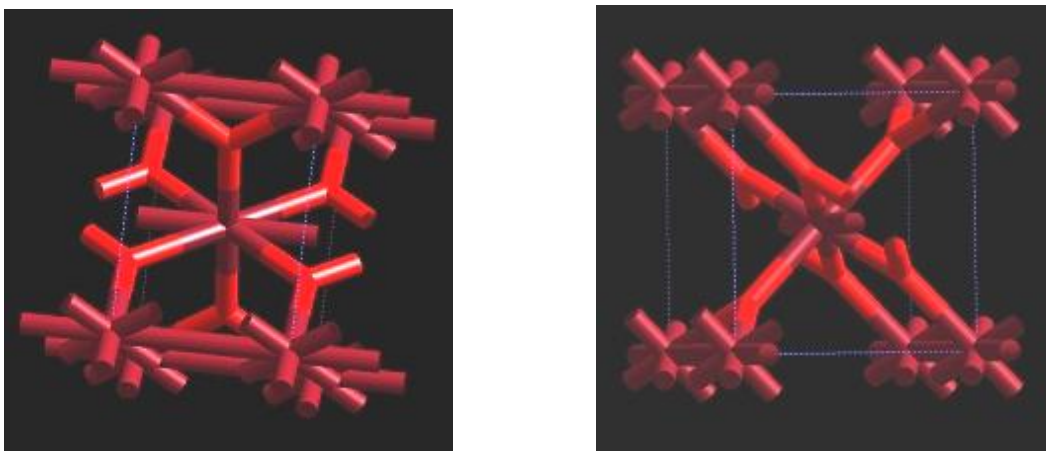

Figure 2.46. Structure of tin oxide (SnO2), rutile teragonal lattice.

Table 2.3. Physical properties of the SnO_2 crystal (Batzill and Diebold, 2006; Samson and Fonstad, 1973).

Property	SnO_2
Mineral name	Cassiterite
Crystal structure	Tetragonal rutile
Lattice constants [nm]	a=0.474, b= 0.319
Density [g cm^{-3}]	6.99
Melting point [^oC]	>1900
Melting point of metal [^oC]	232
Static dielectric constant	$\parallel c$ = 9.6, $\perp c$ = 13.5
Band Gap [eV]	3.6
Refractive index at 550 nm wavelength	1.8-2.0
Electron effective mass	$0.275m_e$
Electron Hall mobility at 300 K [cm^2/Vs]	250

2.10.1. FVAD SnO_2 Thin Films

2.10.1.1. Structure, Composition and Morphology Analyses

Ben-Shalom *et al*. (1993) and Kaplan *et al*. (1996) studied the effect of deposition conditions on the structure of FVAD SnO_2 films using XRD and TEM analyses. Thin films of SnO_2 were prepared using FVAD, operating with a low pressure O_2 atmosphere – 3-10 mTorr. The XRD and TEM data indicated that the films deposited at various deposition conditions without substrate heating have an amorphous structure without any crystalline inclusions. However, polycrystalline films were obtained on substrates heated above 450^{o}C. Parkansky *et al*. (2003) and Alterkop *et al*. (2003) also reported amorphous structure for RT deposited SnO_2 thin films.

Ben-Shalom *et al*. (1993) and Kaplan *et al*. (1996) also studied the composition of the films using AES and XPS diagnostics. A small deviation from film stoichiometry was observed in their films. The XPS results suggested that FVAD tin oxide consists of Sn^{4+} and Sn^{2+} ions or clusters of SnO_2 and SnO. The SnO_2/SnO ratio was depended on the deposition parameters, arc stability, oxygen pressure, and substrate temperature.

Kaplan *et al*. (1996) and Ben-Shalom *et al*. (1993) studied the effect of magnetic field, arc current, and film thickness on the surface morphology of the films using the scanning tunneling microscopy/spectroscopy (STM/STS). No correlation was found between cathode magnetic field and the film surface morphology. The surface had a rugged and grainy structure, with a lateral periodicity close to 20 nm. The average crest height on the films depended on film thickness, e.g. 5 and 0.6 nm for the 50 and 350 nm thick films, respectively. Well defined clusters were reported for 50 nm thick films. In addition, Kaplan *et al*. (1996) hypothesized that nano-clusters of non-degenerate semiconductor having (in STM, I-V measurements) an energy band gap larger than 3 eV, which were deposited with a magnetic field of ~0.4 mT imposed on the cathode, consisted of Sn^{2+}, while nano-clusters of degenerate semiconductor consisted of Sn^{4+} ions.

As transparent coatings, tin oxide thin films are often deposited on glass substrates. Recently, it was reported that polymer (e.g. polycarbonate (PC) and polymethylmethacrylate (PMMA)) were used as substrates owing to their transparency and toughness for applications in aircraft canopies and windows. Mechanical (*e.g.* hardness and scratch resistance) properties of FVAD SnO_2 coatings on polymer substrates were reported by Zhitomirsky *et al*. (2005). The SnO_2 films were deposited at 0.5 Pa for 20, 40, 60, 90 and 120 s on PC substrates and 15, 30 and 45 s on PMMA substrates. All films deposited at RT were amorphous in structure with thickness ranging from 0.2 to 1.2 mm depending on the deposition time. The films were an order of magnitude harder than of the bare polymer substrates. The coatings protected the substrate from scratching, with the scratch depth on coated substrates decreased by factors of 20–60 and the wear rate by a factor of 400–3200, from that of bare substrates. Roughness of the SnO_2 coated PC substrates was in the range of 8–13 nm and there was no clear dependence of roughness on thickness. The roughness of coated PMMA was larger than 15 nm for 160 nm thick films, and 23–25 nm for thicker coatings. For both uncoated substrate materials, the roughness was approximately the same, 5.0–5.4 nm.

2.10.1.2. Optical and Electrical Analyses

The optical properties of FVAD SnO_2 films were analyzed by Ben-Shalom *et al*. (1993) and Kaplan *et al*. (1996), using transmission measurements. High transmission values, >85%, were reported for films 500 nm thick. At lower oxygen pressures (~4×10^{-3} Torr) they obtained brownish films. The film thickness increased with decreasing deposition pressure. The calculated value of the largest optical energy band gap was 4.1 eV. In addition, tin oxide thin films had resistivity of 3×10^{-3} Ωcm and 85% transparency within the deposition pressure of 4–8×10^{-3} Torr. Zhitomirsky *et al*. (2005) also studied the film transmittance for different substrates and it decreased from 87% to 41% as the film thickness increased from 0.16 to 1.2 *m*m.

Ben-Shalom *et al*. (1993) and Kaplan *et al*. (1996) reported that the sheet conductivity and resistivity of films dependent on the deposition pressure, in particular at pressure below 6mTorr. However, the resistivity of films deposited in the 6–10 mTorr pressure range was not affected by the deposition pressure. The lowest film resistivity obtained at RT was 3×10^{-3} Ωcm. Zhitomirsky *et al*. (2005) reported that the sheet conductivity of films increased with increasing thickness and 0.26 *m*m was found to be threshold thickness for the lowest resistivity was ~6.4×10^{3} Ωcm.

2.11. Zinc Stannate (Zn_2SnO_4/$ZnSnO_3$)

Post-transition-metal oxides and their alloys have some unique physical properties. Despite their large band gaps (>3 eV), which makes them transparent under normal conditions, they can sustain a high concentration of carrier electrons with a high mobility. Although ZnO, SnO_2, In_2O_3 are post-transition-metal oxides used in various applications, In_2O_3:Sn (ITO) is by far the preferred material. However, the price and scarcity of In, and the recent growing demand of TCO materials have led to an extensive search for new TCO materials with comparable transparency, conductivity but at lower cost. In addition, ITO was found to be inappropriate for coating on elastic materials, preventing its application on plastic material. Among the many binary and ternary oxides, Zn_2SnO_4, Cd_2SnO_4, In_2CdO_4, and $In_4Sn_3O_{12}$ have emerged as promising TCOs, however, the alloy ZnO-SnO_2 (with various atomic ratios of Zn:Sn) could also be considered. Zinc stannate thin films with two phases, $ZnSnO_3$ and Zn_2SnO_4, are among these promising ternary TCO thin films. In Figure 2.47, combinations of binary TCO semiconductor compounds for thin film transparent electrodes are illustrated.

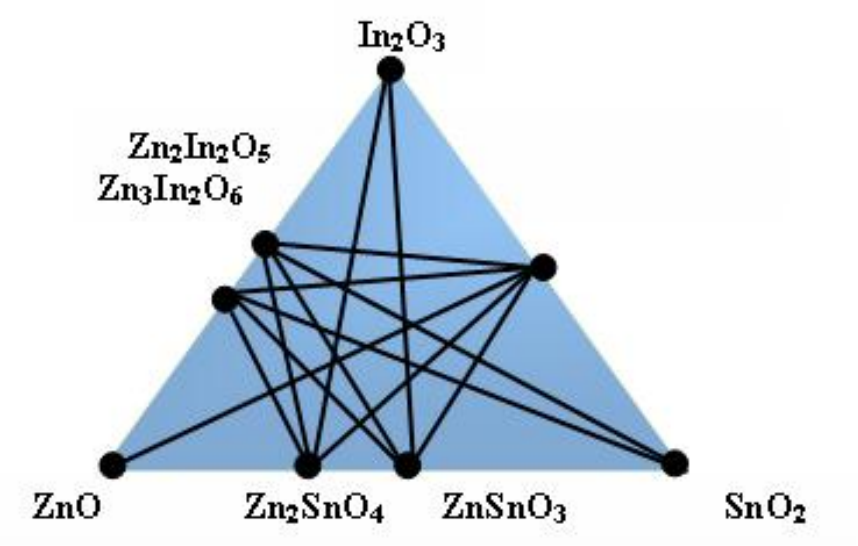

Figure 2.47. Practical TCO semiconductors for thin film transparent electrodes (Minami, 2005).

Zinc stannate and its alloy ZnO-SnO_2 are attractive materials because it is composed of non toxic and inexpensive elements. Although, both **Zn_2SnO_4** and **$ZnSnO_3$** are labeled as zinc stannate, they have different crystallographic structures and Zn:Sn ratios. The orthorhombic phase $ZnSnO_3$ was studied in bulk form by Kovacheva and Petrov and in thin film form by Minami (as reported in Young *et al*., 2002b). Zn_2SnO_4 has a cubic spinel crystal structure. In Figures 2.48(a) and (b), the lattice structure of zinc stannate thin films with spinel AB_2O_4 atomic ratio is presented, where A, B and O correspond to Sn, Zn and O.

These films have the advantages of both ZnO and SnO_2, and are promising for TCO applications as well as gas sensing. Young *et al*. (2002a) reported that zinc stannate thin films has a large band gap (~3.6 eV) and, therefore, zinc thin stannate films exhibit high transparency in the visible region. In Table 2.4 some of physical properties of zinc stannate crystals and thin films are presented.

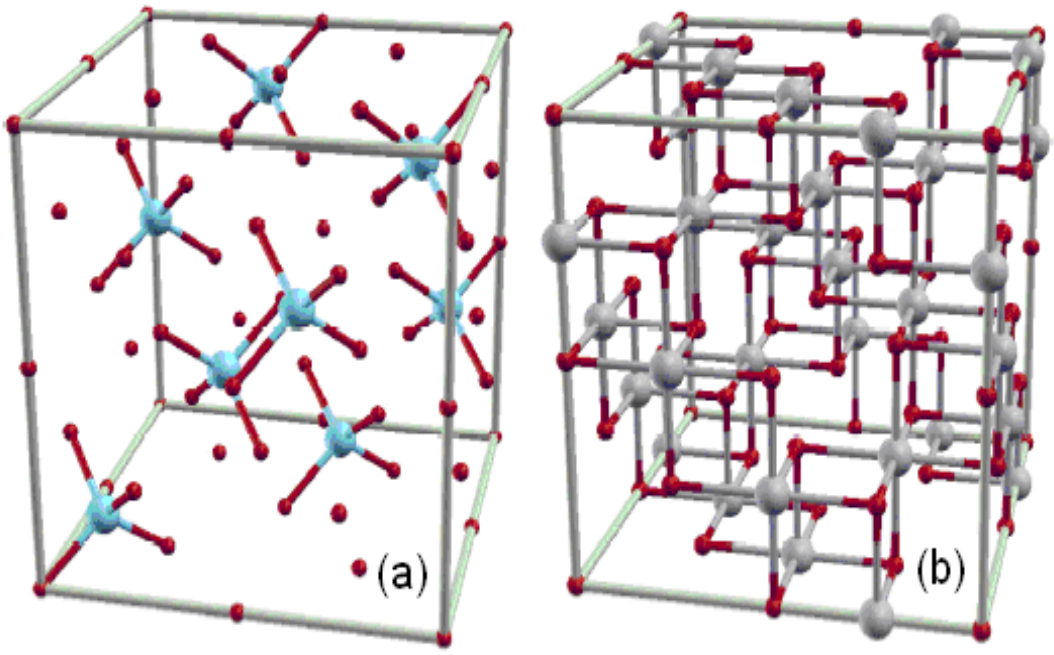

Figure 2.48. (Color online) Ball and stick representation of the normal AB_2O_4 spinel structure, showing the position of the O atoms (small balls) bonded to (a) the A atoms (large balls) at the tetrahedral sites (b) bonded to the B atoms (large balls) at the octahedral sites (Wei and Zhang, 2001, Segev and Wei, 2005).

Table 2.4. Physical properties of the zinc stannate crystal or thin films

Property	Zinc stannate -ZnO-SnO_2
Mineral name	Zinc Tin Oxide
Crystal structure	Spinel
Melting point [^oC]	570 (for $ZnSnO_3$)
Melting point of metal [^oC]	Zn: 420, Sn: 232
Band Gap [eV]	3.6
Refractive index at 550 nm wavelength	2.1
Electron effective mass	$0.23m_e$
Electron Hall mobility at 300 K [cm^2/Vs]	10-15

2.11.1. Characteristics of Zinc stannate and ZnO-SnO_2 Thin Films

2.11.1.1. Structure, Composition and Morphology Analyses

The microstructure and morphology of zinc stannate thin films have been studied using XRD, SEM, and AFM. Some theoretical calculations were also performed to understand the basic structural properties of these materials. Minami *et al*. (1994, 1995) reported that rf magnetron sputtered ZnO-SnO_2 thin films with 33at.% Zn concentration were amorphous if the substrate temperature was below 300^{o}C. Electron probe microanalyses (EPMA) of the deposited films showed that the Zn/Sn ratio was close to that of the sputtering target.

Wu *et al*. (1997) reported on the physical characteristics of rf magnetron sputtered ZTO thin films, observing that all RT deposited films were amorphous. The AFM determined root mean square roughness (RMS) of the films was 20 Å. An amorphous structure was also reported by Perkins *et al*. (2002) for rf magnetron sputtered and PLD films.

In 2002, Young *et al*. (2002a, 2002b) reported two papers on zinc stannate thin films using, XRD, conversion electron Mössbauer spectroscopy (CEMS), SEM, AFM, and TEM analyses. All RT deposited zinc stannate thin films were amorphous, independent of the other deposition conditions. However, films grown at 200 W rf power in Ar gas at a substrate temperatures above 550^{o}C showed a preferred (220) orientation and an XRD pole figure pattern centered about the (400) peak, indicating that the films had a predominantly uniaxial orientation. The AFM results showed that the surface grain size of films deposited on 600^{o}C substrate temperature in Ar was 100 nm, and the observed surface roughness was approximately 4.3 nm. Furthermore, the films were extremely dense, and no voids were observed through the bulk in cross sectional SEM images. In addition, the magnified cross section image of the first 500 nm below the surface revealed columnar growth at a slight angle from perpendicular to the substrate surface. Young *et al*. (2002b) concluded from the peak intensity ratios of XRD patterns of randomly oriented films that the zinc stannate thin films had an inverse spinel structure, with an approximately unity

degree of inversion. This places Sn atoms exclusively in octahedral sites that are usually formed by the close packed oxygen atoms in the spinel structure. The octahedral site dose not has cubic symmetry, and therefore, has an electric field gradient. This gradient produced a quadrupole splitting in the Sn Mössbauer line. If the atomic arrangement was a perfect inverse spinel, single quadrupole splitting should occur. The Sn Mössbauer data revealed two quadrupole splitting, implying that the Sn atoms occupy two different octahedral sites.

The structure of ZnO-SnO_2 thin films deposited using spray pyrolysis was investigated by Bagheri-Mohagheghi *et al*. (2003) as a function of the Zn to Sn ratio in the films. The XRD patterns of films deposited on substrates heated to 480^oC were polycrystalline and highly oriented. With 1.7at.% Zn, a single phase SnO_2 structure with strong (101), (211) and additional weak (110), (200), (111), (002) lines was observed. With 7.2at.% Zn, the intensities of (101) and (211) peaks decreased however, (200) peak increased, and no Zn or zinc oxide lines were detected. However with Zn concentrations exceeding 7.2at.%, a second phase, ZnO, was formed.

Hayashi *et al*. (2004) and Moriga *et al*. (2004) deposited ZnO-SnO_2 and zinc stannate thin films on glass substrates using dc magnetron sputtering. The film structure was determined using XRD as a function of the substrate temperature (150 – 350^oC) and the ratio *d* of the ZnO target current divided by the sum of the ZnO and SnO_2 target currents. Amorphous transparent films were obtained over the range $0.47 \leq \delta \leq 0.80$ (Zn/(Zn+Sn) = 0.28–0.76) at 150^oC substrate temperature, and over the range $0.33 \leq \delta \leq 0.73$ (Zn/(Zn+Sn) = 0.32–0.66) at 250^oC. Crystalline $ZnSnO_3$ and Zn_2SnO_4 were not obtained in any of the as-deposited films, even at $d = 0.62$ (Zn/(Zn+Sn) = 1/2) or $\delta = 0.73$ (Zn/(Zn+Sn) = 2/3). Amorphous $(ZnSnO3)_{1-x}(SnO_2)_x$ films were formed over the range $0.50 \leq \delta \leq 0.62$ ($0 \leq x \leq 0.5$) and $(ZnSnO_3)_{1-y}(ZnO)_y$ over the range of $0.62 \leq \delta \leq 0.73$ ($0 \leq y \leq 0.5$). Similar concentration and the structure were also observed for films deposited on 350^oC substrates. Yıldırım *et al*. (2005) deposited Zn_2SnO_4 thin films on 350^oC substrates using the chemical spray pyrolysis

(CSP). They reported that zinc-tin-oxide ternaries were most probably formed as $Zn_{2(1-x)}Sn_xO_2$, and they found $Zn_{1.6}Sn_{0.2}O_2$ and $Zn_{0.8}Sn_{0.6}O_2$ in their films.

Minami *et al*. (2005) studied vacuum arc plasma evaporated (VAPE) ZTO thin films on heated substrates and reported the effect of deposition conditions on structure and composition. Their deposition rate was 120 nm/s and the thickness of films varied between 220 to 380 nm, depending on deposition conditions, for films deposited on 300^{o}C substrates. All films deposited with 20–80at.% Sn content were amorphous.

2.11.1.2. Optical and Electrical Analyses

The optical and the electrical characteristics of zinc stannate thin films had been extensively studied under various growth conditions by several groups using normal incidence transmission, spectroscopic ellipsometric and hall measurements. Minami *et al*. (1994) deposited highly transparent and conducting $ZnSnO_3$ thin films using RF magnetron sputtering from different ZnO-SnO_2 targets. The optical and electrical properties of the films strongly depended on the deposition conditions, i.e., noble gas pressure, oxygen partial pressure, and substrate temperature. The film thickness was 300 to 500 nm. Optimal electrical resistivity as low as 4×10^{-3} Ωcm and an average transmittance above 80% in the visible spectrum were obtained for undoped zinc stannate films prepared in the substrate temperature range of RT to 300^{o}C using a SnO_2, 78 wt.% target. The hall mobility and the carrier concentration were higher than 10 $cm^2/V.s$ and 10^{20} cm^{-3}, respectively. The transmission of RT deposited ZTO films were improved with increasing deposition pressure; however, the transmission of films deposited on 300^{o}C substrates was independent of deposition pressure. The minimum obtainable resistivity was independent of the substrate temperature. In addition, Minami *et al*. (1995) also reported the effect of the different Zn/(Zn+Sn) target compositions. The minimum resistivity was obtained using a 33at.% Zn target, and was approximately 4×10^{-3} Ωcm. The hall mobility and the carrier concentrations were affected by the oxygen partial pressure. The resistivity of films decreased with increasing pressure, whereas, the hall mobility was

increased and the carrier concentration of films decreased. They also studied the chemical stability of zinc stannate, ZnO and SnO_2 films in different environments. It was found that the resistance of the zinc stannate films was more stable than the SnO_2 films in reducing environments at high temperatures. The SnO_2 films were completely etched by a hydrogen atmosphere at 350^oC, but zinc stannate thin films were not. In addition, etching experiments conducted to evaluate chemical stability showed that zinc stannate thin films were not etched after immersion for 48 h in 36%HCl and 15%NaOH solutions, whereas, ZnO films were completely etched in these solutions after 10 min. The optical characteristics of various TCO materials were reported by Wu *et al*. (1997). The average transmission of zinc stannate films were 90% in the visible for 620 nm thick films, and 80% in the IR spectrum where wavelength was in the range 800 to 2000 nm. The electrical sheet resistivity of zinc stannate thin films was high (~570 Ω/square). However, their work was at an early stage and their process was not yet optimized. A combinatorial study of zinc stannate thin films was reported by Perkins *et al*. (2002), who studied the characteristics of films deposited by different methods. They obtained $ZnSnO_3$ and Zn_2SnO_4 phases of sputtered films by changing the Zn:Sn concentration ratio. The film transmission was 80% in the visible spectrum and the electrical conductivity was 10^{-2}–10^{-1} $\Omega^{-1}cm^{-1}$. Pulsed laser deposited zinc stannate thin films on 400^oC and 500^oC substrates had conductivity, mobility and the carrier concentration of 200 $\Omega^{-1}cm^{-1}$, 35 cm^2/Vs and 3.5×10^{19} cm^{-3} for films deposited on 400^oC substrates, and 54 Ω^{-1} cm^{-1}, 33 cm^2/Vs and 1×10^{19} cm^{-3} on 500^oC substrates, respectively (Perkins *et al*., 2002).

The optical parameters of zinc stannate thin films in the wavelength range of 300-25000 nm were derived by Young *et al*. (2002b) from spectroscopic ellipsometry and FTIR. The absorbance was less than 1.5% over the visible spectrum. A slight rise in the absorbance curve near 2300 nm was observed and attributed to the onset of absorption by free electrons in the conduction band. The optical band edge was 3.35±0.09 eV. The Burstein-Moss shift was observed in transmission measurements depending on carrier concentrations. *n* and *k* parameters were modeled from spectroscopic ellipsometric data between 300–1700 nm and from FTIR data between 2000 and 25000 nm, and were ~2 and ~0 in visible spectrum. In

addition, the electrical resistivity was between, 4.94×10^{-2}– 9.83×10^{-3} Ωcm, the mobility 12–26.1 cm^2/Vs, and the carrier concentration 7.28×10^{18} – 3.33×10^{19} cm^{-3}. The estimated effective mass for the bottom of the conduction band determined from a density of states (DOS) effective mass vs. carrier concentration graph was $0.15m_e$.

The optical transmission spectra of spray deposited ZnO-SnO_2 thin films as function of Zn content was reported by Bagheri-Mohagheghi *et al*. (2003) in the UV-VIS-NIR spectra. The average transmission in the visible range (400-800 nm), was 90% and 80% for 12.5at.% and 20.7at.% Zn concentrations, respectively. The resistivity was 2.25, 6, 25, 1.75×10^2, 9.9, 1.9, and 25.2 Ωcm for 1.7 4.3, 7.2, 12.5 15.6, 20.7, and 28.2at.% Zn, respectively. Hall measurements showed that the carrier concentration increased from 1×10^{15} to 3.0×10^{17} cm^{-3} when the Zn content in films increased from 12.5at.% to 20.7at.%.

Hayashi *et al*. (2004) and Moriga *et al*. (2004) also reported the effect of Zn concentration and substrate temperature on the optical and electrical properties, using planar magnetron and dc sputtering systems, respectively. Hayashi *et al*. (2004) reported average transmissions in the range 75–80% depending on substrate temperature, and the band edge shifted to the higher wavelengths with increasing Zn content. The estimated optical band edge ranged from 3.3 to 3.6 eV. Optical band tailing increased at higher Sn concentrations. The minimum resistivity was 3.6×10^{-2} Ωcm for 250°C substrate temperature, using 33at.% concentration of Zn to (Zn+Sn). Similar results were also reported by Moriga *et al*. (2004), who found that the average transmission increased from 80% to 90% for increased substrate temperature from 150 to 350°C. The lowest resistivity was $(4–6)\times10^{-2}$ Ωcm and the hall mobility in the amorphous phase was ~10 cm^2/Vs.

Yıldırım *et al*. (2005) grew semiconducting thin films of ZnO, SnO_2 and their ternary compounds using chemical spray pyrolysis (CSP). They showed that the ternaries were most probably formed as $Zn_{2(1-x)}Sn_xO_2$. A remarkable increase in the band gap energy from 3.28 eV to 3.45 eV was obtained as the atomic fraction of Sn, *x*, was increased from 0 to 0.6.

Minami *et al*. (2005) studied zinc stannate films that were deposited by vacuum arc deposition as function of composition and substrate temperature. The

optical transmission of films deposited at different substrate temperatures and Zn to (Zn+Sn) concentrations was not changed significantly. However, depending on composition the band edge shifts to lower wavelengths with increasing Sn content. The optimum electrical resistivity, hall mobility and the carrier concentration were ~10^{-2} Ωcm, ~10 cm^2/Vs and ~10^{19} cm^{-3}, respectively, on 300^{o}C substrates. Films deposited at 300^{o}C by rf magnetron sputtering and vacuum arc plasma evaporation (VAPE) system were compared by Minami *et al.* (2005). The VAPE films with Sn content up to 17at.% were prepared without introducing O_2 gas. The resistivity of VAPE films was the same or lower than the rf magnetron sputtered films.

2.12. Annealing of ZnO, SnO_2 and Zinc Stannate Thin Films

2.12.1. ZnO

Annealing of ZnO films has been studied by many groups; however, there is no detailed study of annealing effects on FVAD ZnO thin films. As a result, the properties of annealed ZnO thin films deposited by other deposition methods are presented, for comparison with the present results.

Ogata *et al.* (2000) studied the properties of molecular beam epitaxy (MBE) grown ZnO films. ZnO layers were thermally annealed in N_2 or O_2. The electron carrier density increased, presumably due to re-evaporation of O, if annealed in N_2. In contrast, the electron carrier density decreased from the order of 10^{18} to 10^{17} cm^{-3}, and also the optical properties improved, when annealed in O_2 at lower temperatures. The film crystallinity was increased by annealing. The motilities increased up to 51 cm^2/Vs as the annealing temperature increased. Photoluminescence (PL) increased with annealing temperature (~390 nm), however, PL intensity of ZnO films annealed in O_2 were higher than those annealed in N_2. The intensity of (002) peak in XRD diffraction patterns also increased with annealing temperature. However, lower temperature annealing (~500–700^{o}C) in O_2 improved both the conductivity and crystallinity of ZnO films.

The effect of thermal annealing on ZnO thin films grown by pulsed laser deposition (PLD) were reported by Lu *et al.* (2000). ZnO films were deposited on 600^{o}C silicon substrates and annealed at 600^{o}C in oxygen for 50 min. Highly oriented films were obtained by annealing and the average grain size determined from XRD measurements was 67 nm. The O to Zn ratio was 0.91 and 1.08 for as-deposited and annealed films. Three peaks were observed by XPS analyses, one associated with the O-Zn bond whereas, the second and the third with OH and H_2O bonds. The atomic concentrations of H_2O before (1.46%) and after annealing (2.92%), and OH before (13.67%) and after annealing (17.36%), revealed that the H_2O adsorbed on ZnO thin films was dissociated into H and OH groups. Defects such as vacancies play an important role in initiating the dissociation of water. The defects on the surface could change the physical and chemical properties and even increase dissociation energies. The surface of ZnO films grown by PLD was porous and subject to H_2O adsorption. The STM topographic images indicated that the estimated average grain size was 60 nm which was consistent with the size of 67 nm mentioned above. The as-deposited samples had very low resistivity, about 2.8×10^{-4} Ωcm. After annealing, the resistivity increased to 2.5×10^{-1} Ωcm. The ~10^{3} increase of resistivity was attributed to an increase of O content during annealing.

The effect of annealing temperature in air on ZnO thin films deposited by dc sputtering was reported by Lin *et al.* (2001). (002) oriented crystalline films were deposited, and annealed at 850^{o}C. The XRD peak intensity increased, but with increased temperature it decreased. The calculated average grain size from AFM was 100 nm. Two PL peaks were observed, one centered at 3.18 eV (UV) and the other at 2.38 eV (green). The green PL intensity increased with annealing temperature.

In 2003, Zhi *et al.* studied annealing ZnO films grown by plasma enhanced CVD. To improve the thin film quality, the films were deposited on silicon by plasma enhanced CVD at low temperature (120^{o}C) and were annealed in oxygen at temperatures ranging from 100^{o}C to 600^{o}C. The XRD data indicated that the films had a polycrystalline hexagonal wurtzite structure and the mean grain size of samples annealed at 600, 700 and 900^{o}C were 22, 23 and 38 nm, respectively, whereas, as-deposited films had 21 nm average grain size. The AFM images showed an increase

of ZnO grain size with increasing annealing temperature. The PL emissions were dependent on annealing temperature. The free exciton binding energy deduced from the temperature dependent PL spectra was ~59 meV for films annealed at 900^{o}C, close to the value of the exciton level in good ZnO crystals.

The influence of post-deposition annealing on the properties of ZnO films prepared by rf magnetron sputtering was reported by Chu *et al*. (2003). The films were prepared on unheated substrates and annealed in vacuum in the range of 100^{o}C to 600^{o}C. The XRD line intensities increased with the annealing temperature. The calculated film stress was transformed from compressive to tensile with annealing, however, at 400^{o}C the film stress was released and stress free films were obtained. The AFM images showed that the average surface roughness decreased from 18.8 nm to 9.22 nm with annealing at 100^{o}C and 400^{o}C temperatures, respectively. The electrical resistivity of films was in the range of 10^{6} to 10^{8} Ωcm and increased with annealing temperature.

Schuler *et al*. (2005) also reported on the properties of ZnO films and annealing effects on their properties. The films were deposited on Silicon substrates by dc and rf sputtering deposition. Thermal annealing was performed at up to 900^{o}C in N_2 for 30 min. The samples were dry etched for 30 min using CHF_3 plasma. The effect of different sputtering techniques, annealing and reactive ion etching (RIE) were investigated using X-ray diffraction, Rutherford backscattering (RBS), photoluminescence (PL) spectra, atomic force microscopy (AFM), scanning electron microscopy (SEM), and piezoelectric measurements. The dc sputtered films had a grain size of 200 nm and a surface RMS roughness of 75 nm, while the rf sputtered films had a grain size of around 50 nm and a surface RMS roughness of 7 nm. Films on Si substrates were annealed at 600 to 900^{o}C in N_2 for 30 min. The XRD peak intensities of films increased for annealing temperatures up to 800^{o}C, but for 900^{o}C they decreased. The PL intensity of increased after annealing for both dc and rf sputtered films indicating the films optical and structural quality increased for annealing temperature.

Wei *et al*. in 2007 studied the annealing effect on the microstructure and photoluminescence of thin films obtained by pulsed laser ablation of a ZnO target in

O_2. The films were deposited on 400°C substrates and were then annealed at temperatures from 400 up to 800°C in N_2. The XRD results showed that the films had *c*-axis orientation and the intensity of diffraction peak increased with increased annealing temperature up to 600°C, and then decreased with further increase. In addition, the film grain size increased approximately from 13 to 28 nm with the annealing temperature. The increase of annealing temperature also produced tensile stress in films where as-deposited films had compressive stress. However, the best films obtained at 600°C annealing temperature had good crystallinity and were stress-free; these results were confirmed by SEM and TEM. The film resistivity increased with annealing temperature from 9.6×10^{-2} Ωcm to 28.82 Ωcm. Two emission peaks were observed in the PL spectra. As the post annealing temperature increased, the intensity of the UV emission peak at 368 nm increased, and the intensity of the blue emission at 462 nm decreased, indicating that the optical quality of ZnO film increased and the density of Zn interstitial defects decreased, respectively.

The influence of annealing on the optical properties and surface structure of FVAD ZnO films were first studied by Liu *et al.* (2006) using spectroscopic ellipsometry and AFM. The films were deposited at RT and annealed at 900°C for 3 to 60 min. The average grain size and the surface roughness of the films increased with annealing time from 25 nm to 88 nm, and from 1 nm to 8.2 nm. The refractive index, reflectance and the real part of the dielectric function decreased with annealing time (3 to 60 min), from 2.3 to 1.75, and 18% to 6%, and approximately from 5 to 2, respectively. It was reported that the changes in the optical properties were correlated to the changes in the surface structure as a result of annealing.

2.12.2. SnO_2

In 1987, Banerjee *et al.* studied the properties of tin oxide films deposited using reactive electron beam evaporation. They deposited the films on 350°C substrates without or with low oxygen pressure and they obtained crystalline SnO structure. After annealing in air at 550°C during 2 h, the (002), (110) and (001) SnO

XRD peaks diminished in intensity and (200), (101), (110), (211) and (310) peaks of SnO_2 as well as *b*-SnO peaks appeared. However, after heat treatment a SnO peak was still the most prominent for a films deposited without oxygen. In the case of films deposited with low oxygen pressure and then annealed in air, a SnO_2 peak was the most intense. This was attributed to an initial higher value of x in SnO_x when the film was deposited in the presence of oxygen, which facilitated the formation of the SnO_2 structure. After air annealing, they did not observed a significant change in the diffraction pattern except a marginal sharpening of the peaks. At lower substrate temperatures (~150^{o}C), an amorphous phase was observed that was attributed to insufficient adatom mobility, impeding the formation of an ordered structure. After annealing in air at 550^{o}C for 2 h, the films had a polycrystalline SnO_2 structure, irrespective of the substrate temperature. However, the number of peaks increased with increasing substrate temperature. The lowest film resistivity of SnO_2 films deposited on heated substrates by Banerjee *et al.* (1987) was ~10^{-4} Ωcm, and annealing at 550^{o}C for 2 h decreased the resistivity and improved the electrical properties. The optical transmission and the band gap was studied as a function of the substrate temperature, deposition pressure and annealing. The band gap increased with annealing, for films deposited at 2×10^{-4} Torr oxygen pressure, whereas films deposited at different oxygen pressures did not change significantly.

De and Ray (1991) studied the structure and electronic properties of rf magnetron sputtered tin oxide films as a function of the deposition pressure, substrate temperature and the annealing effects in vacuum and hydrogen. By optimizing the deposition pressure and substrate temperature, SnO_x films with resistivity 6.1×10^{-3} Ωcm and a corresponding optical transmission of ~95% and direct optical band gap of 4.13 eV were deposited. They reported that the SnO_x films prepared at lower substrate temperatures were highly sensitive to hydrogen annealing. In these films, hydrogen easily diffused through the film and altered their characteristic properties because the material was not fully crystalline, but was rather a mixture of crystalline and amorphous phases. During annealing, the observed resistivity decrease was partially due to increased carrier concentration and mobility. They explained this behavior by the increase in the number of oxygen vacancies and

lowered grain boundary barrier height caused by desorption of oxygen in a reducing atmosphere during the annealing. Annealing in vacuum at 400^{o}C increased the carrier concentration, and decreased the resistivity of films deposited on 300 and 400^{o}C substrates. The film characteristics of the films after annealing in hydrogen or in vacuum were similar, but the effects of the former were realized at a lower temperature than the latter. That was explained in terms of the large diffusivity of hydrogen in SnO_x films, which desorbs chemisorbed oxygen atoms from the grain boundaries, resulting in an increase in carrier mobility and concentration.

The annealing effects on the electrical properties of SnO_2 films were reported by Di Giulio *et al.* (1995). The samples were thermally annealed in air up to 450^{o}C and for several successive periods. Selected area electron diffraction (SAD) patterns showed that the increase in annealing temperature to 450^{o}C increased the grain size up to 92 nm. Furthermore, they reported that direct and indirect electron transitions between valance and conduction band were established for as-deposited and annealed films. The optical band edge in transmission plots shifted to lower wavelengths when the annealing temperature was increased up to 450^{o}C, indicating an increase in the optical band gap from 2.98 to 3.23 eV for indirect and from 4.18 to 4.20 eV for direct transitions, respectively. At the same time, the visible spectrum did not significantly change with annealing at 450^{o}C for 90 min. In an additional publication, Di Giulio *et al.* (1995) reported an improvement in the electrical properties of SnO_2 films with increased annealing temperature. The conductivity and the mobility of films increased from 0.04 to 0.32 $\Omega^{-1}cm^{-1}$, and from 0.55 to 4.6 $cm^2\ V^{-1}s^{-1}$, respectively.

Chen *et al.* (2005) studied the effects of annealing on SnO_2 films deposited by PLD using XRD, SEM, EDS, and TEM. The SEM and XRD results demonstrated that the as-deposited films consisted of an amorphous matrix as well as plume-like features. However, the thin films that were annealed for 2 h at 150^{o}C had tetragonal rutile nano-crystalline SnO_2 structures.

The influence of annealing in vacuum, hydrogen, and air for 1 h on the properties of undoped SnO_x thin films were studied by Mukhamedshina *et al.* (2006). The films had higher transparency after annealing in air than in vacuum or hydrogen.

They explained this by the absorption of oxygen that produced stoichiometric composition. The increase in the transparency and the shift of the transmission edge to shorter wavelength after annealing at 550^{o}C was interpreted to indicate the formation of SnO_2 polycrystalline phase. The increase in the annealing temperature resulted in an increase in the film transparency after annealing in air; however, a decrease in the transparency was noted after annealing in vacuum or hydrogen. The refractive index decreased after air annealing in increased temperature, however no definite trend in the change of the refraction index was observed after annealing in vacuum or hydrogen. In contrast, the extinction coefficient did not change with temperature for air annealed films, whereas it increased by ten orders of magnitude after vacuum or hydrogen annealing at higher temperature (400 and 500^{o}C).

The annealing effects on the characteristics of FVAD SnO_2 thin films were studied by Ben-Shalom *et al*. (1993) and Kaplan *et al*. (1996). The amorphous films deposited at low substrate temperatures (<300^{o}C), remained amorphous after rapid thermal annealing (RTA) in Ar at 350^{o}C for 30 s, but crystallized at higher annealing temperatures (>300^{o}C). It was demonstrated by Ben-Shalom *et al*. (1993) and Kaplan *et al*. (1996) that the film conductivity could be improved (one order of magnitude) by post-deposition annealing or by substrate heating below 300^{o}C, while maintaining an amorphous film structure. The lowest resistivity reported by Ben-Shalom *et al*. (1993) was 8×10^{-3} Ωcm where the films were deposited at 6 mTorr deposition pressure and rapid thermal annealed at 300^{o}C.

Parkansky *et al*. (2003) also studied FVAD SnO_2 films, showing that the annealing duration and an applied electric field would greatly affect the conductivity. The conductivity of thin FVAD SnO_2 films monotonically increased by annealing up to 3 min, but started to decrease at longer annealing times. In contrast, the conductivity of thicker films increased with annealing time, reaching a maximum value after 5–7 min. The film structure remained amorphous after annealing in air at 300^{o}C for 10 min. The electric field applied during the annealing affected the film resistivity. The lowest resistivity after annealing at 300^{o}C and applying 100 V across the sample was 0.6×10^{-3} Ωcm, whereas the lowest resistivity of samples annealed at the same temperature without applied electric field was three times higher, 1.8×0^{-3}

Ωcm. Further increase of the applied voltage to 200 V decreased the resistivity, but it was higher than the resistivity of sample annealed at 100 V applied voltage. The highest measured optical transmittance was 89% for 100 V biasing and annealing for 5 min. Alterkop *et al*. (2003) also reported on the composition of tin oxide films deposited at RT and annealed at 300^{o}C. The O/Sn ratio on the film surface decreased from an initial value of 1.98 to 1.4 after annealing for 5 min. Upon further annealing, for 10 min, it increased to 1.7. Interestingly, the O/Sn ratio in the bulk increased from 1.95 to 1.98 after 1 min of annealing, and then decreased monotonically to 1.86 for a longer annealing time, 10 min. AFM measurements revealed that the surface roughness of films strongly dependent on film thickness whereas and did not significantly depend on annealing time.

2.12.3. Zinc Stannate

The characteristics annealed zinc stannate films deposited by rf magnetron sputtering were studied by Minami *et al*. (1995). The zinc stannate thin films were deposited under various substrate temperatures and target compositions. The minimum resistivity, ~10^{-2} Ωcm, (observed by Minami *et al*.) was obtained with targets having 33at.% Zn content, regardless of the substrate temperature (RT or 500^{o}C). All deposited films were amorphous. These films remained amorphous even after they were annealed at temperatures up to 700^{o}C, either in Ar atmosphere or vacuum.

In 2002, Perkins *et al*. reported on the annealing of Zn-Sn-O films deposited by sputtering and PLD. The sputtered films were amorphous, and the films annealed at 650^{o}C in N_2 atmosphere had known XRD lines of randomly oriented crystalline Zn_2SnO_4. The conductivity of the as-deposited sputtered films was in the range 10^{-2} to 10^{-1} $\Omega^{-1}cm^{-1}$, whereas, the conductivity of these annealed films varied from 10^{-5} to 10^{2} $\Omega^{-1}cm^{-1}$. The conductivity of PLD films was approximately 17 $\Omega^{-1}cm^{-1}$. All as-deposited Zn-Sn-O films were amorphous independent of deposition method used, and XRD diffraction lines were observed after annealing at 650^{o}C and 700^{o}C in N_2.

Young *et al*. (2002a) also studied the annealing effects on rf magnetron sputtered amorphous Zn_2SnO_4 films. Post-deposition annealing at 600^oC in Ar produced randomly oriented polycrystalline zinc stannate thin films. Annealing in either flowing Ar or high vacuum at about 550–650^oC for 1 h increased the carrier densities, approximately 8.28×10^{18} to 3.33×10^{19} cm^{-3}. On the other hand, the annealing in O_2 decreased the carrier densities below their measurable limits of a Hall Effect instrument.

The effects of annealing on the structure, optical and electrical properties of zinc stannate thin films deposited by rf magnetron sputtering were also reported by Satoh *et al*. (2005). As-deposited films, produced under different deposition conditions, had amorphous structures. However, the reflection from the (111) planes of the crystalline films were obtained after annealing at 650 and 750^oC in oxygen for 1 h. All films had high transmission (~85%) in the visible spectrum and when the annealing temperature was increased from 650 to 750^oC, the optical transmission edge in the UV shifted to lower wavelengths, indicating decreased disorder in the films. The most pronounced improvement in the crystallinity and optical properties was observed after annealing at 750^oC, where the estimated optical band gap was 4.1 eV. The films deposited in pure Ar had a resistivity $r = 4.1\times10^{-2}$ Ωcm, carrier concentration $n = 8.5\times10^{18}cm^{-3}$, and Hall mobility $m = 18$ cm^2/Vs, while the films deposited in an O_2/Ar mixture were highly resistive. The complex refractive index components *n* and *k* were found to be ~2 and 0, respectively, at 500 nm wavelength.

3. EXPERIMENTAL APPARATUS and PROCEDURE

3.1. Experimental System

3.1.1. Filtered Vacuum Arc Deposition (FVAD) System

The filtered vacuum arc deposition system (FVAD) was designed and constructed in the Electrical Discharge and Plasma Laboratory (EDPL), and was previously used to deposit undoped and doped SnO_2 and ZnO thin films (Ben-Shalom *et al.*, 1993; Kaplan *et al.*, 1996; David *et al.*, 2005), and used in the present investigation to study ZnO, SnO_2 and novel ZnO:Sn and zinc stannate TCO coatings.

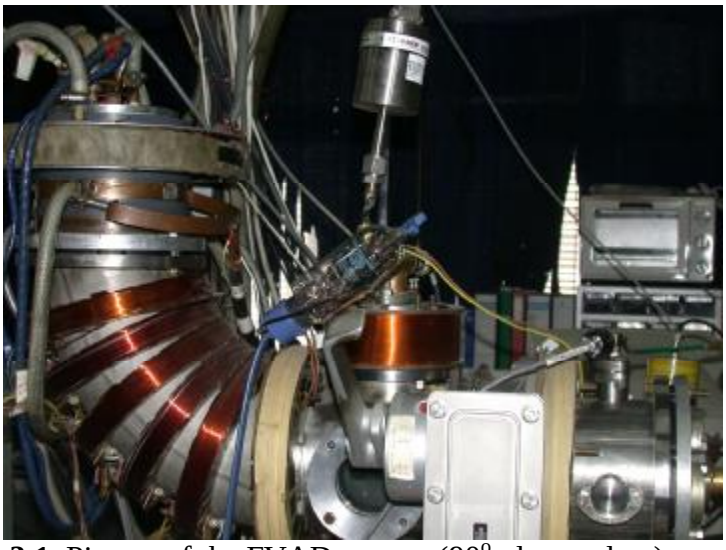

Figure 3.1. Picture of the FVAD system (90^o plasma duct)

A general view of the FVAD system is shown in Figure 3.1, and a schematic diagram of it is presented in Figure 3.2. The system comprised the following main units: a plasma source, a magnetic macroparticle filter, X-Y aligning magnetic coils, a vacuum chamber (a deposition and a sample chamber), a substrate holder, a vacuum system (pumps and gauges), a water-cooling system, and a control system based on a PC, data acquisition and control cards, and auxiliary units.

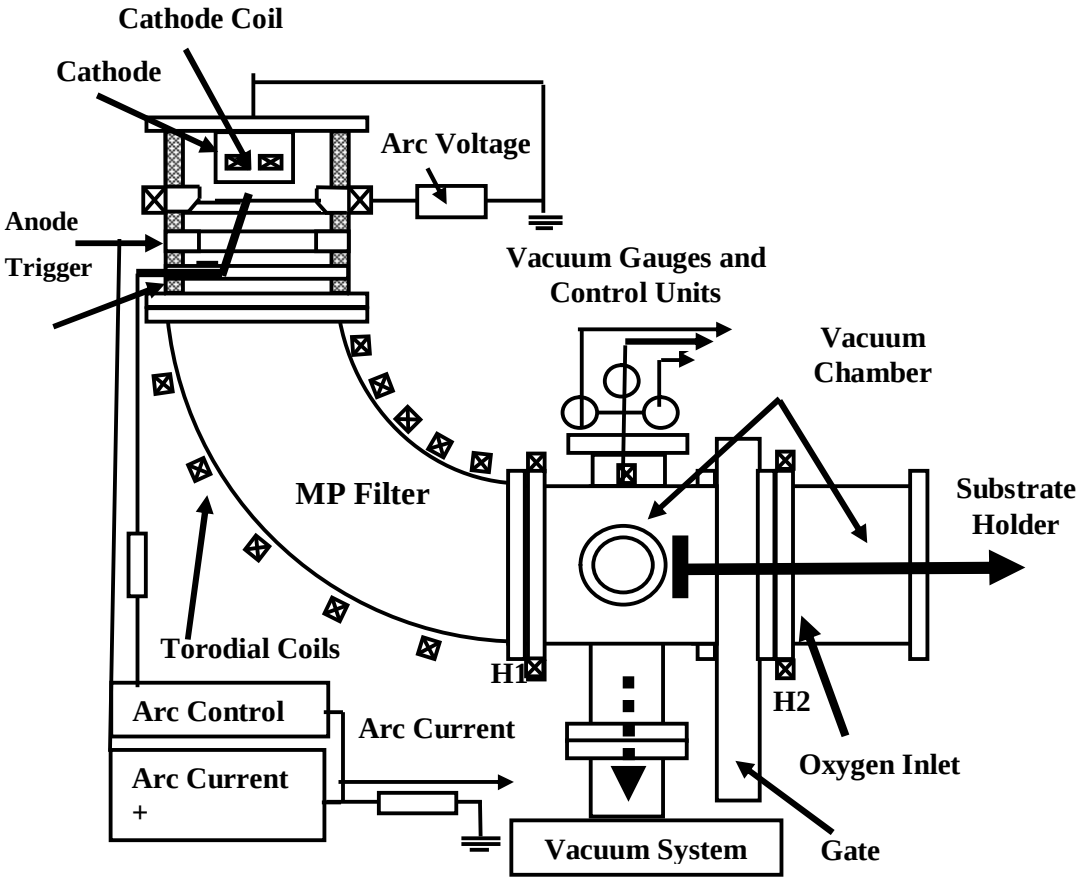

Figure 3.2. Schematic diagram of the 90^{o} plasma duct FVAD.

The key element in the plasma source is a cylindrical cathode, which was 91 mm in diameter and 10 mm in length, and mounted on a water cooled holder. The cathode coil shown in Fig. 3.2 was inserted in a water-cooled cavity in the back side of cathode. The cathode coil current (12 A) was applied by a dc power supply during the deposition, producing a magnetic field that drove the cathode spots along a circular path on the cathode surface ("retrograde motion"), preventing local over-heating. The anode was a Cu annulus, 122 mm in diameter and mounted between the spacer and the filter. A dc arc discharge was ignited by a momentarily contacting a tungsten (W) trigger electrode to the cathode surface. The trigger was connected to the anode via a current limiting resistor. The arc power supply was a Miller XMT 400 dc welder, which could supply arc currents from 30 A up to 400 A. In the

present work, the arc current was in the range of 150-300 A. The plasma emitted by the cathode spots passed through the annular anode into a macroparticle (MP) filter, consisting of a 240 mm major radius and a 80 mm minor radius (toroidal duct diameter 160 mm) quarter torus. The magnetic field in the torus, B_T, was produced by five coils wound on the outside of the torus. The coils were connected in series, generating 6 mT/A along the center line of the torus. In the present work, the toroidal coil current was 2 A and hence, B_T was 12 mT. As described in the literature survey section (2.3.5.5.4), the plasma beam is guided through the toroidal duct by the toroidal magnetic field, which was generally parallel to the duct wall.

The vacuum arc produced plasma of low melting point materials (e.g. Cd, Zn and Sn) is heavily contaminated by macroparticles (MP), and hence plasma filtering was needed in order to deposit macroparticle-free coatings on the substrate. The principle of MP filtering in the present deposition system utilizes the magnetic guiding of the plasma through the quarter torus filter, where the electrons are magnetized, confining them to the magnetic lines. The confined electrons minimize plasma losses to the filter wall by generating a negative space charge that attracts the non-magnetized ions, keeping them in the torus (Boxman and Zhitomirsky, 2006). The values used for B_T were too weak to magnetize the ions. The much heavier and almost neutral macroparticles are not affected by the toroidal field and, generally, impinge on the filter wall, where they may either adhere, bounce, or splatter. Three stainless steel baffles were placed into the filter duct, equally distributed along the duct length, to catch macroparticles rebounding from the filter wall.

After passing through the toroidal filter, the plasma jet entered into the 160 mm diameter vacuum chamber which included two small chambers (deposition and loading). As can be seen from Figures 3.1 and 3.2, the substrates were placed in the deposition chamber. A gate valve separated the two chambers, allowing the interchange of substrates without opening the entire system to the atmosphere. Two Helmoltz coils H1 and H2 are placed on the deposition chamber to collimate the plasma beam. In addition X-Y coils, mounted on the sides of the deposition chamber, were used to adjust the beam position so that it was centered on the substrate. The substrates were mounted on a holder which was equipped with a quartz-halogen

lamp, which could be used to heat the holder and hence the substrate. The substrate temperature was measured with a thermocouple. In the case of heated substrates, the substrate holder was water cooled before opening the vacuum chamber to the atmosphere. An electrically controlled needle valve was used to introduce oxygen gas near the substrate for synthesizing oxides. The deposition chamber was pumped by a diffusion pump backed with a rotary pump.

Figure 3.3. Plasma beam impinging onto substrate, and scanned images of two coated substrates.

Arc current, arc voltage, and background pressure were recorded using a personal computer equipped with an analog input/output card under the control of a LabView based program. Figure 3.3 shows photographs of the plasma beam impinging onto a substrate in the deposition chamber and the deposited films on glass substrates.

3.2. Cathode Preparation

The main part of the arc cathode (Figure 3.4) was made from a cylindrical copper (Cu) rod. At the ends of each cathode rod two cavities were formed; one to contain the cathode coil and the second to contain the coating material. The diameter of the cavity containing the coating material had a 91 mm diameter and was 10 mm deep. It was filled with either 99.99% pure Zn, Sn or a Zn-Sn metal alloy (10, 30 and 50 at.% of Sn). Filled cathodes were prepared by placing ingots of Zn and/or Sn in the cathode cavity, and heating it with a Bunsen burner to above the melting point of the filler metals. After melting, any oxidized scum floating on the surface was skimmed off, the burner was turned off, and the cathode was allowed to cool. The

cathode was then mounted in the vacuum chamber. Newly mounted cathodes were conditioned by initially arcing in vacuum (i.e. without any flow of background gas), and without applying any magnetic field. The pressure in the vacuum system would generally jump upwards initially by several orders of magnitude, due to the release of gas from the surface layers (e.g. oxide) on the surface of the filler metals. The procedure tended to remove these surface layers, and hence cleaned the cathode surface.

Figure 3.4. Cathodes, showing the cavity for metal filling (left) and water cooling cavity (right).

3.3. Substrates

The thin films were deposited on 76×25×1 mm commercial microscope glass slides, and on 50×50×1 mm commercially polished (5 lambda per inch) UV fused silica (UVFS) slides. The glass substrates were washed with diluted 5% HCl acid and then cleaned with deionized water and dried in air. After cleaning, the substrates were mounted on the substrate holder for film deposition. The holder with the substrate was positioned in the deposition chamber and after the system was pumped down to ~0.27 Pa (~ 2×10^{-4} Torr), the deposition process was started.

3.4. Deposition and Annealing Procedures

The deposition and annealing conditions for ZnO, SnO_2, ZnO-SnO_2 and zinc stannate thin films are summarized in Table 3.1. The main deposition parameters were the cathode composition, arc current, deposition pressure and time. The effects

of substrate temperature and annealing on the structure, morphology, composition, optical and electrical properties were studied. The ZnO and SnO_2 films were annealed in Ar at 400 and 600^oC for 50 min, whereas the ZnO:Sn and zinc stannate thin films were air annealed at 500^oC for 60 min, and also in Ar at 500 and 600^oC for 50 min. The annealing time consisted of heating (~5 min), annealing and cooling (~15 min).

Table 3.1. Deposition and annealing parameters

Parameter	**Value**
Substrates	Glass and UVFS slides
Substrate Temperature	ZnO – RT, 400^oC SnO_2 – RT, 400^oC Zinc stannate- ZnO-SnO_2– RT, 200, 400 and 500^oC
Cathode Composition	Zn:Sn (at.% ratio) – 1:0, 9:1, 7:3 and 0:1
Arc Current	ZnO – 150 and 200 A SnO_2 – 150 A Zinc stannate- ZnO-SnO_2 – 150, 200, 250 and 300 A
Cathode Coil Current	12 A
Magnetic Filter Current	2 A
Oxygen Background Pressure	ZnO – 0.53, 0.67, 0.80 and 0.93 SnO_2 – 0.53, 0.67, 0.80 and 0.93 Zinc stannate- ZnO-SnO_2 –0.40, 0.53, 0.67, 0.80 and 1.06 Pa
Deposition Time	60, 90, 120 and 240 s
Annealing Temperature	ZnO – 400 and 600^oC SnO_2 – 400 and 600^oC Zinc stannate- ZnO-SnO_2 – 500 and 600^oC
Annealing Times	50 and 60 min
Annealing Environment	Air and Argon (Ar)

All film characterization and diagnostics were performed at the center of the deposited film, over an area of ~1×1 cm, where the thickness was uniform within ~5%.

3.5. Diagnostics and Optical Models

A detailed introductory section on the diagnostic methods was presented in the literature survey section (2.8). The deposited films were characterized using the following diagnostics and optical methods:

3.5.1. Film Composition

In the present research, the elemental composition of the films was determined using both Energy Dispersive X-Ray Spectroscopy (EDS) and X-ray photoelectron spectroscopy (XPS).

EDS analyses were performed by using a scanning electron microscope (JSM-6300 with an Oxford EDS system), and the elemental composition of the films was analyzed using ISIS-Link Oxford software. The XPS analyses were performed with PHI 5600 scanning AES/XPS multi-technique system. Depth information was obtained by sputtering the film surface with Ar ions, combined with AES/XPS analyses.

3.5.2. Film Structure

The structure of our films was analyzed using an X-ray diffractometer with the CuK_α radiation (wavelength λ=1.54051 Å), equipped with a liquid nitrogen cooled Ge detector. The scanning range was between 2θ =10 and 80° with 0.025° steps, and the film phase was determined by comparing to standard ZnO, SnO_2 XRD patterns.

Crystalline grain size, *D,* was determined from the full-width-half-maximum (FWHM) value of the (002) and (200) reflections for ZnO and SnO_2, respectively, using Eq. (2.88). The lattice parameters of ZnO and SnO_2 films were calculated according to Bragg's law (Eq. (2.89)). The lattice spacing, d_{hkl}, of ZnO and SnO_2 thin films were determined using Eqs. (2.90) and (2.91), respectively.

The stress, s_{st}, parallel to the film surface in ZnO films, was calculated using Eq. (2.92) and estimated from the shift of the diffraction peak relative to the standard values.

3.5.3. Film Surface Morphology

The average grain size and the effect of the deposition conditions on the film microstructure were studied using the SEM and AFM techniques. The SEM analyses were performed using a JEOL JSM-6700 F SEM system, and the AFM analyses were performed using a Park Scientific Instruments model M5 with Proscan image-processing software. The AFM examination used the non-contact mode with UL20B cantilevers and conical tips of 10 nm radius and 12 degree angle.

3.5.4. Film Transmittance and Reflection

3.5.4.1. Film Transmittance

The film transmission was measured with a Jasco V-530 double beam spectrometer in the 200-1100 nm wavelength range in 2 nm steps. In the UV region (190-350 nm) the light source was a deuterium lamp, and in the VS/NIR region (340-1100 nm) a halogen lamp was used as the light source. In all measurements, the film transmission was measured relative to the air, and the glass or UVFS substrate effect was taken into account in the optical models used to derive the optical constants from the transmission data.

3.5.4.2. Spectroscopic Ellipsometry

Determining the optical constants and thickness of the deposited films was one of the major undertakings of this research, and spectroscopic ellipsometry (SE) was the major method employed. The SE data for this report were taken from 191 to 1000 nm and at multiple angles of incidence (45°-75° by 5°). Variable angles improved the confidence in the diagnostics, as the light traveled along different paths

through the film. The data was analyzed with the WVASE 3.51 software package. The procedures and models used in the optical analyses are described in the literature survey section (2.8.2 and 2.8.3).

3.5.5. Thickness Measurements

The thicknesses of the deposited films were determined using the AlphaStep 500 computerized surface profiler (Figure (3.5)) and also from the optical analysis. The profilometer auto-levels and auto-scales step heights up to 13 μm in the high-resolution mode (1 Å vertical resolution), or up to 300 μm in the low resolution mode (100 Å vertical resolution).

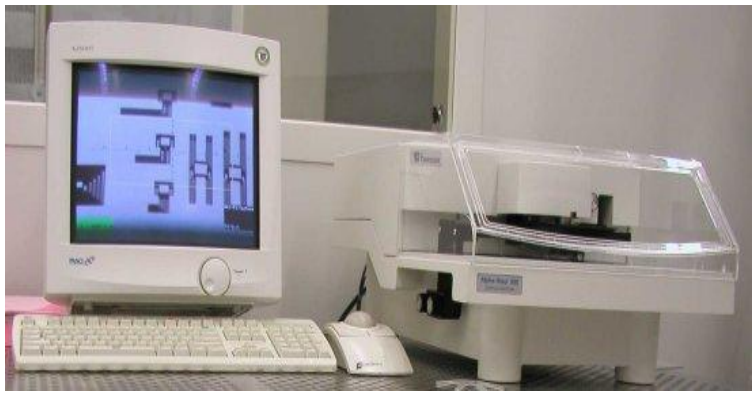

Figure 3.5. Photograph of the Alfa Step Profilometer

3.5.6. Optical Data Analyses

The data from two different and independent measurement methods, normal incidence transmission and spectroscopic ellipsometry, were analyzed by fitting procedure data calculated from optical models to the measured data. The output of this analysis was the functional dependence of the complex dielectric function on the photon energy (or wavelength). The dependence of the optical constants of the films on photon energy could then be calculated from the complex dielectric function.

3.5.6.1. Normal Incidence Spectroscopic Transmission Analysis

The optical constants *n* and *k*, and the film thickness (*d*) of dielectric and semiconducting thin films deposited onto transparent or semitransparent substrates was calculated from normal incidence spectroscopic transmission data. The optical constants (*n*, *k*) of the film as function of photon energy were derived from the complex dielectric function, which was expressed as a function of photon energy according to a single oscillator model (described in the literature survey section (2.6.2.1.1)), depending on four parameters. The parameters of the dielectric function were then derived by calculating the spectroscopic transmission (T_c) using Eq. (2.113), and varying them until the measured (T_{exp}) and calculated (T_c) transmission data closely overlapped. T_c and T_{exp} were fitted using a least squares MATLAB program, presented in Appendix A. The quality of the fit was determined by minimizing the object function defined by the sum of squares (SS) in Eq. (2.116).

3.5.6.2. Variable Angle Spectroscopic Ellipsometry (VASE)

The dielectric function of the films as function of photon energy was expressed by a superposition of three Tauc-Lorentz (TL) and Gaussian oscillators. The optical analyses applied a parametric graded semiconductor model to represent the dispersion in the optical properties within the ZnO and SnO_2 thin films layers, and a homogenous TL model for the zinc stannate samples. The parametric-graded model involves a graded film model, in which the dielectric function was written as a sum of three independent Tauc-Lorentz (TL) oscillator functions depending on the position of the layer in the bulk of the film. The first layer was at the interface film-substrate (at the bottom of the film), whereas the upper layer was at the film-air interface (at the top of the film), and the third one at about 38% into the film from bottom. The optical constants of the substrate were determined using the Cauchy formula. In addition to the optical constants, the film thickness *d* was also determined by the fitting process. The fitting was improved by adding an interface layer between the film and the air, whose optical properties were based on an effective medium

approximation (EMA) with 50% voids in the interface layer. The experimental ellipsometry and the generated data were fitted by minimizing the MSE function (Eq. 2.117).

3.5.6.3. Absorption and Dispersion Calculations

The general optical behavior of any transparent non-metallic thin film is characterized by interference and absorption. The strongest optical absorption involves photons with energy matching the electronic transition across the optical energy band gap existing between the conduction and the valance bands. In addition, much weaker absorption of photons of lower energy ($E<E_g$) occurs. The transmission as function of wavelength is determined by the dispersion of the optical constant, which is described by the theory and optical models presented in the literature survey section (2.6.2.1 and 2.8).

The absorption coefficients were calculated using Eq. (2.19), where the extinction coefficients were derived from normal transmission and SE data analyses. The optical energy band gap (E_g) of the materials was evaluated using the absorption coefficients (a). The value E_g was obtained using Eq. (2.67) and by extrapolating $(\alpha h\nu)^2$ versus E plots to 0 in the range where $E>E_g$, assuming a direct optical transition across the band gap.

In addition, if only the refraction index, n, in the VIS is to be calculated, the simpler formula based on the quantum approach to the refractive index behavior can be applied to data in VIS spectrum. The data of n in the visible can be used to study the energy band structure dependent dispersion and oscillator energy parameters, E_d and E_o, defined by the model proposed by Wemple and DiDomenicco (1971a) where the extinction coefficient, k, is negligible. These parameters were calculated using Eq. (2.56) for ZnO, SnO_2, ZnO:Sn and zinc stannate thin films deposited under different deposition conditions by plotting $(n^2\text{-}1)^{-1}$ versus E.

3.5.7. Electrical Properties

Figure 3.6 shows a schematic diagram of the four-point probe setup used to measure film resistance. In this set-up, an electric field was applied to the sample via the outer probes producing a current in the sample, and the inner probes were used to measure potential difference between two points in the film. The sheet resistance, R_s [Ω/square], of the films were determined as function of deposition parameters by using Eq. (2.73), and the resistivity r was calculated using the measured or optically derived thickness (d). The presented results were the average of 10 individual measurements.

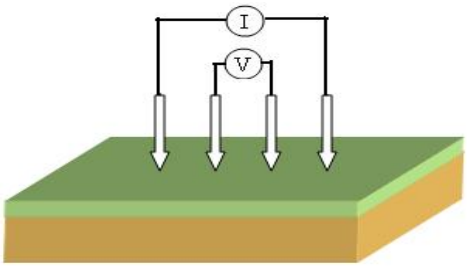

Figure 3.6. Schematic diagram of a four-point probe set-up.

The resistance was determined as function of film temperature using a two-point probe, and the temperature was monitored by a thermocouple touching the sample. The films were deposited on glass substrates and two Al strips with dimensions of 10 mm in width and 25 mm in length and 5 and 10 mm apart were deposited by evaporation through a metal mask put onto film. A schematic diagram of experimental arrangement used in the resistance measurement is presented in Figure 3.7. The current was measured by measuring the voltage across the load resistance (200, or 510 kΩ) which was connected series to the sample. Film temperature was varied between 28^{o}C to 200^{o}C, and the data collected at 5^{o}C increments during the heating (or cooling). The heating time was ~5 min, and ~2 h cooling time was required to return to RT.

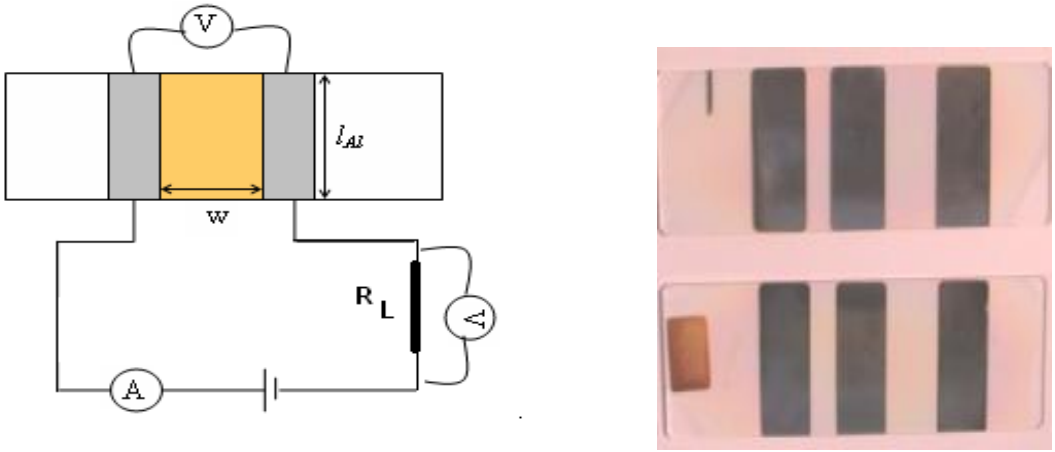

Figure 3.7. Schematic diagram of the two-point probe arrangement used to measure resistivity as a function of temperature, and a photo of deposited Al contacts.

4. EXPERIMENTAL RESULTS

It should be noted that the amount of the data obtained during the present research is too large to be presented in detail either in figures or in tables. Hence, it was feasible to only present selected data in figures and tables. The various results are presented separately for each of the studied oxides.

4.1. ZnO Thin Films

ZnO thin films were prepared using the FVAD system described in the "Experimental Apparatus and Procedure" (section 3.2.1), and the deposition conditions presented in Table 3.1.

4.1.1. Chemical Composition

The chemical composition of the films depended markedly on the deposition conditions. Thus, the chemical composition of the bulk of films deposited on UVFS substrates with 200 A arc current and 0.79 Pa oxygen pressure was found to be stoichiometric, i.e., with atomic concentration ratio 1:1 (Zn:O). The surface layer composition differed markedly from that of the bulk. On the surface, deficiency of oxygen was observed (~38.83at.%). The surface also contained significant concentration of carbon atoms (35at.%) and some Cu impurity (0.86at.%).

The effect of substrate temperature on bulk composition was determined for films deposited on glass substrates using 150 A arc current, at 0.53, 0.67 and 0.80 Pa, oxygen pressures, respectively. In Table 4.1 the surface compositions of these ZnO films as function of substrate temperature (RT and 400^{o}C) and deposition pressure are presented. As can be seen from the table, the surface composition is in most cases again characterized by excess of oxygen and carbon, and no clear trend was found between oxygen pressure and C concentration on the film surface.

The atomic concentration ratios of O to Zn in the bulk of ZnO (R_{OZn}) are presented in Table 4.2 as function of the deposition pressure and substrate

temperature. All ZnO films were oxygen deficient, i.e. R_{OZn}<1.0, the films on heated substrate tended to have larger R_{OZn}, i.e. these films were closer to stoichiometry, however, R_{OZn} was not did not depend in an ordered way on the deposition pressure.

Table 4.1. The surface chemical composition of ZnO thin films deposited on RT and 400°C heated substrates (glass, 150 A).

	Atomic Concentrations (at.%)					
	ZnO					
On film surface	RT			400°C		
Pressure (Pa)	C	O	Zn	C	O	Zn
0.53	19.34	45.88	34.78	-	47.77	52.23
0.67	16.37	46.45	37.18	-	48.62	51.38
0.80	26.06	44.28	29.67	-	47.33	52.67

Table 4.2. The film bulk chemical composition of ZnO thin films deposited on RT and 400°C heated glass substrates using 150 A arc current.

	R_{OM}			
	R_{OZn}		R_{OSn}	
Oxygen Pressure (Pa)	RT	400°C	RT	400°C
0.53	0.91	0.96	2.04	2.05
0.67	0.95	0.95	2.08	1.99
0.80	0.90	0.92	2.09	2.04

In Table 4.3, the surface and in the film bulk compositions of ZnO thin films deposited on RT kept UVFS substrates using 150 A arc current at 0.67 Pa, and later annealed at 400ºC or 600ºC are presented. As can be seen from the table, the surface composition was characterized by excess oxygen and carbon, and also a small amount of Cl. R_{OZn} in as-deposited films was 0.94, i.e. oxygen deficient. R_{OZn} of the annealed films was 0.93 and 0.98 for samples annealed at 400 and 600°C, respectively.

Table 4.3. The surface and bulk film chemical composition of as-deposited (RT) and annealed ZnO thin films (on UVFS using 150 A arc current).

	C (at.%)	Cl (at.%)	Zn (at.%)	O (at.%)
On the surface				
As-deposited	16.37	0	37.18	46.45
400^{o}C	20.50	1.47	37.42	40.61
600^{o}C	24.14	1.52	34.09	40.25
In the film Bulk				
As-deposited	0	0	51.38	48.62
After 400^{o}C Annealing	0	0	51.90	48.10
After 600^{o}C Annealing	0.46	0	50.33	49.21

4.1.2. Crystal Structure

The XRD spectrum of a ZnO thin film deposited with 200 A and 0.80 Pa on RT kept glass substrate is shown in Figure 4.1. A strong diffraction line at $2\theta = 34.31^{o}$, which corresponds to the X-ray reflection from the (002) planes, may be seen. The only other, a very weak feature, is seen at $2\theta = 56.54^{o}$ associated to reflection from the (110) planes. The XRD diffraction lines indicate that the film had a hexagonal wurtzite structure, and was highly texturized, with the *c*-axis oriented perpendicular to the substrate. Both lines in Figure 4.1 are shifted to shorter 2θ relative to their standard values (34.31^{o}, 56.8^{o}), indicating that the film was compressively stressed. The calculated lattice parameter *c* was 0.5224 nm, higher by 0.0018 nm than that of standard ZnO crystals. The average grain size was 23 nm, calculated from the broadening of the (002) line by Eq. (2.88).

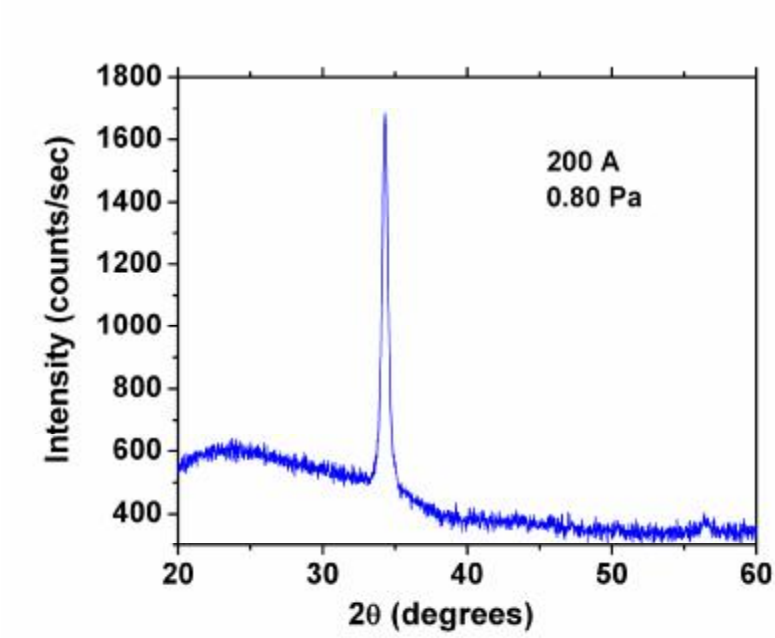

Figure 4.1. XRD spectra of a ZnO film deposited at 0.80 Pa using 200 A arc current.

In Figures 4.2(a-d) XRD the diffraction patterns of ZnO thin films, deposited on RT and 400^{o}C substrates using 150 A arc current at 0.53 and 0.80 Pa deposition pressure, are presented. As can be seen from Figs. 4.2 (a) and (b), strong diffraction from the (002) planes and also very weak diffraction from the (004) planes were detected, indicating that the ZnO films were strongly *c*-axis oriented on both RT and 400^{o}C heated substrate temperatures. The intensity of the diffraction line was considerably higher with the heated substrates. The average ZnO crystallite size in films deposited at 0.53 Pa on RT and 400^{o}C substrates was 16 and 26 nm, whereas that in films deposited at 0.80 Pa was 17 and 22 nm, respectively. Compared with standard data of the (002) peak, *c*-axis reflection peak in Figures 4.2(a) and 4.2(c) shifted to lower values indicating the compressive stress in the films, whereas, in Figures 4.2(b) and 4.2(d) it is shifted to higher values, indicating tensile stress in the films. The stress, s_{st}, calculated using the Eq. (2.92), was -0.83 GPa for both deposition pressures at RT, however, the films deposited on 400^{o}C heated substrates were +0.48 GPa and +0.64 GPa for 0.53 and 0.80 Pa oxygen pressures, respectively.

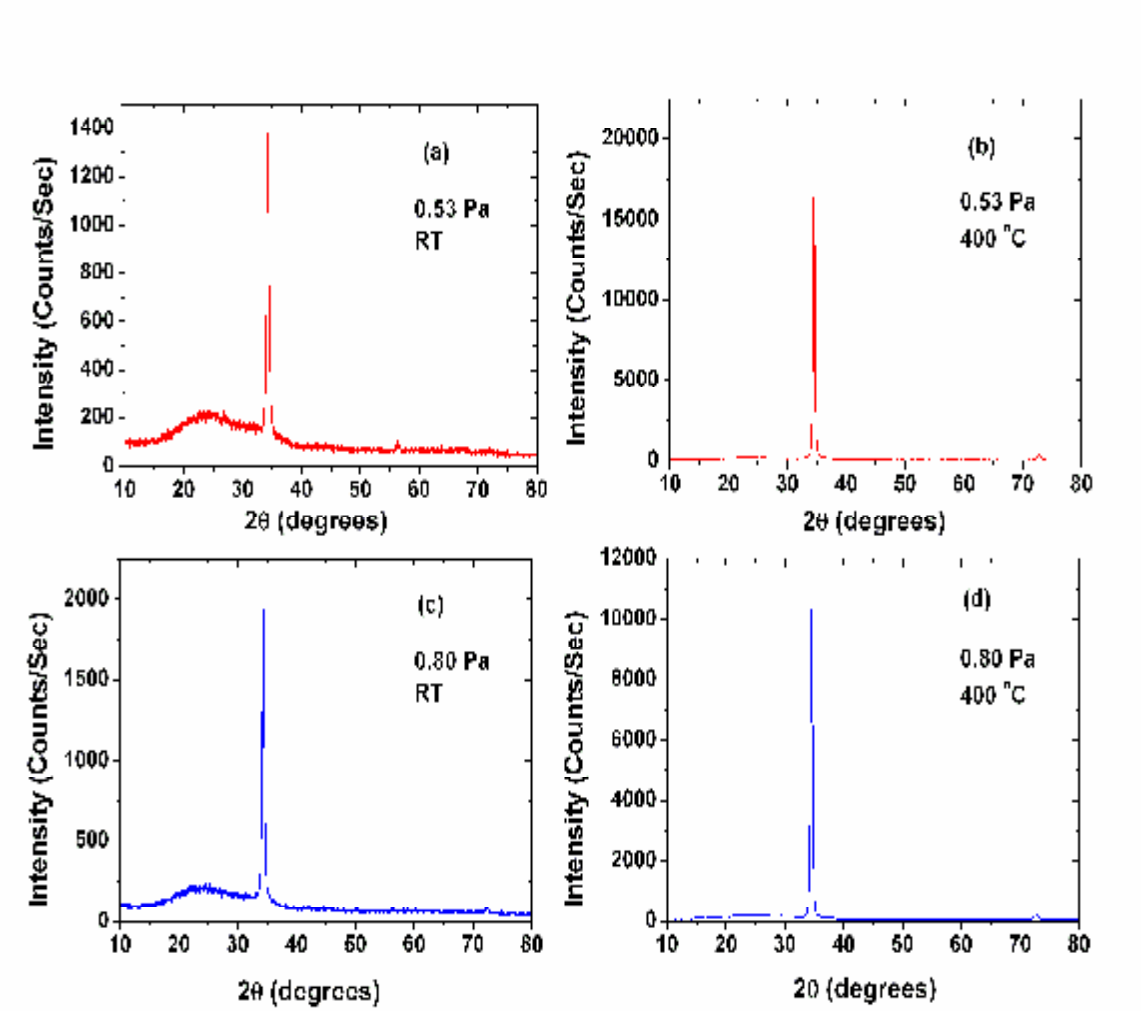

Figure 4.2. **XRD patterns of RT and 400°C deposited ZnO thin films deposited at 0.53 and 0.80 Pa oxygen pressures with a 150 A arc current.**

In Figures 4.3(a-c), XRD the diffraction patterns of ZnO thin films, deposited on RT UVFS substrates using 150 A arc current at 0.67 Pa oxygen pressure, and later annealed in Ar at 400 and 600°C respectively, are presented. As shown, the films were strongly *c*-axis oriented, and the diffraction line intensity increased with the annealing temperature. The calculated average grain size was 17, 20 and 21 nm for as-deposited films and 400°C and 600°C annealed films, respectively. The (002) peak in Figure 4.3(a) shifted to a lower Bragg angle, indicating a compressive stress in the films; calculated to be -0.66 GPa. However, in Figures 4.3(b) and 4.3(c), the shift was to higher diffraction angles, indicating tensile stress in the annealed films; calculated to be 0.65 and 1.30 GPa in films annealed at 400 and 600°C, respectively.

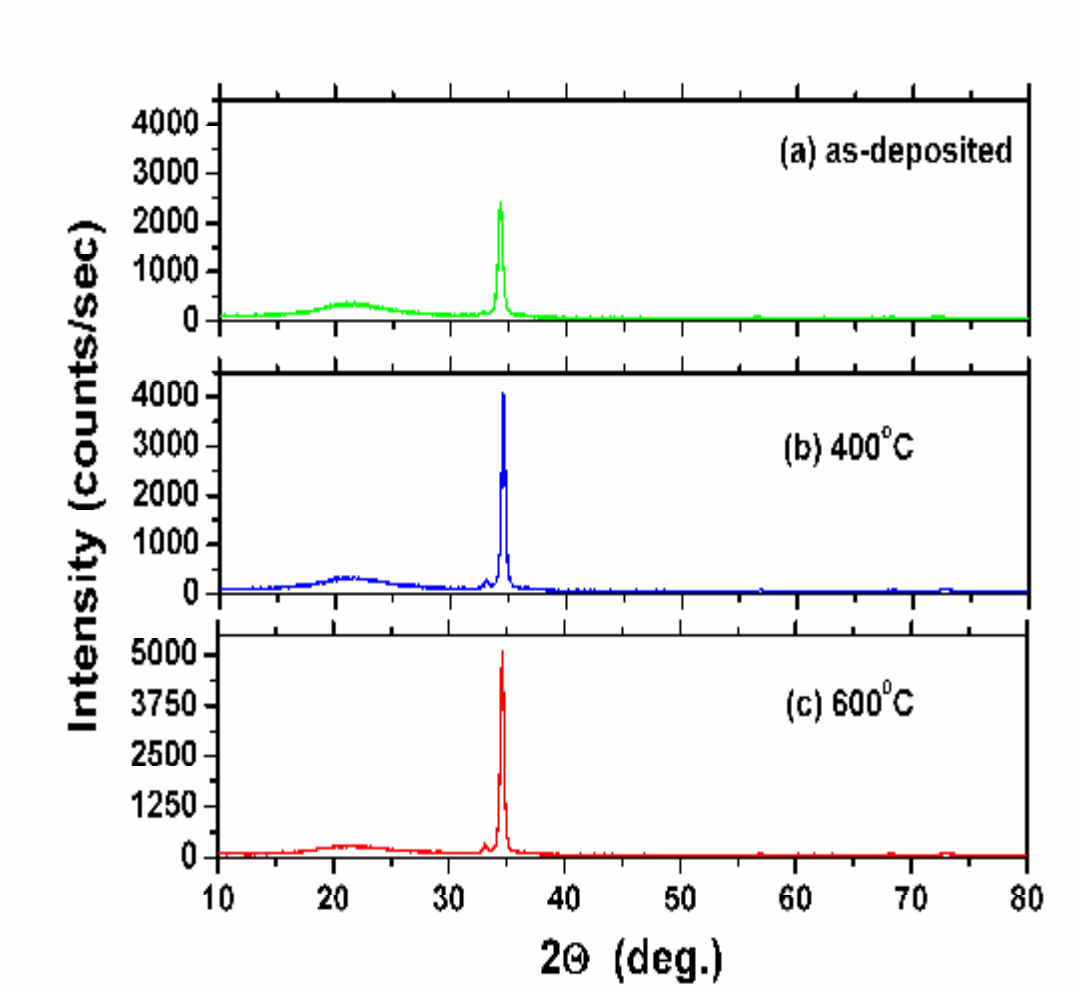

Figure 4.3. XRD patterns of as-deposited (RT), 400 and 600°C annealed ZnO thin films.

4.1.3. Surface Morphology

In Figure 4.4, a SEM image of the granular surface of a film deposited using 200 A arc current at 0.80 Pa oxygen pressure and on RT kept glass substrate is presented. The estimated average grain size was ~21 nm. This agrees reasonably well with average grain size determined from the XRD line-width (23 nm).

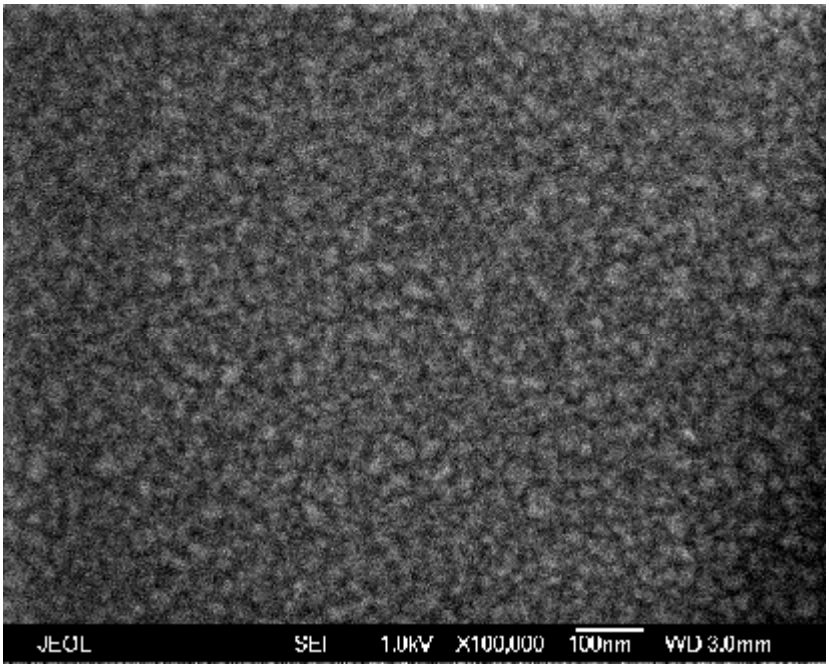

Figure 4.4. SEM image of ZnO thin films deposited at 200 A arc current and 0.80 Pa pressure on RT glass substrate.

The AFM analyses provided a measure of the surface roughness and surface grain size. Figures 4.5(a-b) show typical AFM reconstructed images of ZnO thin films deposited using 150 A arc current at 0.80 Pa oxygen background pressure on glass microscope slides at RT and at 400^{o}C. The surface roughness was measured on 0.5×0.5 *m* m regions. The scale at the left corner of each AFM image indicates the range from the lowest point (the 0-point) to the highest surface peak. The middle value of this range is also indicated. The RMS of ZnO films deposited on RT and 400^{o}C substrates was 1.3 and 5 nm, respectively. The ZnO surface roughness increased with substrate temperature. The average surface grain size increased with substrate temperature for ZnO films, from 24 to 33 nm.

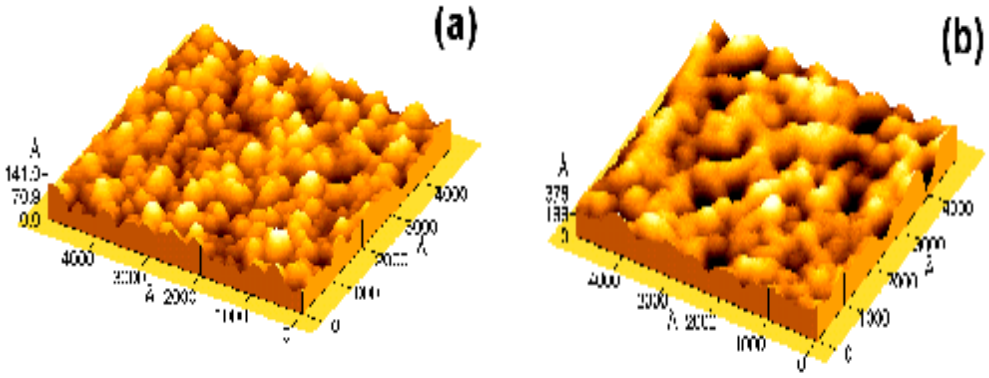

Figure 4.5. AFM images of ZnO films deposited on (a)RT, and (b)400°C substrates.

Figures 4.6(a-c) show typical surface images of as-deposited films on RT kept glass substrates using 150 A arc current and 0.67 Pa oxygen pressure and of films annealed at 400 and 600°C, respectively. The surface roughness was measured over a 0.5×0.5 *m* m regions.

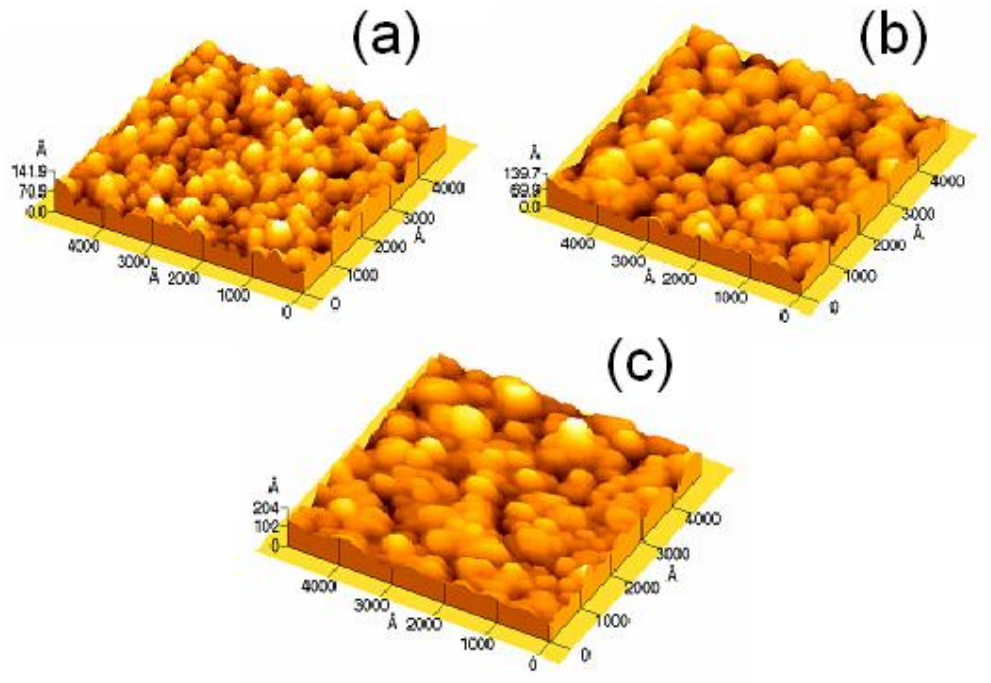

Figure 4.6. AFM images of (a) as-deposited, (b) 400°C, (c) 600°C annealed ZnO thin films.

Table 4.4. Annealing effects on ZnO thin film structure and optical constants.

	Stress (GPa)	D_{XRD} (nm)	D_{AFM} (nm)	R_{AFM} (nm)
As-deposited	-0.67	17	23	1.0
400^{o}C	0.65	20	39	1.3
600^{o}C	1.30	21	59	2.1

In Table 4.4, the average surface roughness (RMS) values and the average surface grain diameters of as-deposited, and Ar annealed ZnO thin films are listed. As seen from Table 4.3, the RMS of these samples is in the range of ~1 to 2.1 nm and the average grain size is in the range 23 to 59 nm, increasing with annealing temperature.

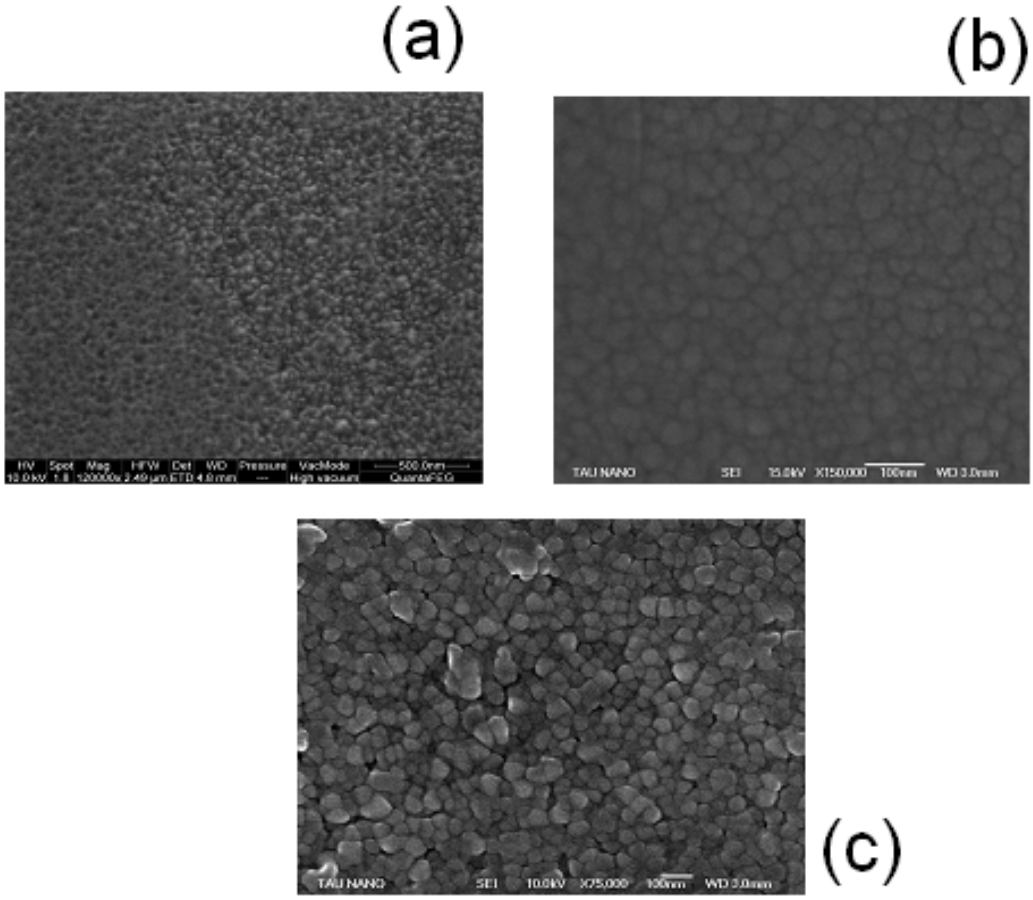

Figure 4.7. SEM images of (a) as-deposited, (b) 400^{o}C and (c) 600^{o}C annealed ZnO thin films.

In Figures 4.7(a-c) HRSEM images of as-deposited (RT, 150 A, 0.67 Pa, glass substrates), 400 and 600^{o}C annealed ZnO thin films are presented, respectively. As can be seen from the images, the grain size increased from ~20 to 59 nm with annealing. Similar results were also observed from AFM analysis, as mentioned above.

4.1.4. Optical Properties

Film optical constants and film thickness were retrieved from the measured normal incidence transmission and from spectroscopic ellipsometry as described in the experimental apparatus and procedure section (3.3.6). Typical plots of the optical transmission, as function of wavelength (350–1100 nm) of films deposited on RT UVFS substrates with 200 A arc current at 0.67, 0.80 and 0.93 Pa oxygen pressures are presented in Fig. 4.8. For all films, the minima and maxima of the transmission for l in the range 400–1100 nm are between 70% and 90%. As can be seen, the pressure affected the transmission curves; in particular it affected the transmission near the optical band edge (λ ~350–450 nm).

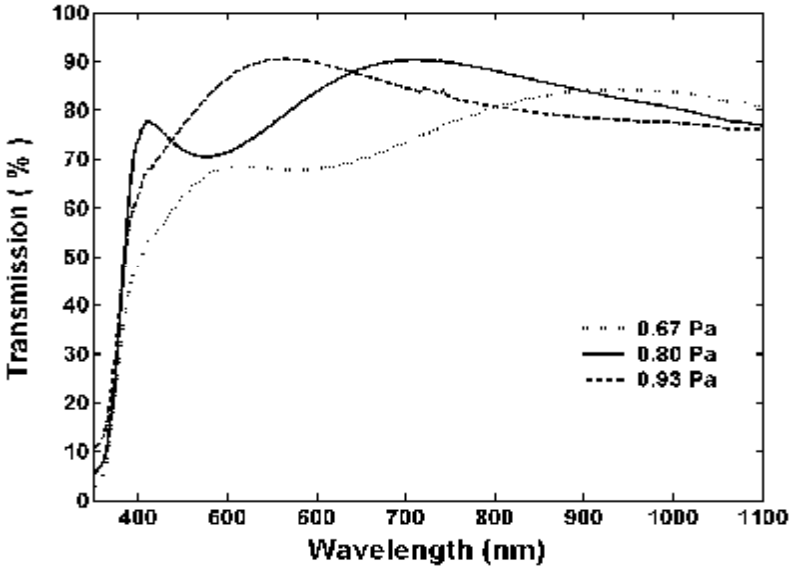

Figure 4.8. Optical transmittance spectra of ZnO thin films obtained with different deposition pressures.

In Figure 4.8, the variation of the transmission with wavelength could partially be accounted by the decrease in film thickness with pressure, e.g., at 0.67 Pa the thickness was ~250 nm and at 0.93 Pa film thickness was ~150 nm. At wavelength above 900 nm, the effect of the pressure on the transmission is smaller due to the significant decrease in the absorption coefficient, which will be discussed below.

The optical parameters of the films were determined using the normal incidence transmission data that was fitted using the transmission model presented by Cisneros (1998), who considered weak absorption in the substrate, and the transmission and reflection at the air/film, film/substrate, and substrate/air interfaces, and the spectroscopic ellipsometric measurements.

In Figures 4.9(a-c) typical plots of the measured and fitted film transmission and ellipsometric functions (Ψ, Δ) are presented. In the optical transmission analysis, a random phase approximation was assumed for the thick (1 mm) glass substrate. Eq. (2.113) was used to calculate the transmission (T_c) which was fitted to the measured transmission (T_{exp}), using the complex refraction index $\tilde{N} = n - ik$, where the index of refraction n, and the extinction coefficient k, are the components of $\tilde{N}$. $\tilde{N}$ is expressed as function of photon energy using a set of parameters. The fit of T_c to T_{exp} required a model for the dependence of the parameters on wavelength, or photon energy. The thickness d of the films was considered as an additional free parameter in the fitting procedure. The fit of T_c to T_{exp} was evaluated by minimizing χ^2, provided the best values for the parameters and d. This value of d was compared to the mechanically measured one, and the goodness of this comparison was an additional criterion for the acceptance of the analysis. The sum of squares (SS, Eq. (2.116)) of the transmission fitting presented in Figure 4.9(a) was 1.32, indicating high fitting quality.

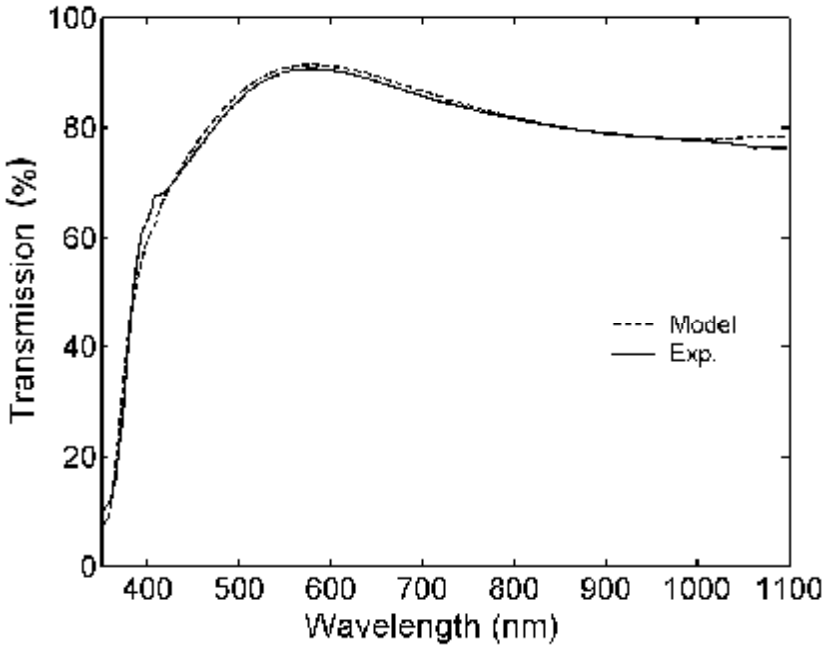

Figure 4.9(a). Plots of the experimental and calculated spectral transmittance of ZnO thin film.

In Figs. 4.9(b) and (c) the ellipsometric function Ψ and Δ are plotted for three incidence angles (60°, 65°, and 70°). The use of three incidence angles increased the accuracy of the data analysis, which was based on fitting model data to the measured data as described in the "Experimental Apparatus and Procedure" section 3.5.6.2. The fitting of the measured data to calculated ellipsometric data resulted with MSE equal to ~13. The fit quality was higher for data at wavelength longer than 400 nm. As can be seen, the main contribution to the MSE value comes from data at shorter wavelengths, where the fitting is affected at lower wavelengths. It should be recalled that the objective of the optical analysis is the derivation of the index of refraction, extinction coefficient, both as function of wavelength, and the value of optical band gap.

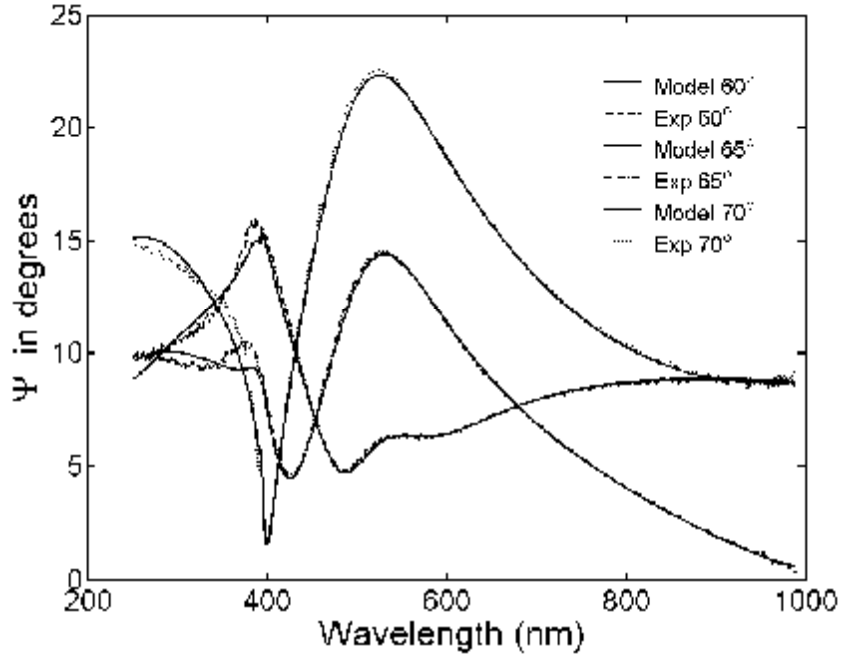

Figure 4.9(b). Plots of measured ellipsometric data, Ψ, and model fit for the sample deposited at 0.93 Pa oxygen pressure.

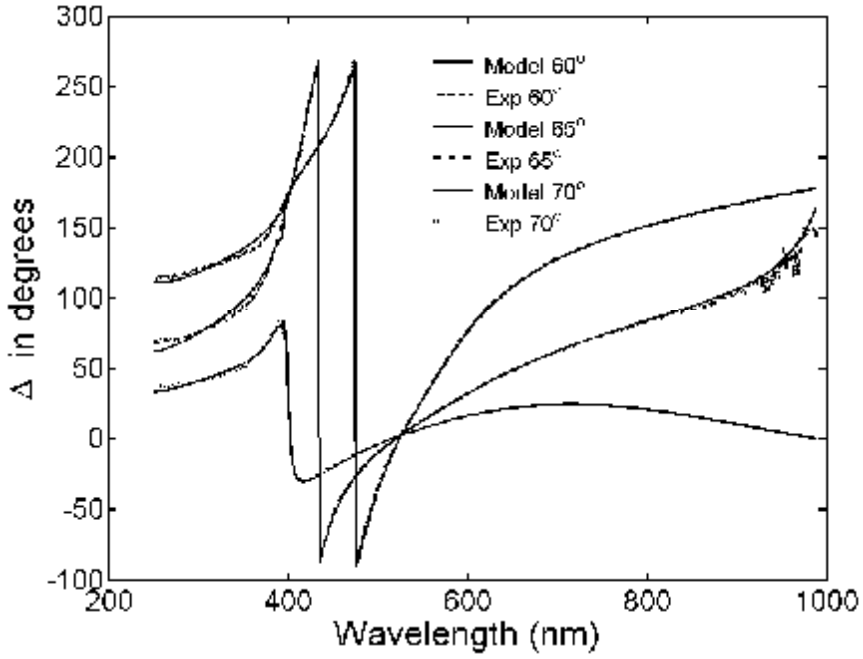

Figure 4.9(c). Plots of measured ellipsometric data, Δ, and model fit for the sample deposited at 0.93 Pa oxygen pressure

In Table 4.5, we list the refractive index and the extinction coefficient at l =500 nm, the optical energy band gap E_g, and the parameters of the dielectric

function (e_∞, e_s, E_0, and G) extracted from the fit of transmission to calculated data of films deposited on glass and UVFS substrates at 0.83 and 0.93 Pa oxygen pressure. As shown in Table 4.5, there is no well defined trend or significant dependence of the optical constants and dielectric function parameters on the pressure. The parameters e_∞, e_s, and E_0 were in the range 3.65–3.70 eV, 3.80–3.87 eV, 3.45–3.50 eV, respectively. The relative variations in the values of the parameter G as function of pressure are larger, but no defined trend on pressure or substrate was found.

Table 4.5. The dependence of the fitted single oscillator model parameters, e_∞, e_s, E_0, and G on the deposition pressure.

Pressure (Pa)	n λ(500nm)	k λ(500nm)	$E_¥$ (eV)	E_s (eV)	E_0 (eV)	G (eV)	Eg (eV)
0.80	1.95	0.005	3.67	3.82	3.49	0.30	3.42
0.80*	1.97	0.004	3.68	3.87	3.50	0.17	3.36
0.93	1.95	0.005	3.65	3.80	3.45	0.30	3.25
0.93*	1.96	0.004	3.70	3.82	3.46	0.26	3.38

Iarc: 200 A, Deposition Time: 60 s. * UVFS Substrates

In Figure 4.10(a-b), we present the graded model results as an example to show the distribution as function of the relative height in the film of n and k for λ = 500 nm, where the zero of the abscissa is the interface film/substrate. In such analysis of this film, the bulk was divided into 10 layers, and the optical constants in each layer were fitted. In Figure 4.10(a), at first, n increased with the relative height from 1.99 to 2.07, and decreased at larger height to 2.04. In Figure 4.10(b), the extinction coefficient k decreased with the relative height, from 0.045 to 0.02. The index n had a maximum value about the center of the film which is interpreted by us to indicate that the film density was maximal at the middle of the film.

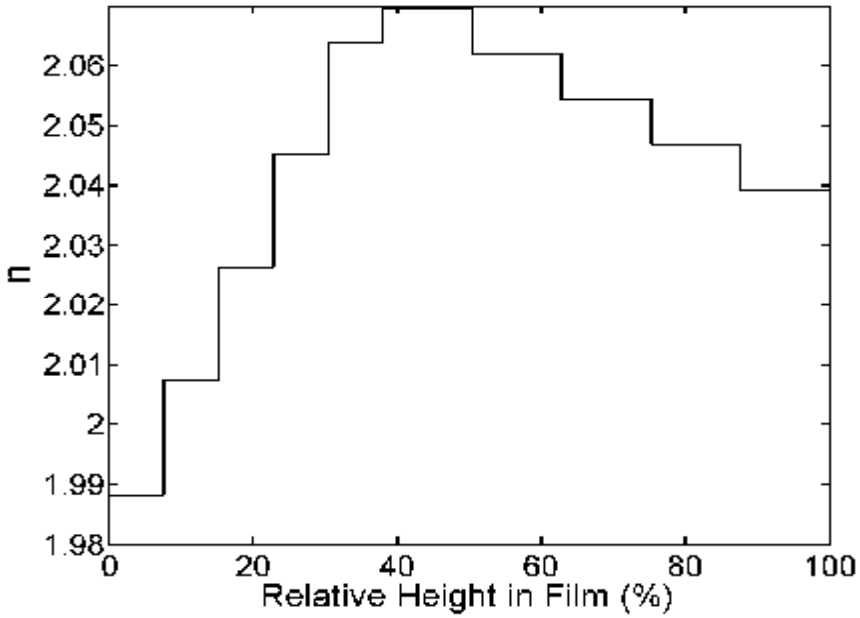

Figure 4.10(a). Examples of graded refractive index profiles. The zero of the abscissa is the interface film/substrate.

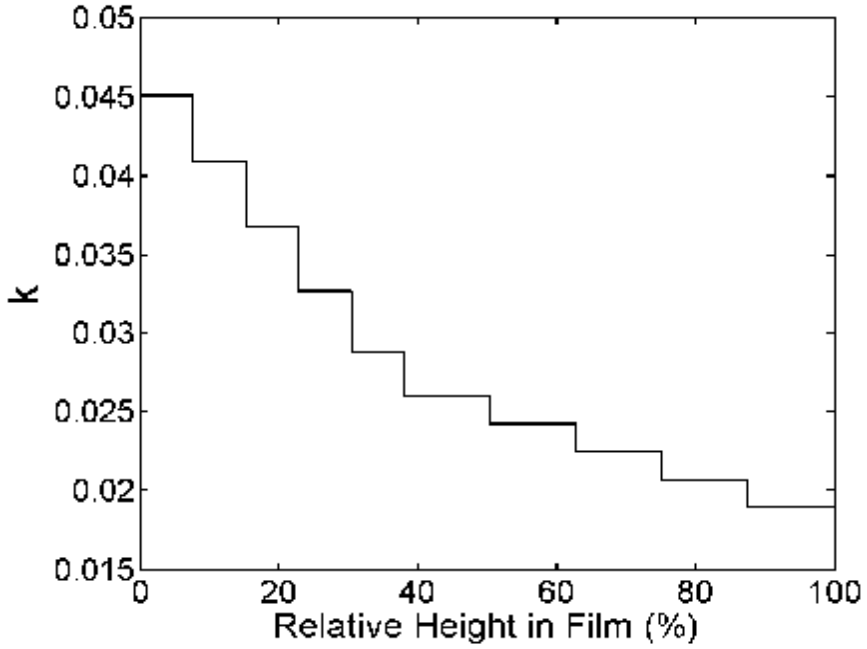

Figure 4.10(b). Examples of graded extinction coefficient profiles.

In Figures 4.11(a) and (b) the refractive index and extinction coefficient, obtained from transmission and ellipsometry analyses of ZnO thin films deposited at

200 A arc current and 0.93 Pa oxygen pressure on RT kept UVFS substrates, are plotted versus wavelength. The values of *n* derived from transmission and ellipsometry data decreased with increasing wavelength in the range ~400 to 1000nm from 2.15 to 1.95 and from 2.15 to 1.9, respectively. The values of *k* derived from transmission and ellipsometry data decreased in the same wavelength range from 0.4 and from 0.33 to approximately zero, respectively. In the 400-900 nm wavelength region the ratio $\Delta n/n$, where Δn is the difference between the refractive index values extracted by the two analysis methods, was smaller than 0.1. The difference between the extinction coefficient values, similarly extracted, was very significant. At l = 450 nm k(ellipsometry) = 0.1 whereas k(transmission) = 0.02. It should be noted that these differences in the derived n and k result from different optical and film modeling. Near the absorption edge (~350 nm) n had a well defined maximum for both analysis methods; however, the maxima were slightly shifted. The extinction coefficient decreased in both cases abruptly at wavelength above 350 nm, by more than one order of magnitude.

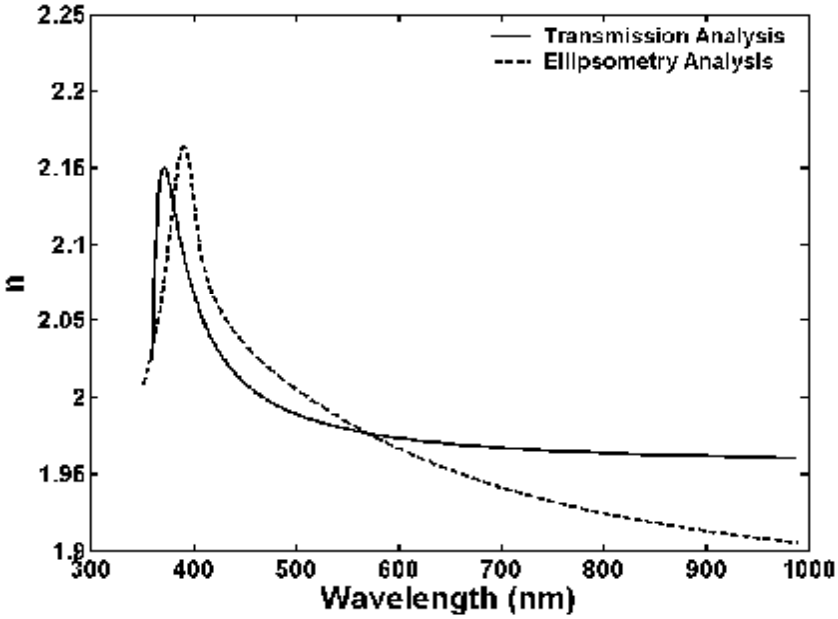

Figure 4.11(a). Refractive index versus wavelength derived from transmission and ellipsometry analyses.

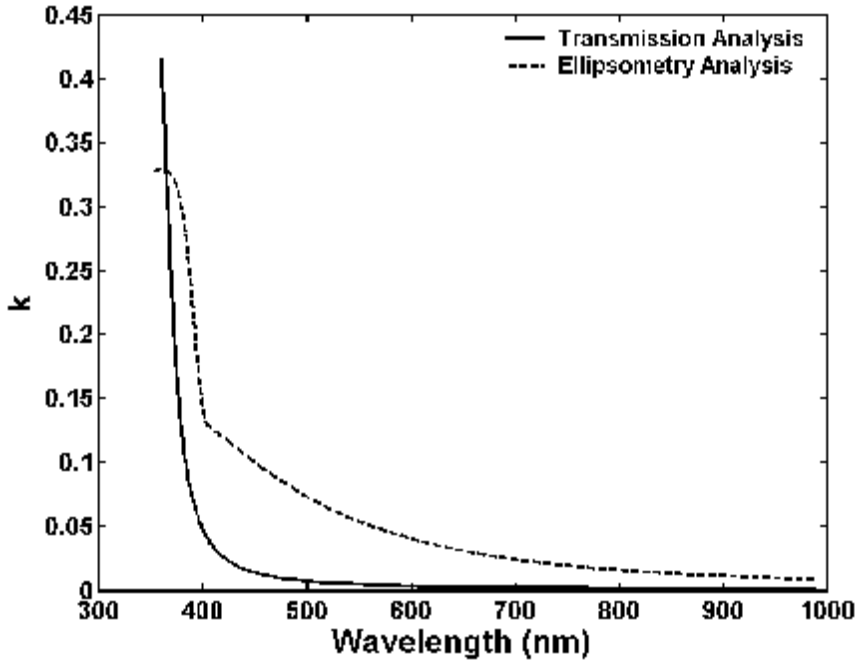

Figure 4.11(b). Extinction coefficients versus wavelength derived from transmission and ellipsometry analyses.

In Figures 4.12(a) and (b) the refractive index *n* and the extinction coefficient *k* as function of wavelength and pressure as a parameter, derived from the spectroscopic ellipsometry (SE) data were presented. The values of *n* (Fig. 4.11(a) and Fig. 4.12(a)) are smaller than the values reported by Heiland and Mollwo (1959) for ZnO single crystal, indicating a lower density of ZnO in our films. It is also seen in Fig. 4.12(a) that the peak *n* in the film deposited with 0.93 Pa was at a longer wavelength than the peak *n* in the film deposited at 0.67 Pa. This shift is associated with the effects of the pressure on the single oscillator frequency, shifting it to higher frequencies at higher pressure. Figure 4.12(b) shows that pressure affected *k* at the absorption edge and in the Urbach tail. The decrease of the tail is faster at higher pressure.

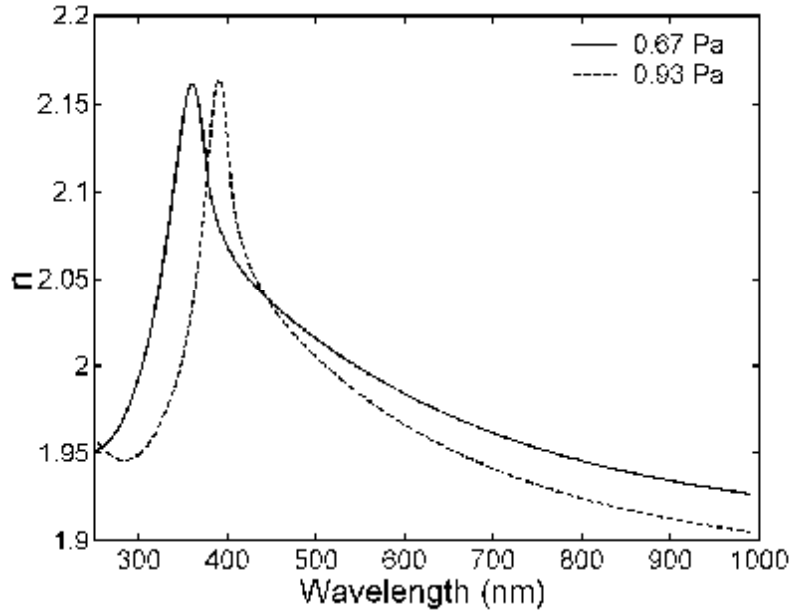

Figure 4.12(a). Plots of the refractive index versus wavelength of ZnO thin films deposited at 0.67 and 0.93 Pa oxygen pressures.

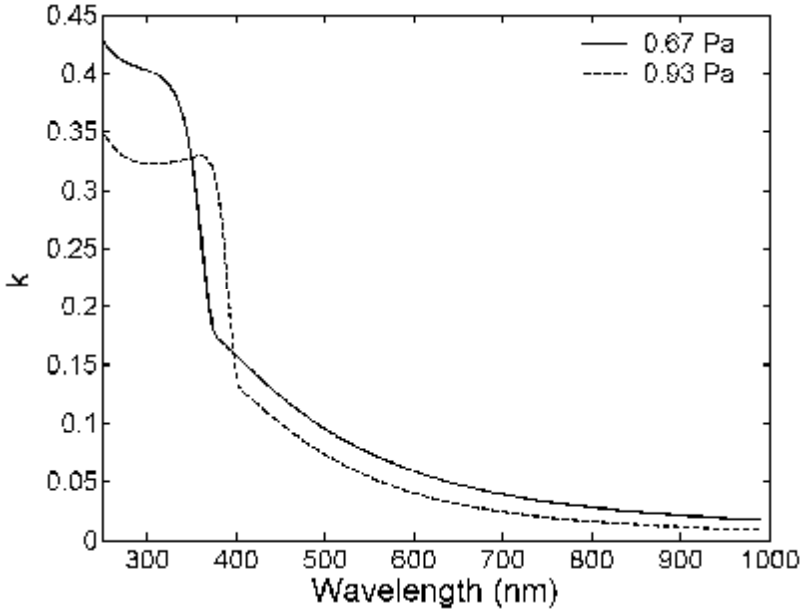

Figure 4.12(b). Plots of the extinction coefficient versus wavelength of ZnO thin films deposited at 0.67 and 0.93 Pa oxygen pressures.

In Figure 4.13, the value of $(n^2\text{-}1)^{-1}$ is plotted versus E^2 using the data for n in the VIS derived by the transmission and ellipsometric analysis. The plot from the

transmission data is not linear, as expected from WD model that entails Eq. (2.56) (Wemple and DiDomenico, 1971), whereas the plot based on the ellipsometric data is linear. The implication of the deviation from linearity observed here is discussed below. In Table 4.6, we list the values of the parameters E_o, E_d, and b calculated by non-linear least squares fit of Eq. (2.56) to the data in Figure 4.13, in the range 500 to 900 nm. The two columns in Table 4.6 correspond to data derived from transmission and ellipsometry analysis, respectively. The values of the parameters E_o and E_d defined by Eq. (2.56) listed by Wemple and DiDomenico (1971) for a ZnO crystal were 6.4 and 17.1 eV, respectively.

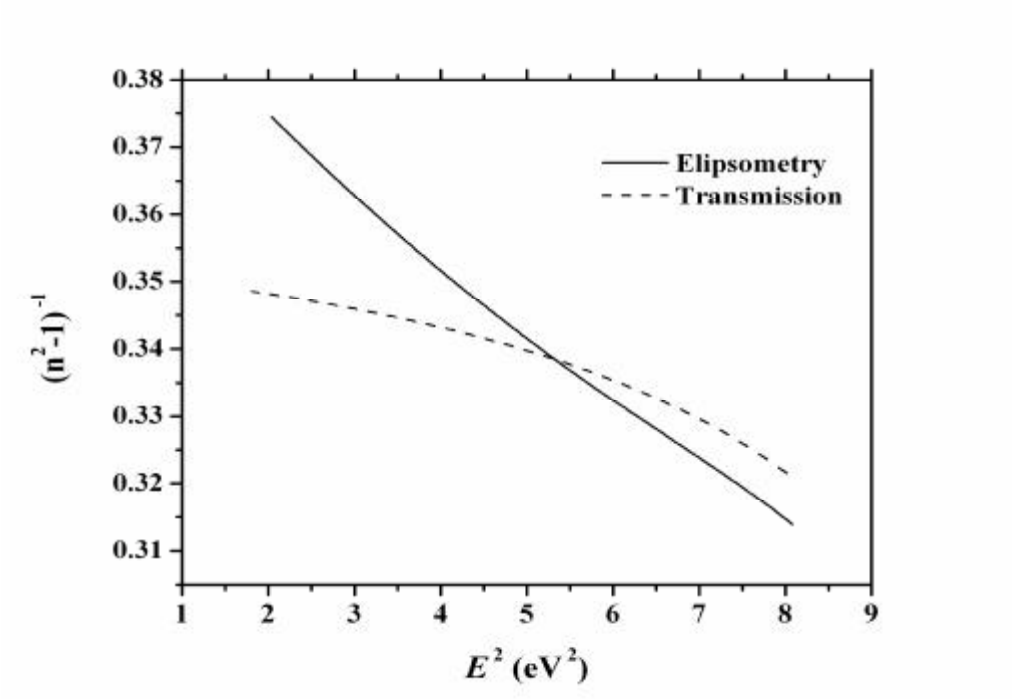

Figure 4.13. Plots of $(n^2-1)^{-1}$ versus E for n obtained from transmission and ellipsometry analyses.

As is seen from the table, E_o and E_d obtained from the ellipsometric data agree well with those of crystalline ZnO. However, E_o and E_d derived from the transmission data deviated markedly from the latter values, although the fit of the calculated transmission to the measured one was statistically significant (SS~0.01). Hence, the accepted good mathematical fit of measured to modeled transmission data does not necessarily result in actual n values. This conclusion is strengthened by considering the parameter b, which is almost constant for a large number of various

oxides (Wemple, 1973). It is seen in the table that *b* obtained from the ellipsometric analysis (0.26) is very close to that reported by Wemple and Didomenicco (1971). It should be noted, that although the analysis of the optical constants depends strongly on the method and modeling, the derived thickness did not depend on them, as can be seen in Table 4.6, where film thickness calculated from both measurements was 143 and 147 nm.

Table 4.6. The comparison of the optical parameters obtained from transmission and spectroscopic ellipsometry analyses.

Optical Parameters	Transmission Measurement	Ellipsometer Measurement
E_o (eV)	9.62	6.37
E_d (eV)	25.36	16.35
b	0.40	0.26
n_∞^2	3.64	3.57
E_g (eV)	3.38	3.33
d (thickness nm)	143	147
n (at 500 nm)	1.96	2.00
k (at 500 nm)	0.004	0.073
Iarc = 200 A, 0.93 Pa, 60 s deposition time on UVFS		

The absorption coefficient was calculated as function of wavelength using the expression $a(l) = \frac{4pk(l)}{l}$. In Figure 4.14, a plot of the values of $(\alpha h\nu)^2$ versus photon energy is presented, based on the extinction coefficient of a film deposited at 200 A and 0.93 Pa oxygen pressure on RT kept glass substrates. As can be seen in Figure 4.14, the magnitude of $(\alpha h\nu)^2$ is negligible below $h\nu$ = 3.1 eV, as the extinction coefficient is negligible for $h\nu < E_g$. At photon energies above 3.4 eV, $(\alpha h\nu)^2$ increases linearly with the photon energy, in agreement with Eq. (2.67). The value of E_g is obtained by extrapolating this linear dependence to $(\alpha h\nu)^2 = 0$. The

value of E_g of films deposited with pressure in the range 0.67– 0.93 Pa on UVFS substrates was in the range 3.2 to 3.42 eV, independent of the diagnostic method.

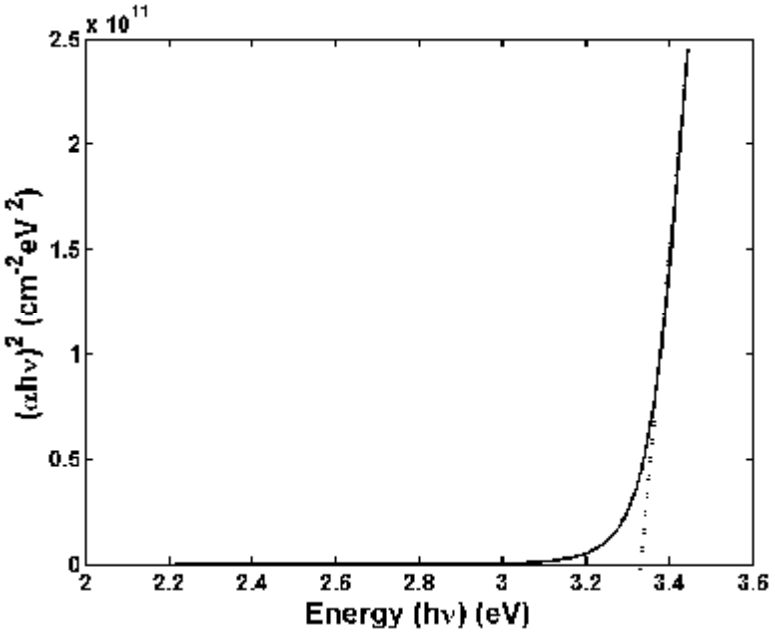

Figure 4.14. Plot of $(ahn)^2$ versus E for a film deposited at 0.93 Pa pressure.

In Figures 4.15(a-b), plots of the optical transmittance versus wavelength (200–1100 nm) of ZnO films deposited with 150 A arc current at 0.53 Pa and 0.80 Pa on RT and 400^{o}C UVFS substrates are presented. As the thickness of these films is practically the same in each figure, the variations in the interference patterns seen at the VIS region reflect the effects of the substrate temperature on the index of refraction (n). No significant difference in the VIS average transmission was observed for films deposited with 0.80 Pa pressure (Figure 4.15(b), implying that substrate temperature has negligible effect on k in the VIS. The strong absorption by the ZnO film at $\lambda < 380$ nm results from the absorption of photon with energy higher than the optical energy band gap. Furthermore, no significant shift resulted in the transmission edge as function of substrate heating. The transmission starts to decreases at λ ~390, forming a sharp transmission edge up to ~360 nm.

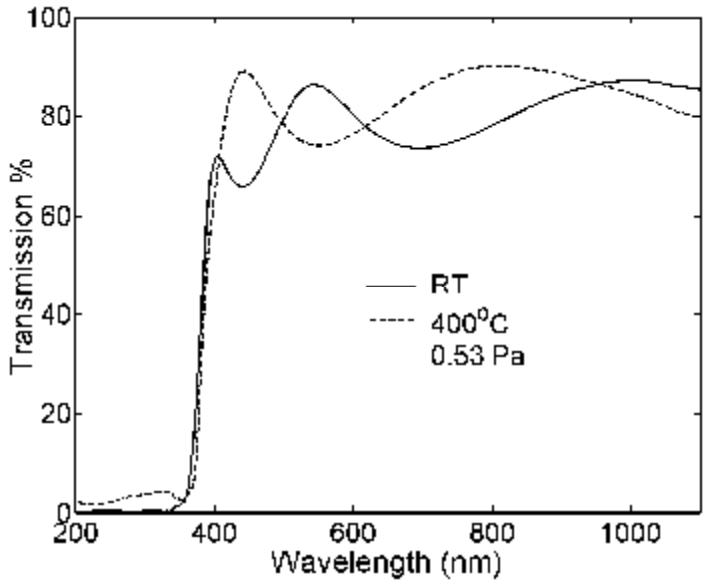

Figure 4.15(a). Transmission versus wavelength plots of films deposited on RT and 400°C substrates using 150 A arc current at 0.53 Pa oxygen pressure.

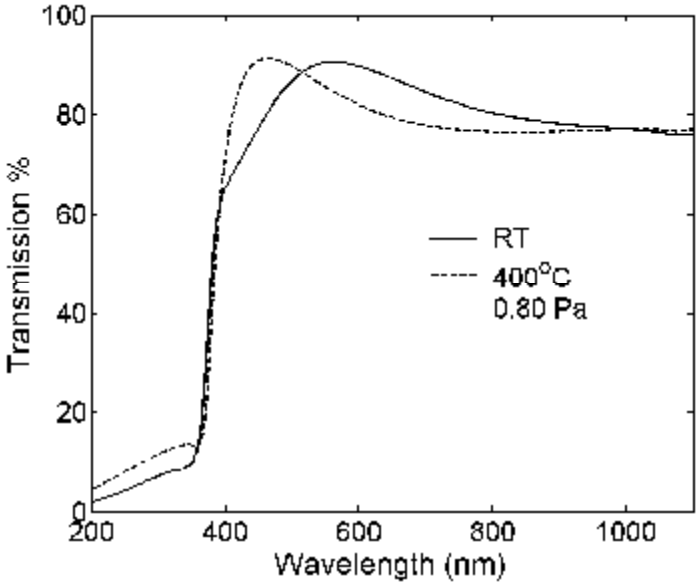

Figure 4.15(b). Transmission versus wavelength plots of films deposited on RT and 400°C substrates using 150 A arc current at 0.80 Pa oxygen pressure.

Plots of the refractive index *n*, and in the extinction coefficients *k* of ZnO films deposited with 150 A arc current at 0.67 Pa oxygen pressure on RT substrates

and 0.8 Pa pressure on 400°C UVFS substrates are presented in Figs. 4.16(a-b). The value of *n* decreased about ~10%, when deposited on hot substrates at 0.8 Pa. Furthermore, the rate of the refractive index decrease with increasing wavelength depended on the deposition conditions: from a peak value of 2.2 to 1.90 for the films deposited at 0.67 Pa on RT substrates, and from 2.0 to 1.71 for films deposited at 0.80 Pa on 400°C substrates. As shown, a minimum *n* at ~310 nm and a maximum at ~380 nm are also observed. The minimum in *n* near the absorption edge is obtained when the dielectric function of the material is described by a Lorentz oscillator with a pole at about the 310 nm. A minimum and maximum are also observed in the plots of the extinction coefficient, *k*, which decreased from a peak of 0.3 to approximately 0.02 at 550 nm wavelength and then to zero. The increase of *k* with decreasing wavelength below 290 nm (below the energy band gap) is related to expressing *k* by the Tauc-Lorentz model.

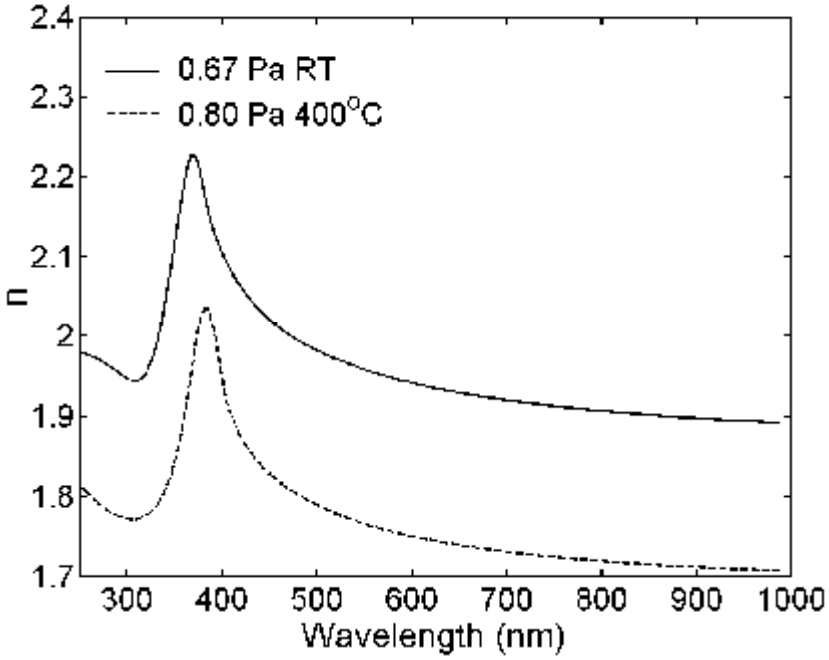

Figure 4.16(a). The refractive index (*n*) versus wavelength plots of films deposited on RT and 400°C substrates using 150 A arc current at 0.67 Pa and 0.80 Pa oxygen pressures.

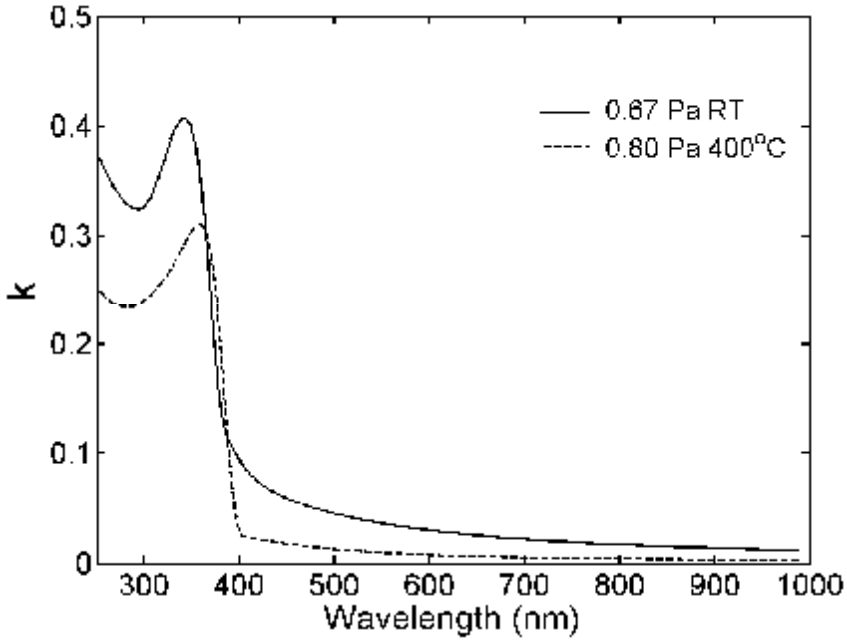

Figure 4.16(b). The extinction coefficient (*k*) versus wavelength plots of films deposited on RT and 400°C substrates using 150 A arc current at 0.67 Pa and 0.80 Pa oxygen pressures.

In Table 4.7, the refractive index and the extinction coefficients at 550 nm are listed as function of the deposition pressure and substrate temperature, representing the typical dependence of these parameters in the VIS on pressure and substrate temperature. The values of *n* for ZnO films deposited on RT substrates were in the range 1.87–2.03, and the values of *k* these films were in the range 0.02–0.04. However, the values of *n* for ZnO films deposited for heated substrates was in the range 1.77–1.98 and the values of *k* was in the range 0.002–0.020. Thus, the effect of hot substrates could reduce the 550 nm ZnO index of refraction by ~10%, depending on the pressure, while extinction coefficient could be lowered by a factor of 20, again depending on pressure. The values of the optical band gap that are also listed in Table 4.7 as function of deposition pressure and substrate temperature were not significantly affected by the substrate temperature, but they increased with increasing oxygen pressure from 3.25 to 3.30 eV for RT and 400°C deposited films.

Table 4.7. Optical constants of ZnO thin films deposited on RT and 400°C heated substrates at 550 nm.

	T_s = RT			T_s = 400°C		
Pressure (Pa)	n (550 nm)	k (550 nm)	E_g(eV)	n (550 nm)	k (550 nm)	E_g(eV)
0.53	1.87	0.020	3.25	1.98	0.020	3.25
0.67	1.96	0.040	3.26	1.85	0.002	3.28
0.80	2.03	0.030	3.30	1.77	0.010	3.30

A typical annealed ZnO thin film transmission spectrum is presented for films deposited using 150 A arc current on RT UVFS substrates at 0.67 Pa in Figure 4.17. The transmission in the visible and near infrared is in the range 70%-90%, as affected by the interference in the film. The transmission drops almost to zero when the photon energy at shorter wavelength approaches that of the optical band gap. As seen, the optical band edge is not significantly affected by the annealing. The most marked effect of annealing was a significant increase of the transmission at wavelengths > 600 nm, reaching 90%.

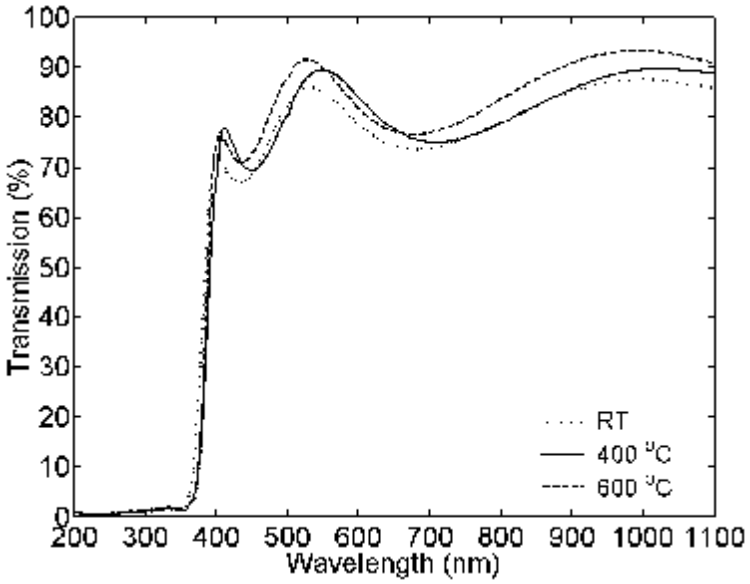

Figure 4.17. Plots of the optical Transmission of as-deposited and annealed ZnO thin films versus wavelength.

Plots of the refractive index, *n* and the extinction coefficient *k* of the same annealed films (of Figure 4.17) as function of wavelength and annealing temperature are presented in Figures 4.18 and 4.19. The refractive indices of as-deposited, and 400 and 600^{o}C annealed films were in the range 1.93 to 2.16, and 1.89 to 2.09 and 1.77 to 1.96, respectively. As shown, the refractive index decreased with annealing. The decrease of the values of *n* determined in the visible region from as-deposited films to those determined from films annealed at 400^{o}C is significantly smaller than the decrease in values of *n* determined from films annealed at 400 and 600°C. Thus, at l = 550 nm, n(RT) = 1.98, n(400°C) = 1.93, a reduction by 2.6%, whereas n(600°C) = 1.80, which is an additional decrease by 7%. The extinction coefficients *k* of as-deposited and annealed films were smaller than 0.05 at wavelengths >400 nm, but increased with decreasing wavelengths, and the peak value of *k* decreased with the annealing temperature up to a minimum value of 0.18 at λ = 350 nm for films annealed at 600^{o}C. The refractive index and the extinction coefficient at 550 nm, and the optical energy band gap values for ZnO thin films are listed in Table 4.8. It may be seen that *k* changed significantly with annealing.

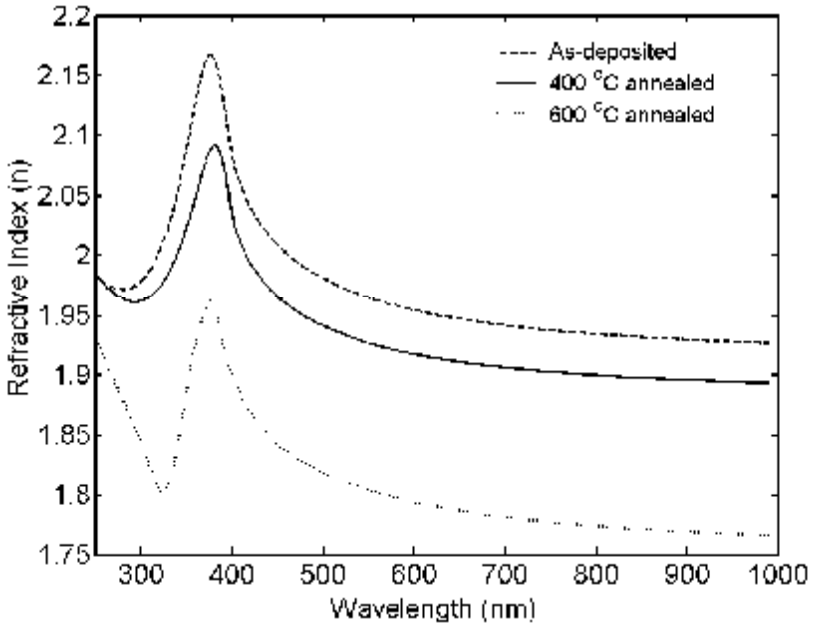

Figure 4.18. The refractive index versus wavelength plots of as-deposited and annealed (at 400^{o}C and 600^{o}C) ZnO thin films.

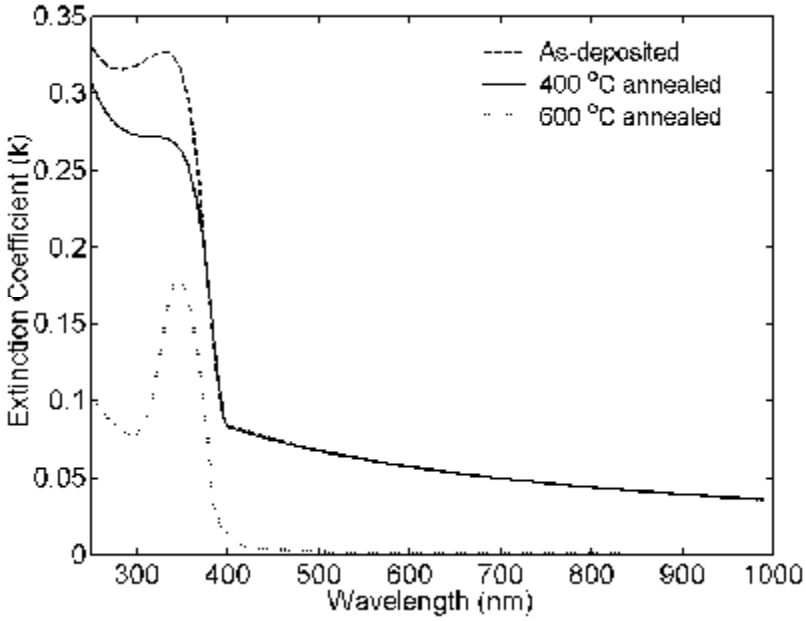

Figure 4.19. The extinction coefficient versus wavelength of as-deposited and annealed (at 400°C and 600°C) ZnO thin films.

Table 4.8. The effect of annealing on the optical parameters.

	ZnO		
	$n(\lambda = 550$ nm)	$k(\lambda = 550$ nm)	E_g(eV)
As-deposited	1.98	0.027	3.21
400°C	1.93	0.061	3.16
600°C	1.80	0.001	3.25

In Figure 4.20 plots of the values of $(aE)^2$ versus E are presented for as-deposited and annealed (at 400 and 600°C) ZnO films, where the linear part of the plot is extrapolated to $(aE)^2 = 0$, to intersect the E axis. The value of E at this point defines the optical band gap energy, E_g. As can be seen from Table 4.8, the optical band gap energy was 3.21 eV for as-deposited films whereas, was 3.16 eV and 3.27 eV for 400 and 600°C annealed films.

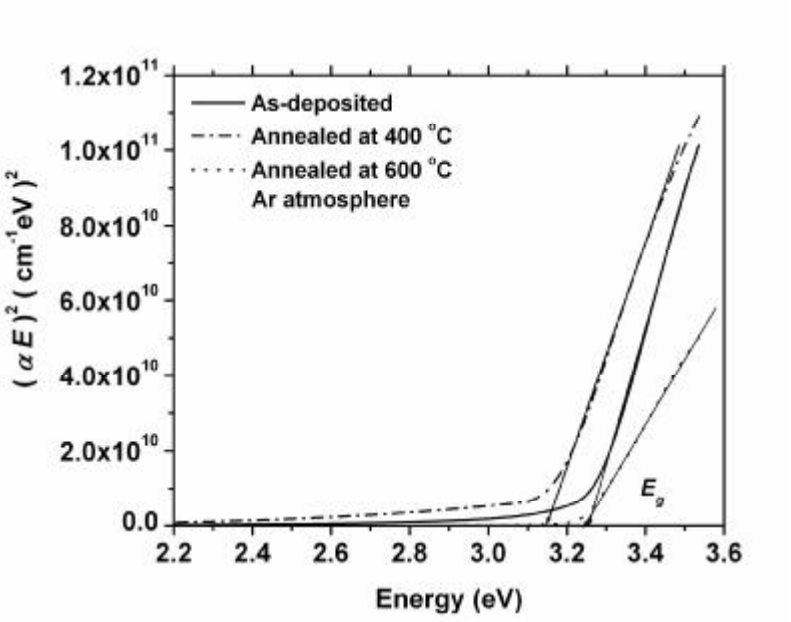

Figure 4.20. Plot of $(\alpha E)^2$ versus E.

4.1.5. Electrical Properties

In Table 4.9, the resistivity of the conducting films, which were deposited with 150 A arc current at on RT and 400°C glass substrates as function of deposition pressure in the range 0.53–0.80 Pa were presented. The resistivity of the films deposited on RT substrates was in the range ~10^{-2}–10^{-1} Ωcm, while that of the films deposited on 400°C substrates was in the range 3.44–12.6 Ωcm. Films annealed at 400 and 600°C were non-conducting ($r > 10^4$ Ωcm).

Table 4.9. Electrical resistivity of ZnO films deposited on RT and 400°C substrates as function of deposition pressure.

Pressure (Pa)	Resistivity (Ωcm)	
	RT	400°C
0.53	1.21×10^{-2}	3.44
0.67	1.80×10^{-1}	12.64
0.80	5.45×10^{-2}	8.35

4.2. SnO_2 Thin Films

SnO_2 thin films were prepared in the FVAD, which was described in the experimental apparatus and procedure section (3.2.1), and the details of deposition conditions were presented in Table (3.1).

4.2.1. Chemical Composition

The composition of the material on the film surface and in the film bulk was determined by XPS. In Table 4.10, the surface compositions of SnO_2 films deposited on RT and 400^oC heated glass substrates as function of deposition pressure in the range 0.53 to 0.80 Pa are presented. As can be seen from the table, the surface of films deposited on RT substrates contained an excess oxygen and carbon, and no correlation was found between deposition conditions and C concentration. The surface composition of films deposited on 400^oC substrates was characterized, however, by a lack of oxygen. The atomic concentration ratios of oxygen to tin (R_{OSn}) in the film bulk is presented in Table 4.11, as function of film temperature and substrate temperature. R_{OSn} of films deposited on RT substrates was higher then 2, i.e. there was an excess of O. The excess oxygen increased as function of deposition pressure. However, R_{OSn} of films deposited on 400^oC heated substrates were closer to 2, i.e. the stoichiometry was improved.

Table 4.10. The chemical surface composition of SnO_2 thin films deposited on RT and 400^oC heated substrates.

	Atomic Concentrations (at.%)					
	SnO_2					
On film surface	RT			400^oC		
Pressure (Pa)	C	O	Sn	C	O	Sn
0.53	30.41	48.21	21.38	14.52	58.78	30.7
0.67	24.59	53.11	22.31	21.04	51.81	27.15
0.80	16.57	55.69	27.74	15.09	55.61	29.3

Table 4.11. The bulk chemical composition of SnO_2 thin films deposited on RT and 400°C substrates.

ROSn		
Oxygen Pressure (Pa)	RT	400°C
0.53	2.04	2.05
0.67	2.08	1.99
0.80	2.09	2.04

In Table 4.12, the surface and bulk compositions of as-deposited and annealed films obtained with higher pressure of 0.93 Pa on UVFS substrates at RT are presented. As can be seen, the surface has oxygen and carbon excess. The bulk of all as-deposited films had relatively marked oxygen excess; independent of the deposition pressure used, however, ROSn decreased with the annealing. ROSn in RT deposited films at 0.93 Pa oxygen pressure was 2.13, higher than the stoichiometric ROSn (2.00). ROSn decreased with the annealing temperature, and was 2.11 and 1.99 in films annealed with 400 and 600°C, respectively. In fact, the annealing at 600°C resulted in stoichiometric films.

Table 4.12. The film bulk chemical composition of as-deposited (RT) and annealed SnO_2 thin films.

	As-deposited	400°C annealed	600°C annealed
O/Sn Atomic ratio (at.%)	2.14	2.11	1.99
C (on surface at.%)	16.57	25.16	21.08
C (in bulk at.%)	0	0	0
Ar annealing for 30 min/ Deposition pressure:0.93 Pa.			

4.2.2. Crystal Structure

In Figures 4.21(a-d), XRD patterns of SnO_2 thin films deposited on RT and 400°C glass substrates at 0.53 and 0.80 Pa deposition pressure are presented, respectively. As can be seen from Figure 4.21(a) and (c), the XRD pattern of films

deposited on RT substrate were amorphous, as all other SnO_2 films deposited on RT substrates were, independent of the oxygen pressure. The XRD pattern contains, in all cases, a contribution from the substrate in a form of a broad band below $2\theta = 40^o$, with a contribution from the film. When the films were deposited on 400°C substrates the SnO_2 films were, however, crystalline, as seen from Figure 4.21(b) and (d). The XRD pattern plots of films deposited at 0.53 Pa oxygen pressure show strong (200) reflection, and also weaker (110), (211) and (321) peaks, superimposed on the substrate wide pattern. The average crystallites size, determined from the width of the (200) line of the tetragonal rutile SnO_2, in films deposited on 400°C substrates at 0.53 Pa and 0.80 Pa was calculated as 12 and 18 nm, respectively.

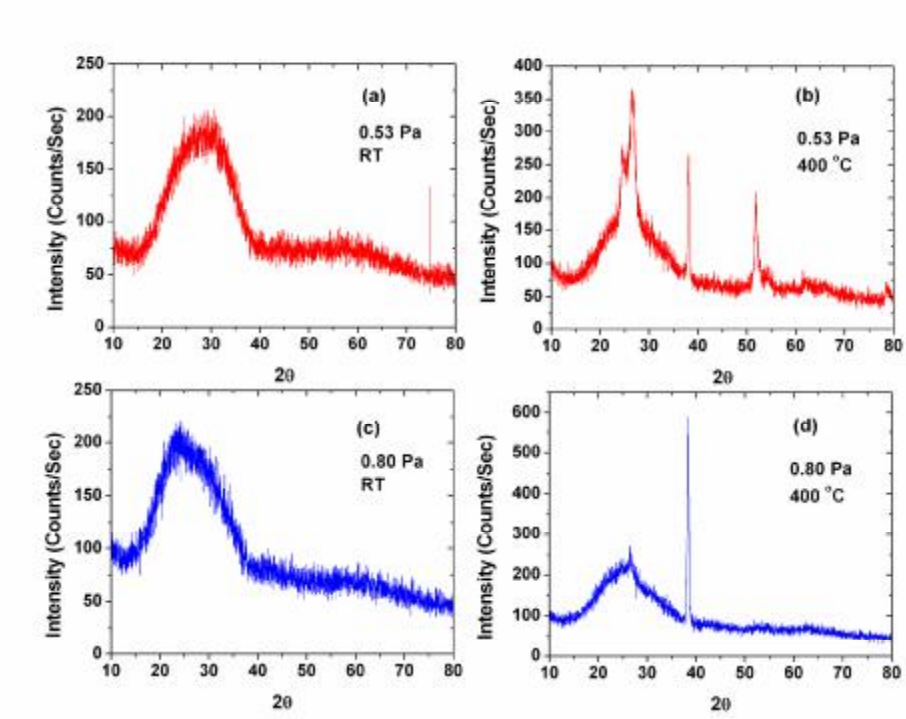

Figure 4.21. XRD patterns of SnO_2 thin films deposited on RT and 400°C substrates at 0.53 and 0.80 Pa oxygen pressure.

In Figures 4.22(a-c), the XRD patterns of SnO_2 thin films are presented of as deposited films and films annealed in Ar for 50 min: (a) 0.67 Pa as-deposited, (b) 0.67 Pa 400°C and (c) 0.67 Pa 600°C. The amorphous band about $2\theta = 21°$ is caused by the UVFS substrate. In Figures 4.23(a-c), similar XRD patterns are presented of SnO_2 thin films deposited on RT UVFS substrates at 0.93 Pa oxygen pressure and later annealed for 50 min

are presented: (a) as-deposited, (b) 400°C and (c) 600°C. All as-deposited RT films were amorphous (as-mentioned above). As Figures 4.22(a-c) and 4.23(a-c) show, polycrystalline tetragonal SnO_2 films were obtained after annealing. The angular positions of Bragg reflections correspond well to the standard XRD pattern of tetragonal SnO_2, and (110), (200), and (211) peaks were observed with a strong (101) peak. The number and the intensity of peaks increased with annealing temperature and also with decreasing deposition pressure number of diffraction peaks increased. Hence, annealing not only resulted in crystalline films, annealing at higher temperature improved the crystallinity.

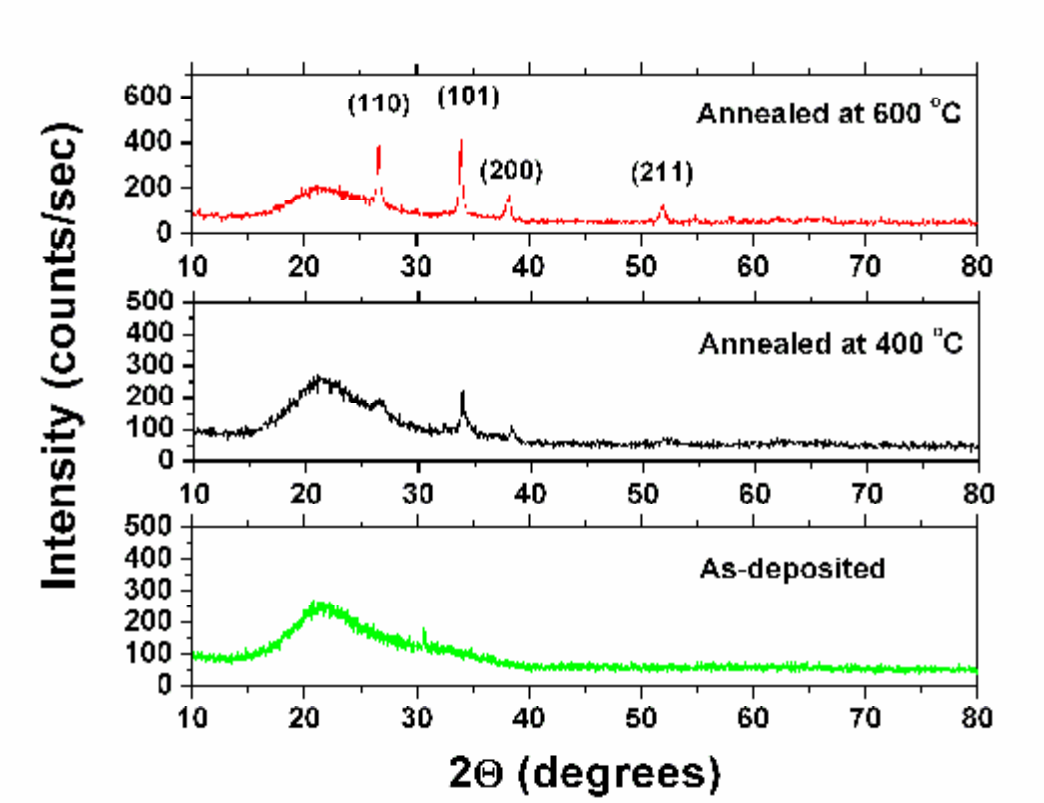

Figure 4.22. XRD patterns of as-deposited, 400 and 600°C annealed SnO_2 films deposited at 0.67 Pa oxygen pressure.

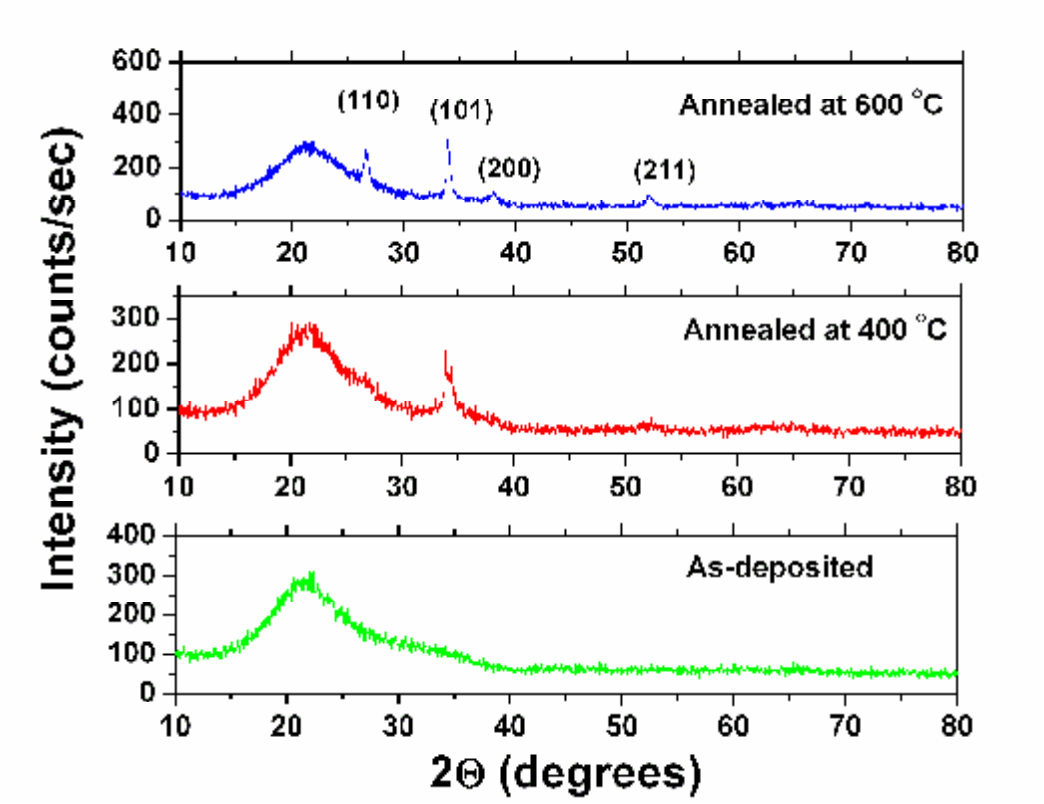

Figure 4.23. XRD patterns of as-deposited, 400 and 600°C annealed SnO_2 films deposited at 0.67 Pa oxygen pressure.

Furthermore, the shape of the diffraction pattern indicates that the films deposited at 0.67 and 0.93 Pa oxygen pressure and annealed at 400°C contain an additional phase besides to SnO_2. The shoulder, appearing near the (101) XRD reflection, indicates the presence of the second phase or the effect of stress in the film. The lattice spacing of this additional phase was 2.642 Å, whereas the standard spacing of (101) is 2.643 Å, and it disappeared when the films were annealed at 600°C.

Table 4.13 presents lattice parameters *a* and *c*, unit cell volume, coherent scattering domain (grain size) size, *D*, for standard SnO_2 powder and the samples deposited at 0.67 Pa and 0.93 Pa oxygen background pressures and annealed at 400 and 600°C in Ar for 50 min. Independent of the deposition pressure, the lattice parameter *a* increased with the annealing temperature, whereas *c* decreased at 600°C annealing when deposited with 0.67 Pa oxygen pressure and increased at 600°C when deposited at 0.93 Pa. With both pressures, the lattice parameters *a* and *c* were close to the standard values at 600°C annealing temperature. Furthermore, as can be seen from Table 4.13, the grain size *D* (derived from Scherer's formula) also increased with annealing temperature from ~8–9 nm to 23–34 nm. As a whole,

the unit cell volume of the deposited SnO_2 increased with annealing temperature, approaching the standard bulk value. Since annealing usually improves the crystal structure, this behavior is rather expected.

Table 4.13. Crystalline characteristics of SnO_2 films calculated from XRD patterns. Grain sizes, lattice parameters and unit cell volume of SnO_2 films calculated from the XRD spectra.

Dep. Pressure (Pa)	Anneal. Temp (°C)	Lattice parameter ***a*** (Å)	Lattice parameter ***c*** (Å)	Unit cell volume ($Å^3$)	Grain Size (nm)
	SnO_2 standard (powder)	4.7382±0.0004	3.1871±0.0001	71.55	-
0.67	400	4.697±0.010	3.196±0.017	70.49	9
0.67	600	4.727±0.006	3.182±0.004	71.09	34
0.93	400	4.706±0.009	3.145±0.009	69.66	8
0.93	600[b]	4.733±0.005	3.176±0.003	71.15	23

4.2.3. Surface Morphology

The surface roughness and surface grain size were measured by AFM. Figures 4.24(a-b) show typical AFM reconstructed images of SnO_2 films deposited at 0.80 Pa oxygen background pressure on microscope glass slides kept at RT and at 400°C. The surface roughness was measured on 0.5×0.5 *m*m regions on the 3D AFM images. The RMS of SnO_2 films deposited on RT and 400°C substrates was 1.5 and 0.5 nm, respectively. The SnO_2 surface roughness decreased with temperature. However, the average surface grain size increased with substrate temperature from 19 to 22 nm.

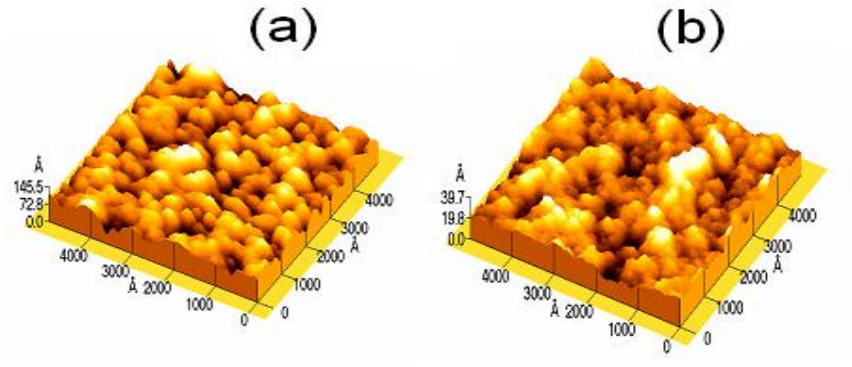

Figure 4.24. AFM images of SnO_2 thin films deposited at 0.80 Pa oxygen pressure on (a) RT, (b) 400^{o}C substrates.

Figures 4.24(a-c) show typical AFM images of the surface of SnO_2 films deposited at 0.93 Pa oxygen background pressure at RT and annealed in Ar at 400 and 600^{o}C. The average surface roughness of as-deposited, 400, and 600^{o}C annealed films were: 0.2, 0.7 and 1.8 nm, respectively. The as-deposited film (Figure 4.25(a)) had a grain size of ~21 nm, and the annealing increased the average grain size (Figure 4.25 (b) and (c)), to 36 nm at 400^{o}C and 46 nm at 600^{o}C.

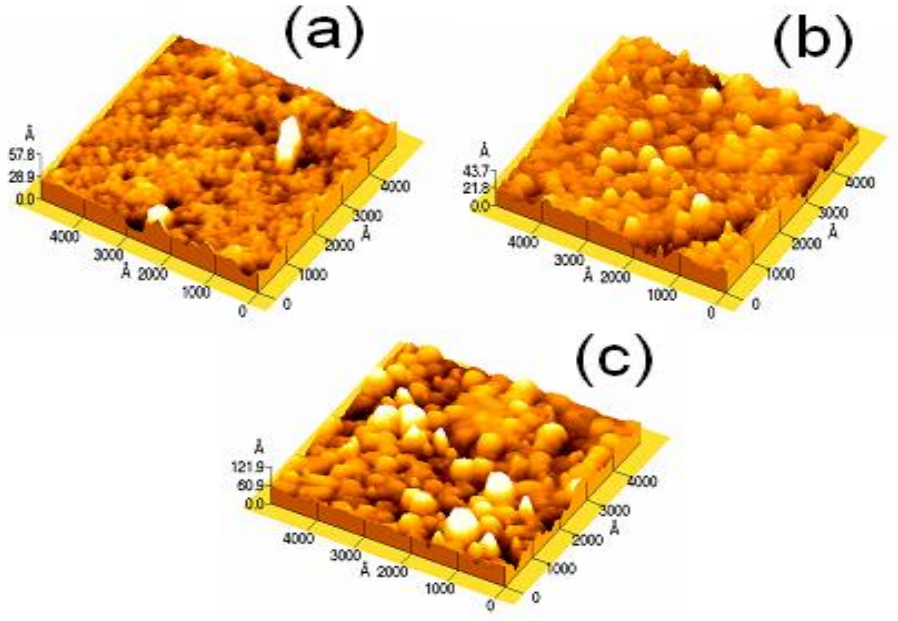

Figure 4.25. AFM images of (a) as-deposited (RT), (b) 400^{o}C annealed, (c) 600^{o}C annealed SnO_2 thin films.

4.2.4. Optical Properties

The optical properties were determined from transmission and *ex situ* variable angle spectroscopic ellipsometry measurements. Figures 4.26(a) and (b) show typically measured and model fitted Ψ and Δ curves of a SnO_2 film deposited at 0.67 Pa background oxygen pressure on RT substrates. The MSE of the fit was 7.3 for the data were measured at 60^o 65^o and 70^o incident angles. The MSE values in fitting Ψ and Δ for all films were in the range 7–24. Lower MSE values, i.e., better fitting, were obtained when the films were deposited on heated substrates.

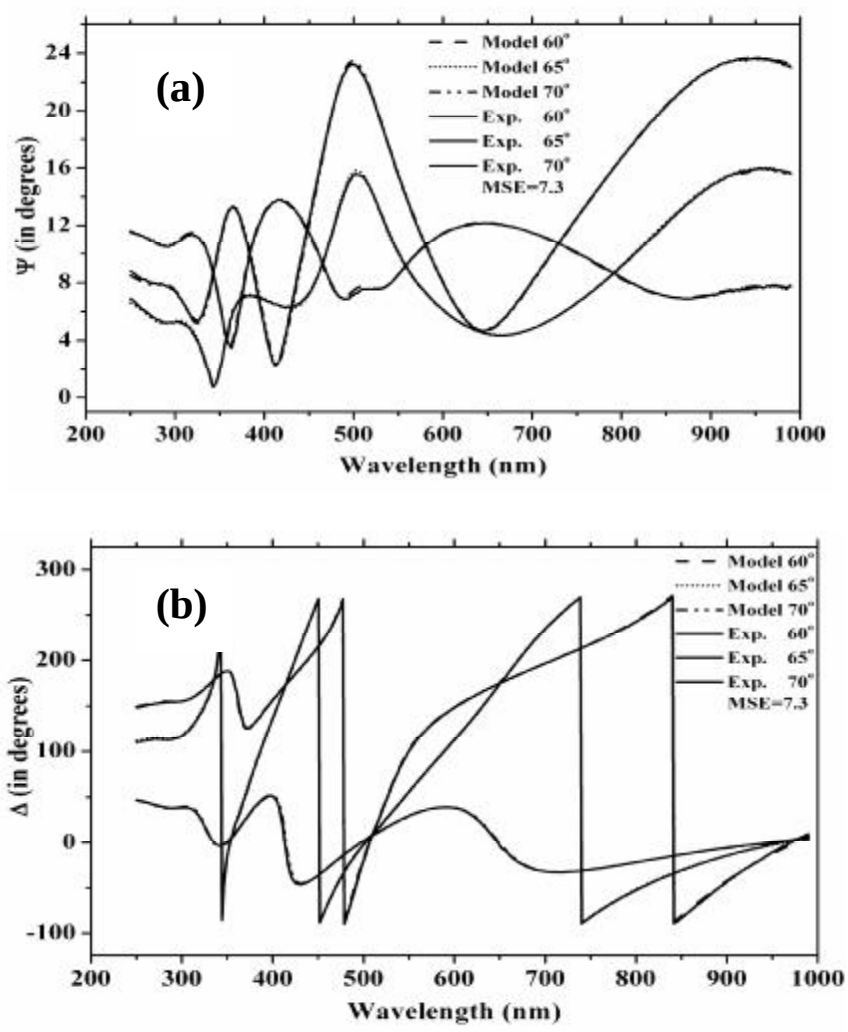

Figure 4.26. Measured: (a) Ψ, (b) Δ data and model fits for a SnO_2 sample deposited at 0.67 Pa oxygen pressure and RT.

The film thickness was also found from the fit of the spectroscopic ellipsometry data, and was in the range 100–363 nm depending on the deposition pressure and deposition duration, which was 90 s. Within the measurement error (~0.5%), the thickness of SnO_2 thin films deposited on heated substrates was equal to that of films deposited on RT substrates.

In Figures 4.27(a-b) plots of the optical transmittance versus wavelength (200–1100 nm) of and SnO_2 films deposited at 0.53 Pa and 0.80 Pa on RT and 400°C UVFS substrates for 120 s are presented. As the thickness of these films is practically the same in each figure, the variations in the interference patterns seen at the VIS region in the plot for SnO_2 in Figure 4.27(b), reflect the effects of the index of refraction (*n*) variations, as no significant difference in the average transmission was observed for films deposited with 0.80 Pa pressure compare to that of films deposited at lower deposition pressures.

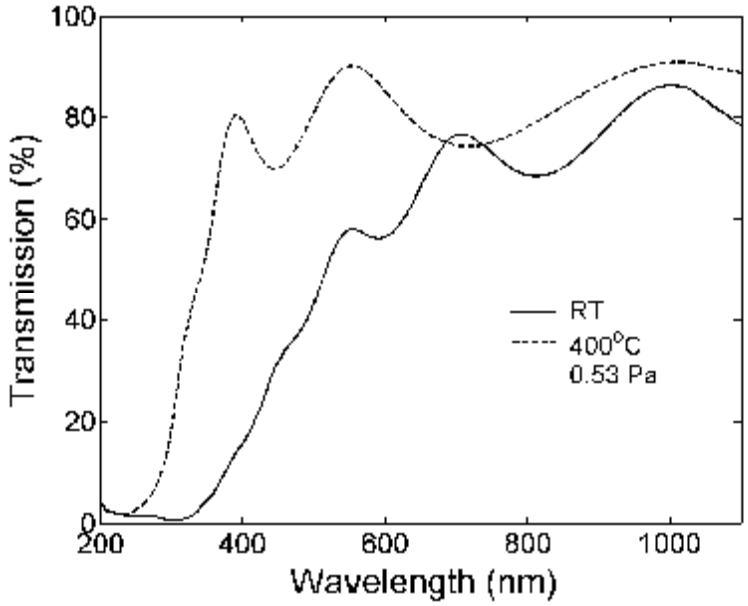

Figure 4.27(a). Plots of the optical transmission of SnO_2 thin films deposited at 0.53 Pa pressure on RT and 400°C substrates versus wavelength.

The transmission plots of SnO_2 thin films deposited on RT and 400°C substrates are markedly different; indicating a significant effect of substrate heating

on the SnO_2 film transmission. As shown in Figure 4.27(a), the transmission of the RT deposited film (0.53 Pa) decreases continuously for $\lambda \leq 550$ nm, reaching ~0 at 310 nm, whereas the transmission of the film deposited on RT substrates at 0.80 Pa (Figure 4.27(b)) starts to decreases at λ ~390, forming a steep transmission edge up to ~290 nm. In contrast, the transmission plots of the films deposited on 400°C substrates, at both 0.53 and 0.8 Pa, has sharp and well defined absorption edges. When deposited at 0.53 Pa, the average optical transmission of the film deposited on RT substrate is much lower than that of film deposited on 400°C substrate. In contrast, the form of the transmission curves of SnO_2 films deposited with 0.80 Pa on RT and hot substrates (Fig. 4.27(a)) was similar, where both curves had a sharp edge of the transmission starting at 390 nm, and an average transmission of 85% in the VIS.

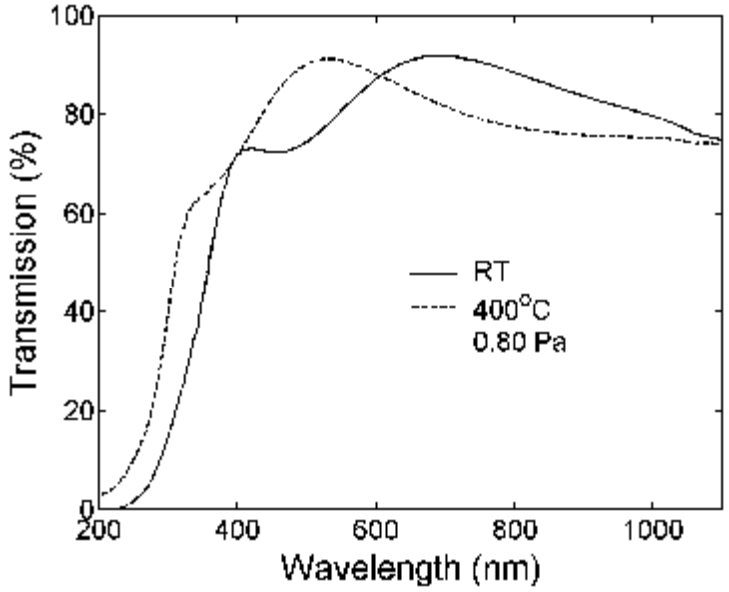

Figure 4.27(b). Plots of the optical transmission of SnO_2 thin films deposited at 0.80 Pa on RT and 400°C substrates versus wavelength.

Plots of the refractive index *n* and extinction coefficients *k* of SnO_2 films deposited with 0.67 and 0.80 Pa oxygen pressure on RT and 400°C substrates are presented in Figs. 4.28(a) and (b), respectively. In the wavelength range 300 to 1000 nm, the refractive index decreased with increasing wavelength from a peak value of 2.2 to 1.88 and from 2.28 to 1.87 for films deposited at 0.67 and 0.8 Pa, respectively.

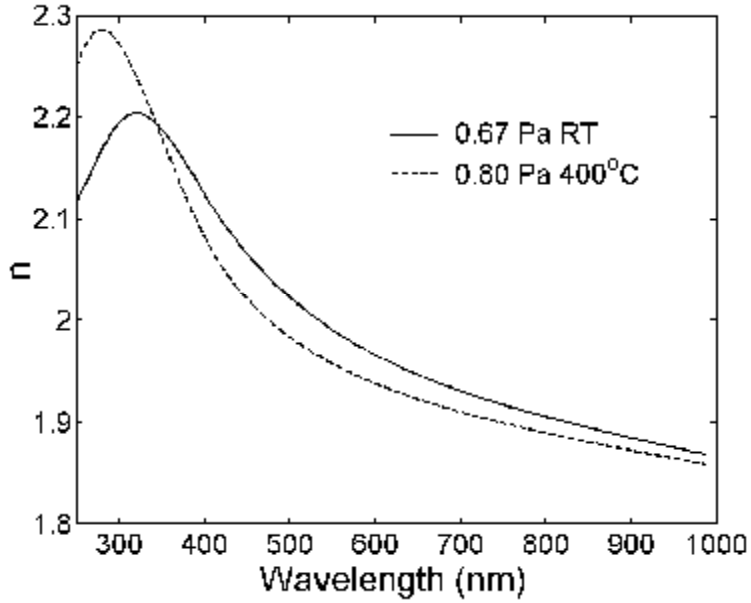

Figure 4.28(a). Plots of the refractive indexes of SnO_2 thin films deposited on RT and 400°C substrates versus wavelength.

The extinction coefficient *k*, also decreased with wavelength from 0.50 at 250 nm to approximately 0.02 at 550 nm, and then to close to zero above 700 nm. As the energy band gap of SnO_2 is much larger than that of ZnO, the Tauc-Lorentz minimum in *k* could not be seen above 250 nm. The general dependence of the optical parameters on wavelength is similar for films deposited on heated substrates; however, the deposition on hot substrate had a significant effect on the values of *n* and *k* of the SnO_2 films. The value *n* was lower when deposited on hot substrates at pressures larger than 0.67 Pa. In addition, the value of *k* also decreased, but the change of *k* was less affected by substrate temperature compare to that of *n*.

In addition, in Table 4.14, the refractive index and the extinction coefficients of the same films at 550 nm are listed as functions of the deposition pressure and substrate temperature. The values of *n*(550 nm) of SnO_2 films deposited on RT substrates were in the range 1.87–1.99, and the values of *k* were in the range 0.01–0.02. The values of *n*(550) of films deposited on 400°C substrates were in the range 1.87–1.97, and *k* was 0.01. No correlation with the pressure was observed in both cases for *n*(550 nm)

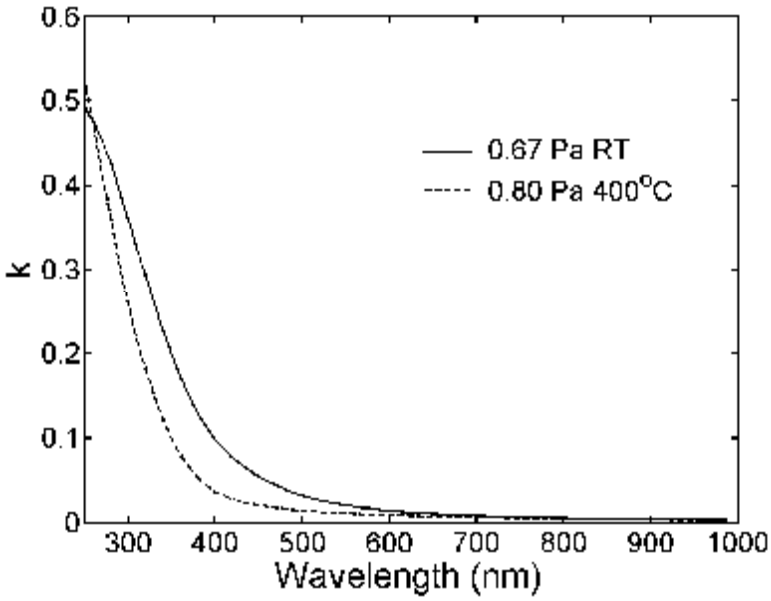

Figure 4.28(b). Plots of the extinction coefficient of SnO_2 thin films deposited on RT and 400°C substrates .

In Table 4.14, the values of the optical band gap are also listed. The optical band gap of the SnO_2 films increased with both deposition pressure and substrate temperature, reaching 3.98 eV at 0.80 Pa and 400 °C.

Table 4.14. Optical properties of SnO_2 thin films deposited on RT and 400°C substrates.

	T_s = RT			T_s = 400 °C		
Pressure (Pa)	*n*	*k*	E_g(eV)	*n*	*k*	E_g(eV)
0.53	1.87	0.010	3.60	1.97	0.010	3.95
0.67	1.99	0.020	3.76	1.87	0.010	3.82
0.80	1.93	0.010	3.90	1.96	0.010	3.98

Typical plots of the transmission of SnO_2 films, as-deposited and annealed are presented in Fig. 4.29. The transmission edge shifted to shorter wavelengths (i.e. to higher photon energy) after the annealing. At longer wavelengths, e.g., in the VIS, no significant dependence of peak or minimal transmission on annealing temperature was observed. The average transmission in the visible spectrum was 85-90%,

independent of annealing temperature and deposition pressure (not shown here). The most marked effect of annealing temperature was on the transmission edge of the SnO_2 films. Furthermore, when as-deposited films had a brownish tint it disappeared after annealing in Ar.

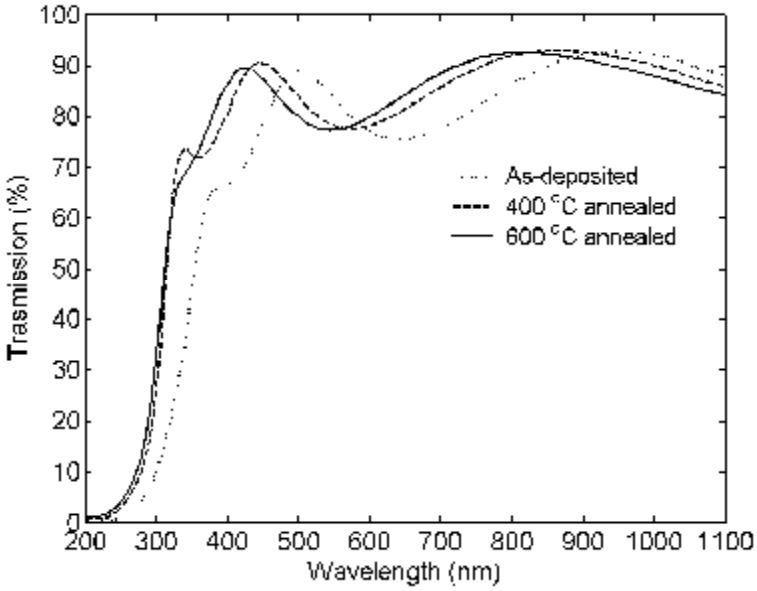

Figure 4.29. Optical Transmission plots of as-deposited (RT) and annealed SnO_2 thin films.

In Figures 4.30 and 4.31, the refractive index and the extinction coefficients of SnO_2 thin films deposited on UVFS substrates at RT with 0.93 Pa pressure and annealed at 400 and 600^oC for 50 min in Ar are presented. In Fig. 4.30, the refractive index *n* decreased with increasing wavelength from approximately 2.3 to 1.85. In addition, below 380 nm the annealing decreased *n* relative to that of as deposited, but there was no significant difference between *n* of films annealed at 400 and 600^oC in the studied wavelength range. The *n* peak of the annealed films, however, was at a shorter wavelength than that of the as-deposited film.

In Figure 4.31, similar dependence on wavelength and annealing temperature is shown for *k*. The *k* values decreased from 0.5 at 250 nm to approximately 0.05 at 390 nm, and then to zero at longer wavelengths. The decrease in *k* seen below 390 nm for annealed samples is very sharp, and *k* was independent of the annealing temperature. In Table 4.15, *n* and *k* at 550 nm and the optical energy band gap values

for SnO_2 thin films are listed. The values of n for SnO_2 thin films deposited at 0.67 and 0.93 Pa at RT were in the range 1.94–1.96 and for films annealed at 400 and 600^oC were in the range 1.90–1.91. The values of k were in the range 0.009–0.010, and significantly decreased at λ<400 nm. The calculated MSE (7–13) was smaller than that of Isidorsson *et al.* (1998), who reported MSE in the range 19–33 for optical fitting of dispersion parameters using a parametric semiconductor model with Lorentz and Gaussian functions for as-deposited films. The surface roughness of films is also determined from spectroscopic ellipsometry analyses and are presented in Table 4.15 (0.7–0.9 nm) and decreased approximately to zero after annealing.

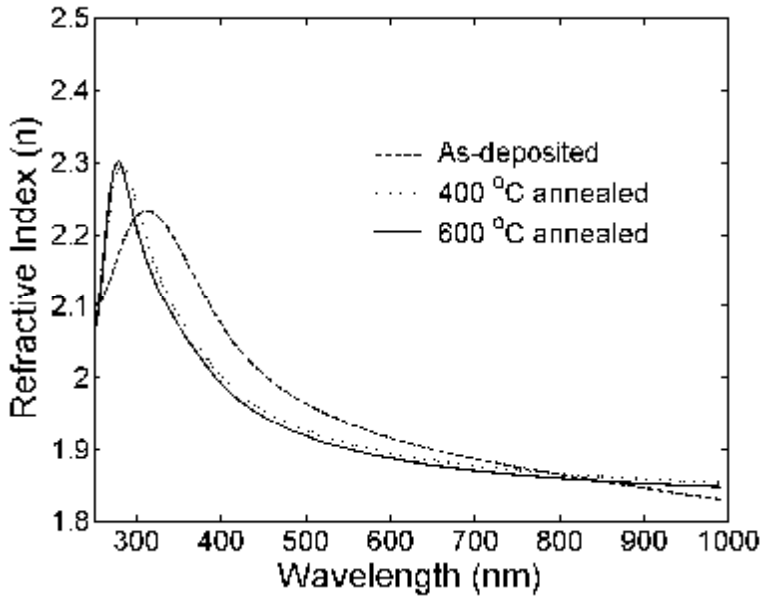

Figure 4.30. Plots of the refractive index of SnO_2 thin films versus wavelength.

Table 4.15. Optical constants, n and k, at 550 nm, and the optical band gap E_g for as-deposited and annealed SnO_2 thin films.

SnO_2				
	Surface Roughness($_{Ellipso}$) (nm)	n	k	E_g(eV)
As-deposited [a]	0.9	1.94	0.009	3.90
400^oC [a]	0.2	1.91	0.009	4.25
600^oC [a]	0.1	1.90	0.009	4.35
As-deposited [b]	0.7	1.96	0.010	3.90
600^oC [b]	0.1	1.91	0.009	4.20
Annealing in Ar for 30 min /Films deposited at [a] 0.93 Pa and [b] 0.67 Pa				

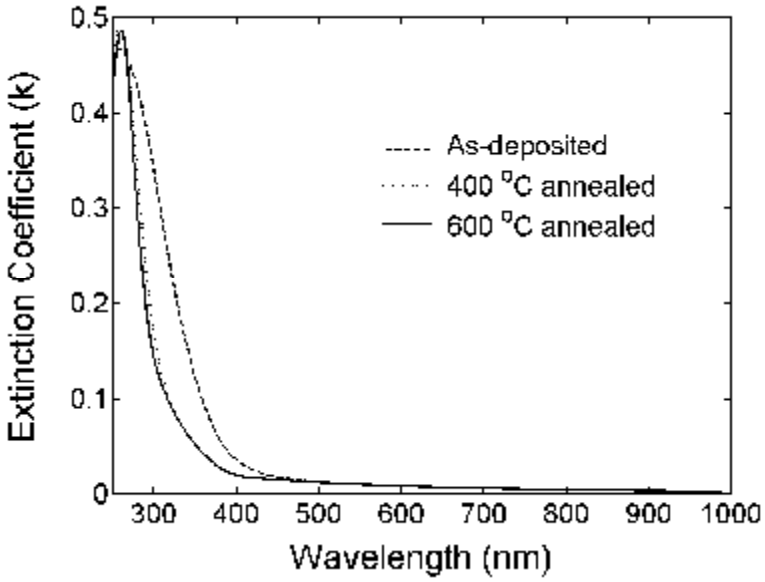

Figure 4.31. Plots of the extinction coefficient of SnO_2 thin films versus wavelength.

In Figure 4.32, the plots of $(aE)^2$ versus E are presented, where the straight line portion of the absorption spectrum is extrapolated to $(a\ E)^2 = 0$, to determine the value of E_g. As can be seen in Table 4.15, annealing increased E_g from 3.90 eV to 4.35 eV. The larger value of E_g of the annealed films correlates well with the transition to crystallinity by annealing.

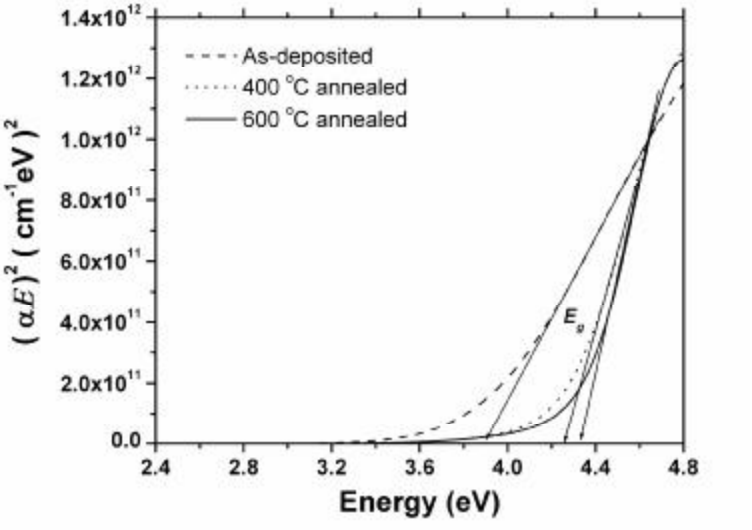

Figure 4.32. Plots of $(\alpha E)^2$ versus E

4.2.5. Electrical Properties

Table 4.16 presents the resistivity of the films, deposited at RT and 400°C, and at deposition pressures of 0.53, 0.67 and 0.80 Pa., The resistivity of films deposited on RT substrates was in the range ~10^{-3}–10^{-2} Ωcm, and 6.61×10^{-3}–1.18×10^{-1} Ωcm if deposited on 400°C. Films annealed at 400 and 600°C were non-conducting (>10^{5} Ωcm)

Table 4.16. Electrical resistivity of SnO_2 films deposited on RT and 400°C substrates as a function of deposition pressure.

Pressure (Pa)	Resistivity (Ωcm)	
	RT	400°C
0.53	$6.70\text{x}10^{-3}$	$1.18\text{x}10^{-1}$
0.67	$8.16\text{x}10^{-3}$	$1.34\text{x}10^{-2}$
0.80	$9.08\text{x}10^{-3}$	$6.61\text{x}10^{-3}$

4.3. ZnO-SnO_2 Thin Films

ZnO-SnO_2 thin films were prepared by the FVAD, which was described in the experimental apparatus and procedure section (3.2.1), and the details of deposition conditions were presented in Table (3.1). As was mentioned above, ZnO films doped with Sn are labeled in this work as ZnO-SnO_2, however, films whose Zn:Sn:O ratio was close to 2:1:4 (Zn_2SnO_4) or 1:1:3 ($ZnSnO_3$) are labeled “zinc stannate”.

4.3.1. Chemical Composition

The elemental composition of ZnO-SnO_2 and zinc stannate thin films was determined by XPS and EDS analyses, as function of the various deposition

conditions, as presented below. The atomic concentration ratio of Zn to Sn when determined for films deposited using a 30at.% Sn cathode at 300 A arc current and 0.53 Pa oxygen pressure for 60 s, was found to have atomic concentrations of 49.4% O, 45.5% Zn, and 5.1% Sn. The atomic concentrations of films deposited using 10at.%, 30at.% and 50at.% Sn cathode compositions with 250 A arc current at 0.80 Pa pressure is presented in Table 4.17 as function of these parameters.

Table 4.17. The atomic ratio of Zn:Sn in the films as function of cathode composition.

Deposition Conditions	Zn(at.%)	Sn(at.%)	O(at.%)
10 at.%	44.7	4.7	50.6
30 at.%	43.9	3.8	52.3
50 at.%	33.9	10.6	55.5

The XPS data in Table 4.17 indicate that films deposited using cathodes with Zn:Sn ratio of 9:1 and 7:3 are actually ZnO films doped with 5at.% and 4at.% Sn, respectively. However, when Sn concentration was increased in the cathode to 50at.%, a material close in composition ratio to Zn_2SnO_4 was deposited (3.1:1:5.2), however with excess of Zn and O.

Table 4.18. The atomic ratio of Zn:Sn in the films as function of deposition pressure and substrate temperature.

Pressure (Pa)	**[Zn]/[Zn]+[Sn] (at.%)**		
	RT	**200^{o}C**	**400^{o}C**
0.53	0.74	0.48	0.50
0.67	0.54	0.56	0.55
0.80	0.49	0.51	0.58
0.93	0.46	0.47	0.48
1.06	0.45	0.46	0.47

The Zn to Sn ratio in films was also determined using EDS as function of the deposition pressure. In Table 4.18, the composition of zinc stannate thin films deposited using 150 A arc current, 60 s deposition time, with an oxygen background pressure in the range 0.53 to 1.06 Pa on RT, 200^{o}C, and 400^{o}C heated glass substrates using a 1:1 Zn:Sn cathode, are presented. As can be seen from the table, the relative Zn atomic concentration ratio, [Zn]/[Zn]+[Sn], varied with the deposition pressure. This relative ratio was in the range 0.45-0.58 for oxygen pressure >0.53 Pa, however, for the 0.53 Pa RT case, the ratio was 0.74. The composition of films deposited at 0.53 Pa at RT was further confirmed by XPS analysis and was similar to that of EDS. Increasing the substrate temperature did not have significant effect on the composition for pressure >0.53 Pa, however, increasing the deposition pressure decreased the Zn atomic concentration in RT deposited films, whereas, the composition of films deposited on 200^{o}C and 400^{o}C substrates was not affected by the deposition pressure, only showing some small oscillations in the composition.

4.3.2. Crystal Structure

Figure 4.33 shows X-ray diffraction patterns for ZnO-SnO_2 and zinc stannate thin films deposited on RT kept glass substrates with Zn:Sn cathodes having 10 at%, 30at.% and 50at.% Sn, at 250 A for 60 s at 0.79 Pa oxygen pressure. As can be seen from the diffraction patterns, a broad band at 2θ in the range 25–30° and no diffraction line feature indicates that all of these films were amorphous. Similar XRD data were obtained for all other ZnO-SnO_2 and zinc stannate thin films deposited using different cathode compositions as function of deposition pressures.

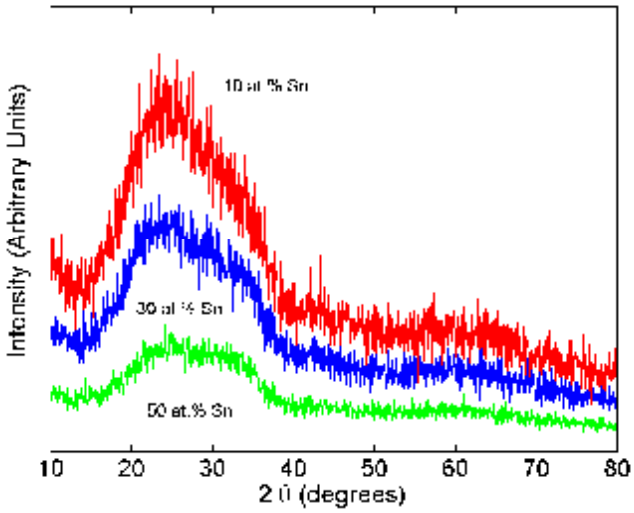

Figure 4.33. XRD results of ZnO-SnO_2 and zinc stannate thin films deposited with different cathode compositions at room temperature.

In Figures 4.34 and 4.35, the XRD diffraction patterns of zinc stannate thin films deposited with 150 A arc current at 0.53, 0.80 and 1.06 Pa oxygen pressures on RT kept glass substrates, and 150 A arc current at 0.67 Pa oxygen pressure on RT and 400^{o}C heated glass substrates for 60 s deposition duration are presented. All of these deposited films were also amorphous independent of deposition pressure and substrate temperature.

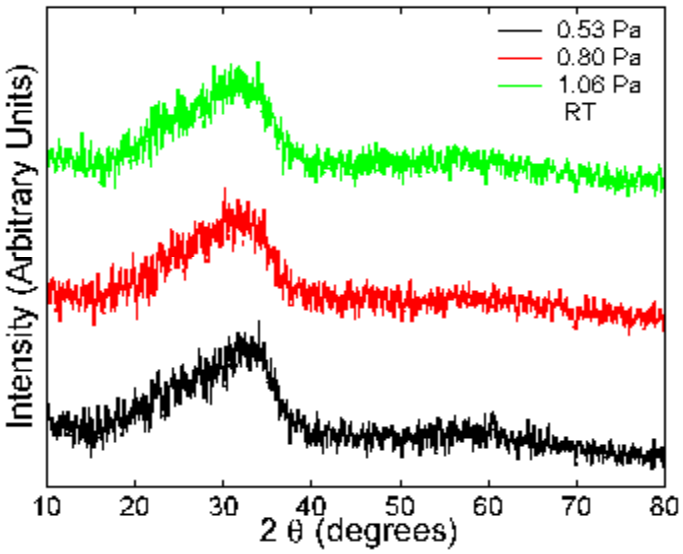

Figure 4.34. XRD results of zinc stannate thin films deposited with different oxygen pressures on RT substrates.

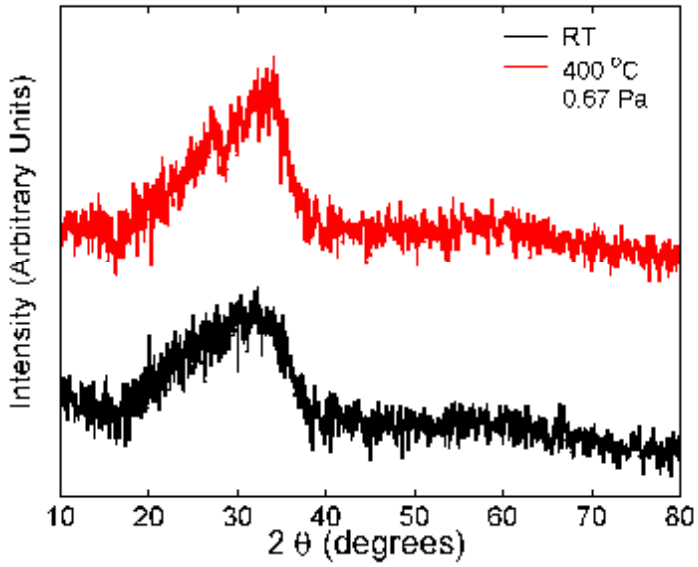

Figure 4.35. XRD results of zinc stannate thin films deposited on RT and 400°C substrates.

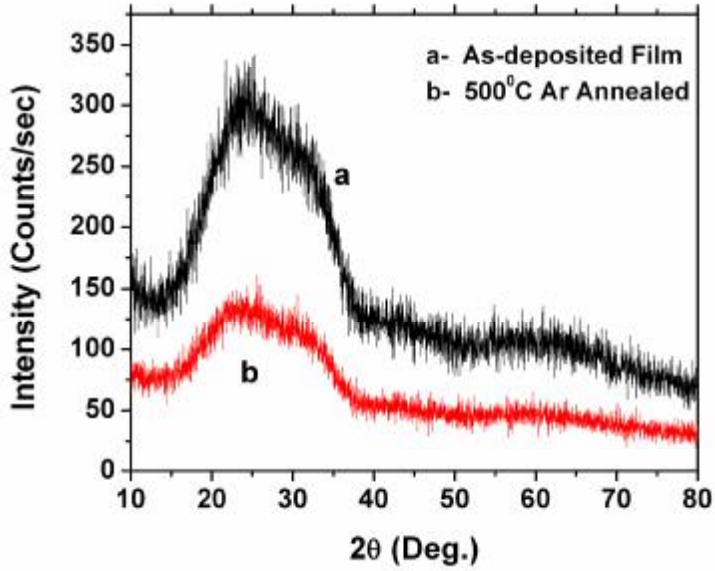

Figure 4.36. XRD patterns of as-deposited (400°C), and 500°C annealed zinc stannate thin films.

In Figure 4.36, XRD diffraction patterns of as-deposited zinc stannate thin films deposited on 400°C heated glass substrate using 150 A arc current at 0.93 Pa pressure for 60 s, and annealed at 500°C in Ar are presented as an example. The amorphous band between 25° and 35° is associated with the glass substrate. All as-deposited films were amorphous, independent of the deposition pressure and substrate temperature. As can be seen in Figure

4.36, the structure of films did not changed after annealing at 500°C in Ar. The films annealed at 600°C cracked, preventing XRD analyses.

4.3.3. Surface Morphology

Figures 4.37(a-c), 4.38(a-c), and 4.39(a-c) show typical surface images of zinc stannate thin films deposited using 150 A arc current at 0.53 Pa, 0.80 Pa and 1.06 Pa oxygen background pressure on RT, 200°C and 400°C glass microscope slides for 60 s, respectively.

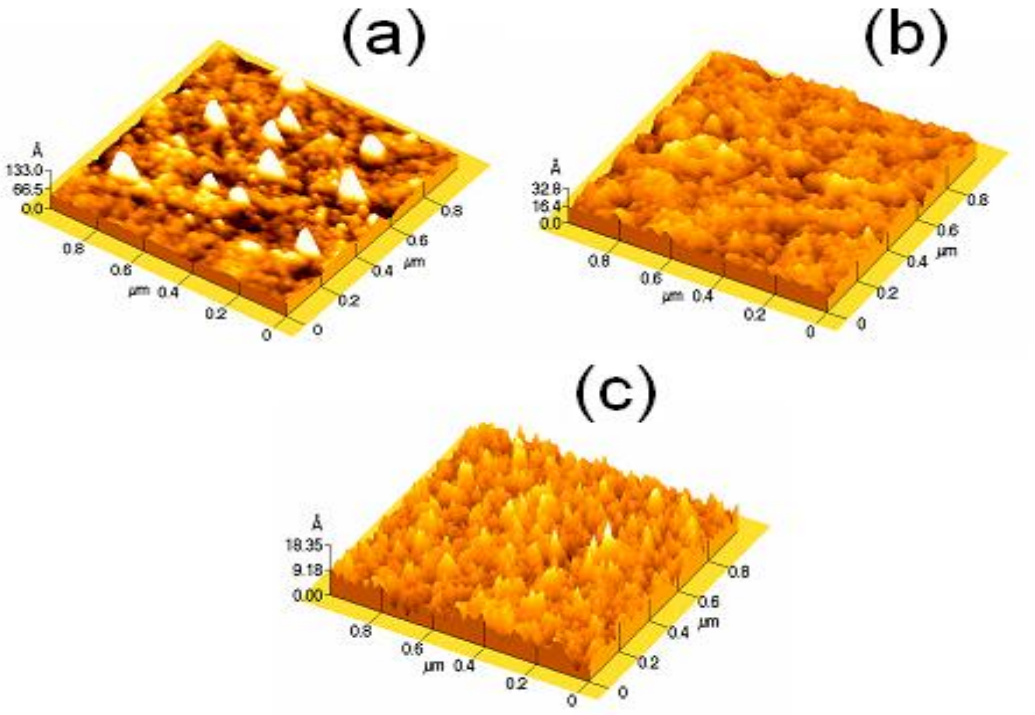

Figure 4.37. AFM images of zinc stannate thin films deposited at 0.53 Pa oxygen pressure on (a) RT, (b) 200°C and (c) 400°C substrates.

The RMS roughness of the samples was in the range 0.2–0.8 nm and grain diameters were in the range 15-20 nm. The surface morphology of samples deposited at 0.53 Pa at RT and 0.80 Pa at 200°C contained particularly big grain size features, which were later excluded in the calculation of the average surface roughness. The

surface morphology for films deposited on 400°C heated substrates at pressure below 0.80 Pa is characterized by having sharp peaks, however, no similar big features, as mentioned above, were observed on these films. It should be noted, that the films deposited at 400°C substrate temperature appeared to be smoother than the films deposited at RT. In general, films deposited at 1.06 Pa pressure were smoother than films deposited lower pressures at all substrate temperatures.

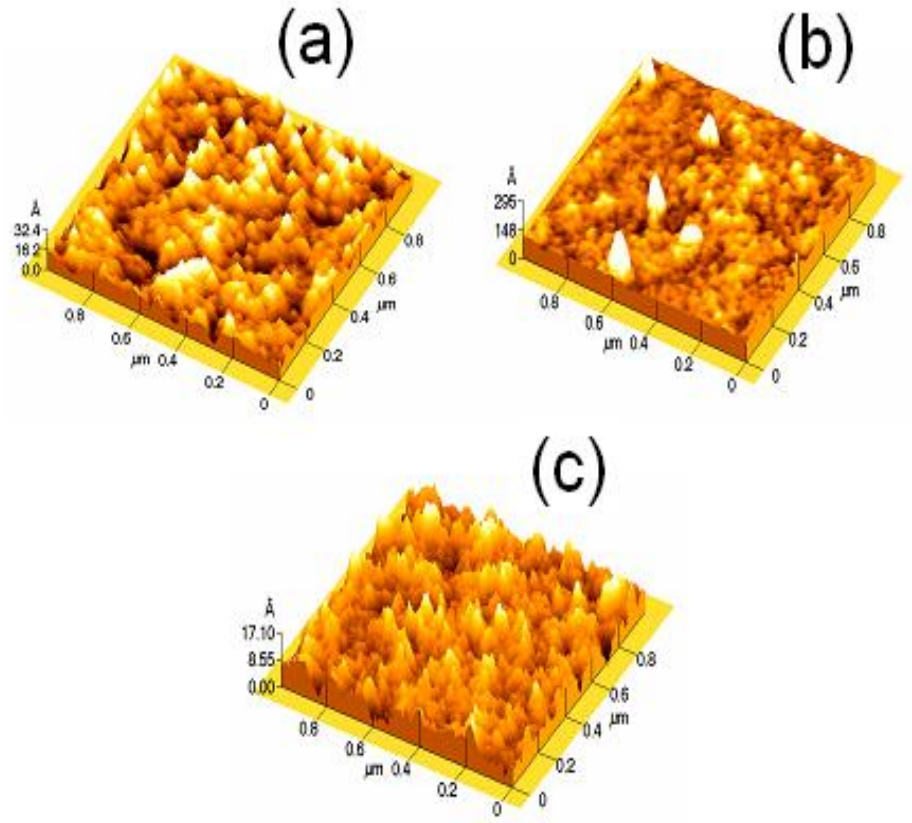

Figure 4.38. AFM images of zinc stannate thin films deposited at 0.80 Pa oxygen pressure on (a) RT, (b) 200°C and (c) 400°C substrates.

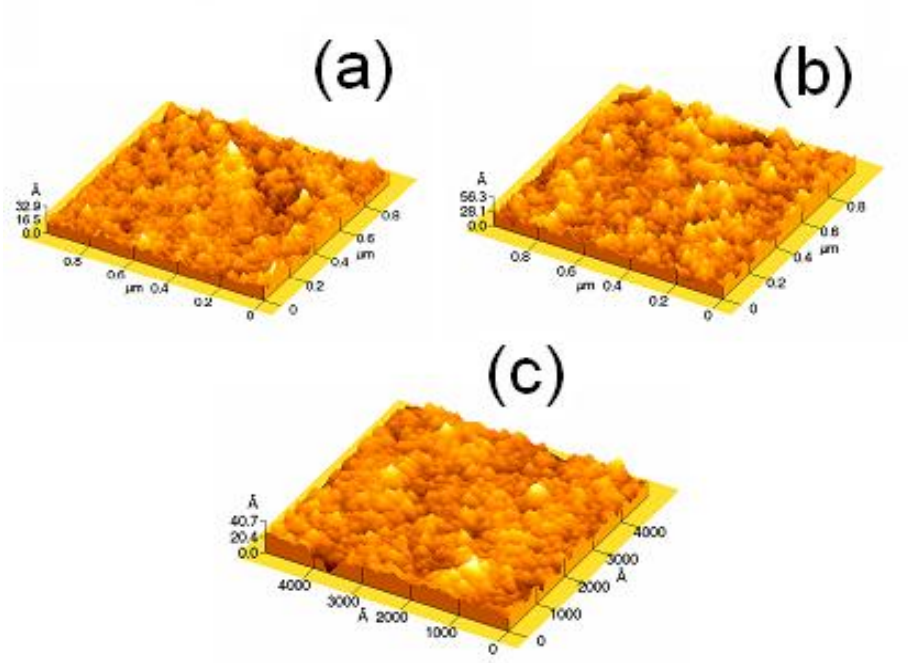

Figure 4.39. AFM images of zinc stannate thin films deposited at 1.06 Pa oxygen pressure on (a) RT, (b) 200°C and (c) 400°C substrates.

4.3.4. Film Thickness

The film thickness was derived from optical analyses of the spectroscopic transmission and spectroscopic ellipsometry measurements, as one of the fitting parameters. As is shown below, the film thickness (*d*) depended on the deposition parameters: arc current, background oxygen pressure, and deposition time. Two sets of *d* values of films deposited using 30at.% Zn:Sn cathode at 300 A at the pressure range 0.53-1.06 Pa, for 60 and 120 s deposition time, are listed in Table 4.19 for films deposited with 300 A. The data indicate a strong decrease of *d* with deposition pressure. The difference between the calculated thickness (d_{cal}) and the measured thickness (d_{mea}) was 1% for films deposited at 1.06 Pa, but reached 25% for films deposited at 0.80 Pa. It could be resulted from the surface roughness of films in which bigger grains could have affect on the measurements. It should also be noted that the thickness is approximately proportional to the deposition time.

Table 4.19. Measured (d_{mea}) and fitted (d_{cal}) film thickness for films deposited by 30at.% Zn:Sn cathode with 300 A, 60, 120 s, and 0.53 -1.06 Pa.

Iarc(A)	Oxygen Pressure (mTorr)	Dep. Time 60s		Dep. Time 120s	
		d_{cal} (nm)	d_{mea} (nm)	d_{cal} (nm)	d_{mea} (nm)
300	0.53	462	394	919	819
300	0.67	389	372	782	691
300	0.80	346	261	629	534
300	0.93	254	218	437	396
300	1.06	167	169	297	306

In Figure 4.40, the dependence of the average calculated film thickness, [(d_{60} + d_{120})/2], as function of arc current and deposition pressure for 30at.% Sn cathode deposited on RT glass substrate is presented. The average deposition rate was derived from the calculated thicknesses, using the formula (d_{60}/60+d_{120}/120)/2. The highest average deposition rate was 7.6 nm/s for ZnO-SnO_2 thin films deposited with 300 A arc current at 0.53 Pa pressure, decreasing with pressure to 2.63 nm/s at 1.06 Pa, at 300 A arc current.

In Fig. 4.41, film thickness, derived from optical analysis, as described in the section literature survey section (3.3.6), is presented as function of deposition pressure. The cathode composition is given as a parameter in the figure. The films were deposited on RT glass substrate for 60 s deposition time at 250 A arc current. As can be seen from the Figure 4.41, the thickness of the films decreased with increasing pressure and also with decreasing Sn concentration. The thickness of films deposited at 0.53 Pa deposition pressure using 30at.% and 50at.% Sn cathodes was 400 nm, implying, a high deposition rate of about 7 nm/s. There was a rather significant dependence of the growth rate on pressure, arc current and cathode composition. It should also be noted that the optical transmission depended on arc pressure and arc current, due to their effects on the thickness, as film absorption increases with thickness.

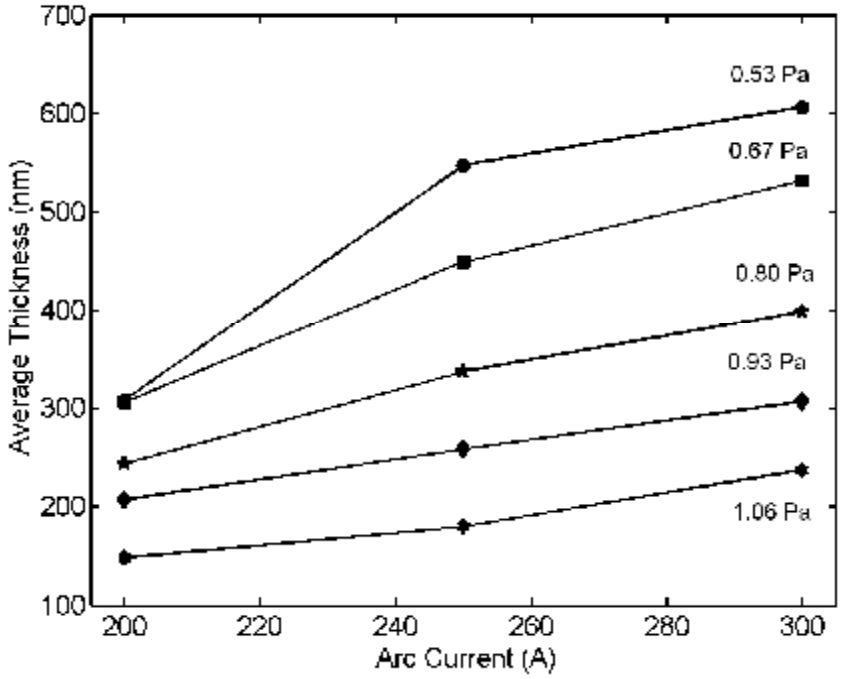

Figure 4.40. Plots of film average thickness as function of arc current and deposition pressure.

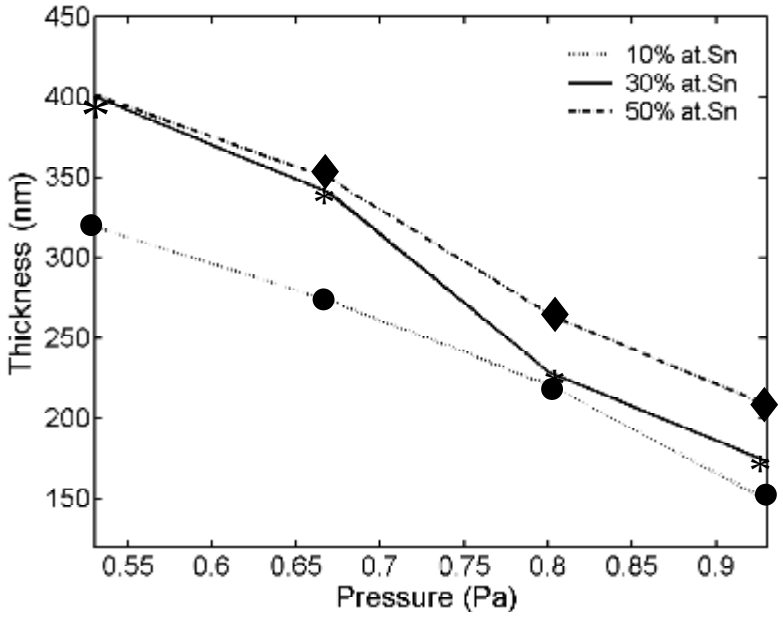

Figure 4.41. Thickness versus arc current plots of $ZnO\text{-}SnO_2$ thin films deposited using different cathode compositions. The symbols indicate the position of measured data. The lines are drawn to aid the eye.

4.3.5. Optical Properties

The results of the optical study are presented by showing typical examples (plots, images and tables) of the dependence of the transmission, spectroscopic ellipsometric data, and the theoretically derived optical constants on various combinations of the deposition and annealing parameters.

In Figures 4.42 and 4.43, plots of the measured optical transmission (T_{exp}) as functions of wavelength in the range 300 to 1100 nm are presented for films deposited on RT kept glass substrates with a 30at.% Sn cathode and 300 A arc current, 120 and 60 s deposition duration, respectively, and oxygen pressure in the range 0.53–1.06 Pa. For wavelength in the range 450–1100 nm, interference effects in the thin film caused T_{exp} to vary between 70% and 90%.

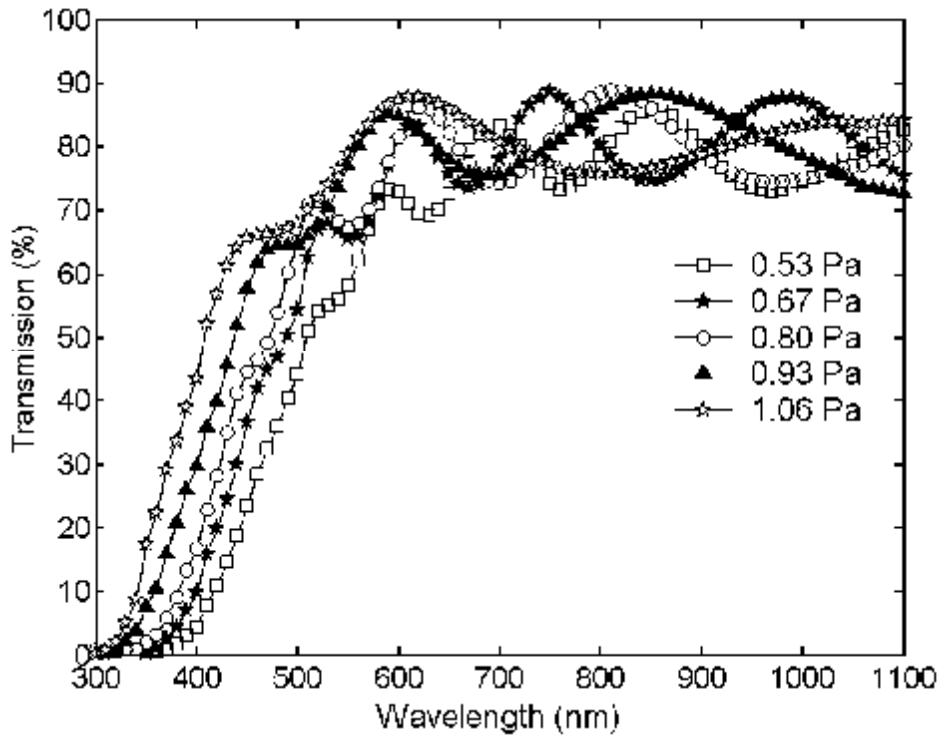

Figure 4.42. The dependence of T_{exp} on wavelength and pressure for films deposited using 30at.% Sn cathode with 300 A arc current for 120 s

As seen, the oscillation of T_{exp} with wavelength depended on the oxygen background pressure, demonstrating the dependence of film thickness and optical parameters on pressure. The measured transmission strongly decreased below 400 nm to an absorption edge, and was close to zero at shorter wavelength. The transition and position of the absorption edge depended on the oxygen pressure, shifting to longer wavelength as the pressure decreased. This absorption edge shift with pressure was observed with all deposition conditions. A sharper absorption edge (the slope of T versus wavelength) is noticed at $\lambda \sim 387$ nm in films deposited at 1.06 Pa oxygen pressure.

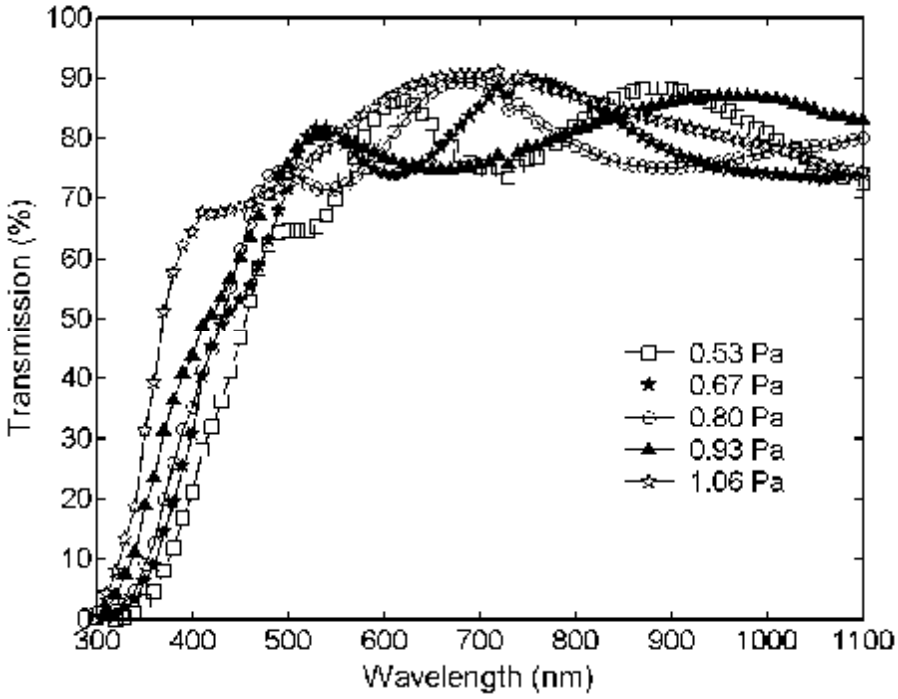

Figure 4.43. The dependence of T_{exp} on wavelength and pressure for films deposited using a 30at.% Sn cathode with 300 A arc current for 60s.

The optical parameters of the films were determined using the normal incidence transmission data analysis that was previously described above in page (11) and also in the experimental apparatus and diagnostics section (3.5.6).

In Figure 4.44, plots of T_{exp} and the fitted transmission T_c are presented as functions of wavelength for a film deposited during 60 s on RT kept glass substrates

using a 30at.% Sn cathode at 300 A arc current, and 0.67 Pa pressure. The standard error of the transmittance fit in the range 350 to 700 nm was below 1% for each studied film.

In Tables 4.20 and 4.21, the dependence of n and k at $\lambda = 500$ nm and the dependence of the parameters e_∞, e_s, w_o and G of the single oscillator model on pressure are presented for films deposited with 30at.% Sn cathode at 300 A arc current for 60 and 120 s deposition duration, respectively. The model of single oscillator parameters e_∞, e_s, w_o and G are presented in the literature survey section (2.39).

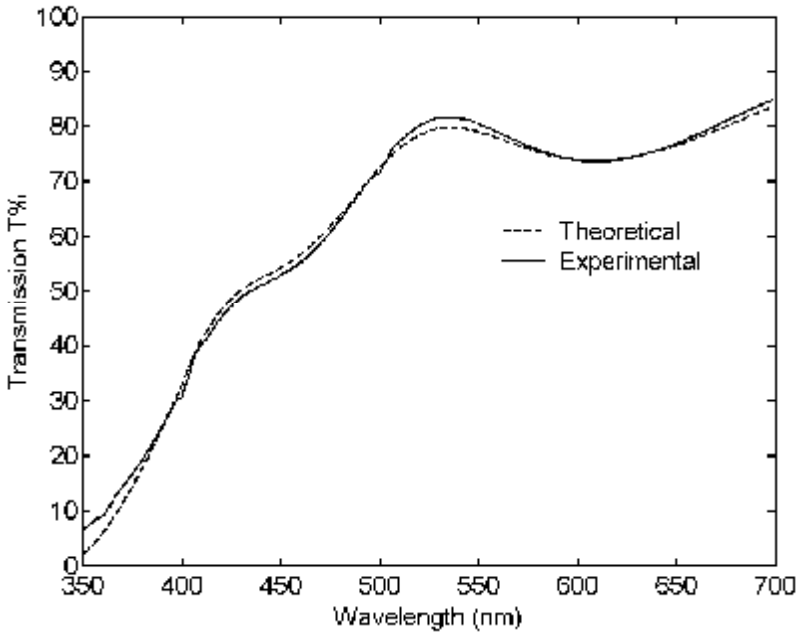

Figure 4.44. Plots of T_{exp} (experimental) and T_c (calculated) as function of wavelength for film deposited using 30at.% Sn cathode at 300 A arc current, 0.67 Pa for 60 s.

The dependence of n on pressure differed with deposition time. When the deposition time was 60 s, n did not vary significantly with the deposition pressure. However, for 120 s deposition time, n increased significantly with pressure where the correlation coefficient between n and the deposition pressure was 0.996. On the other hand k did not depend significantly on pressure, neither at 60 s nor at 120 s deposition times. There is no established explanation of the effect of deposition time

on *n*, however, it could be correlated with higher film temperature reached during longer deposition time, or different film organization in the thicker films. It is seen in the tables that the parameters $e_{¥}$ and e_s did not vary significantly with pressure. The damping parameter *G* in Table 4.20 increased with pressure when the latter increased up to 0.93 Pa, but it decreased at 1.06 Pa for 120 s deposition time (Table 4.21).

Table 4.20. The dependence of the fitted parameters e_∞, e_s, w_0, and *G* of the single oscillator model on pressure for films deposited with 300 A for 60 s.

Pressure (Pa)	*n* λ(500nm)	*k* λ(500nm)	$e_{¥}$ (eV)	e_s (eV)	w_o (eV)	*G* (eV)	E_g (eV)
0.53	2.02	0.022	3.64	4.33	3.95	0.79	3.62
0.67	2.03	0.018	3.76	4.33	3.95	0.79	3.62
0.80	2.02	0.017	3.76	4.29	3.95	0.79	3.62
0.93	2.03	0.019	3.86	4.32	3.98	1.20	3.54
1.06	2.08	0.011	4.10	4.46	3.95	0.79	3.62
300 A, Deposition Time = 60 s							

Table 4.21. The dependence of the fitted parameters e_∞, e_s, w_0, and *G* of the single oscillator model on pressure for films deposited with 300 A for 120 s.

Pressure (Pa)	*n* λ(500nm)	*k* λ(500nm)	$e_{¥}$ (eV)	e_s (eV)	w_o (eV)	*G* (eV)	E_g (eV)
0.53	1.96	0.026	3.29	4.14	3.88	0.66	3.62
0.67	1.99	0.019	3.60	4.17	3.83	0.68	3.54
0.80	2.02	0.018	3.68	4.30	3.94	0.69	3.64
0.93	2.04	0.017	3.86	4.34	3.95	0.90	3.59
1.06	2.07	0.015	4.03	4.46	3.96	0.90	3.59
300 A, Deposition Time =120s							

In Figures 4.45 and 4.46, the dependence of *n* and *k* on λ, of ZnO-SnO_2 thin films deposited on RT glass substrates using 30at.% Sn cathode, in the range 400–700 nm and on pressure for films deposited with 300 A for 120 s is presented. As can be seen from Figure 4.45, *n* in this range of λ decreased with wavelength and pressure. The value of *n* decreased from 2.38 to 2.08 for 0.53 Pa, but for 1.06 Pa the decrease was from 2.18 to 1.98. The values of *n* for λ = 700 nm depended strongly

on deposition pressure for all films, being always lower at higher pressure. The values of *k* decrease as a function of λ, (Fig. 4.46), and no well defined dependence on pressure was observed, similar to the scatter of the values of *G* with pressure as shown in Table 4.21.

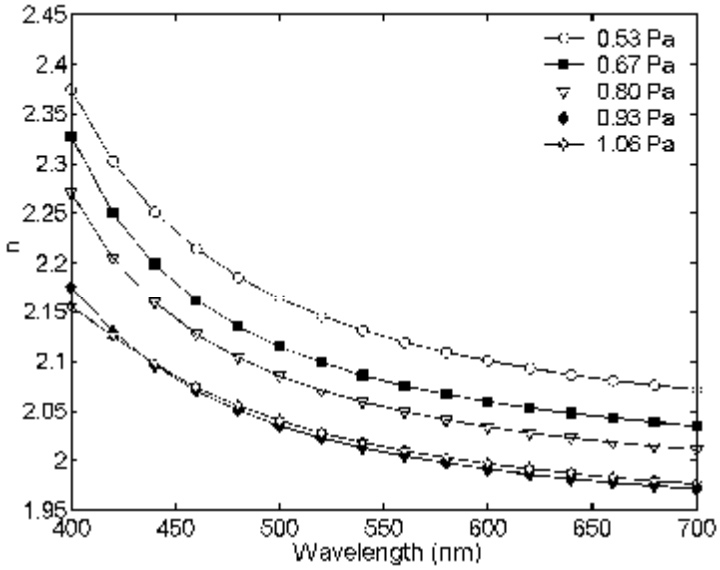

Figure 4.45. The dependence of *n* on wavelength and pressure for film deposited with 300 A for 120s.

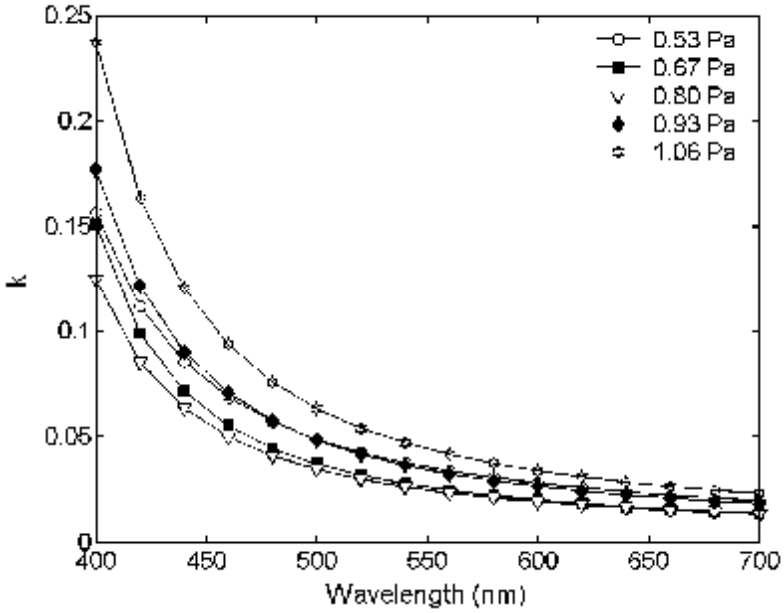

Figure 4.46. The dependence of *k* on wavelength and pressure for film deposited with 300 A for 120s.

In Table 4.22, the dependence of the optical constants, *n* and *k* at 500 nm wavelength, on arc current of films deposited using 30at.% Sn cathode at 0.80 Pa for 120 s on RT glass substrates is shown. As can be seen from the table, *n* and *k* are approximately constant at different arc currents.

Table 4.22. The dependence of *n* and *k* on arc current for films deposited with 0.80 Pa pressure for 120 s.

Arc Current(A)	*n* λ(500nm)	*k* λ(500nm)
200	2.03	0.008
250	1.96	0.016
300	2.02	0.018
Dep. Pressure :0.80 Pa, Dep. Time:120s		

A plot of $(aE)^2$ as a function of E is presented in Figure 4.47, where E is in the range of absorption, i.e., $E > E_g$. The data shown in the figure are for a film deposited on RT glass substrates with 0.53 Pa pressure, 300 A arc current for 120 s. The figure shows the linear fit of $(aE)^2$ on E, as expected from the theory and the values of a could be referred from other parts of the plot as function of E. It was found that at lower energy, e.g., E = 2.48 eV (l = 500 nm), $a = 3.7\times10^4$ cm^{-1} and at higher energy, E = 3.76 eV (l = 330 nm), α was larger by about a factor of 20, equal 7.1×10^5 cm^{-1}. Furthermore, it was found that in films deposited with 30 at% Sn cathodes, a decreased with the deposition pressure. Thus, in this case, the value of a decreased at E = 3.54 eV (l = 350 nm) from 1.1×10^5 cm^{-1} at 0.53 Pa to 6×10^4 cm^{-1} at 1.06 Pa. This behavior could be connected to the transmission band edge shift with deposition pressure in which thinner films deposited at higher pressures and hence lower absorption coefficients at the same wavelength.

The values of E_g listed in Tables 4.20 and 4.21 above, were obtained for films deposited using 30 at% Sn cathode at 300 A arc current, and 0.53 to 1.06 Pa deposition pressure, for 60 and 120 s. They were calculated from the dependence of $(aE)^2$ on E. The E_g values were in most cases approximately 3.62 eV, weakly dependant on deposition pressure. The optical band gap for thinner films, 60 s, was

found not to depend on pressure, whereas, E_g of thicker films, 120 s, varied between 3.54–3.64 eV.

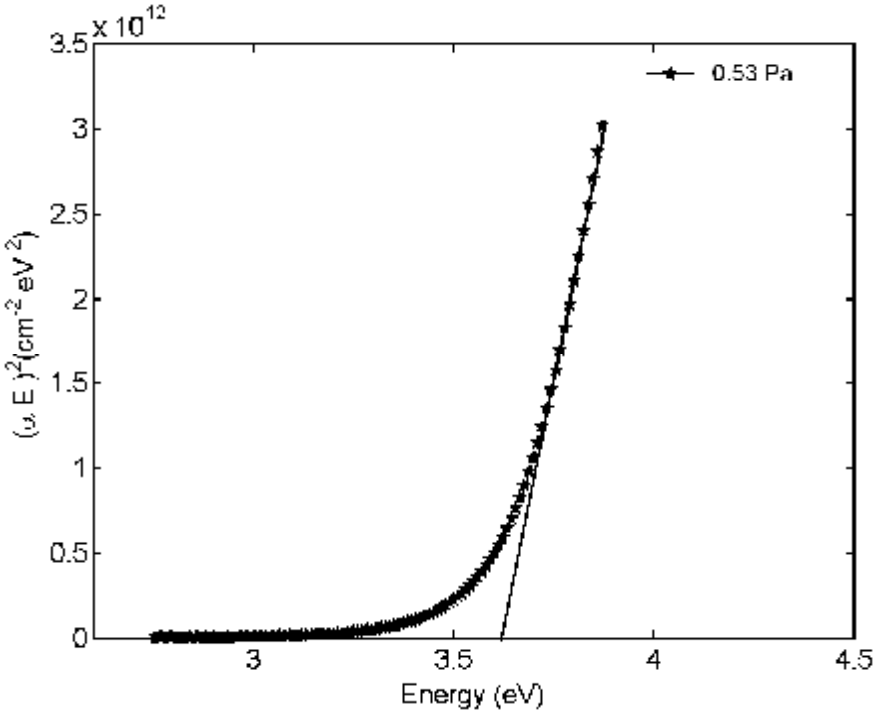

Figure 4.47. $(aE)^2$ versus E graph of ZnO-SnO_2 thin film deposited at 300 A arc current and 0.53 Pa pressure.

The effect of cathode composition and the arc current on the transmission is shown in Figures 4.48 and 4.49 by plotting the transmission against wavelengths, with cathode composition and arc currents as parameters, respectively. It is seen that the optical band edge shifted to longer wavelengths with increasing Sn concentration and with increasing arc current, and this behavior was observed for all films deposited at different pressures. The minimum and maximum transmission values were between 70% and 90%, respectively.

In Figure 4.50, a plot of $(\alpha h\nu)^2$ versus energy graph for a film deposited with a 50at.% Sn cathode is presented. As can be seen from the Figure 4.50, the value of $(\alpha h\nu)^2$ increases from 2.54×10^9 ($cm^{-2}eV^2$) at about λ ~410 nm, where film transmission starts to be below 70%, to 8.2×10^{10} ($cm^{-2}eV^2$) at λ ~350 nm. The band gap E_g is determined from the intercept of a straight line extrapolated the plotted high energy data using Eq. (2.67). In Tables 4.23 and 4.24 values of E_g are listed. In

Table 4.23, E_g varies from 3.13 to 3.59 eV and in Table 4.24, it varies from 3.34 to 3.39 eV, according to the deposition conditions. Its value decreased with concentration from 3.59 to 3.13, and did not depend significantly on the arc current.

Table 4.23. The optical parameters of $ZnO\text{-}SnO_2$ and zinc stannate thin films deposited using different cathode compositions.

Sn Percentage (at.%)	n λ (500nm)	k λ (500nm)	E_o (eV)	E_d (eV)	E_g (eV)	d_{cal} (nm)
10	2.06	0.056	5.08	12.74	3.59	319
30	2.07	0.040	5.05	12.81	3.24	340
50	2.15	0.036	4.86	13.38	3.13	401

I_{arc} = 250 A, 0.53 Pa, 60 s films, T_s =RT and UVFS substrates

Table 4.24. The optical parameters of $ZnO\text{-}SnO_2$ and zinc stannate thin films, deposited from 50at.% Sn cathode, at different arc current.

I_{arc}(A)	n λ (500 nm)	k λ (500 nm)	E_o (eV)	E_d (eV)	E_g (eV)	d_{cal} (nm)
200	2.07	0.03	5.17	13.30	3.34	404
250	2.06	0.03	5.11	12.96	3.39	526
300	2.08	0.03	5.43	14.41	3.35	606

50at.% Sn, 0.79 Pa, 120 s, T_s =RT and UVFS substrates

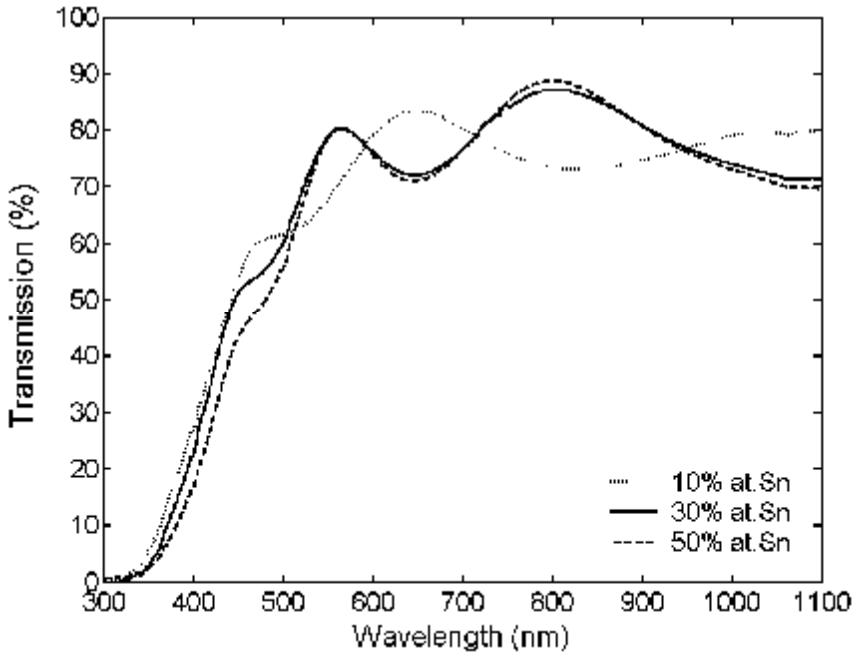

Figure 4.48. Optical transmission versus wavelength of ZnO-SnO_2 and zinc stannate thin films deposited using 300 A arc current with 10, 30 and 50at.% Zn:Sn cathode compositions for 120 s.

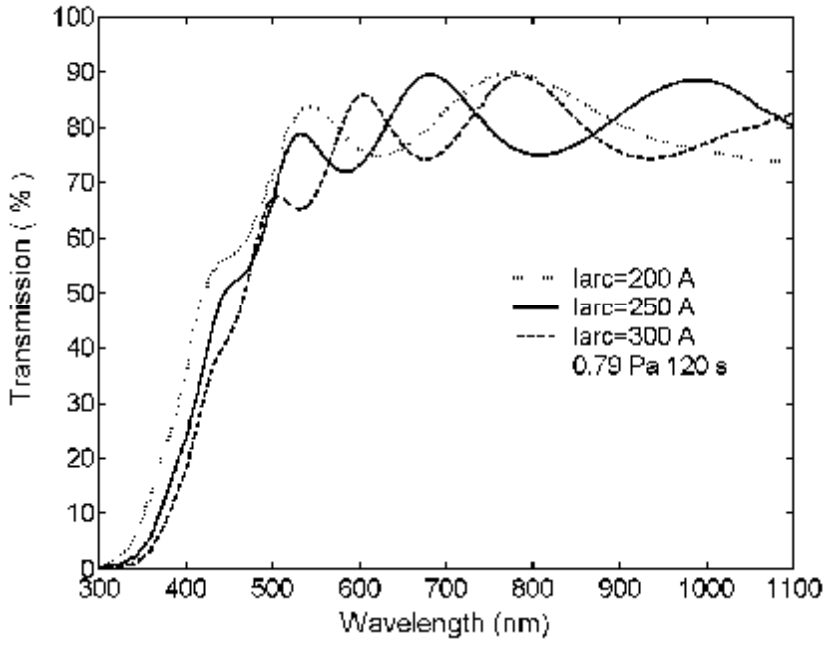

Figure 4.49. Optical transmission versus wavelength graph of zinc stannate films deposited at different arc currents deposited with a 50at.% Sn cathode.

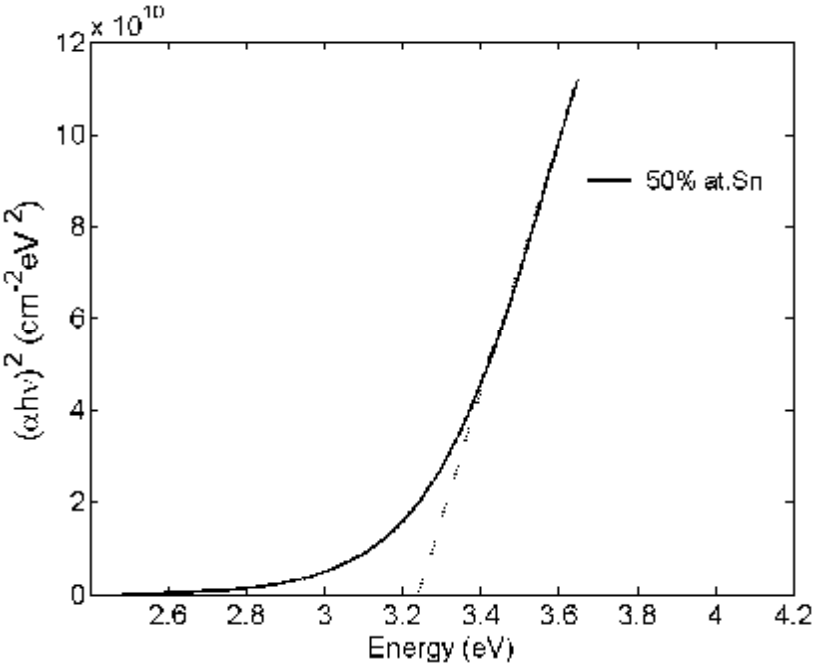

Figure 4.50. $(ahn)^2$ versus E plot of films deposited with 50at.% Sn cathode composition.

In Figures 4.51 and 4.52, the dependence of n and k on the cathode composition, for films deposited on RT kept glass substrates using 250 A arc current and 0.79 Pa for 120 s are presented. The refractive index, n, and the extinction coefficient, k, values were determined from ellipsometer data using a single oscillator model. The n values decreased with increasing wavelength and decreasing Sn concentration from 2.11 to 1.94. The k values also decreased with increasing wavelengths from ~0.07 to approximately zero. While the refractive index values depended on the cathode composition no significant change was observed, however, for the extinction coefficients.

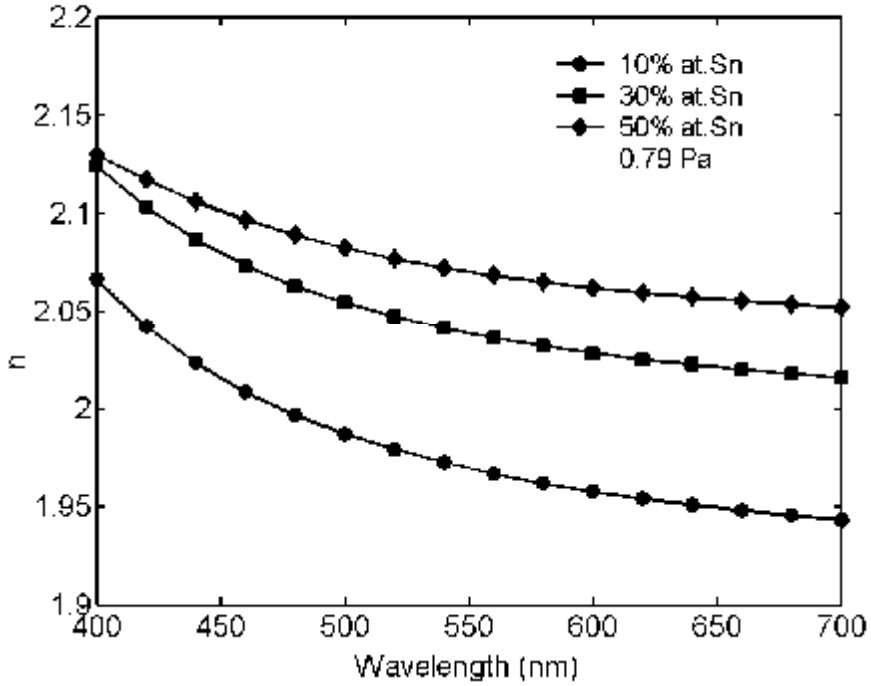

Figure 4.51. *n* versus λ for ZnO-SnO_2 and zinc stannate thin films deposited with different cathode compositions.

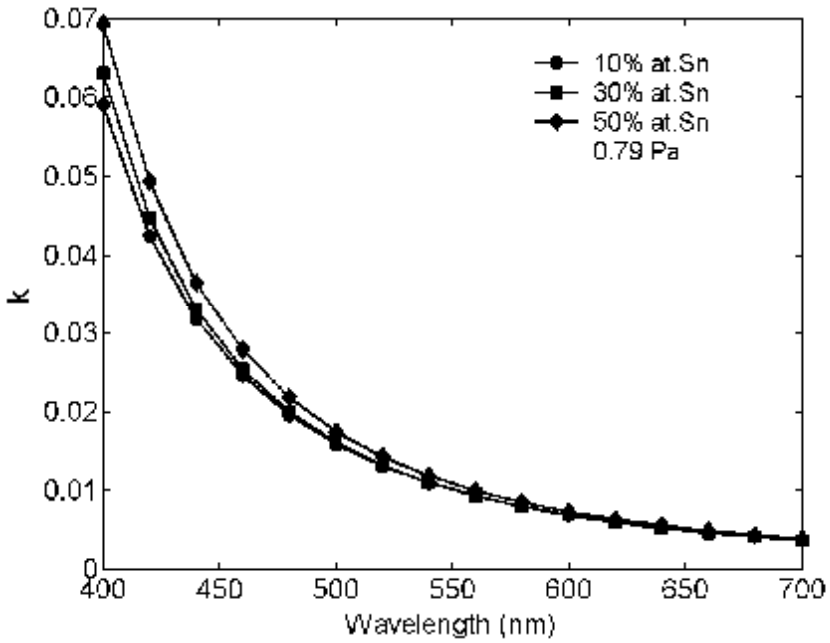

Figure 4.52. *k* versus λ for ZnO-SnO_2 and zinc stannate thin films deposited with different cathode compositions.

Deeper insight into the optical properties of the films was gained by calculating the energy band structure dependent dispersion and oscillator energy

parameters, E_d and E_o, according to the theoretical approach of Wemple and DiDomenico (1973). These parameters were derived from the values of n in the visible, using Eq. (2.56) for ZnO-SnO_2 and zinc stannate thin films deposited under different conditions, and are listed in Tables 4.23 and 4.24. In Table 4.23, E_o is in the range 4.86 to 5.08 eV and E_d is 12.74 to 13.38 eV, while in In Table 4.24, E_o is in the range 5.17 to 5.43 eV and E_d is 13.3 to 14.41 eV. These values are lower than the values for ZnO presented by Wemple and Didomenico (1973) where E_o of ZnO is 6.4 and E_d is 17.1, indicating a lower strength of transition and lower oscillator energy in the present work. When the Sn concentration in the cathode increased from 10at.% to 50at.%, E_d increased by 5% from 12.74 to 13.38 and E_o decreased by 4% from 5.08 to 4.86. In films deposited for 120 s and 0.79 Pa, E_d increased by 8% from 13.3 (at 200 A) to 14.91 (at 300 A). However, it was lower at 250 A arc current. E_o increased by 5%, from 5.17 (at 200 A) to 5.43 (at 300 A) but, it was lower at 250 A (~5.11).

The effect of substrate temperature on film optical properties was analyzed using transmission and *ex situ* variable angle spectroscopic ellipsometry (VASE) measurements. The optical constants of all films were calculated using the data measured by VASE in the range 191-989 nm at three angles of incidence: 60^o, 65^o, and 70^o. The ellipsometric measurement is normally expressed in terms of Ψ and Δ and the associated parameters were defined in the literature survey section (2.8.2.2). In the analyses, we used the Tauc-Lorentz (TL) model to derive the dispersion of the optical properties for ZnO-SnO_2 and zinc stannate thin films, and the effective medium approach (EMA) to account for the film surface roughness. The optical constants of the surface material were determined assuming 50:50 voids (air) to material ratio. The ellipsometry experimental data and calculated data were fitted by varying the dielectric function parameters minimizing the mean-squared error (MSE) function (Eq. 2.117). Figures 4.53 and 4.54 present an example of ellipsometric data fitting, showing the measured and calculated Ψ and Δ for film deposited using 50at.% Sn cathode on 400^oC UVFS substrates at 0.67 Pa background oxygen pressure.

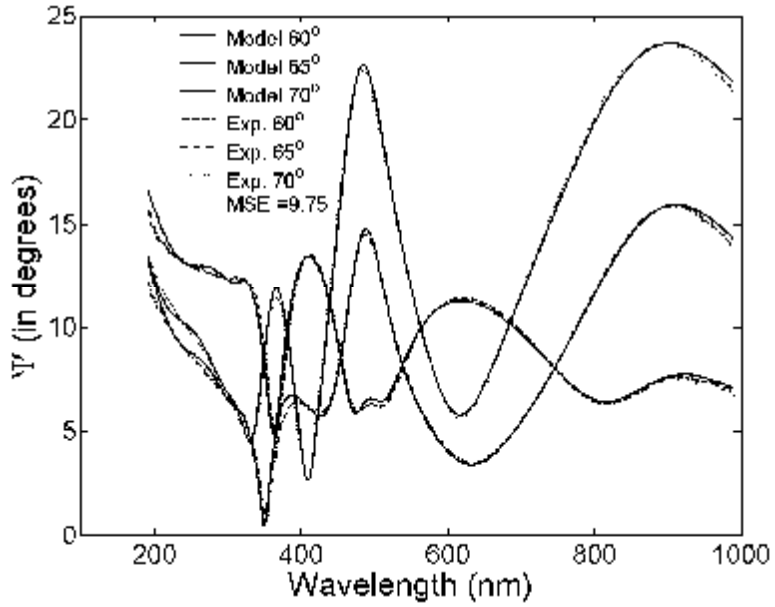

Figure 4.53. Measured Ψ and model fitted for sample deposited with 0.67 Pa oxygen pressure.

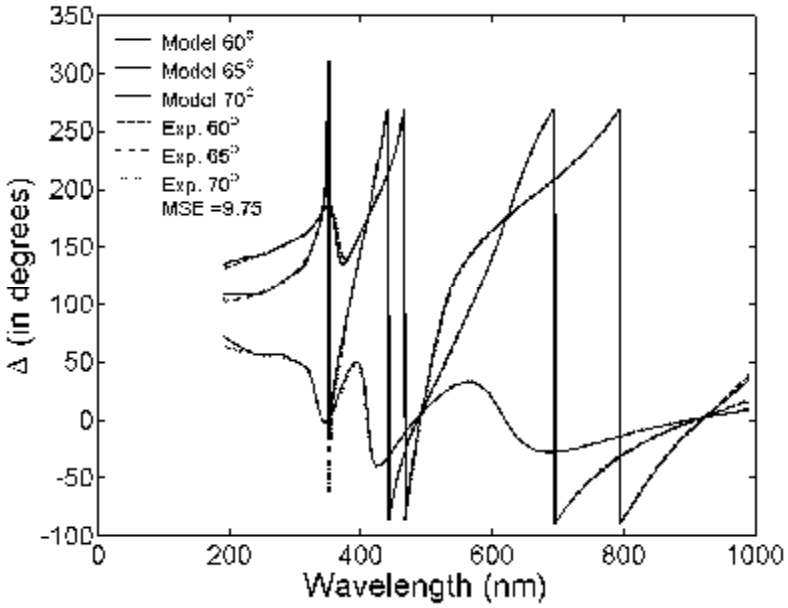

Figure 4.54. Measured Δ and model fitted for a sample deposited with 0.67 Pa oxygen pressure.

In Figure 4.55, plots of the optical transmittance versus wavelength of zinc stannate thin films deposited at 0.93 Pa on RT and heated substrates are presented. The optical band edge of the films shifted to the shorter wavelengths with increasing substrate temperature. In addition, in Figure 4.56, the pressure dependence plots of

the optical transmission is presented for films deposited on 200°C heated UVFS substrates at 0.53 to 1.06 Pa oxygen background pressures, showing that the optical band edge shifted to shorter wavelengths with increasing pressure. The maximum and minimum film transmission in the VIS, as seen in Figures 4.55 and 4.56, were 70% and 90%, respectively, independent of the deposition conditions.

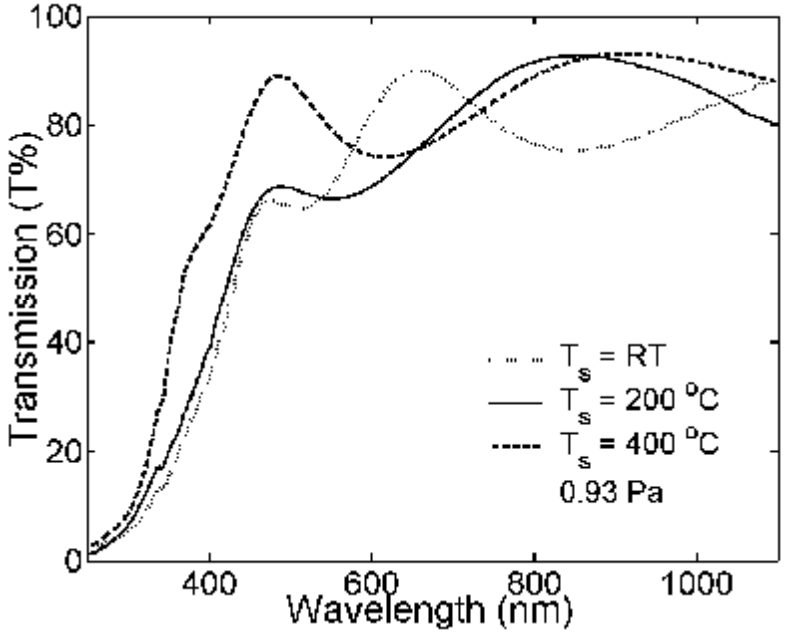

Figure 4.55. Optical transmissions versus wavelength of zinc stannate thin films, deposited with 150 A arc current at 0.93 Pa, for different substrate temperature.

In Figures 4.57 and 4.58 the refractive index *n* and the extinction coefficients *k* for films deposited on RT UVFS substrates using 50at.% Sn cathode with 150 A arc current at 0.80 Pa oxygen pressure on heated substrates are presented. The refraction index of all films in the wavelength range 250-100 nm had a maximum near 300 nm, decreasing with increasing wavelength from 2.34 to 1.96. For all films deposited at different pressures, *n* in the VIS increased when the substrate temperature was increased from RT to 200°C, and then decreased to below the RT value when the substrate temperature was further increased to 400°C. The extinction coefficients showed a similar behavior for all films deposited at all pressures.

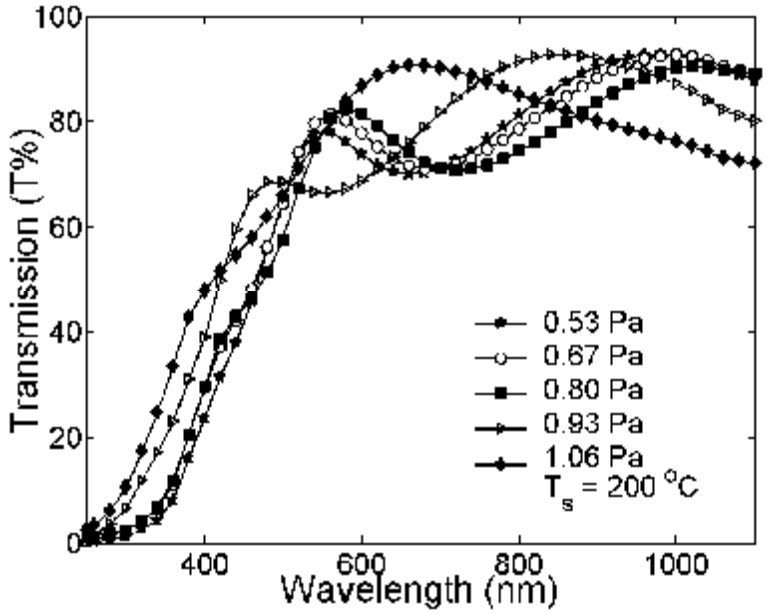

Figure 4.56. The optical transmission versus wavelength plots of zinc stannate thin films, deposited at 200°C substrate temperature, as function of deposition pressure.

Furthermore, in Figures 4.59 and 4.60, the dependence of *n* and *k*, of zinc stannate thin films deposited using 50at.% Zn:Sn cathode with 150 A in the pressure range 0.53 to 1.06 Pa on400oC heated UVFS substrates, on wavelength for different deposition pressures is shown. Both *n* and *k* decreased with increasing wavelength. No correlation was found between the deposition pressure and the values of the refractive index. In Table 4.25, the refractive index and the extinction coefficients at 550 nm for zinc stannate films deposited using 50at.% Zn:Sn cathode with 150 A arc current in the pressure range 0.53 to 1.06 Pa as function of substrate temperature are listed. The values of *n* for films deposited with pressure in the range 0.53 to 1.06 Pa were 2.11 – 2.15, 2.17-2.28, and 2.09-2.10 for RT, 200°C, 400°C, respectively. The values of *k* were 0.018-0.024, 0.028-0.044, and 0.001-0.041 for RT, 200 and 400°C, respectively.

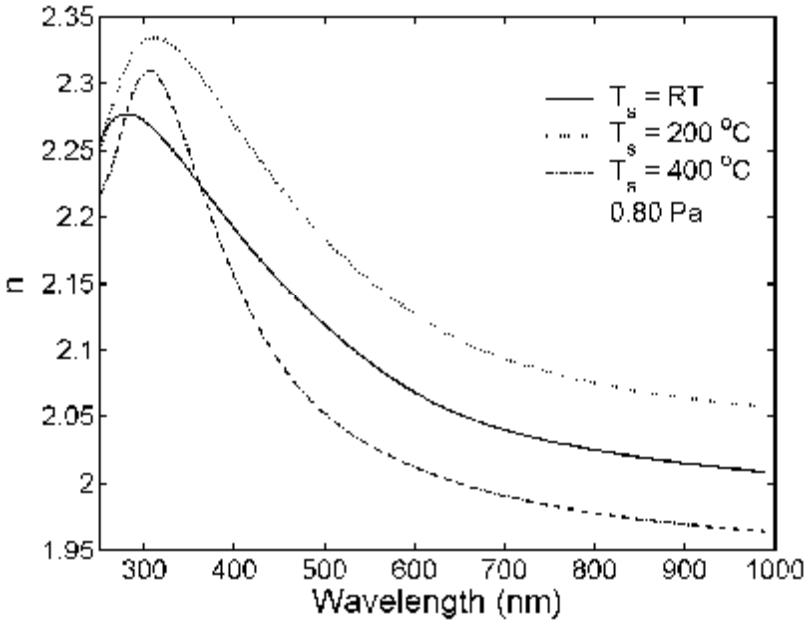

Figure 4.57. The refractive index versus wavelength for zinc stannate thin films, deposited at 0.80 Pa, as function of substrate temperature.

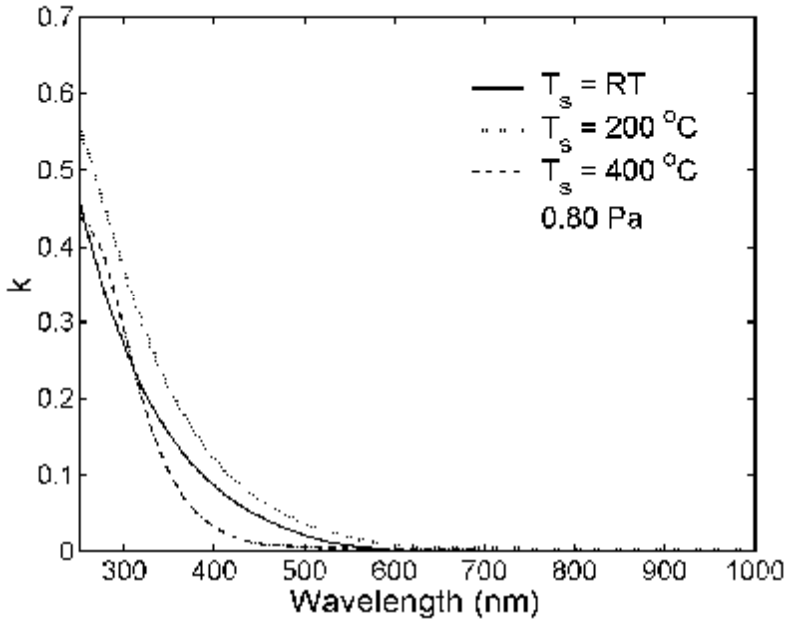

Figure 4.58. The extinction coefficient versus wavelength plots of zinc stannate thin films, deposited at 0.80 Pa, as function of substrate temperature.

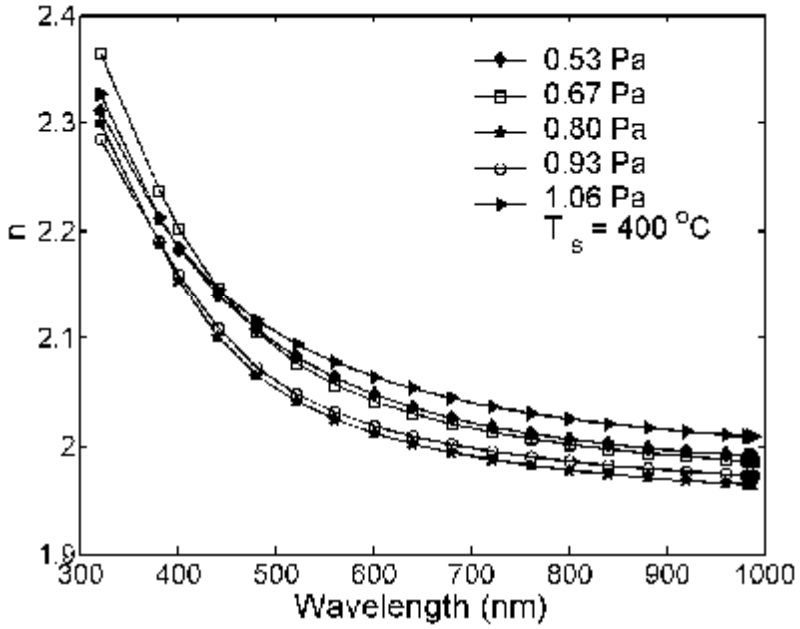

Figure 4.59. The refractive index versus wavelength plots of ZnO-SnO_2 thin films, deposited at 400°C substrate temperature, as function of deposition pressure.

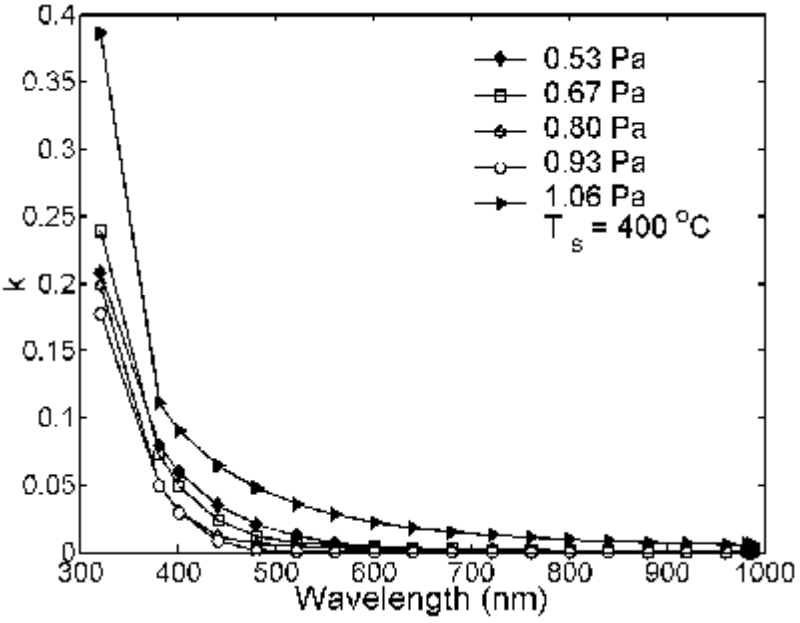

Figure 4.60. The extinction coefficient versus wavelength for ZnO-SnO_2 thin films, deposited at 400°C substrate temperature, as function of deposition pressure.

Table 4.25. The optical parameters of zinc stannate thin films for various deposition pressures and substrate temperatures at 550 nm.

Pressure (Pa)	*n* (RT)	*n* (200°C)	*n* (400°C)	*k* (RT)	*k* (200°C)	*k* (400°C)
0.53	2.15	2.28	2.09	0.018	0.044	0.016
0.67	2.13	2.20	2.09	0.019	0.035	0.009
0.80	2.12	2.18	2.05	0.021	0.036	0.005
0.93	2.11	2.16	2.06	0.019	0.028	0.001
1.06	2.11	2.17	2.10	0.024	0.042	0.041
Iarc = 150 A Dep. Time =60 s, T_s = RT, 200°C and 400°C, *n* and *k* (λ = 550nm)						

The dependence of $(\alpha h\nu)^2$ on photon energy is plotted for films deposited at 0.80 Pa on RT, 200°C and 400°C substrates in Figure 4.61. As can be seen from the figure, the highest values of $(\alpha h\nu)^2$ were obtained on 200°C heated substrate, and was about 4.2×10^{11} cm^{-2}-eV^2 at λ~300 nm. The optical band gap, E_g, was determined from the $(\alpha h\nu)^2$ versus E graph by extrapolating the straight line at higher energy to the 0-intercept.

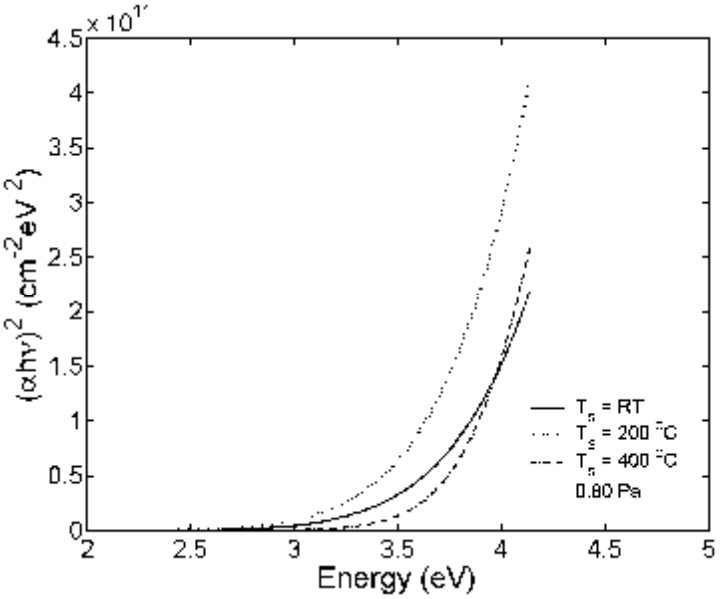

Figure 4.61. $(\alpha h\nu)^2$ versus E plots of ZnO-SnO_2 thin films as function of substrate temperature.

Table 4.26. Thickness and the optical band gap values of zinc stannate thin films for various deposition pressures and substrate temperatures.

Pressure (Pa)	d (nm) (RT)	d (nm) (200°C)	d (nm) (400°C)	E_g (eV) (RT)	E_g (eV) (200°C)	E_g (eV) (400°C)
0.53	254	250	272	3.52	3.43	3.61
0.67	259	249	257	3.56	3.50	3.64
0.80	363	262	274	3.53	3.52	3.70
0.93	340	207	232	3.51	3.53	3.61
1.06	302	154	124	3.50	3.51	3.69
Iarc = 150 A Dep. Time =60 s, T_s = RT, 200°C and 400°C						

In Table 4.26, the thickness and the optical energy band gap values are summarized for films deposited using 50at.% Zn:Sn cathode with 150 A arc current in the pressure range 0.53 to 1.06 Pa as function of substrate temperature. The optical energy band gap, E_g, was in the range 3.43 to 3.70 eV and the estimated thickness (from VASE) was in the range 124 nm to 363 nm, depending on the deposition pressure. The optical band gap values for films deposited at different substrate temperatures were not significantly affected by the deposition pressure, however, their values increased from ~3.4 eV to 3.7 eV with increasing substrate temperature.

The effect of substrate temperature on the optical transmission is also determined for zinc stannate thin films deposited with 250 A arc current at 0.93 Pa oxygen pressure on 400°C and 500°C heated UVFS substrates. In Figure 4.62, the optical transmission versus wavelength plots of zinc stannate thin films are presented. As can bee seen from the figure the optical transmission edge shifted to the lower wavelengths at the higher substrate temperature.

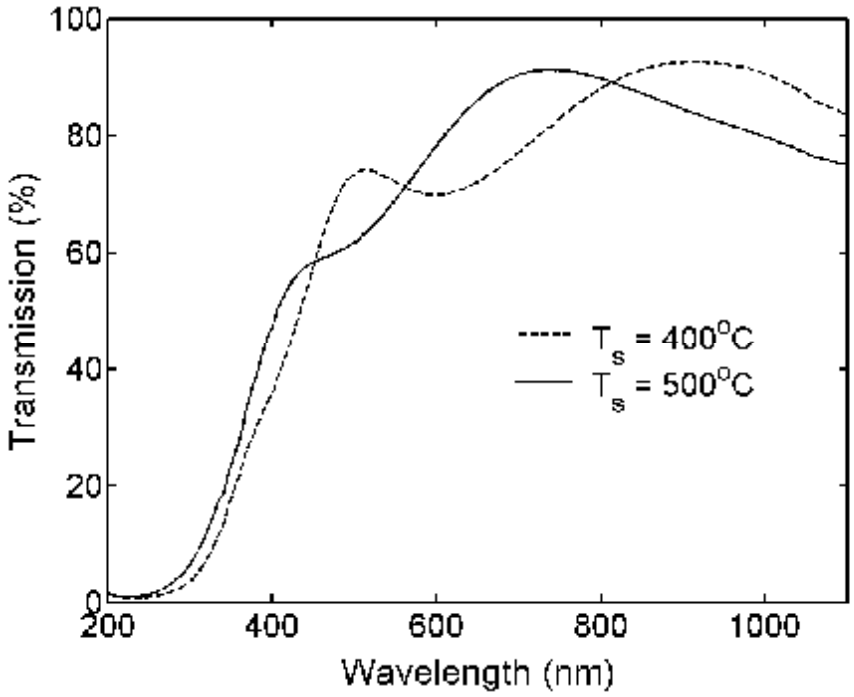

Figure 4.62. Optical transmissions versus wavelength of zinc stannate thin films, deposited with 250 A arc current at 0.93 Pa, for different substrate temperatures.

In Figures 4.63(a-b) the refractive indexes and the extinction coefficients of zinc stannate thin films deposited with 250 A arc current at 0.93 Pa, for different substrate temperatures are presented, respectively. As seen from Figure 4.63(a), the refractive index, *n*, values are lower for films deposited on 500°C substrates in all wavelength region. In addition, in Figure 4.63(b), the *k* values of the film deposited on 500°C are lower at the UV, whereas, in the VIS spectrum *k* values are practically equal.

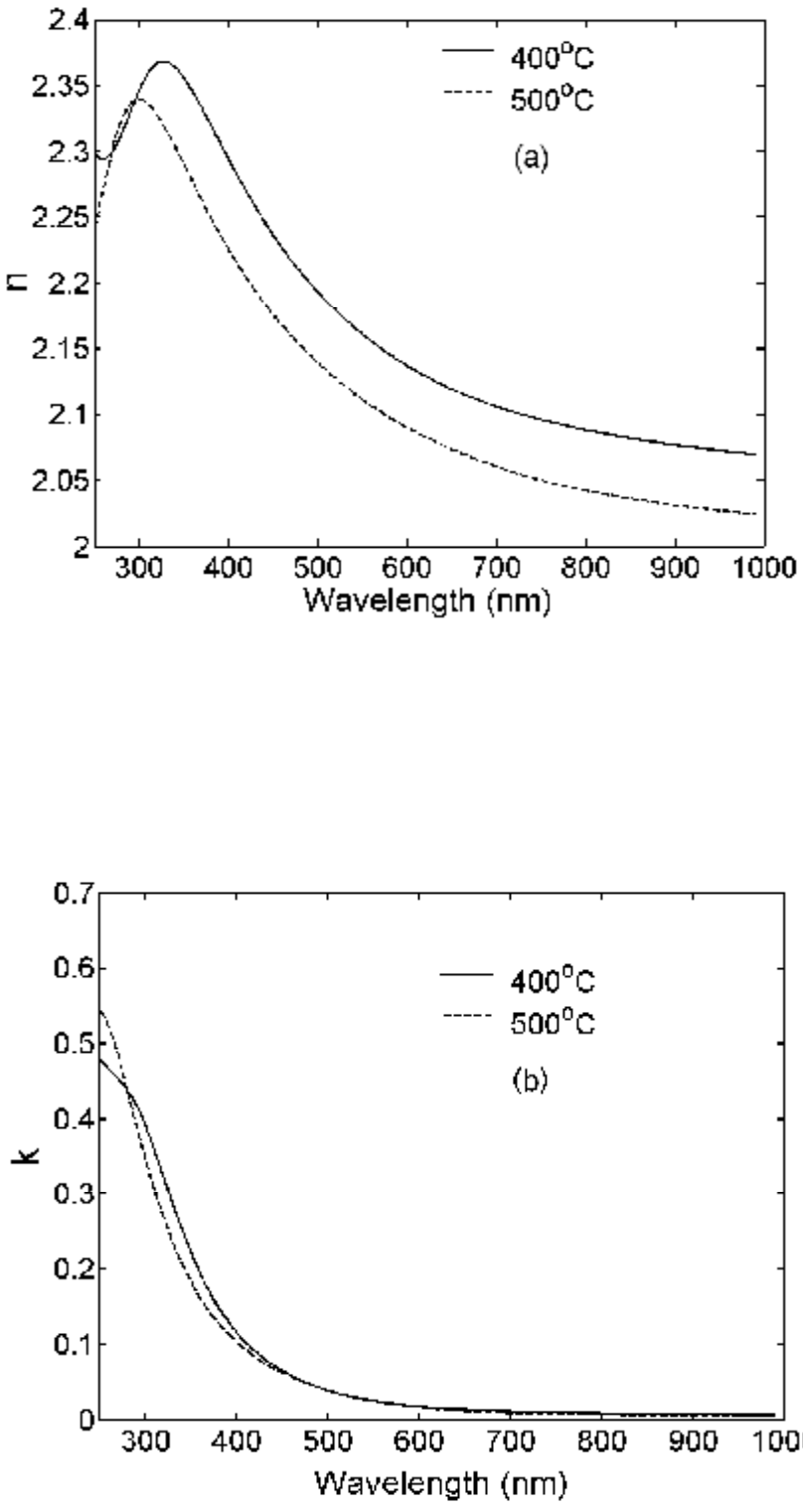

Figure 4.63 (a) Refractive index, **(b)** Extinction coefficient versus wavelength plots of zinc stannate thin films deposited with 250 A arc current at 0.93 Pa, for different substrate temperatures.

The effect of air annealing on the film optical properties (e.g. E_g, n and k) was determined using the measured optical transmission (T_{exp}) of 200-606 nm thick films. The glass substrates had lower optical transmission in the range 300-350 nm (~70% at 300 nm), which was taken account in the following analysis which was performed in the range 300 to 1100 nm. The derivation of the parameters of the dielectric function was based on the same fitting process described above in page (11). The standard deviation of all fitted transmissions was in the range of 1-2%.

In Figure 4.64, the plots of T_{exp} and T_c are presented for as-deposited films, deposited using a 50at.% Sn cathode at 200 A, 0.79 Pa for 120 s. It may be seen that there is good agreement between the measured and model data. The χ^2 value for all samples was < 2. The deviation between T_{exp} and T_c could result from surface roughness, bulk non-uniformity, and interface layers that were not taken into account in the present model. T_{exp} varied between a minimum of 70% and maximum of 90%. The gradual decrease of the transmission as the wavelength decreases from λ=530 nm to λ=300 nm should be noted, as it is typical to amorphous materials.

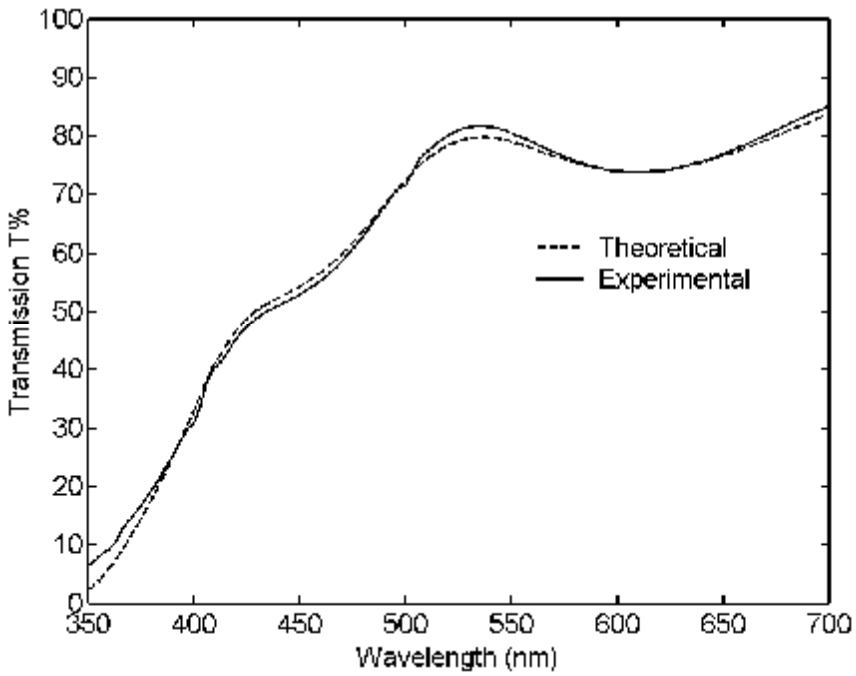

Figure 4.64. Comparison of the measured spectral transmittance curve for a ZnO-SnO_2 sample with a theoretically fitted one.

In Figure 4.65, the optical transmission of zinc stannate thin films deposited using 50at.% Zn:Sn cathode on RT glass substrates using 300 A arc current at 0.79 Pa and annealed at 500^{o}C for 60 min films are presented. As shown, the optical transmission edge at shorter wavelength is well defined of the annealed film was well defined and at ~380 nm. Such well defined transmission edge indicates that the structure order of the annealed film had improved. However, the transmission in the VIS was not significantly affected by annealing. The as-deposited films were visually brownish in color, but after annealing their brownish color disappeared.

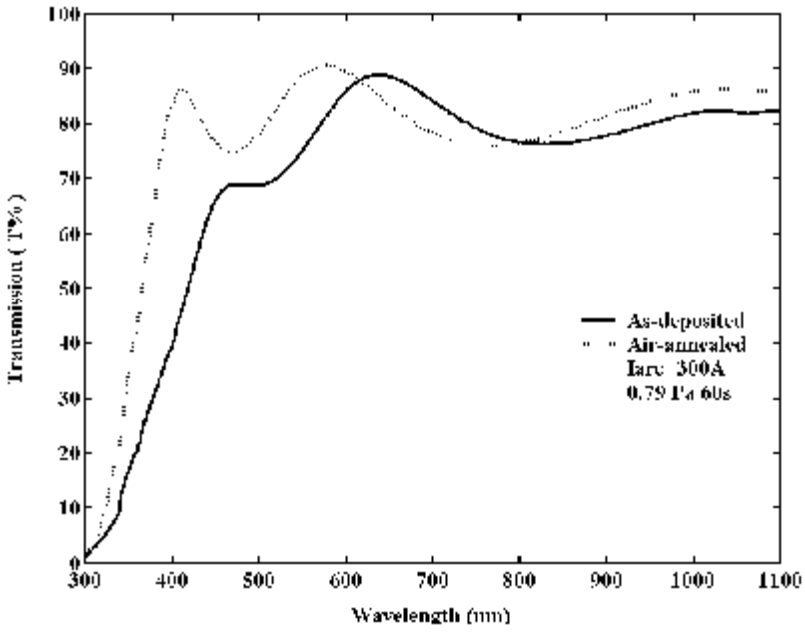

Figure 4.65. Transmission versus wavelength of as-deposited and air-annealed films.

In Figures 4.66 and 4.67, transmission versus wavelength is plotted for as-deposited and annealed films for various arc currents and deposition pressures, respectively. The zinc stannate films were deposited using 50at.% Zn:Sn cathodes on RT kept glass substrates at 0.79 Pa for 60s and annealed in air at 500^{o}C for 60 min. The absorption edge shifts to the lower wavelengths in all annealed films, for all included deposition conditions. The band edge steepness also increased with annealing indicating well defined band edge.

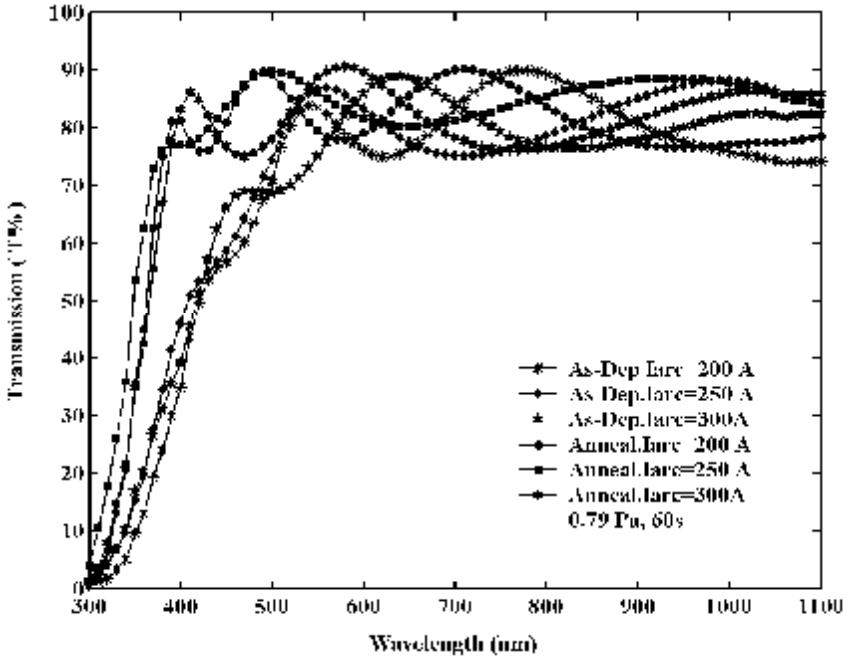

Figure 4.66. Air-annealing effect on the spectral transmission of zinc stannate thin films deposited at different arc currents at 0.79 Pa.

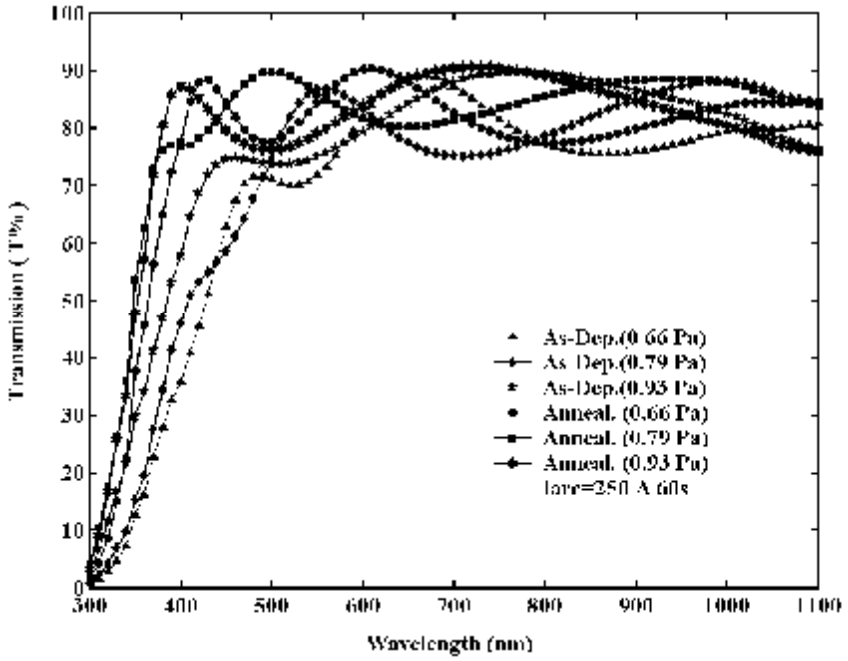

Figure 4.67. Air-annealing effect on the spectral transmission of zinc stannate thin films deposited at 250 A arc current with different deposition pressures.

In Figure 4.68, a plot of $(ahv)^2$ versus energy is shown for a sample deposited using a 50at.% Sn cathode on RT glass substrate at 250 A, and 0.79 Pa for 60 s deposition time and annealed at 500°C in air. The data in Figure 4.68 are compatible with the assumption of direct electron transition, i.e. $(ahv)^2$ varies linearly with E for sufficiently high E. $(ahv)^2$ increased from 0.5×10^{10} ($cm^{-2}eV^2$) at λ ~350 nm to 4.8×10^{10} ($cm^{-2}eV^2$) λ~330 nm. Repeating the same analysis procedure on annealed films showed that the absorption coefficients of the annealed films were one order of magnitude lower than the as-deposited films. The optical band gap values were calculated by extrapolating the linear portion of the curve to zero. The derived E_g values for both as-deposited and annealed films are summarized in Tables 4.27 and 4.28. The values for as-deposited films, for all deposition conditions, were in the range of 3.34-3.43 eV, however, annealing increased E_g up to 3.61 eV.

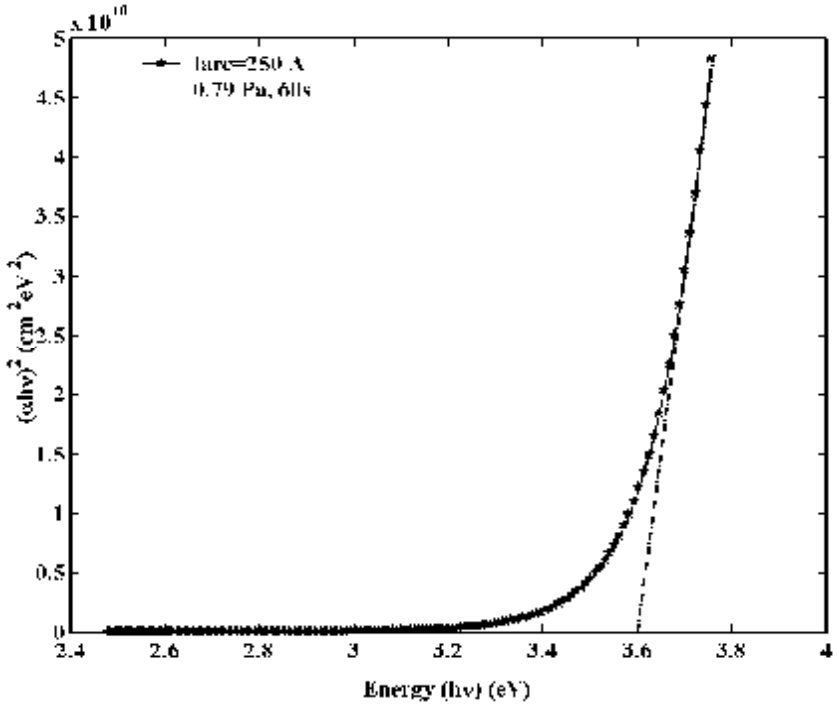

Figure 4.68. Plot of $(ahv)^2$ versus E obtained from a film deposited at 250 A arc current, 0.79 Pa pressure during 60 s and annealed at 500°C.

In Figures 4.69 and 4.70, the dependence of *n* and *k* on wavelength is presented for as-deposited and annealed zinc stannate thin films. The zinc stannate thin films were deposited using 50at.% Zn:Sn cathode at 300 A and 0.79 Pa for 60 s deposition time and annealed in air at 500oC for 60 min. As can be seen from the figures, at λ = 400 nm *n* increased from ~1.97 to ~2.03, and *k* decreased from ~0.07 to ~0.01 with annealing.

In Table 4.27, *n* and *k* at λ = 500 nm are listed as function of arc current for annealed and as-deposited films. The difference in *k* between annealed and as-deposited films is significant, as it is greater than the uncertainty in *k*, indicating a noticeable lower absorption in the visible after annealing However, the difference in *n* is probably significant only for the case 200 A arc current.

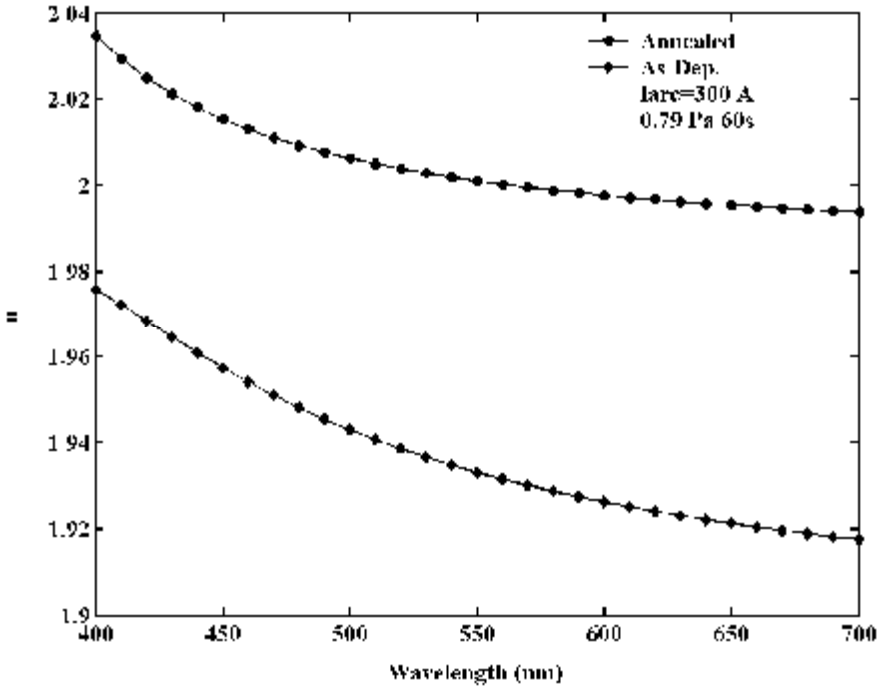

Figure 4.69. Refractive index versus wavelength for as-deposited and air annealed films deposited at 300 A, 0.79 Pa for 60 s.

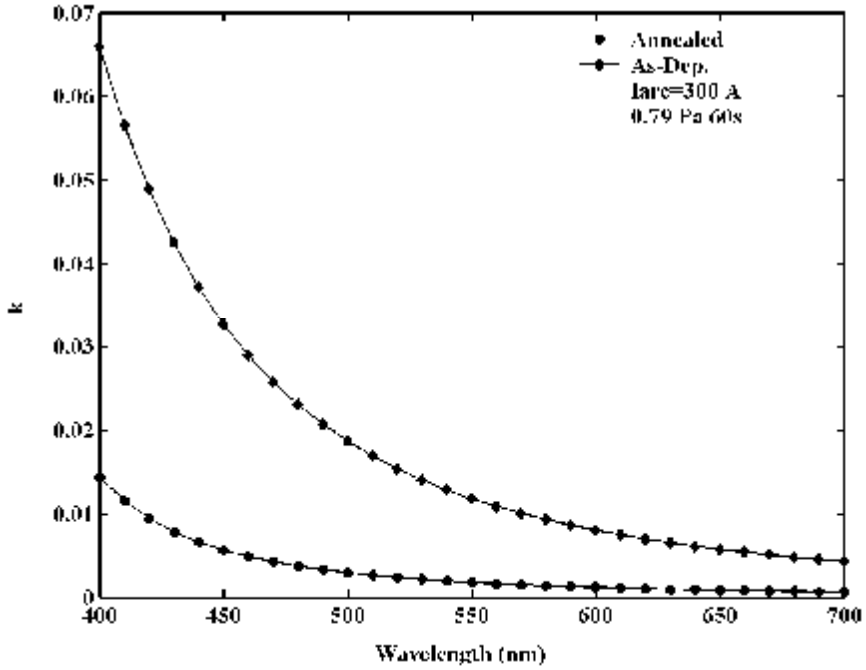

Figure 4.70. Extinction coefficient versus wavelength for as-deposited and air annealed films deposited at 300 A, 0.79 Pa for 60 s.

Table 4.27. Optical parameters of zinc stannate films deposited at different arc currents, before and after air annealing at 500°C for 1 h.

Iarc (A)	n_A	n_D	k_A	k_D	E_{oA} (eV)	E_{oD} (eV)	E_{dA} (eV)	E_{dD} (eV)	E_{gA} (eV)	E_{gD} (eV)
200	1.95	1.99	0.0001	0.017	10.80	9.04	29.02	24.69	3.40	3.34
250	2.00	1.98	0.0014	0.014	9.20	9.16	25.67	24.80	3.60	3.39
300	2.01	2.01	0.0019	0.019	9.29	9.20	26.24	25.82	3.60	3.34
Dep.Pressure:0.79 Pa, Dep.Time:120 s (A:Annealed, D:As-deposited),λ =500nm(*n* and *k*))										

In Table 4.28, *n* and *k* of as–deposited zinc stannate thin films with at λ = 500 nm are listed as function of the deposition pressure for annealed and as-deposited films. The variation in *k* between annealed and as-deposited films as shown in Table 4.28 is again significant, resulting in a marked reduction of *k* after the annealing.

There is only a small effect of the annealing on *n*, which is probably only significant for the 0.79 Pa case. Hence, the change in T_{exp} between annealed and as-deposited films as function of deposition pressure was mainly a result of the variation in *k*.

Table 4.28. Optical parameters of zinc stannate films deposited at different oxygen background pressures, before and after air annealing at 500°C for 1 h.

Pressure (Pa)	n_A	n_D	k_A	k_D	E_{oA} (eV)	E_{oD} (eV)	E_{dA} (eV)	E_{dD} (eV)	E_{gA} (eV)	E_{gD} (eV)
0.66	1.93	1.94	0.003	0.020	10.43	8.61	27.08	21.82	3.50	3.37
0.69	1.90	2.08	0.002	0.018	11.46	8.58	28.52	26.29	3.60	3.39
0.93	1.98	1.96	0.003	0.017	9.93	9.17	27.36	23.59	3.61	3.43
Iarc:250 A, Dep.Time:60 s (A: Annealed, D: As-deposited),λ=500nm(*n* and *k*)										

In Figures 4.71 and 4.72, the dependence of *n* and *k* on wavelength (400 – 700 nm) and on arc current (200, 250, and 300 A), of zinc stannate thin films deposited with 0.79 Pa on RT kept glass substrates, is shown for as-deposited and annealed films (500°C for 60 min). As seen in 4.71, *n* of films deposited with 200 A arc current as function of wavelength decreased from 1.97 to 1.95, *n* of films deposited with 250 A arc current films decreased from 2.07 to 1.97, and that of films deposited with 300 A arc current decreased from 2.09 to 1.98. On the other hand, the extinction coefficient *k* as function of wavelength (400–700 nm) decreased from 0.007, 0.009 and 0.015 to practically zero for films deposited at 200, 250 and 300 A, respectively. It should be noted that both *n* and *k* where ordered according to the deposition current, increasing at any given wavelength with the current.

In Figures 4.73 and 4.74, the dependence on wavelength (400–700 nm) and deposition pressure (0.66, 0.79 and 0.93 Pa) of *n* and *k*, of annealed zinc stannate films deposited with 50 at% Zn:Sn cathode on RT kept glass substrates with 250 A arc current, is presented. As seen in Figure 4.74, *n* for films deposited at 0.66 Pa decreased from 2.01 to 1.97, for 0.79 Pa films it decreased from 1.96 to 1.92, and for 0.93 Pa films it decreased from 1.92 to 1.89. The extinction coefficient *k* as function of wavelength (400–700 nm) for films decreased with pressure from 0.013, 0.009

and 0.014 to practically zero for 0.66, 0.79, 0.93 Pa deposition pressures, respectively.

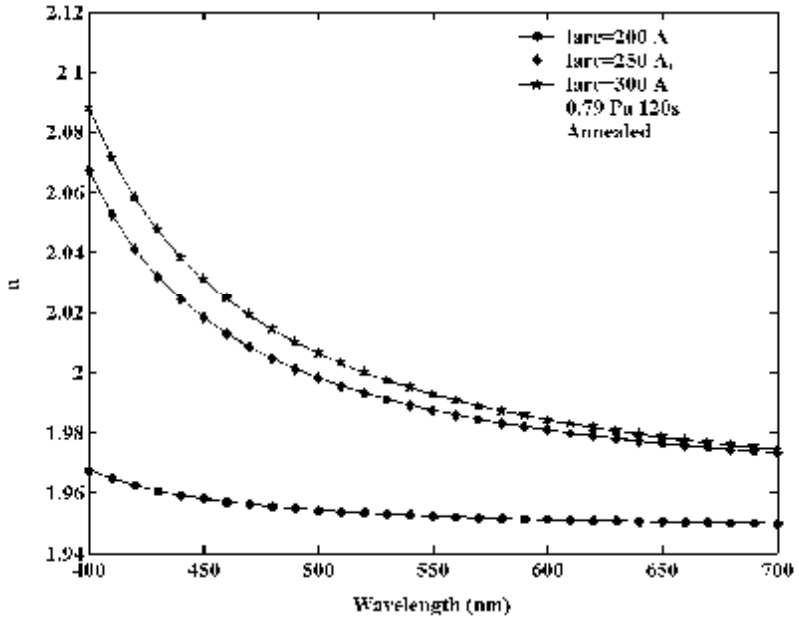

Figure 4.71. Effect of air annealing on refractive index of films deposited at different arc currents.

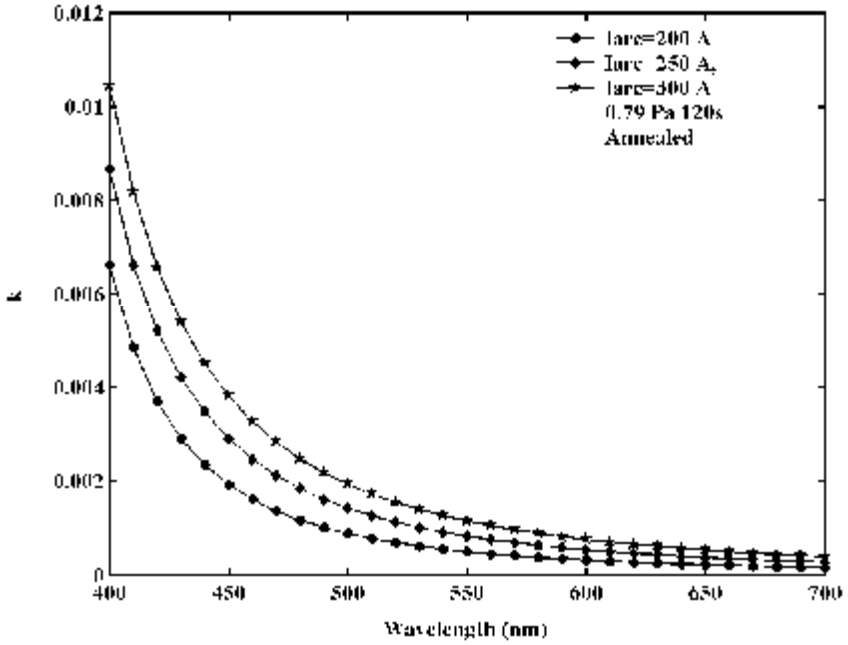

Figure 4.72. Effect of air annealing on the extinction coefficient of films deposited at different arc currents.

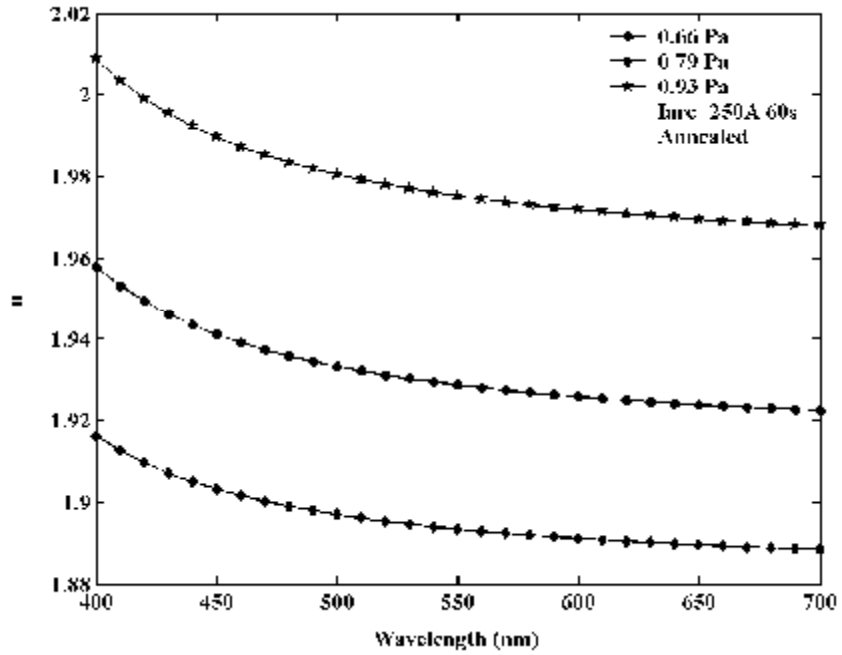

Figure 4.73. Effect of air annealing on the refractive index of films deposited at different oxygen background pressures.

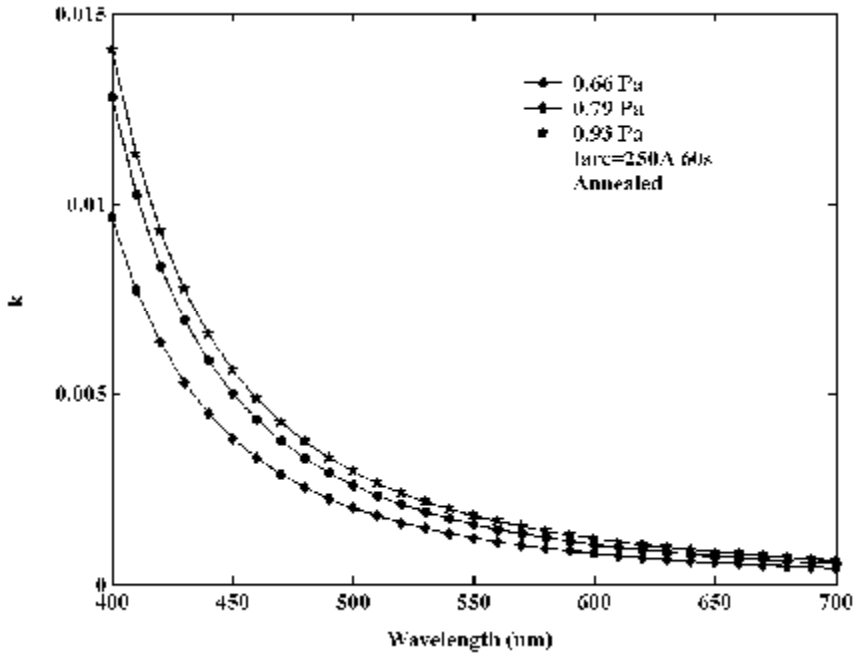

Figure 4.74. Effect of air annealing on the extinction coefficient of films deposited at different oxygen background pressures.

The data of n in the visible was used to study the dispersion and oscillator energy parameters, E_d and E_o. These parameters were calculated using Eq. (2.56) for ZnO-SnO_2 and zinc stannate thin films deposited using 10at.%, 30at.% and 50at.% Zn:Sn cathodes, with 200, 250 and 300 A arc currents, at 0.66, 0.69 and 0.93 Pa oxygen pressures, and annealed in air at 500^{o}C for 60 min.

In Tables 4.27 and 4.28, calculated E_o and E_d values are listed as a function of deposition conditions and annealing. The data in Tables 4.27 and 4.28 indicate that the annealing increased the value of E_d in all cases. From Eq. (2.57), it follows that there should be an increase in at least one of the parameters N_c, Z_a, and N_e. If it is assumed that the annealing results in more ordered material, and thus the parameter that would be more affected is N_c; it should increase. However, although the X-ray analysis indicated that the films remained amorphous even after annealing, the change in the UV absorption supports the indication that annealing had improved arrangement of atoms in the material. It should also be noted that E_o also increased with annealing, indicating an increase of and better defined intraband energy gap. Furthermore, as $E_g \propto E_o$ (Wemple and DiDomenico, 1971), E_g also is expected to increase with annealing, as indeed is shown out in Tables 4.27 and 4.28.

Typical transmission spectra as-deposited and annealed zinc stannate samples, which were deposited using 150 A arc current on 200^{o}C heated UVFS substrates at 0.93 Pa and annealed at 500^{o}C in Ar for 50 min, are presented in Fig. 4.75. As seen, the transmission edge was shifted to shorter wavelengths (or to higher photon energy) after the annealing. The average transmission in the visible spectrum was 80% for as-deposited films, however, for annealed films the average transmission was 85%. Furthermore, as-deposited films at lower deposition pressure (<0.80 Pa) had brownish color and this was disappeared after annealing in Ar atmosphere.

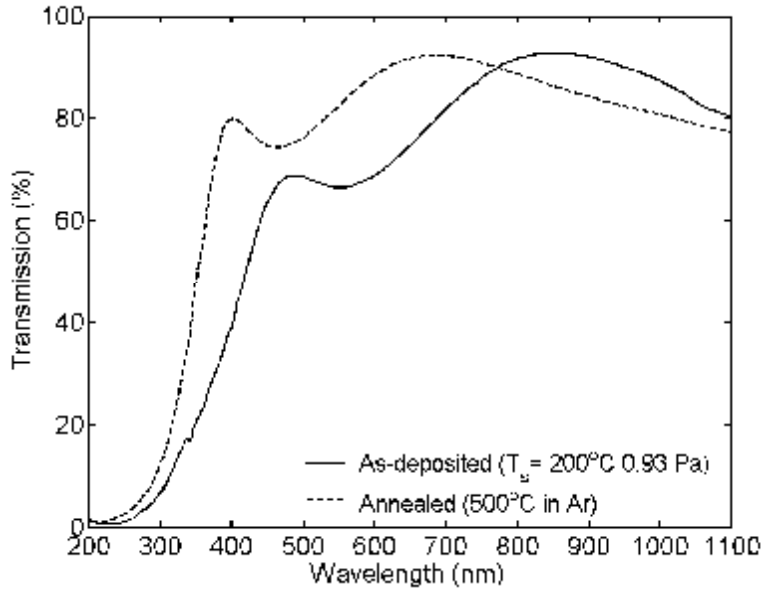

Figure 4.75. Optical transmission plots of as-deposited (at 200°C) and annealed zinc stannate thin films.

In Figs. 4.76(a-b), the optical transmission of zinc stannate thin films deposited on 400°C heated UVFS substrates using 150 A arc current with 0.53 Pa and 0.80 Pa pressure, and annealed at 500°C for 50 min in Ar, are presented, respectively.

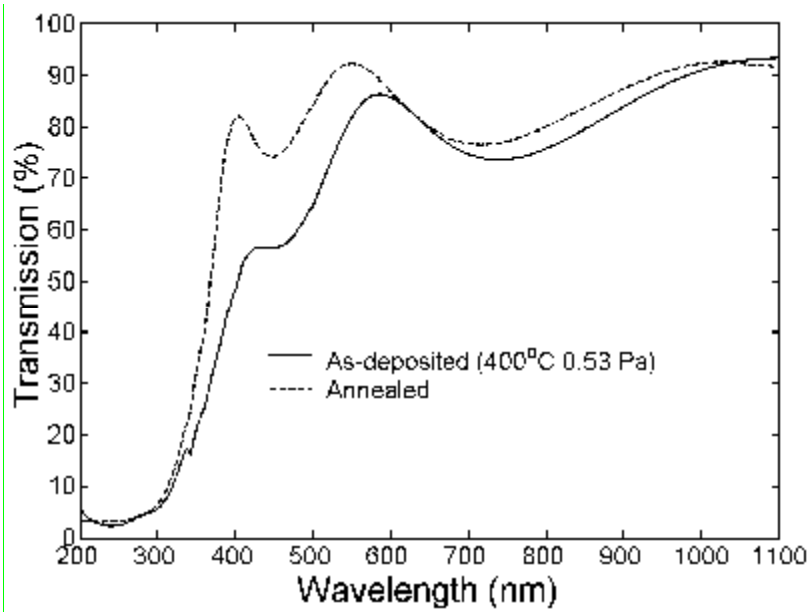

Figure 4.76(a). Optical transmission plots of as-deposited and annealed zinc stannate films deposited on RT UVFS substrate with 150 A arc current at 0.53 Pa.

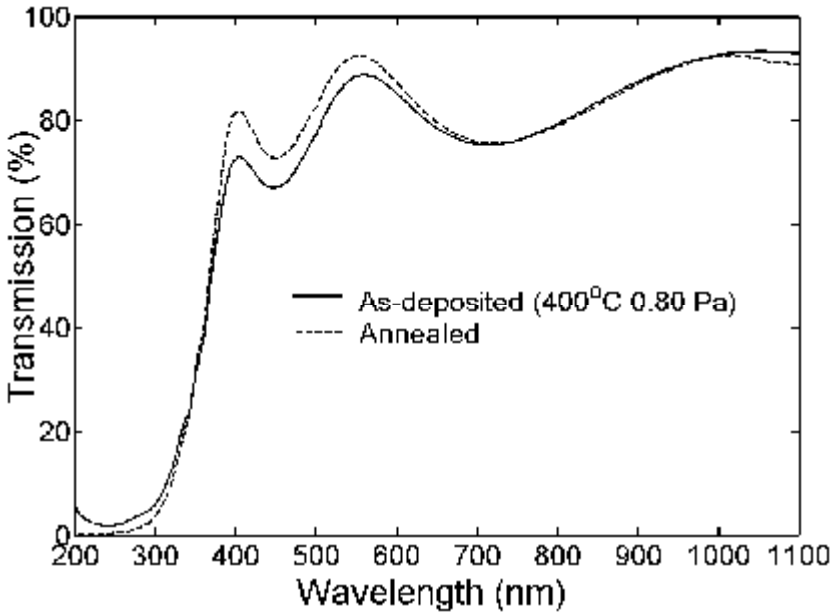

Figure 4.76(b). Optical transmission plots of as-deposited and annealed zinc stannate thin films deposited on RT UVFS substrate with 150 A arc current at 0.80 Pa.

As can be seen from Fig. 4.76(a), the optical band edge was shifted to the shorter wavelengths with annealing; however, this shift was negligible at higher deposition pressures (Fig. 4.76(b)). The highest transmission in the visible was in the range 80-85%, and was not affected by deposition pressure and deposition temperature. The most marked effect of annealing was on the transmission edge of the zinc stannate thin films. The optical transmission in UV spectral range improved significantly, independent of the deposition temperature for deposition pressures <0.80 Pa.

In Figs. 4.77(a-b) the refractive indices of films deposited on 200 and 400^{o}C heated substrates at 0.93 Pa pressure and annealed at 500^{o}C are presented. As shown, the refractive index of the as-deposited films depended significantly on the substrate temperature. However, after the annealing their difference became insignificant (Fig. 4.77(b)). This was also the case for films deposited on different deposition pressure. Furthermore, the effect of the annealing on *n* of the film deposited on 400^{o}C substrate was negligible.

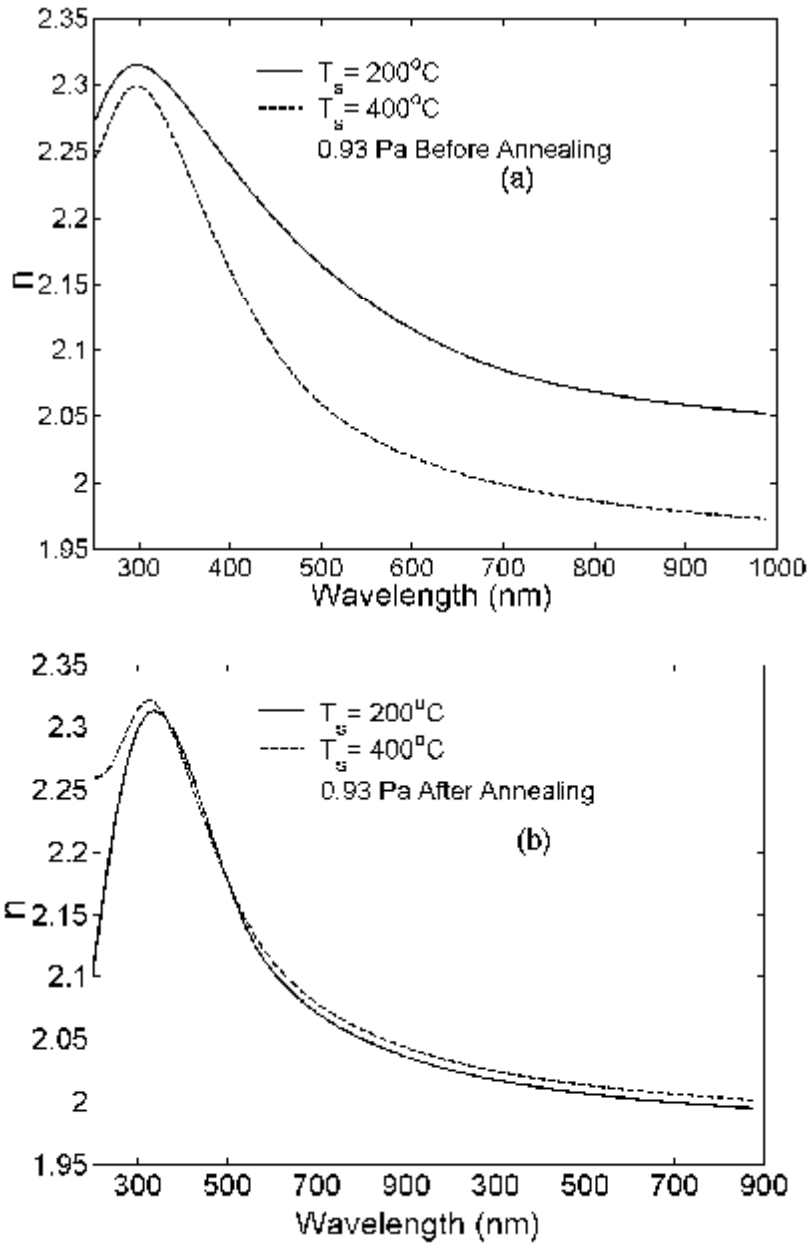

Figure 4.77. Plots of the refractive index of (a) as-deposited and (b) annealed zinc stannate thin films versus wavelength for two different substrate temperatures.

In Figs. 4.78(a-b) the extinction coefficient of films deposited on 200 and 400°C heated substrates at 0.93 Pa pressure and annealed at 500°C are presented. The *k* values decreased from 0.5 at 250 nm to approximately 0.05 and 0.1 at 400 nm, and then to zero at longer wavelengths for films deposited on 200 and 400°C heated substrates, respectively.

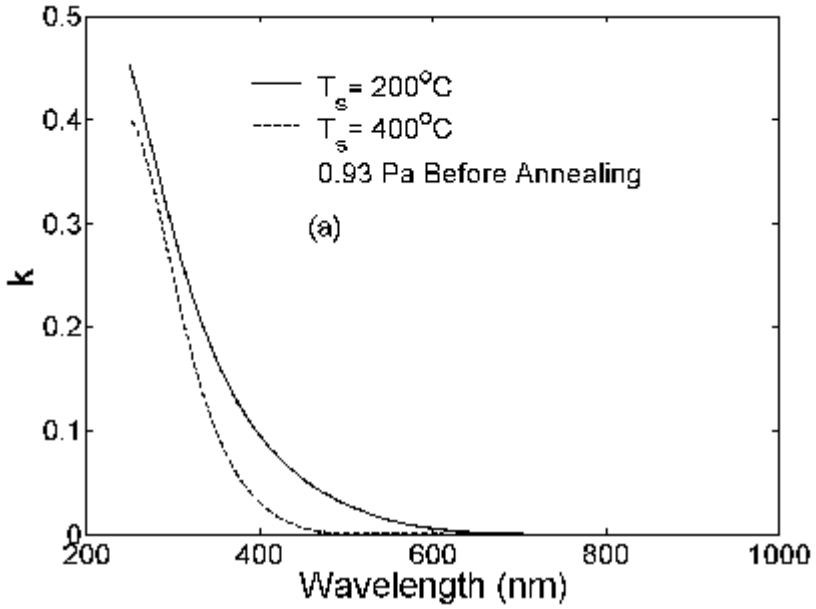

Figure 4.78(a). Extinction coefficients of as-deposited zinc stannate thin films versus wavelength for different substrate temperatures.

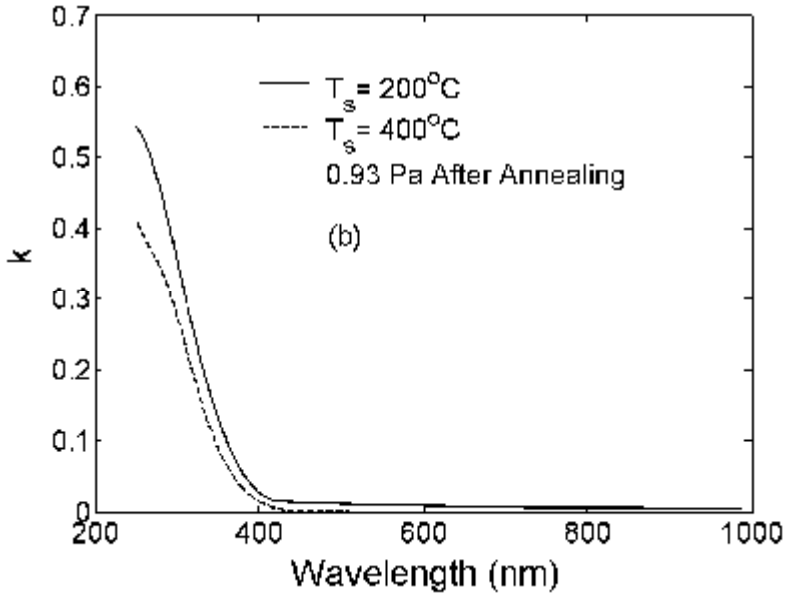

Figure 4.78(b). Extinction coefficients of annealed zinc stannate thin films versus wavelength for different substrate temperatures.

Increasing the substrate temperature decreased the extinction coefficients (Fig. 4.78(a)). The most significant change was observed, for films deposited on

200^{o}C heated substrates, in VIS range of the spectrum (400 to 600 nm). In Fig. 4.78(b), the extinction coefficients of zinc stannate thin films after annealing is seen, as can be seen after the annealing the extinction coefficients of films deposited on heated substrates decreased significantly at lower wavelengths (<400 nm). The decrease in *k* seen below 400 nm as a result of the annealing is very large.

The effect of annealing on the film optical constants that were deposited at 0.53, 0.80 and 1.06 Pa pressures is presented in Figs. 4.79(a-b). No correlation was found between the deposition pressure and the values of the refractive indexes of the as-deposited films, whereas, as seen from Fig. 4.79(b), in the VIS spectrum the values of the refractive index of all of the annealed films were approximately the same, independent of the pressure.

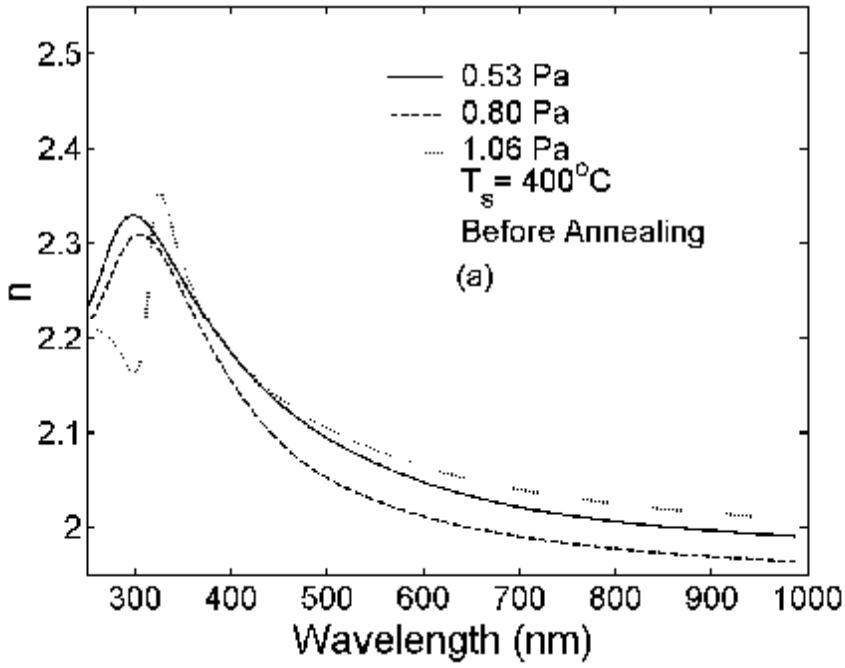

Figure 4.79(a). Refractive indexes of as-deposited zinc stannate thin films versus wavelength as function of deposition pressure.

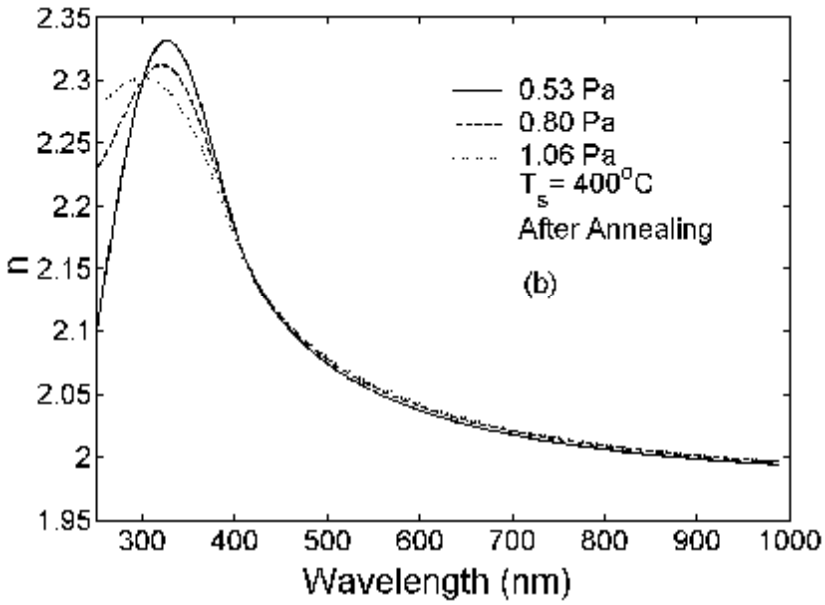

Figure 4.79(b). Refractive indexes of annealed zinc stannate thin films versus wavelength as function of deposition pressure.

In Figs. 4.80(a-b), the extinction coefficients of the zinc stannate thin films deposited with 150 A arc current on 400°C UVFS substrates and annealed films are presented.

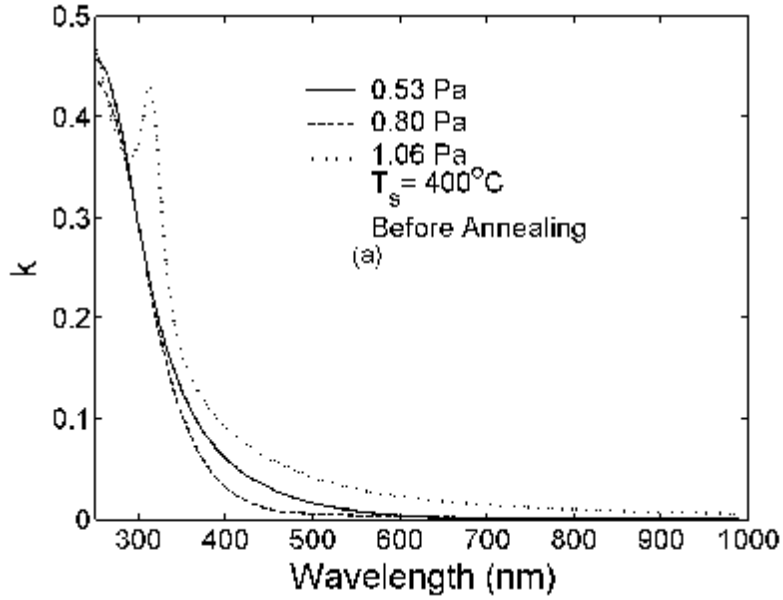

Figure 4.80(a). Extinction coefficients of as-deposited zinc stannate thin films versus wavelength as function of deposition pressure.

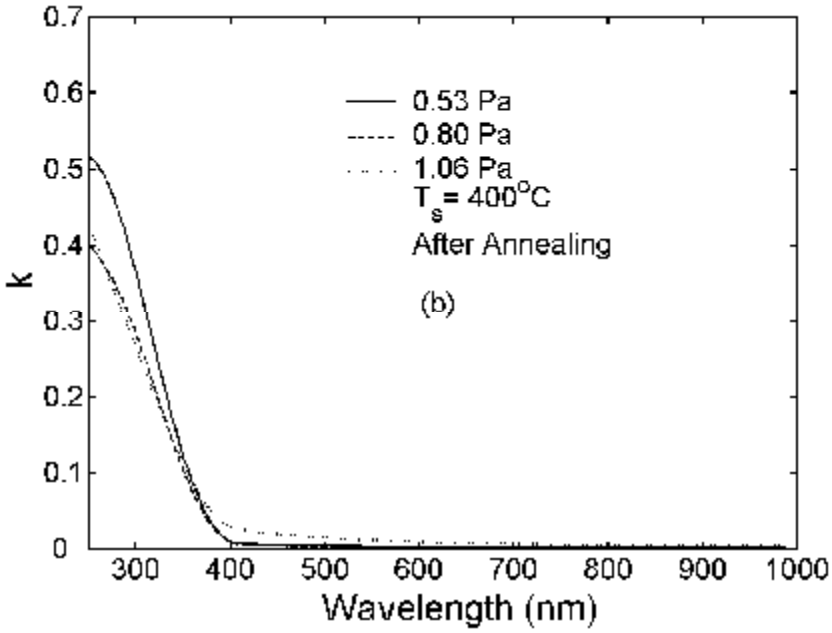

Figure 4.80(b). Extinction coefficients of annealed zinc stannate thin films versus wavelength as function of deposition pressure.

The annealing resulted in lower *k* values, and had lower values in UV region. The dependence of the extinction coefficient on pressure is seen to be significant only at λ<400 nm.

In Table 4.29, the values of the refractive index and the extinction coefficients at 550 nm, and the optical energy band gap for as-deposited zinc stannate thin films deposited with 150 A arc current on 200 and 400^{o}C heated UVFS substrates and annealed at 500^{o}C in Ar, are presented. The refraction index of films deposited on 200^{o}C heated substrates with 0.93 Pa pressure and later annealed at 500^{o}C in Ar was 2.14 and 2.05, respectively. In the case of films deposited on 400^{o}C substrates, the values of *n* varied with the deposition pressure (0.53 to 1.06 Pa), and were in the range 2.03-2.08. After annealing *n* of these films was ~2.05, independent of the deposition pressure. The values of *k* of as-deposited were in the range 0.004-0.03, decreasing by an order of magnitude after the annealing.

Table 4.29. Optical constants, n and k, at 550 nm, and the optical band gap E_g for as-deposited and annealed zinc stannate thin films.

Pressure (Pa)	n_D	n_A	k_D	k_A	E_{qD}(eV)	E_{qA}(eV)
0.53	2.07	2.05	0.010	0.002	3.61	3.65
0.67	2.06	2.05	0.010	0.002	3.64	3.66
0.80	2.03	2.05	0.004	0.001	3.70	3.69
0.93	2.04	2.06	0.001	0.0003	3.68	3.68
1.06	2.08	2.06	0.030	0.010	3.69	3.70
0.93 *	2.14	2.05	0.013	0.01	3.53	3.65

Annealing in Ar for 30 min /Films deposited on *200°C and 400°C substrates. D: as deposited, A: annealed.

It can also be seen in Table 4.29, the derived E_g values for as-deposited films were in the range 3.53-3.69 eV, and 3.65 to 3.72 eV for annealed films. The most significant change of E_g with annealing was observed for films deposited at 0.93 Pa oxygen pressure on 200°C substrates, as can also seen from optical transmission measurements.

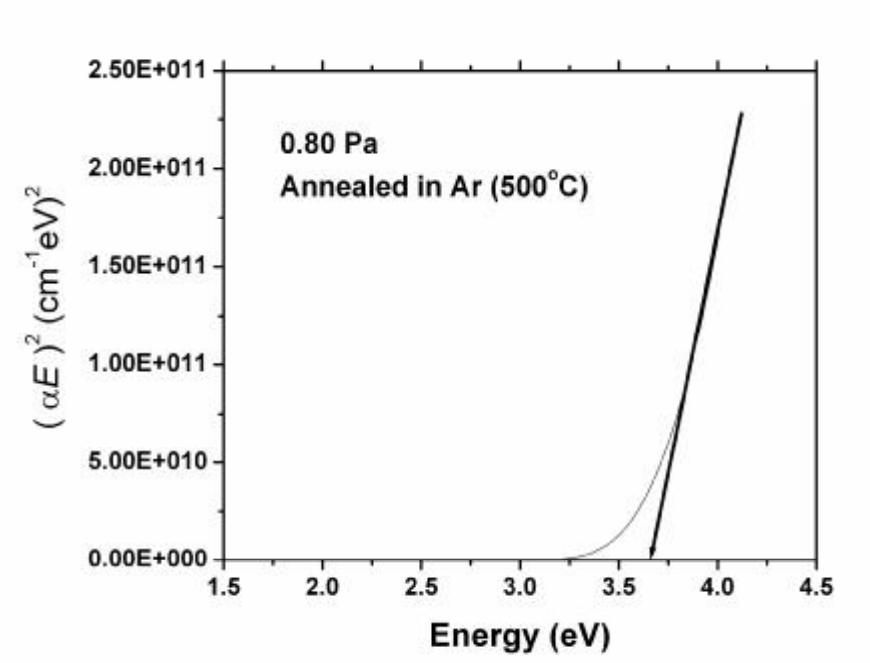

Figure 4.81. Plot of $(\alpha E)^2$ versus E

In Fig. 4.81, the plot of $(aE)^2$ versus E of zinc stannate thin film deposited on RT UVFS substrates using 150 A current at 0.80 Pa and annealed at 500°C for 50

min is presented as an example, where the straight line portion of the absorption spectrum is extrapolated to $(aE)^2 = 0$, to determine the value of E_g.

In Figures 4.82, plots of the optical transmittance versus wavelength of zinc stannate thin films deposited with 250 A arc current at 0.93 Pa on 400°C heated UVFS substrates, and annealed at 500°C in Ar for 50 min are presented. In Fig. 4.82, the optical band edge of the films shifted to the shorter wavelengths with annealing. In addition, in Figure 4.82, small increase in the optical transmission was observed in the VIS spectrum. The maximum and minimum film transmission in the VIS, as seen in Figures 4.82, were 70% and 90%, respectively, independent of the substrate temperature.

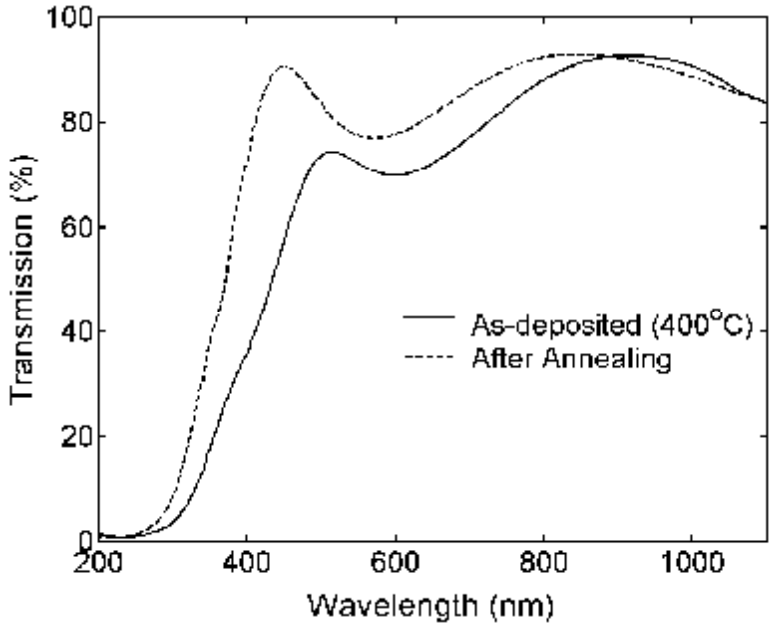

Figure 4.82. Plots of the optical transmission versus wavelength of zinc stannate thin films deposited on 400°C heated UVFS substrate with 250 A arc current at 0.93 Pa, and annealed at 500°C in Ar for 50 min.

In Figures 4.83(a-b), the refractive indexes and the extinction coefficients of zinc stannate thin films deposited with 250 A at 0.93 Pa oxygen pressure on 500°C heated substrates and annealed at 500°C in Ar for 50 min are presented. As seen from Figure 4.83(a), the refractive index of films decreased with annealing, and less dense films were obtained by the annealing. The refractive index of as-deposited films

decreased with increasing wavelength from 2.34 to 2.03, whereas, that of annealed films decreased from 2.3 to 2.0. Similarly, the extinction coefficients also decreased with the annealing. In the VIS range, the value of *k* (4.83(b)) was approximately zero, and no significant change was observed in this region. However, *k* of annealed films significantly decreased with increasing wavelength in the UV, from ~0.3 at 300 nm to approximately zero at 400 nm.

In addition to 500°C Ar and air annealing, some films were annealed at 600°C in Ar. However, the films annealed at 600°C had many cracks which prevented the optical measurements.

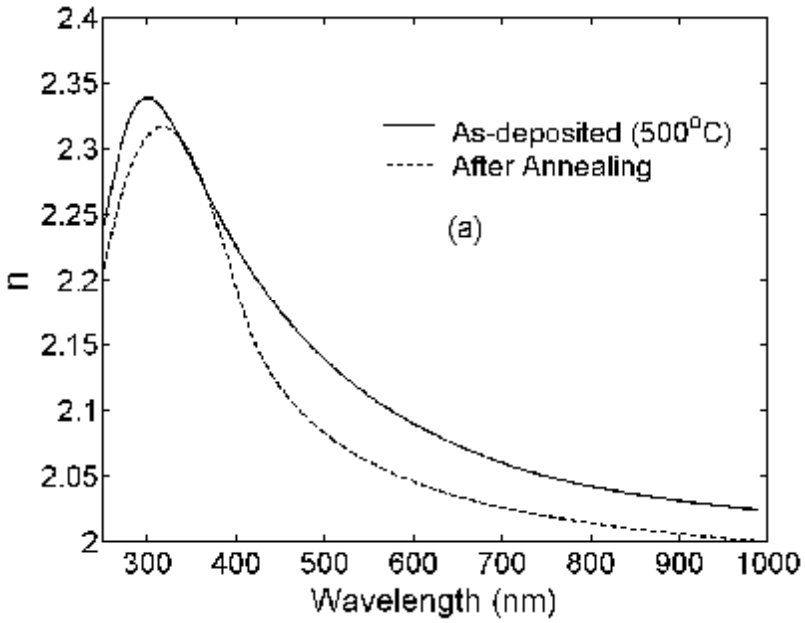

Figure 4.83(a). Refractive index versus wavelength plots of as-deposited and annealed zinc stannate thin films deposited with 250 A arc current at 0.93 Pa oxygen pressure 500°C heated UVFS substrates.

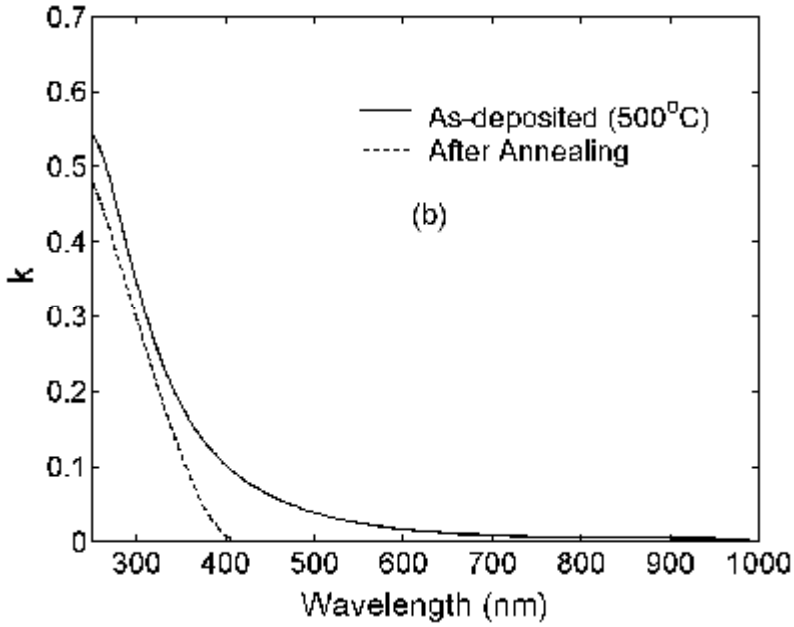

Figure 4.83(b). Extinction coefficient versus wavelength plots of as-deposited and annealed zinc stannate thin films deposited with 250 A arc current at 0.93 Pa oxygen pressure 500°C heated UVFS substrates.

4.3.6. Electrical Properties

The electrical properties of ZnO-SnO_2 and zinc stannate thin films were measured using the four point probe method as described in the experimental apparatus and procedure section (3.3.7). The sheet resistance R_s (Ω/square) and the resistivity of the films were determined as a function of the deposition parameters, i.e., substrate temperature, deposition pressure, cathode composition and arc current.

All RT deposited ZnO-SnO_2 and zinc stannate thin films independent of deposition conditions used, such as arc current, cathode composition, deposition pressure and time, were non-conducting. However, films deposited on heated glass or UVFS substrates were conducting. Although, the films deposited using 50 at.% Zn:Sn cathodes (zinc stannate) on RT substrates were also non-conducting, as can be seen from Table 4.30, the films deposited on substrates heated to 200°C at pressure ≥ 0.80 Pa were weakly conducting (r = 2.18×10^{1}-4.34×10^{2} Ωcm), and the resistivity

depended on the deposition pressure. All of the films deposited at 400°C were conducting, and their resistivities were 3-4 orders of magnitude less than the conducting films deposited at 200°C

Table 4.30. Electrical resistivity of zinc stannate thin films

Pressure (Pa)	Resistivity (Ωcm) RT	200°C	400°C
0.53	Non-Conducting	Non-Conducting	3.29×10^{-2}
0.67		Non-Conducting	1.78×10^{-2}
0.80		4.34×10^{2}	1.54×10^{-2}
0.93		1.85×10^{2}	1.08×10^{-2}
1.06		2.18×10^{1}	1.43×10^{-2}

In Figure 4.84, a plot of the resistivity of the conducting films deposited on substrates at 400°C, versus deposition pressure in the range 0.53-1.06 Pa is presented. The films deposited at 0.93 Pa had the lowest resistivity, ~1.08×10^{-2} Ωcm. With decreasing pressure and temperature film conductivity decreased.

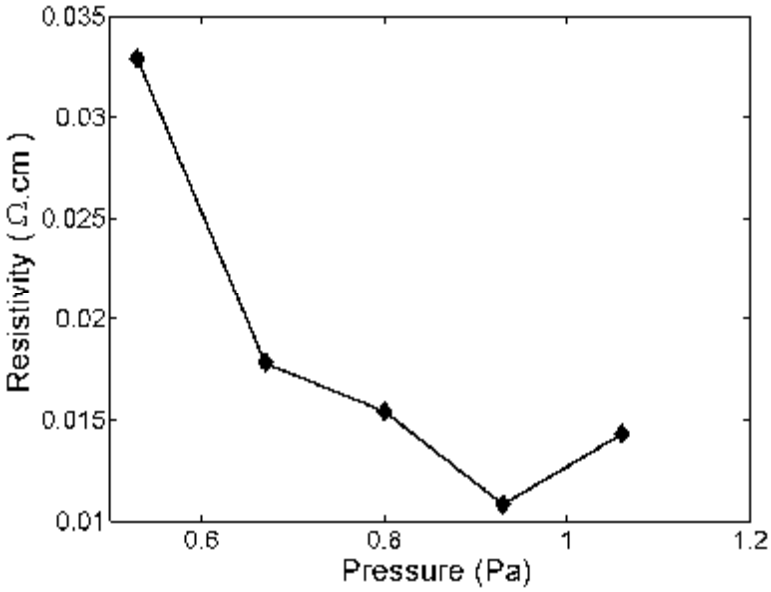

Figure 4.84. Electrical resistivity versus deposition pressure of zinc stannate thin films deposited on 400°C heated UVFS substrates.

The zinc stannate thin films deposited with 250 A arc current at 0.93 Pa oxygen pressure on RT kept substrates were non-conducting, whereas, the films deposited on 400and 500^{o}C substrates were conducting. The resistivity of films deposited with higher arc current (250 A) on 400^{o}C substrate temperature was 7.3×10^{-2} Ωcm, whereas, that of the films deposited on 500^{o}C was 1.63×10^{-2} Ωcm. Increasing substrate temperature also produced conducting films as observed for the films deposited with 150 A arc current.

In addition, the effect on the conductivity of annealing in Ar atmosphere was studied as a function of substrate temperature and deposition pressure. Annealing in Ar at 500^{o}C significantly increased the resistivity (to $>10^{5}$ Ωcm), at all substrate temperatures and the deposition pressures studied. Films annealed in Ar at 600^{o}C were cracked, preventing meaningful electrical measurements.

4.4. Chemical Stability

The chemical stability of these three types of TCO thin films were tested in HCl (18%) and NaOH (15%) solutions up to 27 h. The ZnO thin films deposited on RT and 400^{o}C substrates dissolved after ~10 min of immersion in both solutions. The RT deposited zinc stannate thin films also dissolved after approximately in 2 h immersion into the solutions. However, zinc stannate thin films deposited on 400^{o}C heated substrates were more stable than the RT deposited ones, as they did not dissolve after 27 h in NaOH, but they dissolved in HCl after 2 h.

In Figure 4.85, the transmission plots of zinc stannate thin films deposited on 400^{o}C substrates and immersed in NaOH solution is presented. As can be seen from the figure, the optical transmission of the zinc stannate film decreased in the VIS, but the transmission edge was not affected. The XPS analyses of the zinc stannate thin film treated by NaOH solution showed that the zinc concentration decreased and O concentration increased about 1%; change that was not significant experimentally.

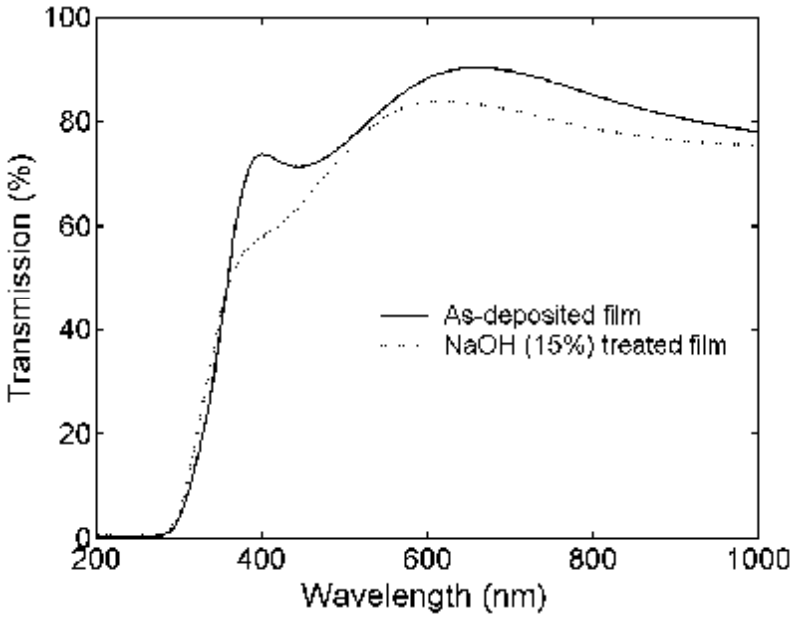

Figure 4.85. Plots of the optical transmission versus wavelength plot of zinc stannate thin film before and after NaOH solution treatment.

In Figure 4.86(a) and (b) plots of optical transmission of SnO_2 thin films deposited on 400^oC substrates before and after immersion in acidic and basic solution are presented, respectively. As can be seen from Figs. 4.86(a-b) the immersion in HCl, and NaOH of 400^oC deposited SnO_2 thin films did not affect their transmission. However, SnO_2 thin films deposited on RT substrates dissolved after 2 h when immersed in HCl solution, whereas, those immersed in NaOH did not dissolve even after 27 h. The XPS analyses of SnO_2 thin film deposited on 400^oC heated substrates treated by HCl solution showed that the atomic concentration ratio of O:Sn did not decrease and was ~2.09, whereas, that of immersed in NaOH solution decreased and was 1.97. The observed change in R_{OSn} ratio was not significant experimentally, since the optical transmission and the electrical resistivity of films were mostly constant.

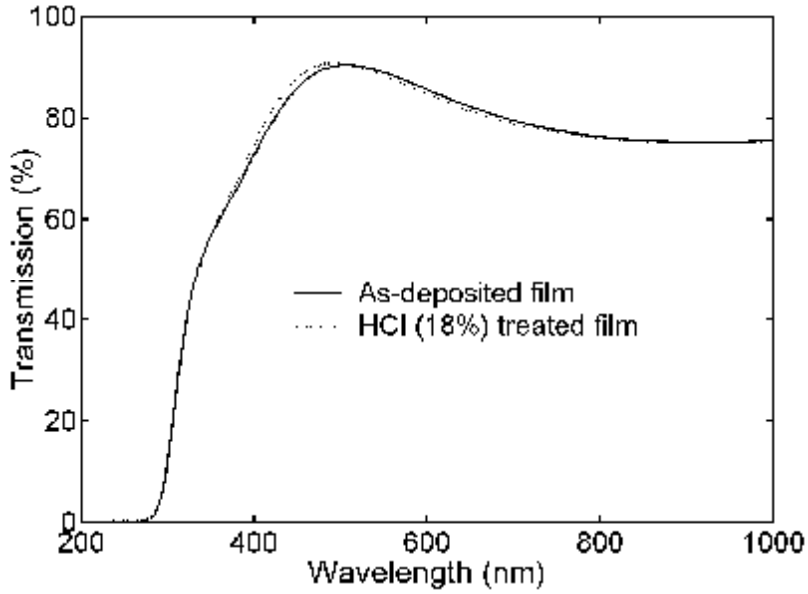

Figure 4.86(a). Optical transmission versus wavelength plot of SnO_2 thin film deposited on 400°C heated substrate before and after HCl (18%) solution treatment.

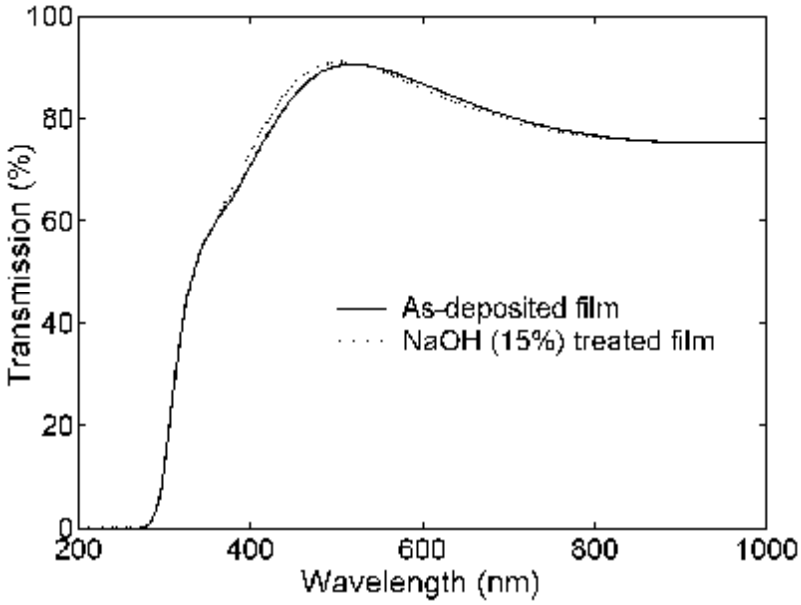

Figure 4.86(b). Optical transmission versus wavelength plot of SnO_2 thin film deposited on 400°C heated substrate before and after NaOH (15%) solution treatment.

In Figure 4.87 similar plots of the transmission of SnO_2 thin films, deposited on RT kept glass substrates using 150 A at 0.93 Pa, before and after immersion in NaOH solution are presented. In this case too, like the case of SnO_2 films deposited

on hot substrates, the immersion in a basic solution did not affect the optical properties.

The electrical resistivity measurements of SnO_2 thin films deposited on RT (only for NaOH) and 400°C (for both NaOH and HCl) substrates were not affected by the immersion in chemical solutions, and were in the range 10^{-3}-10^{-2} Ωcm. It should be recalled, that the effect of immersion in acidic and basic solution on the electrical properties of zinc stannate thin films could only be studied for films deposited on 400°C substrates. The immersion of zinc stannate in NaOH solution did not affect the electrical properties of films, having resistivity in the range ~10^{-2} Ωcm.

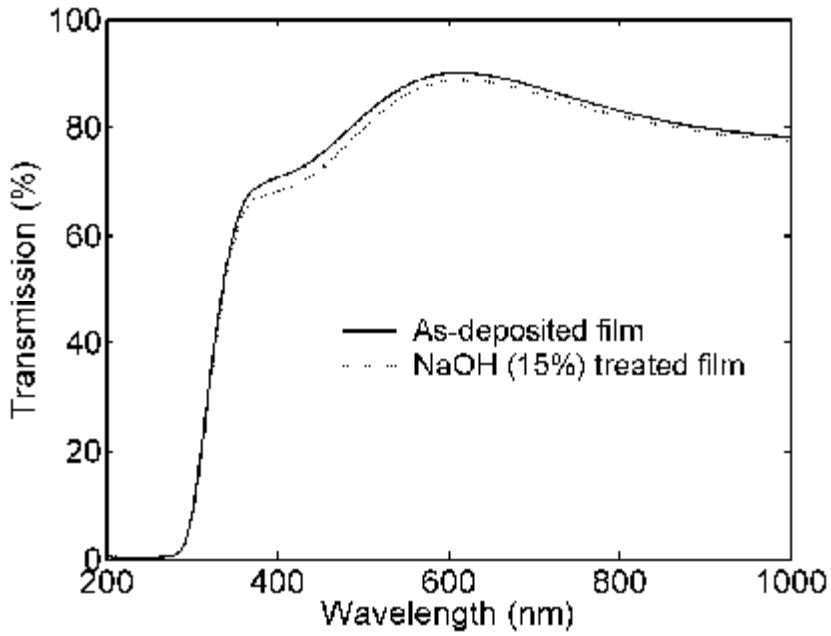

Figure 4.87. Optical transmission spectra of a SnO_2 thin film deposited on RT kept substrate, before and after NaOH (15%) solution treatment.

4.5. Thermal Stability

Thermal stability of the film electrical resistance was carried out by using two point probe technique to measure its resistance in the temperature range 28°C (RT) to 200°C, which is similar to that used by Minami *et al.* (1988, 1994, 1995), in their

study of the stability of ZnO, SnO_2 and zinc stannate films. In Figs. 4.88 (a), (b) and (c), the resistance versus temperature plots of ZnO, SnO_2 and zinc stannate thin films are presented, respectively. The ZnO and SnO_2 thin films used in the thermal stability investigation were deposited on RT glass substrates using 150 A at 0.93 Pa oxygen pressure, in addition, the zinc stannate thin films deposited on 400^oC glass substrates, 250 A arc current at 0.93 Pa oxygen pressure were also used in this investigation. The films selected for the thermal stability investigation were those which had the lowest resistivity. As can be seen from Figs. 4.88 (a) and (b), the resistance of ZnO thin films increased significantly at temperature >80^oC, by two orders of magnitude, whereas, the resistance of SnO_2 thin films (Fig. 4.88(b)) only increased at temperatures >150^oC. The resistance of zinc stannate thin films was less affected by heating in comparison to that of the ZnO and SnO_2 thin films. Their resistance increased only at temperatures >200^oC by factor of 2.

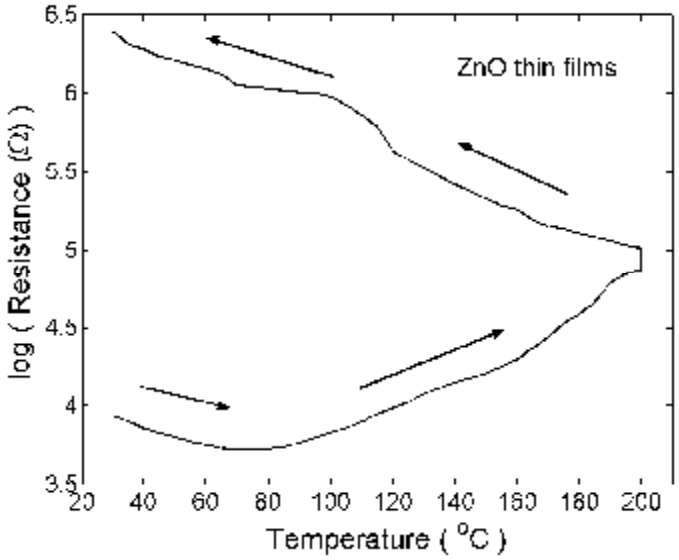

Figure 4.88(a). Electrical resistance versus temperature plot of ZnO thin film.

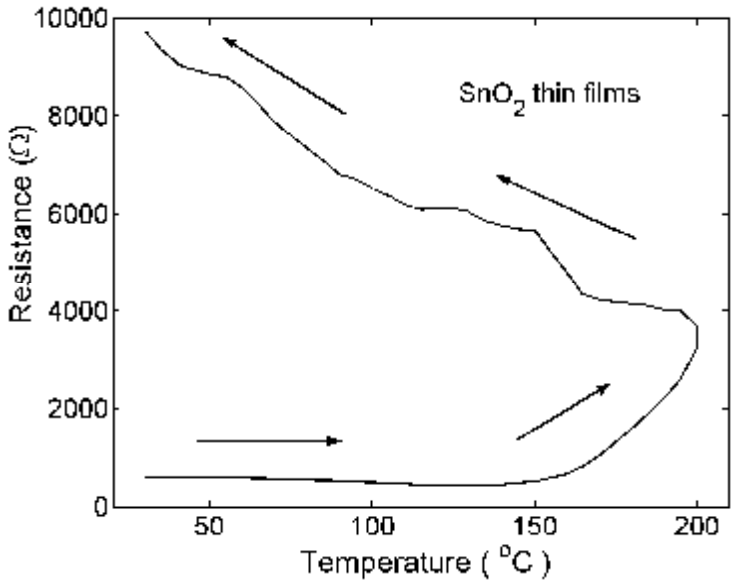

Figure 4.88(b). Electrical resistance versus temperature of SnO_2 thin film

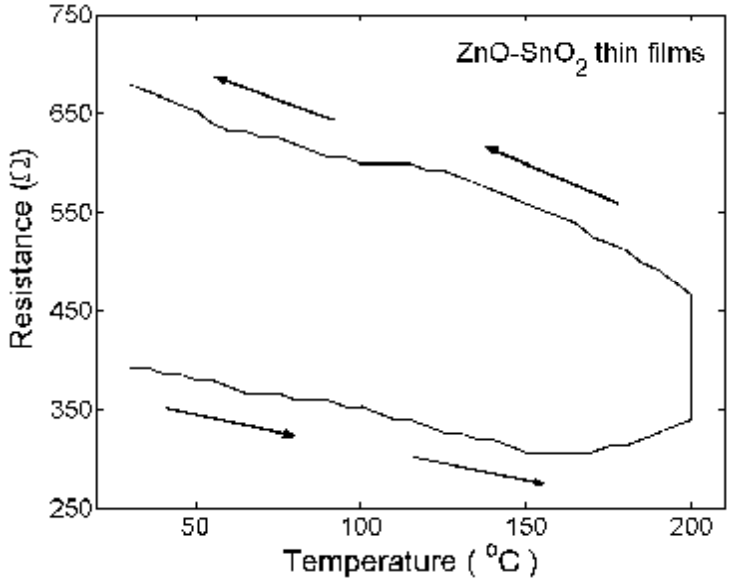

Figure 4.88(c). Electrical resistance versus temperature plot of zinc stannate thin film.

The plots in Figs. 4.88 indicate two interesting phenomena, (1) a hysteresis loop in the resistance as function of the heating and cooling cycle, and (2) the growth of the resistance continued also during the cooling part of the cycle.

5. DISCUSSION

5.1. ZnO Thin Films

5.1.1. Film Composition, Structure and Surface Morphology

The chemical composition of the ZnO thin films deposited using various deposition conditions was determined on their surface and in their bulk by XPS. The bulk composition of the films deposited using 200 A arc current at 0.79 Pa oxygen pressure composition was established to be stoichiometric, i.e. with a O:Zn atomic concentration of 1:1. However, this was not the general case, as films deposited with 150 A arc current at 0.53, 0.67 and 0.80 Pa on RT or heated substrates were non-stoichiometric, with an oxygen deficiency that varied with the deposition pressure (see Table 4.2). In addition, all ZnO thin films deposited on 400°C heated substrates were also oxygen deficient; however, the R_{OZn} of these films and also of annealed films was larger than that of RT deposited films. Thus by depositing the films on hot substrates or by annealing them a composition closer to stoichiometry was obtained. This increase in R_{OZn} is not always significant, as the data accuracy was ±3%. It should be also mentioned that R_{OZn} was closer to 1.0 at higher annealing temperatures, as the R_{OZn} of ZnO thin films was 0.93 and 0.98 when annealed at 400 and 600^{o}C, respectively.

The deficiency of oxygen in deposited ZnO films, and the effect of annealing or the deposition on hot substrates on that deficiency, is well documented in literature (Özgür *et al*., 2005, Goldsmith, 2006). In general, the deficiency decreases with the annealing when deposited in air or in an inert atmosphere. However, the effects of annealing on the chemical composition of ZnO thin films deposited at 600^{o}C by a PLD system and annealed at 600^{o}C in air were reported by Lu *et al*. (2000), who found that R_{OZn} was ~0.62 and 0.66 for as-deposited and annealed films, i.e., annealing did not markedly affect the stoichiometry. Schuler *et al*. (2005) determined R_{OZn} of rf magnetron sputtered ZnO films by

Rutherford Backscattering (RBS), obtaining R_{OZn} = 1.0. In their case, annealing in air increased the O content to >1 and produced highly resistive films.

The present film composition should be compared with that reported by David *et al*. (2005), who observed that ZnO thin films deposited using the same system and method were non-stoichiometric at arc currents <200 A, with R_{OZn} 0.68-0.80. The causes for the differences in R_{OZn} between the work of David *et al*. (2005) and the present one could be attributed to difference in the pressure stability during the deposition or the use of different magnetic fields in centering the plasma beam, and the arc current. However, at present, there is no definite explanation for the observed differences between this research and the work of David *et al*. (2005) in film composition associated with arc current.

The effect of deposition in air on the oxygen content can be attributed to oxygen diffusion into the film during deposition. Also ions trapped in the deposited material, e.g., Zn excess trapped in grain boundaries, could move and more readily combine with the diffusing oxygen. However, some competing processes could balance and even reverse this process. For example, at higher temperatures evaporation of excess Zn should also be considered.

The surface layer composition differed markedly from that of the bulk in that the film surfaces were oxygen excess for films deposited on RT substrates, and were oxygen deficient for films deposited on 400^{o}C heated substrates. The surface also contained significant concentration of carbon (C) atoms for RT deposited films, and in some cases Cu and small amounts of Cl. No correlation was found between deposition conditions and these impurities. The carbon source might be CO outgassed from the stainless steel deposition chamber, CO_2 absorption from atmosphere, and various solvents and pump fluids present in the deposition chamber. The source of the Cu and Cl atoms could be the copper cathode, and the diluted HCl (5%) used in cleaning the substrate, respectively. The excess of oxygen on the surface could be result from Zn-O bonds broken by highly energetic Zn ions during the deposition (Xu *et al.*, 2001b). The bulk composition of films deposited on RT and 400^{o}C substrates were oxygen deficient, whereas, the films deposited on heated substrates were closer to stoichiometry.

It was found in this study that highly *c*-axis oriented polycrystalline ZnO thin films with wurtzite type crystalline lattice were deposited using FVAD. Depositing on heated substrates and annealing in Ar improved the crystallinity and increased the average grain size, as could be seen in the increased intensity of the (002) line and the narrowed FWHM. Tse *et al*. (2004), who studied FVAD of ZnO thin films on 420^{o}C substrates, observed similar phenomena. Similarly, Liu and Özgür (Quoted by Özgür *et al*., 2005) observed that samples annealed at 950 and 1000°C showed the sharpest (002) XRD peak. This supports the hypothesis that the ions are rearranged during annealing (Thornton, 1977).

The displaced positions of the X-ray diffraction peaks also indicate that the films were stressed. As-deposited RT ZnO thin films were compressively stressed, as was found by David *et al*. (2005) and Wang *et al*. (2003). The compressive stress reported by David *et al*. (2005) was in the range -1.5 to -2.5 GPa and no correlation was found between the stress and the deposition parameters. Wang *et al*. (2003) showed that the thermal strain introduced during the deposition by the difference in the thermal expansion coefficients of ZnO and the substrate cannot explain the observed compressive strain, and suggested that the observed compressive stress is mainly caused by growth processes taking place during the deposition. In the present work, annealing with 400 and 600^{o}C produced tensile stress in films. Similarly, Chu *et al*. (2003) indicated that the compressive stress was relieved by 400^{o}C annealing, but that further increase in annealing temperature produced tensile stress in their ZnO films. The tensile stress resulted from the different expansion coefficients of the film and the substrates, hence, the differential contraction of the film and the substrates during cooling from high temperature to RT. Related results were reported when ZnO thin films, deposited by PLD, PECVD, rf and dc magnetron sputtering, were annealed with O_2 or N_2. Chu *et al*. (2003), Ogata *et al*. (2000), and Zhi *et al*. (2003), reported an increase in the XRD (002) line intensity and narrowing of the FWHM when ZnO thin films were annealed with temperatures in the range 500 to 900°C. The values for the average grain size in the film bulk reported by Zhi *et al*. (2003) were between 22 to 38 nm for annealing temperature below 600°C, very close to the 21 nm grain size obtained by us. Furthermore, the grain size

reported by Ogata *et al.* (2000) for ZnO films annealed in O_2 at 500°C was ~23 nm, similar to that reported by us. The increase in ZnO grain size with the increase of the annealing temperature can be related to the interface merging induced by the thermal annealing. The interface reactions can be related to the existence of interface defects at the grain boundaries. On the ZnO grain boundaries there are many zinc or oxygen defects (dangling bonds). These defects are amenable to merging, resulting in larger ZnO grains. In addition, the merging process is also indicated by the increase in the intensities of the diffraction peaks with the annealing temperature.

Typical AFM images of ZnO thin films grown using various deposition techniques under different deposition conditions indicated that the average surface grain size and surface roughness increase with substrate temperature and also with annealing. This increase was associated with the tendency of the grains to grow by fusing adjacent grains when sufficient energy for surface rearrangement is provided by the elevated temperature. Larger grains are associated with higher surface roughness. The present observation that the average grain size and surface roughness RMS of ZnO films increased with substrate temperature was also reported by Xu *et al.* (2001a), where the RMS was ~4.56 nm for films deposited on 430^{o}C substrates. They attributed the increase in the roughness to the increase in grain size. The increased surface roughness and average surface grain size with the annealing temperature was also reported by Liu *et al.* (2006) for FVAD ZnO films in which the surface roughness increased from ~1.2 nm to ~48.6 nm with annealing time in the range 1 to 60 min. In contrast, the morphology of rf magnetron sputtered ZnO thin films annealed at 100 and 400^{o}C in vacuum was reported by Chu *et al.* (2003), who found that surface roughness of films annealed for one hour at 400°C decreased to ~9 nm. This is the only case where annealing reduced roughness and denser and more homogeneous films were produced at higher annealing temperatures. In addition, the data presented by Chu *et al.* (2003) indicated that the average surface grain size was significantly larger than average grain size in the film bulk derived from the XRD FWHM, as found in the present work. The significant difference between the average grain size determined from XRD and AFM data is due to the fact that the AFM measurement is more sensitive to the surface structure and that of the XRD is

sensitive to the structure of the film bulk. The columns that grow during the deposition tend to have larger diameter at the surface, resulting in larger surface grains than average grain size in the film bulk (Thornton, 1977).

5.1.2. Film Optical and Electrical Properties

Only partial improvement of the TCO properties of ZnO thin films was achieved by the deposition on substrates heated to 400°C. On one hand, the deposition on the heated substrates increased the optical transmission and improved the crystallinity of the samples. On the other hand, the electrical conductivity of these films was markedly reduced, compared to that of films deposited on RT substrates by FVAD. This result disagrees with the conductivity increase reported by Xu *et al*. (2001a), who studied ZnO films deposited on 430^{o}C substrates, where they obtained increased conductivity. However, an increase in the resistivity, up to 1.32 Ωcm, was also reported by them for films deposited on 230^{o}C substrates Xu *et al*. (2001). Stoichiometric ZnO has high resistivity, as deficiency of oxygen is assumed to be the cause of conductivity (Tomlins *et al*., 2000). Thus, as the ZnO films deposited on heated substrates were found in the present research to be closer to stoichiometry, and the reduction in the conductivity could be associated with this. The improved stoichiometry of the films could be caused by increased diffusion of oxygen into the sample, and enhanced oxidation at higher temperatures. There is a definite relation between film composition and resistivity. It is generally assumed that the electrical conductivity of ZnO films is related to the existence of shallow donor levels near the conduction band formed by a large concentration of oxygen vacancies. This assumption agrees well with the observed oxygen deficiency (R_{OZn}<1). However, as shown by Zhang *et al*. (2001), the conductivity is related to Zn interstitials, also related to R_{OZn} <1. Hence, a decrease in Zn interstitials by annealing producing samples closer to stoichiometry should also result in films with higher resistivity. Thus, if the observed increase in R_{OZn} with annealing is significant, i.e., not an artifact of the XPS accuracy, the annealing at high

temperature is correlated with a decrease in Zn interstitials and produces more stoichiometric films.

The optical transmission in the visible region of all as-deposited ZnO films was in the range 80% to 85%. Heating the substrate during ZnO deposition did not affect the optical transmission in the VIS and the UV spectral range. In contrast, annealing increased the average optical transmission in the visible region up to 90%, however, it did not affect the optical band edge region (λ<400 nm). The improvement in the transmission also correlated with the increase in grain size (as observed by AFM and XRD), possibly because of reduced scattering by the grains.

The refractive index *n* of ZnO thin films deposited on hot substrates with oxygen pressure ≥ 0.67 Pa was considerably lower than that of films deposited on RT substrates with the same pressure. A lower *n* is generally associated with an increase of the density of voids in the film; hence, the on hot substrates could result in less dense films. It is usually expected that less voids would be found in films deposited on hot substrates, as the adatoms can move faster to proper locations. However, this is not the case here, and there could be several effects to cause it as described in the literature survey section (2.4): first, higher rate of sputtering and adatom reflection, and second, a higher rate of oxygen diffusion and inclusion trapping. The increase in the surface roughness with substrates temperature supports the assumption of larger void fraction. The presented *n* and *k* of the RT deposited ZnO films do not differ significantly from other reported data, obtained from as-deposited ZnO thin films by Yoshikawa *et al*. (1997), David *et al*. (2004) and Liu *et al*. (2006).

A significant decrease of *n* was also observed in the VIS region for films annealed at 400 and 600^{o}C, which could be related to changes in structure (e.g., the increase in surface roughness), composition, and film stress, caused by the annealing. More detailed study is required to identify the processes leading to the decrease in *n*. After the annealing, *k* also decreased with annealing temperature at wavelengths below the band gap. This decrease indicates weaker photon absorption by electron transitions across the band gap, where less intermediate defect levels could be present after the annealing. Liu *et al*. (2006) studied the influence of annealing on the optical properties of FVAD ZnO films as a function of annealing time in an O_2

atmosphere at 900^{o}C. In their case, *n* also decreased significantly with the annealing time; but *k* was not affected. They suggested a different mechanism for the *n* decrease, associating it to a larger surface layer and a larger interface layer between the film and the substrate. These were larger after annealing in their case, as the surface roughness increased significantly with the annealing. Hence the combination of ZnO and voids in the surface layer could effectively reduce the average film density. However, in the present experiment, the surface roughness change was negligible, and thus the reduction in *n* should be caused by another effect.

5.2. SnO_2 Thin Films

5.2.1. Composition, Structure and Morphology

The surface composition of all deposited SnO_2 films had an excess of oxygen, and some amount of C on the film surface, however, no correlation was found between the deposition conditions and the surface O and C concentrations. The ratio of oxygen to tin atomic concentration, R_{OSn}, was decreased from 2.14 to 1.99 in the film bulk by the annealing in Ar. This change in R_{OSn} could be attributed to oxygen desorption during the annealing. However, it is not evident if this effect is responsible for the change in R_{OSn}. The effects of annealing on FVAD deposited thin films were previously reported by Alterkop *et al*. (2003) in which they studied the effect of time (1 to 10 min) of air-annealing on the conductivity and composition of FVAD films, prepared under different deposition conditions. With relatively short annealing times (≤ 7min), R_{OSn} decreased, but it started to increase with larger annealing times. Unlike the composition observed in the present work, their films were found to be oxygen deficient in the bulk, with R_{OSn} first decreasing from ~1.85 to ~1.45 and increasing to 1.6 with longer (10 min) annealing. It is tempting to speculate that had Alterkop *et al*. (2003) investigated the effects of annealing at longer times (like ours), they would find similar R_{OSn} values. The composition of the material in the film could contain several intermediate compounds of tin and oxygen (Mäki-Jaskari *et al*., 2004). However, it was beyond the scope of this work to

explicate in detail the exact nature of the conductivity mechanism, as it is the subject of separate investigations. Furthermore, it was reported by Murken *et al.* (1973) and Moreno *et al.* (1992) that unstable compounds of tin oxide were formed in films consisting of excess SnO together with SnO_2. In our case, for as-deposited RT films, the excess of oxygen could be associated with the formation of unstable Sn_2O_3 or Sn_3O_4 phases in the interface between the stable oxides (Murken *et al.*, 1973, Moreno *et al.*), when annealed at 400^oC.

XRD indicated that FVAD SnO_2 films on RT substrates were amorphous, independent of the deposition pressure and arc current, in agreement with most reports in literature (Kaplan *et al.*, 1993, Parkansky *et al.*, 2003). Films deposited on heated substrates or annealed after deposition were, however, crystalline, and their XRD patterns clearly showed the diffraction of the SnO_2 phase, correlating with Sn^{+4}. As reported by Banerjee and Das (1987) tin oxide thin films could become amorphous when they deposited on RT substrates, however, when deposited on hot substrates in oxygen rich environment or annealed at high temperatures could become crystalline SnO_2. A similar change of phase of amorphous tin oxide was associated with the oxidation and crystallization of SnO during annealing (De and Ray, 1991). In the present experiment, post-deposition annealing of amorphous tin oxide in Ar at 400 and 600^oC produced polycrystalline, rutile SnO_2. It should be noted that the composition of the films deposited on heated substrates and those annealed at temperatures >400^oC had R_{OSn} close to 2, i.e., these films could not be amorphous SnO. The composition of the as-deposited films suggests that they were most probably amorphous due to deviation from the arrangement of the SnO_2 crystalline phase. The intensity of the SnO_2 XRD patterns of films annealed in Ar at 600^oC was significantly greater than that of 400^oC annealed films, and the FWHM of the lines were narrower, indicating an increase in grain size. In addition, more diffraction lines were observed after 600^oC annealing. As the annealing was done in Ar, oxidation phase transformation was unlikely, suggesting that the structure was rearranged by the annealing. Amorphous FVAD SnO_2 films on RT substrates were also reported by Ben-Shalom *et al.* (1993) and Alterkop *et al.* (2003). However, depending on the oxygen pressure during the FVAD, polycrystalline SnO and SnO_2

phases were observed after annealing in air or Ar at temperatures larger than 300^{o}C. Lower oxygen pressure resulted in SnO films. In the present work, the crystalline SnO phase was not observed after annealing in Ar, as the deposition pressure was greater than that reported by Ben-Shalom *et al*. (1993), and the films contained sufficient oxygen. Amorphous tin oxide films, deposited by evaporation and PLD, were reported by Shamala *et al*. (2004) and Chen *et al*. (2004) for SnO_2 films. The evaporated films were found to be amorphous in the temperature range up to 200°C, whereas films prepared on substrates at temperature of 300-370°C by spray pyrolysis were polycrystalline.

All deposited SnO_2 films consisted of nanometric grains, independent of the deposition method. The grains were affected by the post-deposition annealing and by the substrate temperature. PLD of SnO_2 films and subsequent micro-structural transformation induced by heat treatment at 150^{o}C for 2 h were reported by Chen *et al*. (2004), observing that the average grain size was approximately 6 nm. Song *et al*. (1999) and Choi *et al*. (1996) reported increased crystallinity of films as a function of the ion beam energy and different substrates, where the average grain size was in the range 7-10 nm for as-deposited films. The data presented by Chen *et al*. (2004) indicated that the average grain size of annealed films was larger than the average grain size of as-deposited films, as found in the present work. The values for the average grain size in the film bulk reported in the literature are 6 to 11 nm for as-deposited and annealed SnO_2 films, respectively, very close to the 8-9 nm obtained by us for 400^{o}C annealed films.

The average surface grain size was observed in the present work to increase from 21 nm (RT) to 36 nm (400°C) and to 46 nm (600°C) with annealing. Similarly, the surface roughness also increased with the annealing temperature. This increase was associated with the tendency of the grains to grow by the fusion of adjacent grains when sufficient energy for surface rearrangement is provided by the elevated temperature. Larger grains are also associated with higher surface roughness. Typical surface images of SnO_2 thin films grown using various deposition techniques were presented by Di Giulio *et al*. (1993), Song *et al*. (1999), Alterkop *et al*. (2003), and Chen *et al*. (2005). Di Giulio *et al*. (1993) also reported that the grain size of

reactively sputtered SnO_2 films increased from 12 nm (as-deposited) to 92 nm with annealing after at 450^oC for 1 h. Chen *et al*. (2004) obtained TEM images of SnO_2 films, annealed at 300^oC for 30 min, observing 8-12 nm grains. This grain size, however, was larger than that derived from XRD. They attributed this grain size difference to significant agglomeration of the grains on the surface. We also observed differences in the average grain size determined from AFM and XRD data, where the AFM is sensitive to the surface structure and XRD to that of the film bulk (as also observed for the ZnO thin films). This difference could be attributed to columnar growth of films during deposition that tends to have larger diameter at the top of the column, resulting in larger surface grains than the average grain size in the film bulk (Thornton, 1977). Alterkop *et al*. (2003) who also studied the effect of film thickness, annealing temperature and time on FVAD SnO_2 thin films, found a dependence of surface roughness on film thickness, but only weak dependence on the annealing time. As a function of film thickness the surface roughness was 4.4 nm and 2.6 nm for 150 and 780 nm thick films, respectively.

5.2.2. Optical and Electrical Properties

The optical transmission of the SnO_2 films in the visible spectral region was in the range 85% to 90 %, similar to that reported previously in the literature (e.g., Di Giulio *et al*., 1993, Shamala *et al*., 2004) and did not differ from that reported for previous FVAD thin SnO_2 films (>85%) (Kaplan *et al*., 1993). The transmittance of SnO_2 films in the UV region was strongly affected by the annealing, which produced a steep gradient in the film transmission in this region, shifting the optical transmission edge to shorter wavelengths, and indicated that the annealing widened the optical band gap with fewer defects in the band gap. Similarly, FVAD of SnO_2 films on hot substrates also shifted the optical transmission edge to shorter wavelengths, produced a steeper gradient in the transmission in this region, and significantly increased the average optical transmission. The most noticeable effect was observed on films deposited with 0.53 Pa, where the average transmission in the 400–1100 nm range increased from 58% to 85%. A similar increase in the average

transmissions, from 75% to 85 %, was observed by Hamzaoui and Adnane (2000), for sputtered SnO_2 thin films deposited on 50°C and 350°C substrates. The shift in the optical band edge to shorter wavelengths and the sharp slope of the transmission curve edge again indicated that when hot substrates were used the optical band gap was larger and had fewer inter-gap defect levels. It should be noticed that the observed dependence of the band gap on the deposition pressure and substrate temperature could in principle be related to a change in carrier concentration, the Burstein-Moss effect, and also the improved structure of SnO_2 films. The Burstein-Moss effect in band gap broadening requires a significant increase in the carrier density, which increases the conductivity. De and Ray (1991) and Banerjee (1987) reported that the increasing of E_g observed by them in SnO_2 was due to the Burstein-Moss effect, where the former reported an increase of E_g from 3.83 to 4.13 eV, and the latter from 3.5 to 4.4 eV. However, as is discussed below, we suggest that the effects of film composition and improved structure are a more significant in increasing the values of E_g.

In films consisting of SnO, SnO_2 and intermediate compounds, regions of low E_g (E_g(SnO) ~2.7 eV) and regions of high E_g (E_g(SnO_2) ~3.9 eV) could be found at different locations on the same film (Choi *et al.*, 1995). The overall effect of such film composition is to move the absorption edge to a longer wavelength and to lower the effective value of E_g (derived from the absorption coefficient data). This situation was observed with films deposited on RT substrates at 0.53 Pa pressure where E_g = 3.6 eV, smaller than the 3.9 eV obtained with films on hot substrates, indicating the presences of a small fraction of SnO in the films. However, as E_g was in the range 3.90-3.98 when the films were deposited on hot substrates, or when deposited with 0.8 Pa on RT substrates, we conclude that the under such conditions the SnO concentration was significantly reduced. The observation that only SnO_2 lines were observed in the XRD spectra of films deposited on hot substrates, (i.e. no SnO lines) supports this conclusion.

The optical constants n and k depended on the deposition conditions. The values of n of tin oxide films deposited on RT substrates were close to those reported by Shamala *et al*. (2004) and Hamzaoui and Adnane (2000), 1.88 – 2.05, for films

deposited on heated substrates. The value of *k* in the VIS region generally decreased when deposited on hot substrates, indicating weaker photon absorption by electrons transitions to defect levels within the band gap, i.e., less inter band gap defect levels were present. It should be noted that the optical transmission of films deposited on RT substrates with 0.53 Pa had relatively low transmission compared to high deposition pressures, resembling that presented by Ben-Shalom *et al.* (1993), and indicating larger *k* values.

The values *n* and *k* presented in the current work do not differ significantly from those of as-deposited and annealed SnO_2 thin films reported in the literature (Demiryont *et al.*, 1987, Isidorsson *et al.*, 1998, Mukhamedshina *et al.*, 2006). The *n* and *k* values reported by Mukhamedshina *et al.* (2006) decreased with annealing (at 200-550^{o}C) in the VIS λ>500 nm, from ~2.1 to 1.9. In addition, the shift of the refractive index peak to shorter wavelengths with annealing temperature occurred together with the shift of the optical transmission edge. The decrease of *k* in the shorter wavelength region after annealing corresponded to improved UV transparency and decreased absorption coefficient. The decrease of *k* indicated weaker photon absorption by electron transitions to defect levels in the band gap, indicating that after annealing there are fewer inter-band defects. We believe that the change in the phase of SnO_2, i.e., reduction or elimination of SnO, increased E_g, and changed the optical parameters.

The change in the oxide composition and structure caused by the deposition on heated substrates resulted not only in improved UV transmission but also affected the electrical conductivity. This effect is more intricate, as it involves changes of the electron carrier density and the mobility. It was argued by Samson *et al.* (1973), that the electrical conductivity of TCO films is related to the existence of shallow donor levels near the conduction band formed by a large concentration of oxygen vacancies. However Kılıç and Zunger (2002) showed that tin interstitials are more effective in producing the shallow donor level. Thus, according to these arguments, conductivity requires non-stoichiometric composition with tin excess. The mobility was shown to depend on the grain size and the grain boundary potential (Barsan and Weimar, 2001, Oprea *et al.*, 2006). The composition and resistivity measured in the

current work conflict with the models mentioned above, as films with excess of oxygen were conducting. Thus, the resistivity of the tin oxide films deposited on RT substrates was (7-9)×10^{-3} Ωcm, depending weakly on the deposition pressure, and the resistivity of the 400^{o}C deposited films was higher by one or two orders of magnitude. The observed conductivity with oxygen excess could be explained by assuming that the oxygen excess is not distributed uniformly in the film bulk, as the films could consist of physically connected regions which were oxygen deficient, distributed throughout the film, and in which the current was conducted. In fact, having R_{OSn} >2 does not exclude the presence of tin interstitials in distinct connected islands, whereas the XPS data represent an average bulk value. Tin and oxygen interstitials also produce shallow donor and acceptor levels, but the effect of tin interstitials is much stronger. Hence although we found R_{OSn} >2, we assume that the observed conductivity should be due to locally distributed tin interstitials and not oxygen vacancies. The low conductivity of annealed samples could be explained by a decrease in the islands of tin interstitials during the annealing, i.e., the destruction of separated regions with high content of oxygen or high content of tin. Furthermore, annealing in Ar could reduce the oxygen excess by desorption. Increasing the uniformity and order of the film structure correlates reasonably well with the improvement in the UV transmission.

5.3. ZnO:Sn / Zinc Stannate Thin Films

5.3.1. Film Composition, Structure and Morphology

Cathodes with several different Zn and Sn concentrations were used to deposit ZnO:Sn and zinc stannate, in order to investigate the effect of Sn doping in ZnO thin films and the properties of zinc stannate thin films. When the Zn to Sn atomic concentration ratio in the cathode was 1:1, the ratio in the film was close to 1:1, deviating by no more than ±2%. However, the films deposited using 10at.% and 30at.% of Sn in the cathode contained only 10at.% of Sn in the film bulk.

Minami *et al*. (1995, 2005) used vacuum arc evaporation and magnetron sputtering using 1:1 cathodes to deposit ZnO-SnO_2 thin films, and obtained a film composition close to that of their cathodes.

As mentioned in chapter 4, all XRD patterns indicated that the ZnO:Sn and zinc stannate thin films were amorphous. Amorphous ZnO:Sn and zinc stannate thin films were also deposited by Moriga *et al*. (2004) and Young *et al*. (2002b), using magnetron sputtering, and Minami *et al*. (2005) using vacuum arc evaporation. Moriga *et al*. (2004) studied the structure of ZnO-SnO_2 thin films deposited at 150^{o}C, 250^{o}C and 350^{o}C with Zn:Sn atomic ratios in the range of 0-1. The crystallinity of the films depended on the composition and the deposition temperature. With low Zn content, below ~20%, only the diffraction lines of SnO_2 were observed, while with Zn content larger than 80%, only ZnO lines were observed. In the intermediate region, the films were amorphous. However, by post-deposition annealing at 660^{o}C, the films become crystalline. Young *et al*. (2002b) found that RT deposited zinc stannate was amorphous. The Zn to Sn atomic concentration ratio was in the range ~1.4-1. A similar observation was made by Minami *et al*. (1995) who found that ZnO-SnO_2 films, deposited using vacuum arc evaporation and magnetron sputtering at 300^{o}C were amorphous when the Zn atomic concentration ratio was in the range 20-80%. When Minami *et al*. (1995, 2005) used a cathode with Zn to Sn atomic ratio of 1:1 to deposit zinc stannate thin films, they also obtained film composition with a ratio of ~1:1.

The surface roughness of zinc stannate films (~0.2 nm) derived from AFM images was comparable to that reported by Wu *et al*. (1997), but the grain size was smaller than that presented by Young *et al*. (2002a) (~100 nm). In comparison, the surface layer thickness (which should not be equated with roughness) obtained from ellipsometry analyses were in the range 0-0.8 nm. The morphology of the films represented by Young *et al*. (2002a) differed significantly from that presented here, having larger grains and less roughness.

5.3.2. Optical and Electrical Properties

The optical properties of the ZnO-SnO_2 and zinc stannate thin films were derived from the measured transmission and ellipsometric data. As was presented above, the transmission of the films between 400 to 700 nm was high, in the range 80 to 90%, as was also reported by others (Minami *et al.*, 1994, Young *et al.*, 2002a, Moriga *et al.*, 2004). The films deposited on heated substrates and those later annealed had also an average transmission in the VIS of ~80% to 90%. In the UV, however, the substrate temperature and the annealing had a significant effect on the optical transmission. After annealing, the UV transmittance edge shifted to shorter wavelengths, and had a steeper gradient in this region, indicating a well defined and a wider optical band gap. Crystal's defects and disordered material could affect optical transmission and electronic properties. The effect on the optical properties could be established from the transmission spectra, whose dependence on wavelength was affected by defects and disorder that could be associated with band tailing. As the optical transmission edge shifted with substrate heating and annealing, it is plausible that annealing and substrate heating reduced the band tailing and crystallization had only a secondary role. This hypothesis is supported by the observation that annealing or deposition on heated substrates improved UV transmission even though the films remained amorphous. Furthermore, it was observed that the improved UV transmission after annealing was more significant in films that were deposited at lower pressures than in films deposited at higher pressure, whereas the band tailing was stronger in films deposited at lower deposition pressures (<0.80 Pa). The optical transmission is mostly determined by the film thickness, the optical refraction index n and the extinction coefficient k. It is worthwhile, therefore, to analyze the dependence of these three parameters on the deposition conditions in order to obtain the general dependence of the transmission on the deposition conditions. For this purpose, the optical parameters and their dependence on the deposition conditions were derived in the present work from ellipsometry data, and as presented above were indeed found to depend on the deposition conditions. The values and the dependence on wave length of the optical

parameters, *n* and *k*, of the films that are reported here do not differ significantly from the values reported by Young *et al*. (2002a) and Satoh *et al*. (2005) for as-deposited films, although a different deposition method was used (rf-magnetron sputtering). Thus, the value of *n* decreased with wavelength from ~2.3 at 300 nm to 2 at 1000 nm, and the value of *k* decreased from 0.6 at 300 nm to practically zero at 600 nm. The values of *n* and *k* at 550 nm reported by Young *et al*., (2002a) and 600 nm Satoh *et al*. (2005) were approximately 2 and zero, respectively. It should be noted that (1) values of *n* and *k* of films deposited with different deposition methods, were very close and (2) the optical parameters decreased rather moderately with wavelength, and (3) the decrease was much stronger in ZnO and SnO_2 (See optical analyses results in Experimental Results Section for ZnO and SnO_2 thin films). The refraction index of the zinc stannate films differed from that of the ZnO-SnO_2 thin films by having a peak value at ~300 nm. This peak was not observed with ZnO-SnO_2 thin films. The peak in the refractive index vs. wavelength curve was not affected significantly by the annealing -- it did not shift to the shorter wavelengths, and was not correlated with the shift of the UV transmission edge. The UV transmission edge shift is correlated with the decrease of *k* in the shorter wavelength region after annealing, which improved the transparency in the UV region. As in the case of ZnO and SnO_2 thin films, this decrease of *k* indicated weaker photon absorption by electron transitions to inter-band gap levels, indicating that fewer intermediate defect levels were present after the annealing. As no transformation to crystalline zinc stannate or ZnO-SnO_2 by annealing or by deposition on hot substrates was observed, it is not possible to correlate the improvement of the UV transmission with an increase in structure order. It is possible, yet, to assume the density of dangling bonds was reduced by annealing and by use of hot substrates, and this correlates with improved UV transmission. The increase of E_g, whose values were derived from the absorption coefficients, also indicates a decrease in inter-band gap defects. The reported optical band gap of the films by Young *et al*. (2002a) was in the range 3.35-3.89 eV, within the range observed by us (3.43-3.70 eV).

The effect of substrate temperature and pressure on *n* and *k* was analyzed statistically by using ANOVA single and two factor variance analyses to determine

the significance of the difference between sets of *n* and *k* according to the deposition parameters. The chosen level of significance was 0.05 (Lurie and Moore, 1994). As function of pressure, there were 10 sets of *n* and *k* ordered by the deposition temperature, and as function of temperature there were 6 sets of *n* and *k*. The sets of *n* and *k* derived for films with a pressure of 0.80 Pa with temperatures of RT, 200^{o}C and 400^{o}C are significantly different, as was demonstrated in Figs. 4.57 and 4.58, where the dependence of *n* and *k* on wavelength is not ordered according to temperature. We concluded that substrate temperature had a marked effect on the optical constants. Furthermore, the lowering of *n* with annealing is problematic, as it could indicate a decrease of film density with annealing, i.e., a possible increase in voids in the film or reduced defects by annealing. However, it is not evident that annealing produces voids, and this issue requires further study.

The discreet values of *n* and *k* at wavelengths 250, 300, 400, 500, 600, 700, 800, and 900 nm, were analyzed statistically using two factor ANOVA, where the factors were deposition pressure and deposition temperature. As shown before, the temperature was found to be a good discriminator at 600, 700, 800 and 900 nm for *n*, however, the deposition pressure did not have a significant effect on *n* at longer wavelengths (>500 nm). In addition, the extinction coefficient *k* did not depend significantly on the deposition conditions (pressure and temperature) for wavelength >500 nm. Below 500 nm *k* did not depend on pressure except at 250 nm. *k* did not depend significantly on the substrate temperature except at 300 nm. The refractive index *n* did not depend on temperature or pressure for wavelengths below 400 nm, however, at 400 and 500 nm *n* was affected by temperature, and not affected by pressure at 500 nm.

In Table 4.28 the parameters E_o and E_d of Wemple and DiDomenico (1971) are listed, where the first signify the oscillator energy and the latter the quantum oscillator strength. This is the first time that these parameters are reported for zinc stannate. Two interesting observations are made when the films are annealed. First, the oscillator energy increases with the annealing, second, the transition strength is also markedly larger after the annealing. This can be interpreted as an improvement in the energy levels in the material, although it remains amorphous.

The resistivity of the $ZnO\text{-}SnO_2$ and zinc stannate films is a very significant condition for their use as replacement material to ITO. The lowest resistivity $ZnO\text{-}SnO_2$ and zinc stannate films observed in the current work is higher by at least one order of magnitude than that of ITO ($\sim 10^{-4}$ Ωcm). This relatively low conductivity of $ZnO\text{-}SnO_2$ and zinc stannate films had been already noted before, in the study of these films deposited using other methods. Other investigators also reported a dependence of the resistivity on the deposition conditions. Thus, Moriga *et al*. (2004) observed that their resistivity of $ZnO\text{-}SnO_2$ thin films depended on the Zn:Sn concentration ratio, and the deposition temperature. Films deposited at 150°C with Zn:Sn concentration ratio in the range 1:4-4:1, i.e. amorphous films, had resistivity in the range 10^{-1}-1 Ωcm. Lower resistivity, in the range $(1\text{-}5)\times 10^{-2}$ Ωcm, was reported by Young *et al*. (2002a), also for amorphous films. Minami *et al*. (1995) also observed a dependence of the resistivity on Zn:Sn concentration when the films were amorphous: resistivity (r) in the 10^{-2}-10^{-1} Ωcm range. In the present research, the films deposited at 400°C showed the lowest resistivity whereas the others were non-conducting. The resistivity of these films decreased when the pressure increased from 0.53 to 0.93 Pa, and then increased with further increase in the pressure. Similar temperature dependence of these films resistivity has been reported previously (Perkins *et al*., 2002, Young *et al*., 2002a, Moriga *et al*., 2004, Minami *et al*., 2005). Local minima in the temperature dependence of resistivity were reported by Moriga *et al*. (2004), Young *et al*. (2002a) and Perkins *et al*. (2002) were in the range $2\text{-}5\times 10^{-2}$ Ωcm for films deposited at 350°C, $4\text{-}6\times 10^{-2}$ Ωcm at 550-650°C and 2×10^{-2} Ωcm, respectively.

The effect of substrate temperature and deposition pressure on the film resistivity was not systematic. Although all films deposited on RT and 200°C substrates and at lower pressure were non-conducting, the films deposited on 200°C substrates but at higher pressure were conducting. In contrast, all films deposited on 400°C substrates were conducting. The films deposited on 400°C substrates with 0.93 Pa pressure had the lowest resistivity. The post-deposition annealing in Ar at 500°C had a different effect than that of depositing on hot substrates; it produced non-conducting films with resistivity $>10^{5}$ Ωcm independent of deposition

conditions. Satoh *et al*. (2005) also studied the effect of Ar/O_2 flow ratio on film resistivity and the post-deposition annealing. The films deposited with Ar/O_2 mixture had ~10^5 Ωcm resistivity, whereas, the films deposited in pure Ar had on the order of 10^{-2} Ωcm. Post-deposition annealing yielded a number of cracks, and thus the electrical properties could not be measured. This was attributed to the different thermal expansion coefficients of the substrate and the film.

5.4. Chemical and Thermal Stability of ZnO, SnO_2 and Zinc Stannate Thin Films

An important additional factor in evaluating the applicability of a TCO material is its stability in aggressive environments. This criterion should be considered together with its inherent electrical and optical parameters. In the present work, in addition to the study of the optical and electrical characteristics of FVAD ZnO, SnO_2, ZnO-SnO_2, and zinc stannate thin films and their dependence on the deposition conditions, their stability in thermal, acidic, and basic environments was determined and compared.

FVA deposited zinc stannate thin films on 400^{o}C substrates were more chemically stable than any FVAD ZnO films. However, SnO_2 thin films had an advantage over both ZnO and zinc stannate thin films, being more chemically stable than the others. The electrical resistances of SnO_2 and zinc stannate thin films, which did not change after immersion in acidic and basic solutions, remained 10^{-3} and 10^{-2} Ωcm for SnO_2 and zinc stannate thin films, respectively. These results indicate the advantage of using SnO_2 thin films in chemically aggressive environment.

The variation of film resistance during film heating depended strongly on its material. Generally film resistance started to increase after a certain critical temperature. Beyond this temperature, the resistance could increase by several orders of magnitude. This observation has important implication if such TCO films are to be used in hot environments. The lowest critical temperature was observed for ZnO. ~80^{o}C, while that of SnO_2 was higher (~145^{o}C). However, that of zinc stannate was ~200^{o}C, implying that zinc stannate is more applicable in hot environments. It is

interesting to note that during cooling, the film resistance continued to increase, however at a lower rate. The films cooled to RT had relatively high resistance, with ZnO having the largest resistance after reaching RT, and zinc stannate the lowest. Such irreversible change of the resistance limits the applicability of the films at elevated temperature. Similar results were also reported by Minami *et al*. (1988, 1994, and 1995), for rf magnetron sputtered ZnO, SnO_2 and zinc stannate thin films.

The variation in resistivity as a function of substrate temperature could be attributed to a change in the oxygen content of the film. This assumption agrees well with the models of Tomlins *et al*. (2000), and Kılıç and Zunger (2002) for the conductivity of ZnO and SnO_2, where excesses of Zn and Sn are essential to obtain conductivity in these oxides. Hence, possibly the increase in the resistance with temperature of ZnO and SnO_2 resulted from oxidation. It is not currently possible to similarly explain the resistance increase of zinc stannate, as no equivalent conductivity model was reported.

In summary, the resistance of FVAD zinc stannate thin films on heated substrates was more thermally stable than that of ZnO and SnO_2 thin films. In addition, SnO_2 and zinc stannate thin films were more chemically stable than the ZnO thin films; however, SnO_2 thin films were more stable in acidic solution than the others.

6. SUMMARY and CONCLUSIONS

The filtered vacuum arc deposition (FVAD) system was successfully used to deposit thin ZnO, SnO_2, ZnO:Sn and zinc stannate films. The effects of the cathode composition, arc current, deposition pressure, substrate temperature and post-deposition annealing were comprehensively studied. High deposition rates, up to 11 nm/s, were obtained. The present results were internally consistent.

6.1. ZnO Thin Films

The composition, morphology, structure, optical and electrical characteristics of FVAD ZnO thin films were found to significantly depend on the deposition pressure, substrate temperature, and post-deposition annealing. With all deposition parameters, the ZnO thin films had a polycrystalline hexagonal-wurtzite structure. The crystal quality of the deposited films increased with substrate temperature and by post-deposition annealing. While the average grain size of as-deposited films on RT substrates was in the range 10-20 nm that of films deposited on heated substrates was in the range 20-23 nm. The post-deposition annealing further increased the average grain size up to 59 nm. As-deposited films on RT and heated substrates had compressive stress; however, post-deposition annealing produced tensile stress. The surface roughness of deposited films decreased with increasing substrate temperature.

All of the FVAD ZnO thin films were highly transparent, independent of the deposition conditions used. The average optical transmission, in the VIS spectrum, was in the range 80 to 90%. Post-deposition annealing increased the visible transmission by approximately 5%. The visible transmission was mainly affected by reflection and interference in the film, where n = ~2, and not by absorption, as k was ~0. As-deposited films on RT substrates had higher refractive indices and extinction coefficients than on heated substrates, and hence lower film reflectivity. The estimated optical energy band gap of the ZnO thin films was in the range 3.20 to 3.42 eV, which did not significantly change after annealing.

The electrical resistivity of the ZnO thin films deposited on RT substrates was on the order of 10^{-2} Ωcm, whereas, that of films deposited on heated substrates were two orders of magnitude higher, independent of the deposition pressure. Furthermore, the post-deposition annealing in Ar did not improve the resistivity of ZnO thin films, increasing their resistivity by additional two orders of magnitude.

6.2. SnO_2 Thin Films

Deposition of SnO_2 thin films on hot substrates and annealing at 400 and 600^oC resulted in polycrystalline films, whereas, SnO_2 films deposited on RT substrates were amorphous. The grain size of the films increased with substrate temperature and post-deposition annealing. The average surface grain size of as-deposited films was ~16 nm, whereas that of films deposited on heated substrates or annealed were larger, 26 to 34 nm. The surface roughness of the SnO_2 thin films increased with substrate temperature. The film composition approached the stoichiometric value with deposition on heated substrates and with annealing.

The optical transmission in the UV-VIS of the films considerably increased when they were deposited on hot substrates, ore were annealed. The maximum optical transmission of as-deposited films was about 80-85%, however the deposition on 400^oC heated substrates, and also annealing in Ar atmosphere at 400 and 600^oC for 50 min, significantly shifted the transmission edge to shorter wavelengths and markedly increased the average UV transmission. Both *n* and *k*, of the SnO_2 films decreased when they were deposited on heated substrates or annealed. The decrease in *n* decreased the film reflectivity, and hence increased the transmission. Furthermore, the direct optical band gap was increased from 3.90 to 4.35 eV. Deposition on hot substrates at 0.80 Pa produced the best combined TCO properties; however, annealing at high temperatures severely decreased the film conductivity. It should be noted that although annealing at high temperature improved the UV transmission, it decreased the electrical conductivity.

6.3. ZnO:Sn and Zinc Stannate Thin Films

Sn doped ZnO thin films and zinc stannate thin films were deposited with FVAD at rates up to 11 nm/s. The deposition rate, however, depended on pressure and decreased down to 2 nm/s for films deposited with higher pressure and lower arc current on heated substrates. The Zn:Sn atomic concentration ratio in the films depended on the ratio in the cathode, but generally differed from it. However in the specific case when the Zn:Sn ratio was 1:1 in the cathode, zinc stannate films with a Zn:Sn:O ratio close to 2:1:4 were obtained. The Zn:Sn atomic ratio in the zinc stannate thin films was ~0.50 for all deposited films independent of deposition conditions. The surface roughness and the grain size of these films were in the range 0.2-0.8 and 15-20 nm, respectively. Only amorphous films were obtained, independent of the deposition conditions such as deposition pressure, substrate temperature and arc current. Annealing at 500^{o}C in Ar or air atmospheres did not affect the film structure.

The as-deposited films had maximum VIS transmission of about 85-90%, independent of the deposition conditions. The transmission edge depended on the deposition pressure and substrate temperature. The deposition conditions, however, significantly affected the UV optical properties. Annealing also improved the average UV transmission, by at least 10%, for all films. The improved UV transmission was associated with a shift of the optical transmission edge in UV region to the shorter wavelengths and an increase in optical band gap, E_g. This was most significant for films deposited at lower deposition pressures and the shift of the UV transmission edge indicated a decrease in defect levels in optical band gap.

All RT deposited films were non-conducting (>10^5 Ωcm). The lowest resistivity was ~1.08×10^{-2} Ωcm for films deposited at 0.93 Pa on 400^{o}C substrates; the films were non-conducting at lower pressures and substrate temperatures. Annealing at 500^{o}C improved the UV transmission, but it had a detrimental effect on the electrical conductivity. Annealing at higher temperatures (≥600^{o}C) damaged all FVA deposited zinc stannate thin films. The optical constants *n* and *k*, and hence the reflectivity, decreased with substrate temperature and after annealing.

6.4. Chemical and Thermal Stability of ZnO, SnO_2 and Zinc Stannate Thin Films

Zinc stannate thin films deposited on 400^{o}C substrates were more chemically stable than any FVAD ZnO films. However, SnO_2 thin films had better chemical stability than either ZnO or zinc stannate thin films. The electrical resistances of SnO_2 and zinc stannate thin films did not change after immersion in acidic and basic solutions, and remained 10^{-3} and 10^{-2} Ωcm, respectively. Thus SnO_2 thin films are preferably for use in chemically aggressive environment.

The film resistance of ZnO, SnO_2 and zinc stannate increased as a function of temperature, above a certain critical value. With continued heating beyond the critical temperature, the resistance of ZnO and SnO_2 thin films could increase by several orders of magnitude; the increase was significantly lower in zinc stannate films. Thus zinc stannate thin films are more applicable in hot environments. The resistance increase was not reversible, and the film resistance continued to increase during cooling, however at lower rate. The films cooled to RT retained a relatively high resistance. ZnO films had the largest retained resistance after reaching RT, and zinc stannate had the lowest. This irreversible resistance change limits the applicability of the films at elevated temperatures.

6.5. Summary

In summary, 200 to 800 nm thick ZnO, SnO_2, and zinc stannate films with high optical transmission (85-90%), high refractive index ($n \geq 2$), and resistivity in the range 0.01 to 0.001 Ωcm, which are suitable for various optoelectronic applications, were produced using FVAD. The resistance of the FVAD zinc stannate thin films deposited on heated substrates was more thermally stable than that of ZnO and SnO_2 thin films. In addition, SnO_2 and zinc stannate thin films had better chemical stability than ZnO thin films; however SnO_2 thin films were more stable in acidic solution than the others. With regard to the major research question: “Could the investigated zinc stannate thin films match ZnO and SnO_2 thin films in electro-optical devices or

gas sensors?" the answer is a partial "yes". The investigated films are more applicable when high optical transmission, moderate electrical conductivity, and more robust films are required. They are, however, more advantageous for use in aggressive environment.

6.6. Proposals for Future Research

Further research effort should be made to enhance the understanding of additional characteristics of the FVAD multi-component zinc stannate thin films.

- The relation between the composition and the electrical resistivity needs to be clarified. The effect of grain boundaries and the effects of different types of electron scattering mechanisms on the film resistivity need to be studied using Hall measurements. The research should include the effects of grain boundary scattering and carrier trapping, and their correlation with electrical and optical constants.
- The experimental parameters had significant effect on the film properties. The detailed study of additional experimental parameters such as substrate bias during the deposition, and the post-deposition annealing in various other atmospheres, e.g., nitrogen or vacuum, could result in the deposition of films with improved characteristics.
- The electrical resistivity, mobility and the carrier concentration of deposited films could also be improved by doping. The research should be extended by measuring the electrical characteristics (the carrier density and the mobility) of doped films independently. In addition, the effects of various deposition conditions such as; doping material (such as, Al, Sb) and concentration, annealing time (preferably shorter annealing time) and the environment should be studied to determine their dependencies on various conditions.
- The sensitivity of the films in aggressive environments such as CO and CO_2 could be tested to asses their applicability in gas sensors.

REFERENCES

ALTERKOP, B., PARKANSKY, N., GOLDSMITH, S., BOXMAN, R.L., 2003. Effect of Air Annealing on Opto-Electrical Properties of Amorphous Tin Oxide Films, J. Phys. D: Appl. Phys., 36:552.

ALTERKOP, B., GIDALEVICH, E., GOLDSMITH, S., BOXMAN, R.L., 1996. Vacuum Arc Plasma Jet Propagation in a Toroidal Duct, J. Phys. D: Appl. Phys., 79(9):6791.

ALTERKOP, B., GIDALEVICH, E., GOLDSMITH, S., BOXMAN, R.L., 1998. Propagation of a Magnetized Plasma Beam in a Toroidal Filter, J. Phys. D: Appl. Phys., 31:873.

ANDERS, A., 1999. Approaches to Rid Cathodic Arc Plasmas of Macro- and Nanoparticles: A Review, Surface and Coatings Technology, 120-121, 319.

ANDERS, A., 2000. Handbook of Plasma Immersion Ion Implantation and Deposition, John Wiley & Sons Inc. New York. P736.

BAGHERI-MOHAGHEGHI M.-M, SHOKOOH-SAREMI M., 2003. Investigations on the Physical Properties of the SnO_2–ZnO Transparent Conducting Binary–Binary System Deposited by Spray Pyrolysis Technique, Thin Solid Films, 441:238.

BANERJEE, R., DAS, D., 1987. Properties of Tin Oxide Films Prepared by Reactive Electron Beam Evaporation, Thin Solid Films, 149:291.

BARDEEN, J., BLATT, F.J., HALL, L.H., 1954. Photoconductivity Conference, Atlantic City, John Wiley and Sons, Inc., New York, 146.

BARSAN, N., and WEIMAR, U., 2001. Conduction Model of Metal Oxide Gas Sensors, J. Electroceramics, 7:143.

BÄDEKER, K., 1907. Über die electrische Leitfühigkeit und die Thermoelektrische Kraft Einiger Schwermetallverbindungen, Ann. Phys. Lpz. 22:749.

BATZILL, M., DIEBOLD, U., 2005. The Surface and Materials Science of Tin Oxide, Progress in Surface Science, 79:47-154.

BEN-SHALOM, A., KAPLAN, L., BOXMAN, R.L., GOLDSMITH, S., and NATHAN, M., 1993.SnO_2 Transparent Conductor Films Produced by Filtered Vacuum Arc Deposition, Thin Solid Films, 236:20.

BILEK, M.M.M., ANDERS, A., 1999. Designing Advanced Filters for Macroparticle Removal from Cathodic Arc Plasmas, Plasma Sources Sci. Technol., 8:488-493.

BORN, M., WOLF, E., 1999. Principles of Optics, 7th Ed. Cambridge University Press.

BOXMAN, R.L., GOLDSMITH, S., SHALEV, S., YALOZ, H., BROSH, N., 1986. Fast Deposition of Metallurgical Coatings and Production of Surface Alloys Using a Pulsed High Current Vacuum Arc, Thin Solid Films, 139:41-52.

BOXMAN, R.L., GOLDSMITH, S., 1989. Principles and Applications of Vacuum Arc Coatings, IEEE Transactions on Plasma Science, 17(5):705.

BOXMAN, R.L., GOLDSMITH, S., 1992. Macroparticle Contamination in Cathodic Arc Coatings: Generation, Transport and Control, Surface and Coatings Technology, 52(1):39-50.

BOXMAN, R.L., MARTIN, P., SANDERS, D., 1995. Handbook of Vacuum Arc Science and Technology, Noyes Publications (Park Ridge, NJ).

BOXMAN, R.L., GOLDSMITH, S., GREENWOOD, A., 1997. Twenty-Five Years of Progress in Vacuum Arc Research and Utilization, IEEE Transactions on Plasma Science, 25(6):1174.

BOXMAN, R.L., 2001. Recent Developments in Vacuum Arc Deposition, IEEE Transactions on Plasma Science, 29(5):762.

BOXMAN, R.L., ZHITOMIRSKY, V.N., 2006. Vacuum Arc Deposition Devices, Review Scientific Instruments, 77:021101.

CHEN, Z.W., LAI, J.K.L., and SHEK, C.H., 2004. Insights into Microstructural Evolution from Nanocrystalline SnO_2 Thin Films Prepared by Pulsed Laser Deposition, Pysical Rev. B, 70:165314.

CHEN, Z.W, LAI, J.K.L., SHEK, C.H., CHEN, H.D., 2005. Production of Amorphous Tin Oxide Thin Films and Microstructural Transformation Induced by Heat Treatment, Appl. Phys. A, 81:1073-1076.

CHOPRA, K. L., MAJOR, S., and PANDYA, D.K., 1983. Transparent Conductors-A Status Review, Thin Solid Films, 102:1.

CHOI, W.K., JUNG, H.J., KOH, S.K., 1996. Chemical Shifts and Optical Properties of Tin Oxide Films Grown by a Reactive Ion Assisted Deposition, J. Vac. Sci. Technol. A, 14(2):359.

CHU, S.Y., WATER, W., LIAW, J.T., 2003. Influence of Postdeposition Annealing on the Properties of ZnO Films Prepared by RF Magnetron Sputtering, J. of European Ceramic Society, 23:1593.

CISNEROS, J.I., 1998. Optical Characterization of Dielectric and Semiconductor Thin Films by Use of Transmission Data, Applied Optics, 37:5262.

CONRADS, H., SCHMIDT, M., 2000. Plasma Generation and Plasma Sources, Plasma Sources Sci. Technol., 9:441-454.

DAALDER, J.E., 1975. Erosion and the Origin of Charged and Neutral Species in Vacuum Arcs, J. Phys. D:Appl. Phys., 8:1647.

DAALDER, J.E., 1981. Cathode Spots and Vacuum Arcs, Physica C, 104:91-106.

DAVID, T., GOLDSMITH, S., BOXMAN, R.L., 2004. Electro-optical and Structural Properties of Thin ZnO Films, Prepared by Filtered Vacuum Arc Deposition, Thin Solid Films, 447-448:61.

DAVID, T., GOLDSMITH, S., BOXMAN, R.L., 2005. Dependence of Zinc Oxide Thin Film Properties on Filtered Vacuum Arc Deposition Parameters, J. Phys. D: Appl. Phys., 38,: 2407.

DEMIRYONT, H., NIETERING, K.E., SUROWIEC, R., BROWN, F.I., PLATTS, D.R., 1987. Optical Properties of Spray-Deposited Tin Oxide Films, Applied Optics, 26 (18):3803.

DE, A., RAY, S., 1991. A Study of the structural and electronic properties of magnetron sputtered tin oxide films, J. Phys. D: Appl. Phys., 24,:719.

Di GIULIO, M., MANNO, D., MICOCCI, G., RELLA, R., SICILIANO, P., 1993. Growth and Characterization of Tin Oxide Thin Films Prepared by Reactive Sputtering, Solar Energy Materials and Solar Cells, 31:235.

DJURIŠĆ, A.B., CHAN, Y., LI, E.H., 2002. Progress in the Room-Temperature Optical Functions of Semiconductors, Mater. Scien & Engineering R, 38:237.

DOLECKI, R., 2007. http://www.art.com/asp/sp-asp/_/pd--10291635/sp--A/ Lightning_Striking_Tree.htm.

GLÄSER, H.J., 2000. Large Area Glass Coating, Von Ardenne Anlagentechnik GMBH, Dresden, 472.

GOLDSMITH, S., 2006. Filtered Vacuum Arc Deposition of Undoped and Doped ZnO Thin Films: Electrical, Optical, and Structural Properties, Surface & Coatings Technology 201:3993–3999.

GORBUNOV, A.A., POMPE, W., SEWING, A., GAPONOV, S.V., AKHSAKHALYAN, A.D., ZABRODIN, I.G., KASKOV, I.A., KLYENKOV, E.B., MOROZOW, A.P., SALASCHENKO, N., DIETCH, R., MAI, H., VÖLLMAR, S., 1996. Ultrathin Film Deposition by Pulsed Laser Ablation Using Crossed Beams, Appl. Surf. Sci., 96-98:649.

GREENAWAY, D.L., HARBEKE, G., 1968. Optical Properties and Band Structure of Semiconductors, Pergamon Press Ltd. Headington Hill Hall Oxford.

HAMZAOUI, S., ADNANE, M., 2000. Effects of Temperature and r.f. Power Sputtering on Electrical and Optical Properties of SnO_2, Appl. Energy, 65:19.

HARTNAGEL, H.L., DAWAR, A.L, JAIN, A.K, JAGADISH, C., 1995. Semiconducting Transparent Thin Films, Institude of Physics Publishing.

HAYASHI, Y., KONDO, K., MURAI, K., MORIGA, T., NAKABAYASHI, I., FUKUMOTO, H., TOMINAGA, K., 2004. ZnO–SnO_2 Transparent Conductive Films Deposited by Opposed Target Sputtering System of ZnO and SnO_2 Targets, Vacuum, 74:607.

HEAVENS, O.S., 1965. Optical Properties of Thin Solid Films, NewYork, Dover, 261.

ISIDORSSON, J., GRANQVIST, C.G., ROTTKAY, K.V., and RUBIN, M., 1998. Ellipsometry on Sputter-Deposited Tin Oxide Films: Optical Constants versus Stoichiometry, Hydrogen Content, and Amount of Electrochemically Intercalated Lithium, Applied Optics, 37(31):7334.

JELLISON Jr., G.E., MODINE, F.A.,1996a. Prametrization of the Optical Functions of Amorphous Materials in the Interband Region, Appl. Phys. Lett., 69(3):371.

JELLISON Jr., G.E., MODINE, F.A.,1996b. Erratum: Prametrization of the Optical Functions of Amorphous Materials in the Interband Region, Appl. Phys. Lett., 69(14):2137.

KAPLAN, L., RUSMAN, I., BOXMAN, R.L., GOLDSMITH, S., NATHAN, M., and BEN-JACOB, E., 1996. STM and XPS Study of Filtered Vacuum Arc Deposited Sn-O films, Thin Solid Films 290-291:355.

KILIC, C., ZUNGER, A., 2002. Origins of Coexistence of Conductivity and Transparency in SnO_2, Physical Review Letters, 88(9):095501-1

LEE, H.W., LAU, S.P., WANG, Y.G., TAY, B.K., HNG, H.H., 2004. Internal Stress and Surface Morphology of Zinc Oxide Thin Films Deposited by Filtered Cathodic Vacuum Arc Technique, Thin Solid Films, 458:15-19.

LIN, B., FU, Z., JIA, Y., LIAO, G., 2001. Defect Photoluminescence of Undoping ZnO Films and Its Dependence on Annealing Conditions, J. Electrochemical Society, 148(3):G110-G113.

LINDFORS, P.A., MULARIE, W.M., 1986. Cathodic Arc Deposition Technology, Surface and Coatings Technology, 29:275-290.

LIU, Y.C., TUNG, S.K., HSIEH, J.H., 2006. Influnce of Annealing on Optical Properties and Surface Structure of ZnO Thin Films, J. Crystal Growth, 287:105-111.

LU, Y.F., NI, H.Q., MAI, Z.H., REN, Z.M., 2000. The Effects of Thermal Annealing on ZnO Thin Films Grown by Pulsed Laser Deposition, J. Appl. Phys. 88(1):498.

LURIE, D., MOORE, R.H., 1994. Applying Statistics, US Nuclear Regulatory Commission, Washington, DC, ch.12.

MÄKI-JASKARI, M.A., RANTALA, T.T., 2004. Possible Structures of Non-Stoichiometric Tin Oxide: The Composition Sn_2O_3, Modelling Simul. Mater. Sci. Eng., 12:33-41.

MARTIN, P.J., BENDAVID, A., 2001, Review of the Filtered Vacuum Arc Process and Materials Deposition, Thin Solid Films, 394:1-15.

MESSIER, R., GIRI, A., ROY, R.A., 1984. Revised Structure Zone Model for Thin Film Physical Structure, J. Vac. Sci. Technol., A2: 500-503.

MESSIER, R., 1986. Toward Qualification of Thin Film Morphology, J. Vac. Sci. Technol., A4: 490-495.

MIERNIK, K., WALKOWICZ, J., BUJAK, J., 2000. Design and Performance of the Microdroplet Filtering System Used in Cathodic Arc Coating Deposition, Plasmas and Ions, 3:41-51.

MINAMI, T., NANTO, H., and TAKATA, S., 1988. Highly Conducting and Transparent SnO_2 Thin Films Prepared by RF Magnetron Sputtering on Low-Temperature Substrates, Jpn. J. Appl. Phys., 27: L287.

MINAMI, T., SONOHARA, H., TAKATA, S., and SATO, H., 1994. Highly Transparent and Conductive Zinc-Stannate Thin Films Prepared by RF Magnetron Sputtering, Jpn. J. Appl. Physics., 33: L1693.

MINAMI, T., TAKATA, S., SATO, H., SONOHARA, H., 1995. Properties of Transparent Zinc-Stannate Conducting Films Prepared by Radio Frequency Magnetron Sputtering, J.Vac. Sci. Technol., A13(3):1095.

MINAMI, T., 2000.New *n*-Type Transparent Conducting Oxides, MRS Bull. 25,38.

MINAMI T., 2005. Transparent Conducting Oxide Semiconductors for Transparent Electrodes, Semicond. Science Technol., 20:S35-S44.

MINAMI T, TSUKADA S., MINAMINO Y., MIYATA T., 2005. Preparation of Transparent and Conductive Multicomponent Zn-In-Sn Oxide Thin Films by Vacuum Arc Plasma Evaporation, J. Vac. Sci. Technol., A23(4):1128.

MONTERIO, O.R., 2001. Thin Film Synthesis by Energetic Condensation, Annu., Rev. Mater. Res., 31:111.

MORIGA, T., HAYASHI, Y., KONDO, K., NISHIMURA, Y., 2004. Transparent Conducting Amorphous Zn-Sn-O Films Deposited by Simultaneous DC Sputtering, J.Vac. Sci. Technol., A22(4):1705.

MORENO, M.S., MERCADER, R.C., BIBILONI, A.G., 1992. Study of Intermediate Oxides in SnO Thermal Decomposition, J. Phys.: Condensed Matter, 4:351:355.

MURKEN, G., TRÖNEL, M., 1973. Uber das bei der Disproportionierung von SnO entstehende Zinnoxid, Sn_2O_3, Z. Anorg. (Allg.) Chem. 397:117.

MOSS, T.S., 1961. Optical Properties of Semiconductors, London: Butterworths, 279.

MUKHAMEDSHINA, D.M., BEISENKHANOV, N.B., MIT, K.A., VALITOVA, I.V., and BOTVIN, V.A., 2006. Investigation of Properties of Thin Oxide Films SnO_x Annealed in Various Atmospheres, Thin Solid Films, 495:316.

O'CONNOR, D.J., SEXTON, B.A., SMART, R.St., 1992. Surface Analysis Method in Materials Science, Springer-Verlag, Heidelberg.

OGATA, K., SAKURAI, K., FUJITA, Sz., FUJITA, Sg., MATSUSHIGE, K., 2000. Effects of Thermal Annealing of ZnO Layers Grown by MBE, J. Crystal Growth, 214-215:312-315.

OPREA, A., MORETTON, E., BARSAN, N., BECKER, W.J., WÖLLENSTEIN, J. WEIMAR, U., 2006. Conduction Model of SnO_2 Thin Films Based on Conductance and Hall Effect Measurements, J.Appl. Phys., 100:033716.

ÖZGÜR, Ü., ALIVOV, Y.I., LIU, C., TEKE, A., RESHCHIKOV, M.A., DOĞAN, S., AVRUTIN, V., 2005. A Comprehensive Review of ZnO Materials and Devices, J. Appl. Physics, 98:041301.

PARKANSKY, N., ALTERKOP, B., GOLDSMITH, S.,and BOXMAN, R.L., 2003. Effect of an Applied Voltage During Annealing on the Resistivity and Transparency of the Amorphous Tin Oxide Films, J. Vac. Sci. Technol., A21(6):1923.

PERKINS, J.D, DEL CUETO, J.A., ALLEMAN, J.L., WARMSINGH, C., KEYES, B.M., GEDVILAS, L.M., PARILLA, P.A., TO, B., READEY, D.W., GINLEY, D.S., 2002, Combinatorial Studies of Zn-Al-O and Zn-Sn-O Transparent Conducting Oxide Thin Films, Thin Solid Films, 411:152.

POELMAN, D., SMET, P.F., 2003. Methods for the Determination of the Optical Constants of Thin Films from Single Transmission Measurements: a Critical Review, J.Phys. D: Appl. Phys., 36:1850.

PULKER, H.K., 1984. Coatings on Glass, Amsterdam: Elsevier, 484.

RAIZER, Y.P., 1991. Gas Discharge Physics, Berlin, Springer-Verlag, 449.

RYABCHIKOV, A.I., STEPANOV, I.B., 1998. Investigations of Forming Metal-Plasma Flows Filtered From Microparticle Fraction in Vacuum Arc

Evaporators, Rev. Sci.Instrum., 69:810.

SAMSON, S., FONSTAD, C.G., 1973. Defect Structure and Electronic Donor Levels in Stannic Oxide Crystals, J. Appl. Phys., 44(10):4618.

SATOH, K., KAHEHI, Y., OKAMOTO, A., MURAKAMI, S., URATANI, F., YOTSUYA, T., 2005. Influence of Oxygen Flow Ratio on Properties of Zn_2SnO_4 Thin Films Deposited by RF Magnetron Sputtering, Jpn. Journal of Applied Physics, 44(1):L34-L37.

SCHULER, L.P., ALKASISI, M.M., MILLER, P., REEVES, R.J., MARKWITZ, A., 2005. Comparison of DC and RF Sputtered Zinc Oxide Films with Post-Annealing and Dry Etching and Effect on Crystal Composition, Jpn. J. Appl. Phys., 44(10):7555.

SCHEMATIC DIAGRAM OF AN AFM (http://www.che.utoledo.edu, 2006).

SCHEMATIC GEOMETRY OF AN ELLIPSOMETRY EXPERIMENT (www.uta.edu/optics/research/ellipsometry/ellipsometry.htm, 2006).

SEGEV, D., WEI, S.-H., 2005. Structure Derived Electronic and Optical Properties of Transparent Conducting Oxides, Physical Review B, 71:125129.

SESHAN, K., 2002. Handbook of Thin Film Deposition Propcesses and Techniques, Noyes Publications, William Andrew Publishing, Norwich, NewYork, U.S.A.

SETO, J.Y.W, 1975. The Electrical Properties of Polycrystalline Silicon Films, J. Appl. Phys., 46:5247.

SHALEV, G., 2004. The Effect of Annealing in Air and Concurrent Current Injection on the Electrical Conductivity of Zinc Oxide Thin Films Deposited by Filtered Vacuum Arc System, Tel-Aviv:University of Tel-Aviv, 2004.

SHAMALA, K. S., L. C. MURTHY, K. NARASIMHA, R., 2004. Studies on Tin Oxide Films Prepared by Electron Beam Evaporation and Spray Pyrolysis Methods, Bull. Mater. Sci., 27(3):295.

SMITH, R.A., 1969. Wave Mechanics of Crystalline Solids, 2nd Edition, London :Chapman and Hall.

SONG, S.K., 1999. Characteristics of SnO_x Films Deposited by Reactive-Ion-Asisted Deposition, Physical Review B, 60(5):11137.

TAUC, J., GRIGOROVICI, R., VANCU, A., 1966. Optical Properties and Electronic Structure of Amorphous Germanium, Phys. Stst. Sol., 15:627.

TAY, B.K., ZHAO, Z.W., CHUA, D.H.C., 2006. Review of Metal Oxide Films Deposited by Filtered Cathodic Vacuum Arc Technique, Materials Science and Engineering R 52:1-48.

TAYLOR, W.E., ODELL, N.H., and FAN, H.Y., 1952. Grain Boundary Barriers in Germanium, Phys. Rev. 88:867.

THORNTON, J.A, 1974. Influence of Apparatus Geometry and Deposition Conditions on the Structure and Topography of Thick Sputtered Coatings, J. Vac. Sci. Technol., 11:666-670.

THORNTON, J.A, 1977. High Rate Thick Film Growth, J. Vac. Sci. Technol., 11:666-670.

TOMLINS, G.W., ROUTBORT, J.L., MASON, T.O., 2000. Zinc Self-Diffusion, Electrical Properties, and Defect Structure of Undoped, Single Crystal Zinc Oxide, J. Appl. Phys., 87(1):117.

TSE, K.Y., HNG, H.H., LAU, S.P., WANG, Y.G., YU, S.F., 2004. ZnO Thin Films Produced by Filtered Cathodic Vacuum Arc Technique, Ceramics International, 30:1669.

VOLTAGE-CURRENT CHARACTERISTICS OF DC DISCHARGES http://science-education.pppl.gov/SummerInst/SGershman/Structure_of_Glow_Discharge.pdf

WANG, Y.G., LAU, S.P., LEE, H.W., YU, S.F., and TAY, B.K., ZHANG, X.H., TSE, K.Y., HNG, H.H., 2003. Comprehensive Study of ZnO Films Prepared by Filtered Cathodic Vacuum Arc at Room Temperature, J. Appl. Phys. 94(3):1597.

WEI, S.-H., ZHANG, S.B., 2001. First-Principles Study of Cation Distribution in Eighteen Closed-Shell A^{II} $B_2^{III}O_4$ and $A^{IV}B_2^{II}O_4$ Spinel Oxides, Phys. Rev. B, 63: 045112.

WEI, X.Q., ZHANG, Z.G., LIU, M., CHEN, C.S., SUN, G., XUE, C.S., and ZHUANG, H.Z., MAN, B.Y., 2007. Annealing Effect on the Microstructure and Photoluminescence of ZnO Thin Films, Mater. Chem. & Phys. 101:285.

WEIS, T., LIPPERHEIDE, R., WILLEA, U., and BREHME, S., 2002. Barrier-Controlled Carrier Transport in Microcrystalline Semiconducting Materials: Description Within a Unified Model, J. App. Phys. 92:1411.

WEMPLE, S.H., DIDOMENICO, M., 1971. Behavior of the Electronic Dielectric Constant in Covalent and Ionic Materials, Phys. Rev. B, 3/4: 1338.

WEMPLE, S.H., 1973. Refractive-Index Behavior of Amorphous Semiconductors and Glasses, Phys. Rev. B 7/8:3767.

WOOLLAM, J.A., JOHS, B., HERZINGER, C., HILFIKER, J., SYNOWICKI, R., BUNGAY, C.L., 1999. Overview of Variable Angle Spectroscopic Ellipsometry (VASE), Part I: Basic Theory and Typical Applications, Critical Reviews of Optical Science and Technology, Denver /Colorado, Vol CR72:3.

WOOTEN, F., 1972. Optical Properties of Solids, Academic Press Inc., p115.

WU, X., COUTTS, T.J., MULLIGAN, W.P., 1997. Properties of Transparent Conducting Oxides Formed from CdO and ZnO Alloyed with SnO_2 and In_2O_3, J. Vac. Sci. Technol., A15 (3):1057.

XU, X.L, LAU, S.P., CHEN, J.S., CHEN, G.Y., TAY, B.K., 2001b. Polycrystalline ZnO Thin Films on Si(100) Deposited by Filtered Cathodic Vacuum Arc, J. Cryst. Growth, 223:201.

XU, X.L., LAU, S.P., TAY, B.K., 2001a. Structural and Optical Properties of ZnO Thin Films Produced by Filtered Cathodic Vacuum Arc, Thin Solid Films, 398-399:244.

XU, X.L., LAU, S.P., CHEN, J.S., SUN, Z., TAY, B.K., and CHAI, J.W., 2001c. Dependence of Electrical and Optical Properties of ZnO Films on Substrate Temperature, Materials Science in Semiconductor Processing 4:617-620.

YILDIRIM, T., GUR, E., TUZEMEN, S., BILGIN, V., KOSE, S., and ATAY, F., AKYUZ, I., 2005. Wide-bandgap modification of polycrystalline ZnO using Sn component on the basis of developing quantum-well hetero-structure Physica E 27:290.

YOSHIKAWA, H., ADACHI, S., 1997. Optical Constants of ZnO, Jpn. J. Appl. Phys., 36:6237-6243.

YOUNG, D.L., MOUTINHO, H., YAN, Y., COUTTS, T.J., 2002a. Growth and Characterization of Radio Frequency Magnetron Sputter-Deposited Zinc Stannate, Zn_2SnO_4, Thin Films, J. Appl. Physics, 92:310.

YOUNG, D.L., WILLIAMSON, D.L., COUTTS, T.J., 2002b. Structural Characterization of Zinc Stannate Thin Films, J. Appl. Phys. 91(3):1464.

ZHANG, S.B., WEI, S.-H., and ZUNGER, A., 2001. Intrinsic *n*-type versus *p*-type Doping Asymmetry and the Defect Physics of ZnO, Phys. Rev. B, 63:075205.

ZHI, Z.Z., LIU, Y.C., LI, B.S., ZHANG, X.T., LU, Y.M., D.Z., SHEN, FAN, X.W., 2003. Effects of Thermal Annealing on ZnO Films Grown by Plasma Enhanced Chemical Vapour Deposition from $Zn(C_2H_5)_2$ and CO_2 Gas Mixtures, J. Phys. D: Appl. Phys., 36:719-722.

ZHITOMIRSKY, V.N, DAVID, T., BOXMAN, R.L., GOLDSMITH, S., VERDYAN, A., SOIFER, Y., RAPOPORT, L., 2005. Properties of SnO_2 Coatings Fabricated on Polymer Substrates Using Filtered Vacuum Arc Deposition, Thin Solid Films, 492:187-194.

APPENDIX

Ellipsometry Data Analysis Using Lorentz-Dielectric Function:

```
function FunFitVer001_Orig()

%%%%%%%%%%%%%%%%%%%%%%%%%%%%%%%%%%%%
%%% Clearing before run
%%%%%%%%%%%%%%%%%%%%%%%%%%%%%%%%%%%%
close all;
clc;
pause(0.1);
warning off;
figure(1);
% set(1,'MenuBar','None','Position',[4 291 302 448],'NumberTitle','off','Name','1');
set(1,'MenuBar','None','Position',[4 530 302 210],'NumberTitle','off','Name','1');
figure(2);
set(2,'MenuBar','None','Position',[318 530 302 210],'NumberTitle','off','Name','2');
figure(3);
set(3,'MenuBar','None','Position',[629 530 391 210],'NumberTitle','off','Name','3');

%%%%%%%%%%%%%%%%%%%%%%%%%%%%%%%%%%%%
%%% Defining varibles
%%%%%%%%%%%%%%%%%%%%%%%%%%%%%%%%%%%%
vEllipNumLambda=512; vEllipNumTheta=4;
vLambdaIndexMin=136; vLambdaIndexMax=512; vLambdaIndexStep=5; vLambdaValue=[ ];
vThetaIndexMin=1; vThetaIndexMax=1; vThetaIndexStep=1; vThetaValue=[ ];
vPsi=[ ]; vDelta=[ ]; vPsiError=[ ]; vDeltaError=[ ];
vAsMeasured=[ ]; vAsMeasuredError=[]; vAsTheoryValue=[ ]; vAsTheoryBest=[ ];
vBsMeasured=[ ]; vBsMeasuredError=[ ]; vBsTheoryValue=[ ]; vBsTheoryBest=[ ];
vFitN=[ ]; vFitLoopsTime=60*60*60; vFitPlotsTime=10; vFitPlotsNextTime=0;
vFitPauseTime=0.001;
vChisqValue=[ ]; vChisqBest=[ ]; vChisqPoints=[ ]; vChisqWeight=0.00001;
vLambdaI=[ ]; vThetaI=[ ]; vN=[ ]; vFid=[ ]; vTmp=[ ]; vNs=[ ]; vDs=[ ];
vChisqLast=[ ];
vEllipFile='Znsn_090.dat';
vFitSaveFile=strcat(vEllipFile,'.res');

vFitMethod='AllVariblesOneRange';

vN=1;  vVarName{vN}='d3';   vVarStart{vN}=247.70; vVarMin{vN}=50.000;
vVarMax{vN}=900.00; vVarDiff{vN}=0.100; vVarValue{vN}=vVarStart{vN};
vVarBest{vN}=vVarValue{vN};
vN=2;  vVarName{vN}='einf'; vVarStart{vN}=3.1000; vVarMin{vN}=2.0000;
vVarMax{vN}=9.0000; vVarDiff{vN}=0.010; vVarValue{vN}=vVarStart{vN};
vVarBest{vN}=vVarValue{vN};

vN=3;  vVarName{vN}='ATO';  vVarStart{vN}=2.2600; vVarMin{vN}=0.0000;
vVarMax{vN}=5.0000; vVarDiff{vN}=0.010; vVarValue{vN}=vVarStart{vN};
vVarBest{vN}=vVarValue{vN};
vN=4;  vVarName{vN}='ETO';  vVarStart{vN}=3.7500; vVarMin{vN}=3.0000;
vVarMax{vN}=4.0000; vVarDiff{vN}=0.010; vVarValue{vN}=vVarStart{vN};
vVarBest{vN}=vVarValue{vN};
```

```
vN=5;  vVarName{vN}='GTO';  vVarStart{vN}=0.4000; vVarMin{vN}=0.0000;
vVarMax{vN}=2.2000; vVarDiff{vN}=0.010; vVarValue{vN}=vVarStart{vN};
vVarBest{vN}=vVarValue{vN};
vN=6;  vVarName{vN}='EP';   vVarStart{vN}=0.2000; vVarMin{vN}=0.0000;
vVarMax{vN}=1.0000; vVarDiff{vN}=0.0010; vVarValue{vN}=vVarStart{vN};
vVarBest{vN}=vVarValue{vN};
vN=7;  vVarName{vN}='GP';   vVarStart{vN}=0.1000; vVarMin{vN}=0.0000;
vVarMax{vN}=2.0000; vVarDiff{vN}=0.0010; vVarValue{vN}=vVarStart{vN};
vVarBest{vN}=vVarValue{vN};

vN=8;  vVarName{vN}='d2';   vVarStart{vN}=04.100; vVarMin{vN}=00.000;
vVarMax{vN}=40.000; vVarDiff{vN}=0.100; vVarValue{vN}=vVarStart{vN};
vVarBest{vN}=vVarValue{vN};
vN=9;  vVarName{vN}='d4';   vVarStart{vN}=01.000; vVarMin{vN}=00.000;
vVarMax{vN}=40.000; vVarDiff{vN}=0.100; vVarValue{vN}=vVarStart{vN};
vVarBest{vN}=vVarValue{vN};
vN=10; vVarName{vN}='f13';  vVarStart{vN}=0.5000; vVarMin{vN}=0.5000;
vVarMax{vN}=0.5000; vVarDiff{vN}=0.0010; vVarValue{vN}=vVarStart{vN};
vVarBest{vN}=vVarValue{vN};
vN=11; vVarName{vN}='q13';  vVarStart{vN}=0.3300; vVarMin{vN}=0.3300;
vVarMax{vN}=0.3300; vVarDiff{vN}=0.0010; vVarValue{vN}=vVarStart{vN};
vVarBest{vN}=vVarValue{vN};
vN=12; vVarName{vN}='f35';  vVarStart{vN}=0.5000; vVarMin{vN}=0.5000;
vVarMax{vN}=0.5000; vVarDiff{vN}=0.0010; vVarValue{vN}=vVarStart{vN};
vVarBest{vN}=vVarValue{vN};
vN=13; vVarName{vN}='q35';  vVarStart{vN}=0.3300; vVarMin{vN}=0.3300;
vVarMax{vN}=0.3300; vVarDiff{vN}=0.0010; vVarValue{vN}=vVarStart{vN};
vVarBest{vN}=vVarValue{vN};

vN=1;  vString{vN}='lambda=vLambdaValue';
vN=2;  vString{vN}='E=1240./lambda';
vN=3;  vString{vN}='e1=1.00^2*lambda./lambda';
vN=4;  vString{vN}='e3=einf.*(1+ATO./(ETO^2-E.^2-i*E*GTO)-(EP.^2)./(E.^2+i*E*GP))';
vN=5;  vString{vN}='e5=1.53^2*lambda./lambda';

vN=6;  vString{vN}='k=(1-q13)/q13';
vN=7;  vString{vN}='a=k';
vN=8;  vString{vN}='b=-f13.*e3-(1-f13).*e1-k.*f13.*e1-k.*(1-f13).*e3';
vN=9;  vString{vN}='c=e1.*e3';
vN=10;  vString{vN}='e2=(-b+sqrt(b.^2-4.*a.*c))./(2.*a)';

vN=11;  vString{vN}='k=(1-q35)/q35';
vN=12;  vString{vN}='a=k';
vN=13;  vString{vN}='b=-f35.*e5-(1-f35).*e3-k.*f35.*e3-k.*(1-f35).*e5';
vN=14;  vString{vN}='c=e3.*e5';
vN=15;  vString{vN}='e4=(-b+sqrt(b.^2-4.*a.*c))./(2.*a)';

vN=1; vEpsilonValue{vN}=[ ]; vEpsilonBest{vN}=[ ]; vEpsilonD{vN}=0;
vEpsilonFormula{vN}='vEpsilonValue{1}=e1; vEpsilonD{1}=0';
vN=2; vEpsilonValue{vN}=[ ]; vEpsilonBest{vN}=[ ]; vEpsilonD{vN}=0;
vEpsilonFormula{vN}='vEpsilonValue{2}=e2; vEpsilonD{2}=d2';
vN=3; vEpsilonValue{vN}=[ ]; vEpsilonBest{vN}=[ ]; vEpsilonD{vN}=0;
vEpsilonFormula{vN}='vEpsilonValue{3}=e3; vEpsilonD{3}=d3';
vN=4; vEpsilonValue{vN}=[ ]; vEpsilonBest{vN}=[ ]; vEpsilonD{vN}=0;
vEpsilonFormula{vN}='vEpsilonValue{4}=e4; vEpsilonD{4}=d4';
```

```
vN=5; vEpsilonValue{vN}=[ ]; vEpsilonBest{vN}=[ ]; vEpsilonD{vN}=0;
vEpsilonFormula{vN}='vEpsilonValue{5}=e5; vEpsilonD{5}=0';

%%%%%%%%%%%%%%%%%%%%%%%%%%%%%%%%%%%%
%%% Getting the ellipsometry data
%%%%%%%%%%%%%%%%%%%%%%%%%%%%%%%%%%%%
vFid=fopen(vEllipFile,'r');
vTmp=fgetl(vFid);
vTmp=fgetl(vFid);
vTmp=fgetl(vFid);
vTmp=fgetl(vFid);
for vThetaI=1:vEllipNumTheta
   for vLambdaI=1:vEllipNumLambda
      vLambdaValue(vLambdaI)=fscanf(vFid,'%f',1);
      vThetaValue(vThetaI)=fscanf(vFid,'%f',1)*pi/180;
      vPsi(vLambdaI,vThetaI)=fscanf(vFid,'%f',1)*pi/180;
      vDelta(vLambdaI,vThetaI)=fscanf(vFid,'%f',1)*pi/180;
      vPsiError(vLambdaI,vThetaI)=fscanf(vFid,'%f',1)*pi/180;
      vDeltaError(vLambdaI,vThetaI)=fscanf(vFid,'%f',1)*pi/180;
   end
end
fclose(vFid);
vLambdaValue=vLambdaValue(vLambdaIndexMin:vLambdaIndexStep:vLambdaIndexMax);
vThetaValue=vThetaValue(vThetaIndexMin:vThetaIndexStep:vThetaIndexMax);
vPsi=vPsi(vLambdaIndexMin:vLambdaIndexStep:vLambdaIndexMax,vThetaIndexMin:vThetaIndex
Step:vThetaIndexMax);
vDelta=vDelta(vLambdaIndexMin:vLambdaIndexStep:vLambdaIndexMax,vThetaIndexMin:vThetaIn
dexStep:vThetaIndexMax);
vPsiError=vPsiError(vLambdaIndexMin:vLambdaIndexStep:vLambdaIndexMax,vThetaIndexMin:vT
hetaIndexStep:vThetaIndexMax);
vDeltaError=vDeltaError(vLambdaIndexMin:vLambdaIndexStep:vLambdaIndexMax,vThetaIndexMi
n:vThetaIndexStep:vThetaIndexMax);

%%%%%%%%%%%%%%%%%%%%%%%%%%%%%%%%%%%%
%%% Calculating A.m... B.m...
%%%%%%%%%%%%%%%%%%%%%%%%%%%%%%%%%%%%
vAsMeasured=real(tan(vPsi).*exp(i*vDelta));
vBsMeasured=imag(tan(vPsi).*exp(i*vDelta));
vAsMeasuredError=sqrt((cos(vDelta).*vPsiError./(cos(vPsi)).^2).^2+(tan(vPsi).*sin(vDelta).*vDelta
Error).^2);
vBsMeasuredError=sqrt((sin(vDelta).*vPsiError./(cos(vPsi)).^2).^2+(tan(vPsi).*cos(vDelta).*vDeltaE
rror).^2);

%%%%%%%%%%%%%%%%%%%%%%%%%%%%%%%%%%%%
%%% Starting the fit loop
%%%%%%%%%%%%%%%%%%%%%%%%%%%%%%%%%%%%
tic;
vFitN=0;
while toc<=vFitLoopsTime
   vFitN=vFitN+1;

 %%%%%%%%%%%%%%%%%%%%%%%%%%%%%%%%%%%%
 %%% Changing the vVarValue
 %%%%%%%%%%%%%%%%%%%%%%%%%%%%%%%%%%%%
 if strcmp(vFitMethod,'AllVaribles AllRange')
```

```
      for vN=1:length(vVarName)
         vVarValue{vN}=vVarMin{vN}+vVarDiff{vN}*floor(rand*((vVarMax{vN}-
vVarMin{vN})/vVarDiff{vN}+1));
      end
   end
   if strcmp(vFitMethod,'AllVariblesOneRange')
      for vN=1:length(vVarName)
         vVarValue{vN}=vVarBest{vN}+vVarDiff{vN}*floor(rand*3-1);
         if vVarValue{vN}>vVarMax{vN} | vVarValue{vN}<vVarMin{vN}
            vVarValue{vN}=vVarBest{vN};
         end
      end
   end
   if strcmp(vFitMethod,'OneVariblesAllRange')
      vN=floor(rand*length(vVarName)+1);
      vVarValue{vN}=vVarMin{vN}+vVarDiff{vN}*floor(rand*((vVarMax{vN}-
vVarMin{vN})/vVarDiff{vN}+1));
   end
   if strcmp(vFitMethod,'OneVariblesOneRange')
      vN=floor(rand*length(vVarName)+1);
      vVarValue{vN}=vVarBest{vN}+vVarDiff{vN}*floor(rand*3-1);
      if vVarValue{vN}>vVarMax{vN} | vVarValue{vN}<vVarMin{vN}
         vVarValue{vN}=vVarBest{vN};
      end
   end

   %%%%%%%%%%%%%%%%%%%%%%%%%%%%%%%%%%%%
   %%% View Change Graph
   %%%%%%%%%%%%%%%%%%%%%%%%%%%%%%%%%%%%
   if isempty(findstr(vFitMethod,'View'))==0
      close all; pause(0.1);
      vTmpN=0;
      vTmpVarVec=[ ];
      for vTmp=1:length(vVarName)
         if vVarMax{vTmp}~=vVarMin{vTmp}
            vTmpN=vTmpN+1;
            vTmpVarVec(vTmpN)=vTmp;
         end
      end
      for vTmpVarNum=vTmpVarVec
         figure('MenuBar','none','Name',vVarName{vTmpVarNum},'NumberTitle','off');
         hold on;
         for vVarPlace=-10:10
            for vN=1:length(vVarName)
               eval(sprintf('%s=%f;',vVarName{vN},vVarStart{vN}));
               if vN==vTmpVarNum

vVarValue{vTmpVarNum}=vVarStart{vTmpVarNum}+vVarDiff{vTmpVarNum}*vVarPlace;
                  eval(sprintf('%s=%f;',vVarName{vN},vVarValue{vN}));
               end
            end
            for vN=1:length(vString)
               eval(sprintf('%s;',vString{vN}));
            end
            for vN=1:length(vEpsilonFormula)
```

```
            eval(sprintf('%s;',vEpsilonFormula{vN}));
        end
        vChisqValue=0;
        vChisqPoints=0;
        for vLambdaI=1:length(vLambdaValue)
            for vThetaI=1:length(vThetaValue)
                for vN=1:length(vEpsilonValue)
                    vTmp1=real(sqrt(vEpsilonValue{vN}(vLambdaI)));
                    vTmp2=imag(sqrt(vEpsilonValue{vN}(vLambdaI)));
                    vNs(vN)=vTmp1-i*vTmp2;
                    vDs(vN)=vEpsilonD{vN};
                end

vTmp=FunLayerOptic('R','P',vNs,vDs,vThetaValue(vThetaI),vLambdaValue(vLambdaI))./...
                    FunLayerOptic('R','S',vNs,vDs,vThetaValue(vThetaI),vLambdaValue(vLambdaI));
                vAsTheoryValue(vLambdaI,vThetaI)=real(vTmp);
                vBsTheoryValue(vLambdaI,vThetaI)=imag(vTmp);
                vChisqValue=vChisqValue+...
                    ((vAsTheoryValue(vLambdaI,vThetaI)-
vAsMeasured(vLambdaI,vThetaI))/vAsMeasuredError(vLambdaI,vThetaI))^2+...
                    ((vBsTheoryValue(vLambdaI,vThetaI)-
vBsMeasured(vLambdaI,vThetaI))/vBsMeasuredError(vLambdaI,vThetaI))^2;
                vChisqPoints=vChisqPoints+1;
            end
        end
        vChisqValue=vChisqValue./(2*vChisqPoints);
        if vVarPlace==-1
            vTmpDiff=vChisqValue;
        end
        if vVarPlace==1
            vTmpDiff=vTmpDiff-vChisqValue;
        end

        plot(vVarValue{vTmpVarNum},vChisqValue,'o');
        if vVarPlace==0
            plot(vVarValue{vTmpVarNum},vChisqValue,'or');
        end
        fprintf('.');
    end
    hold off;
    title(sprintf('%s : %f',vVarName{vTmpVarNum},vTmpDiff));
    ylabel('\chi^2');
    xlabel(vVarName{vTmpVarNum});
    axis tight;
    fprintf('%s; vTmpDiff=%f\n',vVarName{vTmpVarNum},vTmpDiff);
    pause(0.1);
  end
  fprintf('=== Ended ===\n');
  return;
end

%%%%%%%%%%%%%%%%%%%%%%%%%%%%%%%%%%%%
%%% Calculating the dynamic vars
%%%%%%%%%%%%%%%%%%%%%%%%%%%%%%%%%%%%
for vN=1:length(vVarName)
```

```
      eval(sprintf('%s=%f;',vVarName{vN},vVarValue{vN}));
   end
   for vN=1:length(vString)
      eval(sprintf('%s;',vString{vN}));
   end
   for vN=1:length(vEpsilonFormula)
      eval(sprintf('%s;',vEpsilonFormula{vN}));
   end

   %%%%%%%%%%%%%%%%%%%%%%%%%%%%%%%%%%%%
   %%% Calculating the vChisqValue
   %%%%%%%%%%%%%%%%%%%%%%%%%%%%%%%%%%%%
   vChisqValue=0;
   vChisqPoints=0;
   for vLambdaI=1:length(vLambdaValue)
      for vThetaI=1:length(vThetaValue)
         for vN=1:length(vEpsilonValue)
            vTmp1=real(sqrt(vEpsilonValue{vN}(vLambdaI)));
            vTmp2=imag(sqrt(vEpsilonValue{vN}(vLambdaI)));
            vNs(vN)=vTmp1-i*vTmp2;
            vDs(vN)=vEpsilonD{vN};
         end
         vTmp=FunLayerOptic('R','P',vNs,vDs,vThetaValue(vThetaI),vLambdaValue(vLambdaI))./...
            FunLayerOptic('R','S',vNs,vDs,vThetaValue(vThetaI),vLambdaValue(vLambdaI));
         vAsTheoryValue(vLambdaI,vThetaI)=real(vTmp);
         vBsTheoryValue(vLambdaI,vThetaI)=imag(vTmp);
         vChisqValue=vChisqValue+...
            ((vAsTheoryValue(vLambdaI,vThetaI)-
vAsMeasured(vLambdaI,vThetaI))/vAsMeasuredError(vLambdaI,vThetaI))^2+...
            ((vBsTheoryValue(vLambdaI,vThetaI)-
vBsMeasured(vLambdaI,vThetaI))/vBsMeasuredError(vLambdaI,vThetaI))^2;
         vChisqPoints=vChisqPoints+1;
      end
   end
   vChisqValue=vChisqValue./(2*vChisqPoints);

   %%%%%%%%%%%%%%%%%%%%%%%%%%%%%%%%%%%%
   %%% Saving the best from vChisq
   %%%%%%%%%%%%%%%%%%%%%%%%%%%%%%%%%%%%
   if isempty(vChisqBest)
      vChisqBest=vChisqValue;
      vAsTheoryBest=vAsTheoryValue;
      vBsTheoryBest=vBsTheoryValue;
      for vN=1:length(vVarName)
         vVarBest{vN}=vVarValue{vN};
      end
      for vN=1:length(vEpsilonFormula)
         vEpsilonBest{vN}=vEpsilonValue{vN};
      end
   end
   vTmp=vChisqValue-vChisqBest;
   if rand<=((vTmp<=-vChisqWeight)+(vTmp>-vChisqWeight & vTmp<=vChisqWeight)*(-
vTmp/(2*vChisqWeight)+1/2)+0)
      vChisqBest=vChisqValue;
      vAsTheoryBest=vAsTheoryValue;
```

```
      vBsTheoryBest=vBsTheoryValue;
      for vN=1:length(vVarName)
         vVarBest{vN}=vVarValue{vN};
      end
      for vN=1:length(vEpsilonFormula)
         vEpsilonBest{vN}=vEpsilonValue{vN};
      end
   end

   %%%%%%%%%%%%%%%%%%%%%%%%%%%%%%%%%%%%
   %%% Display and Plot the data
   %%%%%%%%%%%%%%%%%%%%%%%%%%%%%%%%%%%%
   if toc>vFitPlotsNextTime
      vFitPlotsNextTime=vFitPlotsNextTime+vFitPlotsTime;
      clc; clf;
      fprintf('=== Fit Data ===\n');
      fprintf('Lambda=%d:%d:%d [%.2f ...
%.2f]\n',vLambdaIndexMin,vLambdaIndexStep,vLambdaIndexMax,vLambdaValue(1),vLambdaValu
e(length(vLambdaValue)));
      fprintf('vEllipFile=%s  vFitMethod=%s\n',vEllipFile,vFitMethod);
      fprintf('vFitN=%d  ',vFitN);
      fprintf('toc=%7f  ',toc);
      fprintf('toc/vFitN=%.7f  ',toc/vFitN);
      fprintf('vChisqBest=%.7f  ',vChisqBest);
      fprintf('vChisqPoints=%d  ',vChisqPoints);
      fprintf('\n=== Fit Varibles ===\n');
      for vN=1:length(vVarName)
         if vVarMax{vN}==vVarMin{vN}
            fprintf('%s=%.7f[f]  ',vVarName{vN},vVarBest{vN});
         else
            fprintf('%s=%.7f  ',vVarName{vN},vVarBest{vN});
         end
         if mod(vN,7)==0
            fprintf('\n');
         end
      end
      fprintf('\n=== End ===\n');

      fprintf(' ');
      for vN=1:length(vVarName)
         if vVarMax{vN}~=vVarMin{vN}
            fprintf('%s\t',vVarName{vN});
         end
      end
      fprintf('%s\n','vChisqBest');
      fprintf(' ');
      for vN=1:length(vVarName)
         if vVarMax{vN}~=vVarMin{vN}
            fprintf('%.4f\t',vVarBest{vN});
         end
      end
      fprintf('%.2f\n\n',vChisqBest);

      figure(1);
      for vN=1:length(vThetaValue)
```

```
        subplot(length(vThetaValue),2,2*vN-1);

plot(vLambdaValue,vAsMeasured(:,vN)+vAsMeasuredError(:,vN),'.m',vLambdaValue,vAsMeasured
(:,vN)-vAsMeasuredError(:,vN),'.m'); hold on;
        plot(vLambdaValue,vAsMeasured(:,vN),'.r',vLambdaValue,vAsTheoryBest(:,vN),'.b'); hold
off;
        if vN==1, title('A'); end
        % legend('MeasErr','MeasErr','Measured','Theory');
        axis tight; grid on;
        ylabel(sprintf('\\theta=%.2f [deg]',vThetaValue(vN)*180/pi)); xlabel('\lambda [nm]');
        subplot(length(vThetaValue),2,2*vN);

plot(vLambdaValue,vBsMeasured(:,vN)+vBsMeasuredError(:,vN),'.m',vLambdaValue,vBsMeasured(
:,vN)-vBsMeasuredError(:,vN),'.m'); hold on;
        plot(vLambdaValue,vBsMeasured(:,vN),'.r',vLambdaValue,vBsTheoryBest(:,vN),'.b'); hold
off;
        if vN==1, title('B'); end
        % legend('MeasErr','MeasErr','Measured','Theory');
        axis tight; grid on; xlabel('\lambda [nm]');
    end
    figure(2);
    for vN=1:length(vEpsilonFormula)
        subplot(length(vEpsilonFormula),2,vN*2-1);
        plot(vLambdaValue,real(vEpsilonBest{vN}),'.b');
        if vN==1, title('Real'); end
        axis tight; grid on; ylabel(sprintf('\\epsilon_%d',vN)); xlabel('\lambda [nm]');
        subplot(length(vEpsilonFormula),2,vN*2);
        plot(vLambdaValue,imag(vEpsilonBest{vN}),'.b');
        if vN==1, title('Imag'); end
        axis tight; grid on; xlabel('\lambda [nm]');
    end

    figure(3);
    for vN=1:length(vVarName)
        if vVarMax{vN}==vVarMin{vN}
            vTmp002(vN)=50;
        else
            vTmp002(vN)=100*(vVarBest{vN}-vVarMin{vN})/(vVarMax{vN}-vVarMin{vN});
        end
    end
    bar(vTmp002,'g'); axis tight; title('Varibles Place in Range');
    vTmp001=strvcat(vVarName);
    ylabel('[%]'); set(get(3,'children'),'XTickLabel',vTmp001);
    set(get(3,'children'),'XTickLabelMode','manual');
    set(get(3,'children'),'YLim',[0 100]); grid on;

    save(vFitSaveFile);

    if isempty(vChisqLast), vChisqLast=vChisqBest; end
    vTmp=figure(1);
    set(vTmp,'name',sprintf('%d | -%.5f | %.5f',vTmp,vChisqLast-vChisqBest,vChisqBest));
    if vChisqLast==vChisqBest, beep; end
    vChisqLast=vChisqBest;

  end
```

```
    pause(vFitPauseTime);
end
disp('=== Ended ===');
return;

%%%%%%%%%%%%%%%%%%%%%%%%%%%%%%%%%%%%%%%%
%%%%%%%%%%%%%%%%%%%%%%%%%%%%%%%%%%%%%%%%
%%% function FunLayerOptic
%%%%%%%%%%%%%%%%%%%%%%%%%%%%%%%%%%%%%%%%
%%%%%%%%%%%%%%%%%%%%%%%%%%%%%%%%%%%%%%%%
function [Out]=FunLayerOptic(RT,PS,N,D,theta,lambda)
theta=asin(N(1).*sin(theta)./N);
NumLayers=length(N);
if PS=='P'
   for n=1:NumLayers-1
      R=(N(n+1).*cos(theta(n))-
N(n).*cos(theta(n+1)))./(N(n+1).*cos(theta(n))+N(n).*cos(theta(n+1)));
      T=2.*N(n).*cos(theta(n))./(N(n+1).*cos(theta(n))+N(n).*cos(theta(n+1)));
      MS(1,1,n)=1./(1+R);
      MS(1,2,n)=R./(1+R);
      MS(2,1,n)=R./(1+R);
      MS(2,2,n)=1./(1+R);
   end
end
if PS=='S'
   for n=1:NumLayers-1
      R=(N(n).*cos(theta(n))-
N(n+1).*cos(theta(n+1)))./(N(n).*cos(theta(n))+N(n+1).*cos(theta(n+1)));
      T=2.*N(n).*cos(theta(n))./(N(n).*cos(theta(n))+N(n+1).*cos(theta(n+1)));
      MS(1,1,n)=1./(1+R);
      MS(1,2,n)=R./(1+R);
      MS(2,1,n)=R./(1+R);
      MS(2,2,n)=1./(1+R);
   end
end
for n=2:NumLayers-1
   Delta=2.*pi.*N(n).*cos(theta(n)).*D(n)./lambda;
   ML(1,1,n)=exp(-i.*Delta);
   ML(1,2,n)=0;
   ML(2,1,n)=0;
   ML(2,2,n)=exp(i.*Delta);
end
M=MS(:,:,1);
for n=2:NumLayers-1
   M=M*ML(:,:,n)*MS(:,:,n);
end
if RT=='R'
   Out=M(1,2)./M(2,2);
end
if RT=='T'
   Out=1./M(2,2);
end
```

Transmission Data Analysis Using Lorentz-Dielectric Function:

```
function TransMatlab()
close all; clc; pause(0.8);

%%% Load the Spec Data %%%

filename_data='ZNO002C.TXT';
fid=fopen(filename_data,'r');
for n=1:19
   tmp=fgetl(fid);
end
data=fscanf(fid,'%f',[2 inf]);
fclose(fid);
lambda=data(1,:);
Tmea=data(2,:)./100;

filename_glass='FUSDSILAA.TXT';
fid=fopen(filename_glass,'r');
for n=1:19
   tmp=fgetl(fid);
end
data=fscanf(fid,'%f',[2 inf]);
fclose(fid);
lambda=data(1,:);
Tglass=data(2,:)./100;

tmp=0;
for n=1:length(lambda)
   if lambda(n)>320 & lambda(n)<800
      tmp=tmp+1;
      tmp_n(tmp)=n;
   end
end
min_i=min(tmp_n);
max_i=max(tmp_n);
lambda=lambda(min_i:max_i);
Tmea=Tmea(min_i:max_i);
Tglass=Tglass(min_i:max_i);

lambda=lambda(1:1:length(lambda));
Tmea=Tmea(1:1:length(Tmea));
Tglass=Tglass(1:1:length(Tglass));

%%% Define the Variables %%%

fit_mod=1;
einf=3.6;        einf_min=2;        einf_max=4.5;     einf_diff=0.001;   einf_best=einf;
es=3.8;          es_min=2;          es_max=4.5;       es_diff=0.001;     es_best=es;
Eo=3.5;          Eo_min=2;          Eo_max=4.5;     Eo_diff=0.001;     Eo_best=Eo;
Gamma=0.1;   Gamma_min=0;    Gamma_max=2.5;  Gamma_diff=0.01;  Gamma_best=Gamma;
d=205;       d_min=100;     d_max=1200;   d_diff=0.1;       d_best=d;

%%% Start Fitting Loop %%%
flag=0;
```

```
fit_i=0;
while 0==0
   fit_i=fit_i+1;

   if fit_mod==1
      einf=einf_best+einf_diff*((rand>0.5)*2-1);
      if einf>einf_max | einf<einf_min, einf=einf_best; end
      es=es_best+es_diff*((rand>0.5)*2-1);
      if es>es_max | es<es_min, es=es_best; end
      Eo=Eo_best+Eo_diff*((rand>0.5)*2-1);
      if Eo>Eo_max | Eo<Eo_min, Eo=Eo_best; end
      Gamma=Gamma_best+Gamma_diff*((rand>0.5)*2-1);
      if Gamma>Gamma_max | Gamma<Gamma_min, Gamma=Gamma_best; end
      d=d_best+d_diff*((rand>0.5)*2-1);
      if d>d_max | d<d_min, d=d_best; end

   end

   if fit_mod==2
      einf=einf_min+(einf_max-einf_min)*rand;
      es=es_min+(es_max-es_min)*rand;
      Eo=Eo_min+(Eo_max-Eo_min)*rand;
      Gamma=Gamma_min+(Gamma_max-Gamma_min)*rand;
      d=d_min+(d_max-d_min)*rand;
   end

  %%% Calc.. the Other Variables %%%

   E=1240./lambda;
   n1=1*lambda./lambda;
   k1=0*lambda./lambda;
   e=einf+(es-einf).*Eo.^2./(Eo.^2-E.^2-i*Gamma.*E);
   n2=real(sqrt(e));
   k2=imag(sqrt(e));
   n3=(1+(1-Tglass.^2).^0.5)./Tglass;
   k3=0*lambda./lambda;

   rho=((n1-n3).^2+k3.^2)./((n1+n3).^2+k3.^2);
   fi=4*pi*n2*d./lambda;
   alfad=4*pi*k2*d./lambda;
   Ts=(1-rho)./(1+rho);
   u=(n1-n2).^2+k2.^2;
   v=(n2-n3).^2+k2.^2;
   s=(n1+n2).^2+k2.^2;
   t=(n2+n3).^2+k2.^2;
   Y=n2.^2-n1.^2+k2.^2;
   Z=n2.^2-n3.^2+k2.^2;
   U=(1-rho).^2/(2.*Ts)+((1-rho).^4./(4*Ts.^2)+rho.^2).^0.5;
   U=1./U;
   A=16*n3.*(1-rho).*(n2.^2+k2.^2).*U;
   B=s.*t-U.*s.*v.*rho;
   C=(2*(4*n3.*k2.^2-Z.*Y).*cos(fi)+4*k2.*(n3.*Y+Z).*sin(fi))-rho.*U.^2.*(4.*k2.*(Z-
n3.*Y).*sin(fi)-2*(Z.*Y+4*n3.*k2.^2).*cos(fi));
   D=u.*v-U.^2.*t.*u.*rho;
   Tcal=A.*exp(alfad)./(B.*exp(2.*alfad)+C.*exp(alfad)+D);
```

```
%%% Calc. chisq %%%

chisq=sum((Tcal-Tmea).^2)/length(lambda);

%%% Choose Best %%%
if flag==0
   chisq_best=chisq;
   einf_best=einf;
   es_best=es;
   Eo_best=Eo;
   Gamma_best=Gamma;
   d_best=d;
   flag=1;
end
if chisq<chisq_best
   chisq_best=chisq;
   einf_best=einf;
   es_best=es;
   Eo_best=Eo;
   Gamma_best=Gamma;
   d_best=d;
end

%%% Print Data %%%
if mod(fit_i,100)==1
   einf=einf_best;
   es=es_best;
   Eo=Eo_best;
   Gamma=Gamma_best;
   d=d_best;
   E=1240./lambda;
   n1=1*lambda./lambda;
   k1=0*lambda./lambda;
   e=einf+(es-einf).*Eo.^2./(Eo.^2-E.^2-i*Gamma.*E);
   n2=real(sqrt(e));
   k2=imag(sqrt(e));
   n3=(1+(1-Tglass.^2).^0.5)./Tglass;
   k3=0*lambda./lambda;
   rho=((n1-n3).^2+k3.^2)./((n1+n3).^2+k3.^2);
   fi=4*pi*n2*d./lambda;
   alfad=4*pi*k2*d./lambda;
   Ts=(1-rho)./(1+rho);
   u=(n1-n2).^2+k2.^2;
   v=(n2-n3).^2+k2.^2;
   s=(n1+n2).^2+k2.^2;
   t=(n2+n3).^2+k2.^2;
   Y=n2.^2-n1.^2+k2.^2;
   Z=n2.^2-n3.^2+k2.^2;
   U=(1-rho).^2/(2.*Ts)+((1-rho).^4./(4*Ts.^2)+rho.^2).^0.5;
   U=1./U;
   A=16*n3.*(1-rho).*(n2.^2+k2.^2).*U;
   B=s.*t-U.*s.*v.*rho;
   C=(2*(4*n3.*k2.^2-Z.*Y).*cos(fi)+4*k2.*(n3.*Y+Z).*sin(fi))-rho.*U.^2.*(4.*k2.*(Z-
n3.*Y).*sin(fi)-2*(Z.*Y+4*n3.*k2.^2).*cos(fi));
   D=u.*v-U.^2.*t.*u.*rho;
```

```
      Tcal=A.*exp(alfad)./(B.*exp(2.*alfad)+C.*exp(alfad)+D);
      figure(1);
      plot(lambda,n2,'-');
      xlabel('Wavelength (nm)')
      ylabel('n')
     figure(2);
      plot(lambda,k2,'-');
      xlabel('Wavelength (nm)')
      ylabel('k')
      figure (3);
      plot(lambda,Tcal*100,'--',lambda,Tmea*100,'-');
      xlabel('Wavelength (nm)')
      ylabel('Transmission T%')
      legend('Theoretical','Experimental')
      fprintf('fit_i=%d\n',fit_i);
      fprintf('chisq_best=%.15f\n',chisq_best);
      fprintf('einf_best=%f',einf_best); fprintf(' [%.3f%%]\n',100*(einf_best-einf_min)./(einf_max-
einf_min));
      fprintf('es_best=%f',es_best); fprintf(' [%.3f%%]\n',100*(es_best-es_min)./(es_max-es_min));
      fprintf('Eo_best=%f',Eo_best); fprintf(' [%.3f%%]\n',100*(Eo_best-Eo_min)./(Eo_max-
Eo_min));
      fprintf('Gamma_best=%f',Gamma_best); fprintf(' [%.3f%%]\n',100*(Gamma_best-
Gamma_min)./(Gamma_max-Gamma_min));
      fprintf('d_best=%f',d_best); fprintf(' [%.3f%%]\n',100*(d_best-d_min)./(d_max-d_min));
      pause(1);
      clc;
   end
end
```

CURRICULUM VITAE

Eda Çetinörgü was born in Germany in 1974. She finished Çukurova Anatolian Technical High School, and continued her studies in Physics in University of Çukurova obtaining a BSc in Physics in 1999 and MSc in Physics in 2001. She wrote a master thesis on the subject “Chemical Bath deposited CdS thin Films” under the supervison of Prof. Esen. She continued her Ph.D. research under the supervison of Prof. Ufuktepe. Her research was performed at the Laboratory of Electrical Discharges and Plasma at Tel Aviv University, under the supervison of Prof. S. Goldsmith and Prof. R.L. Boxman. Her research was on characteristics of ZnO-SnO_2 thin films deposited by Filtered Vacuum Arc. In 2006, she presented in the international conference on metallurgical coatings and thin films her study of the optical characteristics of ZnO-SnO_2 thin films.